

N72 -13811
NASA CR 121047

GEOTECHNICAL ENGINEERING

LUNAR SURFACE ENGINEERING PROPERTIES EXPERIMENT DEFINITION

FINAL REPORT: VOLUME I OF IV
MECHANICS, PROPERTIES, AND STABILIZATION OF
LUNAR SOILS

by

J. K. MITCHELL
W. N. HOUSTON
T. S. VINSON
T. DURGUNOGLU
L. I. NAMIQ
J. B. THOMPSON
D. D. TREADWELL

**CASE FILE
COPY**

PREPARED FOR GEORGE C. MARSHALL SPACE FLIGHT CENTER
HUNTSVILLE, ALABAMA, UNDER NASA CONTRACT NAS 8-21432

JULY 1971

SPACE SCIENCES LABORATORY



UNIVERSITY OF CALIFORNIA • BERKELEY

Space Sciences Laboratory
University of California
Berkeley, California 94720

LUNAR SURFACE ENGINEERING PROPERTIES EXPERIMENT DEFINITION

FINAL REPORT: VOLUME I OF IV

MECHANICS, PROPERTIES, AND STABILIZATION OF LUNAR SOILS

by

J. K. Mitchell
W. N. Houston
T. S. Vinson
T. Durgunoglu
L. I. Namiq
J. B. Thompson
D. D. Treadwell

Prepared for Marshall Space Flight Center,
Huntsville, Alabama, under NASA Contract
NAS 8-21432.

Control Number DCN 1-X-80-00058 S1 (IF)

July 1971

Space Sciences Laboratory Series 11 Issue 48

This report was prepared by the University of California, Berkeley, under Contract Number NAS 8-21432, Lunar Surface Engineering Properties Experiment Definition, for the George C. Marshall Space Flight Center of the National Aeronautics and Space Administration. The work was administered under the technical direction of the Space Sciences Laboratory of the George C. Marshall Space Flight Center.

PREFACE

This report presents the results of studies conducted during the period July 19, 1969 – July 19, 1970, under NASA Research Contract NAS 8-21432, "Lunar Surface Engineering Properties Experiment Definition." This study was sponsored by the Lunar Exploration Office, NASA Headquarters, and was under the technical cognizance of Dr. N. C. Costes, Space Science Laboratory, George C. Marshall Space Flight Center.

The report reflects the combined effort of five faculty investigators, a research engineer, a project manager, and eight graduate research assistants, representing several engineering and scientific disciplines pertinent to the study of lunar surface material properties. James K. Mitchell, Professor of Civil Engineering, served as Principal Investigator and was responsible for those phases of the work concerned with problems relating to the engineering properties of lunar soils and lunar soil mechanics. Co-investigators were William N. Houston, Assistant Professor of Civil Engineering, who was concerned with problems relating to the engineering properties of lunar soils; Richard E. Goodman, Associate Professor of Geological Engineering, who was concerned with the engineering geology and rock mechanics aspects of the lunar surface; Paul A. Witherspoon, Professor of Geological Engineering, who was concerned with fluid conductivity of lunar surface materials in general; Franklin C. Hurlbut, Professor of Aeronautical Science, who was concerned with experimental studies on fluid conductivity of lunar surface materials; and D. Roger Willis, Associate Professor of Aeronautical Science, who conducted theoretical studies on fluid conductivity of lunar surface materials. Dr. Karel Drozd, Assistant Research Engineer, performed laboratory tests and analyses pertinent to the development of a borehole jack for determination of the in situ characteristics of lunar soils and rocks; he also helped in the design of the borehole jack. H. Turan Durgunoglu, H. John Hovland, Laith I. Namiq, Parabaronen Raghuraman, James B. Thompson, Donald D. Treadwell, C. Robert Jih, Suphon Chirapuntu, and Tran K. Van served as Graduate Research Assistants and carried out many of the studies leading to the results presented in this

report. Ted S. Vinson, Research Engineer, served as project manager until May 1970, and contributed to studies concerned with lunar soil stabilization. H. John Hovland served as project manager after May 1970, and contributed to studies concerned with soil property evaluation from lunar boulder tracks.

Ultimate objectives of this project were:

- 1) Assessment of lunar soil and rock property data using information obtained from Lunar Orbiter, Surveyor, and Apollo missions.
- 2) Recommendation of both simple and sophisticated in situ testing techniques that would allow determination of engineering properties of lunar surface materials.
- 3) Determination of the influence of variations in lunar surface conditions on the performance parameters of a lunar roving vehicle.
- 4) Development of simple means for determining the fluid conductivity properties of lunar surface materials.
- 5) Development of stabilization techniques for use in loose, unconsolidated lunar surface materials to improve the performance of such materials in lunar engineering application.

The scope of specific studies conducted in satisfaction of these objectives is indicated by the following list of contents from the Detailed Final Report which is presented in four volumes. The names of the investigators associated with each phase of the work are indicated.

VOLUME I

MECHANICS, PROPERTIES, AND STABILIZATION OF LUNAR SOILS

1. Lunar Soil Simulant Studies
W. N. Houston, L. I. Namiq, J. K. Mitchell, and D. D. Treadwell
2. Determination of In Situ Soil Properties Utilizing an Impact Penetrometer
J. B. Thompson and J. K. Mitchell
3. Lunar Soil Stabilization Using Urethane Foamed Plastics
T. S. Vinson, T. Durgunoglu, and J. K. Mitchell
4. Feasibility Study of Admixture Soil Stabilization with Phenolic Resins
T. Durgunoglu and J. K. Mitchell

VOLUME II

MECHANICS OF ROLLING SPHERE-SOIL SLOPE INTERACTION

H. J. Hovland and J. K. Mitchell

1. Introduction
2. Analysis of Lunar Boulder Tracks
3. Model Studies of the Failure Mechanism Associated with a Sphere Rolling Down a Soil Slope
4. Pressure Distribution and Soil Failure Beneath a Spherical Wheel in Air-Dry Sand
5. Theoretical Studies
6. Rolling Sphere Experiments and Comparison with Theoretical Predictions
7. Utilization of Developed Theory
8. Conclusions and Recommendations

VOLUME III

BOREHOLE PROBES

1. Summary of Previous Work
R. E. Goodman, T. K. Van, and K. Drozd
2. An Experimental Study of the Mechanism of Failure of Rocks
Under Borehole Jack Loading
T. K. Van and R. E. Goodman
3. A Borehole Jack for Deformability, Strength, and Stress
Measurements in a 2-inch Borehole
R. E. Goodman, H. J. Hovland, and S. Chirapuntu

VOLUME IV

FLUID CONDUCTIVITY OF LUNAR SURFACE MATERIALS

1. Studies on Fluid Conductivity of Lunar Surface Materials —
Theoretical Studies
P. Raghuraman and D. R. Willis
2. Studies on Fluid Conductivity of Lunar Surface Materials —
Experimental Studies
F. C. Hurlbut, C. R. Jih, and P. A. Witherspoon

VOLUME I

CONTENTS

	Page
PREFACE	iii
CHAPTER 1. LUNAR SOIL SIMULANT STUDIES	1-1
W. N. Houston, L. I. Namiq, J. K. Mitchell, and D. D. Treadwell	
INTRODUCTION	1-1
MODIFICATION OF LUNAR SOIL SIMULANT	1-1
STRENGTH AND STRESS-STRAIN CHARACTERISTICS	1-5
Principal Stress Difference at Failure σ_{df}	1-7
Cohesion, c	1-10
Friction Angle, ϕ	1-13
Axial Strain at Failure, ϵ_{af}	1-13
Tangent Modulus for Plane Strain, E_{tps}	1-17
Ratio of Lateral Strain to Axial Strain at Failure, $(\epsilon_l/\epsilon_a)_f$	1-27
Tangential Lateral Strain Ratio for Plane Strain, $(\epsilon_l/\epsilon_a)_{tps}$	1-31
Principal Stress Difference at Failure, σ_{df}	1-39
Axial Strain at Failure, ϵ_{af}	1-39
Tangent Modulus for Plane Strain, E_{tps}	1-39
Ratio of Lateral Strain to Axial Strain at Failure, $(\epsilon_l/\epsilon_a)_f$	1-39
Tangential Lateral Strain Ratio, $(\epsilon_l/\epsilon_a)_{tps}$	1-40
ONE-DIMENSIONAL COMPRESSION CHARACTERISTICS	1-41
DETERMINATION OF DENSITY VARIATION WITH DEPTH	1-52
PLATE LOAD TESTS	1-55
Soil Placement	1-60

VOLUME I (Cont'd)

	Page
Test Plates	1-65
Test Procedure	1-65
Basic Test Data	1-66
BOOT IMPRINT TESTS	1-79
PENETROMETER TESTS	1-82
CORE TUBE STUDIES	1-93
Requirements	1-101
CONCLUSIONS	1-102
RECOMMENDATIONS	1-104
SYMBOLS	1-106
REFERENCES	1-109
 CHAPTER 2. DETERMINATION OF IN SITU SOIL PROPERTIES UTILIZING	
AN IMPACT PENETROMETER	2-1
J. B. Thompson and J. K. Mitchell	
INTRODUCTION	2-1
LITERATURE REVIEW	2-3
Theoretical Investigations	2-4
Experimental Investigations	2-4
Statistical Investigations	2-4
QUALITATIVE STATE OF THE ART	2-56
Effect of Penetrometer Characteristics	2-56
Pre-Impact Flight Parameters	2-56
Effect of Soil Parameters	2-57
Effect of Air Pressure	2-58

VOLUME I (Cont'd)

	Page
THEORETICAL APPROACH	2-59
Existing Theoretical Solutions	2-60
Another Theoretical Approach Evaluated	2-62
Conclusions	2-62
EMPIRICAL APPROACH	2-63
Existing Empirical Analytical Expressions	2-63
Extrapolation to the Lunar Environment	2-65
Conclusions	2-65
EXPERIMENTAL PROGRAM	2-66
Dependent Variables	2-66
Penetrometer	2-66
Soils	2-67
Independent Variables	2-67
Velocity Generating and Measuring Devices	2-68
Vacuum Chamber	2-70
Conclusion	2-70
CONCLUSIONS	2-70
SYMBOLS	2-72
REFERENCES	2-74
 CHAPTER 3. LUNAR SOIL STABILIZATION USING URETHANE FOAMED PLASTICS	 3-1
T. S. Vinson, T. Durgunoglu, and J. K. Mitchell	
INTRODUCTION	3-1
PREVIOUS STUDIES	3-2
Chemistry of Polyurethane Foamed Plastics	3-2

VOLUME I (Cont'd)

	Page
Experimental Laboratory Results	3-3
DESIGN AND PERFORMANCE OF VACUUM APPARATUS	3-8
Introduction	3-8
Design and Performance of Vacuum Apparatus	3-8
FOAM FORMATION IN VACUO	3-13
Theory	3-13
Experimental Results	3-13
ADMIXTURE STABILIZATION	3-19
CONCLUSIONS AND RECOMMENDATIONS	3-21
Lunar Soil Stabilization by Soil Grouting	3-21
Admixture Lunar Soil Stabilization Using Urethane Foamed Plastics	3-21
Pour and Spray-on Urethane Foam System Applications	3-21
REFERENCES	3-22
 CHAPTER 4. FEASIBILITY STUDY OF ADMIXTURE SOIL STABILIZATION WITH PHENOLIC RESINS	4-1
T. Durgunoglu and J. K. Mitchell	
INTRODUCTION	4-1
LABORATORY PRECEDURES	4-1
Chemistry of Phenolic Resins	4-1
Analytical Laboratory Procedure	4-5
Experimental Laboratory Procedure	4-7
RESIN SYSTEMS DEVELOPED	4-9
ENGINEERING PROPERTIES OF STABILIZED SOIL MASSES	4-9
SUMMARY AND CONCLUSIONS	4-9
REFERENCES	4-13

VOLUME I

Mechanics, Properties, and Stabilization of Lunar Soils

Chapter 1. LUNAR SOIL SIMULANT STUDIES

W. N. Houston, L. I. Namiq, J. K. Mitchell, and D. D. Treadwell*

INTRODUCTION

The study of lunar soil properties has been continued using simulated lunar soil. To better represent the actual lunar soil as revealed by the Apollo 11 and 12 missions, the lunar soil simulant used in previous studies (Mitchell and Houston, 1970), was modified as described in the following sections.

Special emphasis was placed on the determination of stress-strain, strength, compressibility, and trafficability parameters and their variations with density. Stress-deformation characteristics were determined through plate-load, boot-imprint, and penetrometer tests.

The lunar soil simulant was also used in feasibility studies for several simple geotechnical tests, which have been proposed for later Apollo missions. These include penetrometer tests, plate load tests, trenching, and core tube sampling. The results of these studies with the lunar soil simulant are being used as a basis for recommendations for modification of existing Apollo hand tools and for the design of new devices for the in situ study of lunar surface materials.

MODIFICATION OF LUNAR SOIL SIMULANT

The lunar soil simulant used prior to August 1969 is described in detail in Volume 1 of the Final Report (Mitchell and Houston, 1970). The selection of this simulant, hereafter referred to as Lunar Soil Simulant No. 1 (LSS No. 1), was based primarily on the results of early Surveyor missions.

*D. D. Treadwell's contribution is primarily in connection with the core tube studies.

Following the Apollo 11 mission, gradation data for the actual lunar soil were obtained in the Lunar Receiving Laboratory, MSFC. The data obtained were most reliable for the particle size distribution in the coarse range. It was found, for example, that the per cent larger than 1 mm was about 7 to 10. Unfortunately, the gradation data for sizes less than the No. 100 sieve were not as reliable because only dry sieving (in a nitrogen atmosphere) was used and the fine particles were observed to aggregate, as do most terrestrial soils in this size range.

Additional data of great value were obtained on earth-returned samples of Apollo 11 material by performing penetration tests using 1/4-inch-diameter rod on the material packed in a 3.5-inch-diameter, 2-inch high container (Costes et al., 1970). These tests were performed using the minus-1-mm fraction of the soil. A similar series of 1/4-inch-rod penetration tests were performed on the minus-1-mm fraction of Lunar Soil Simulant No. 1. For each series, the value of G (the slope of the stress-penetration curve) was plotted against void ratio, e . Void ratio rather than density was used, because the value of specific gravity for the Apollo 11 soil, 3.1, differed significantly from the value 2.88 for LSS No. 1. Figure 1-1 may be used to convert void ratio to density for the actual lunar soil and the lunar soil simulant.

Penetration test results for the two soils are compared in Figure 1-2. The excellent agreement for the G -void ratio relationships indicates that the minus-1-mm fraction of LSS No. 1 is a good match for the minus-1-mm fraction of the Apollo 11, at least in regard to penetration resistance behavior of the material. It follows that if the plus-1-mm fraction of LSS No. 1 could be made similar to that of Apollo 11 soil, a good match overall could be obtained. As a matter of fact, however, the gradation data for the Apollo 11 material show that the per cent plus-1-mm is sufficiently small that the characteristics of this fraction should be relatively unimportant in influencing the mechanical behavior of the whole soil.

On the basis of these test results and observations, it was decided to reduce the percentage of plus-1-mm material in LSS No. 1 from the original value of 30 to a value of 7 to 10, so as to more closely match the Apollo 11 material. To produce the 7000 lb of simulant needed for

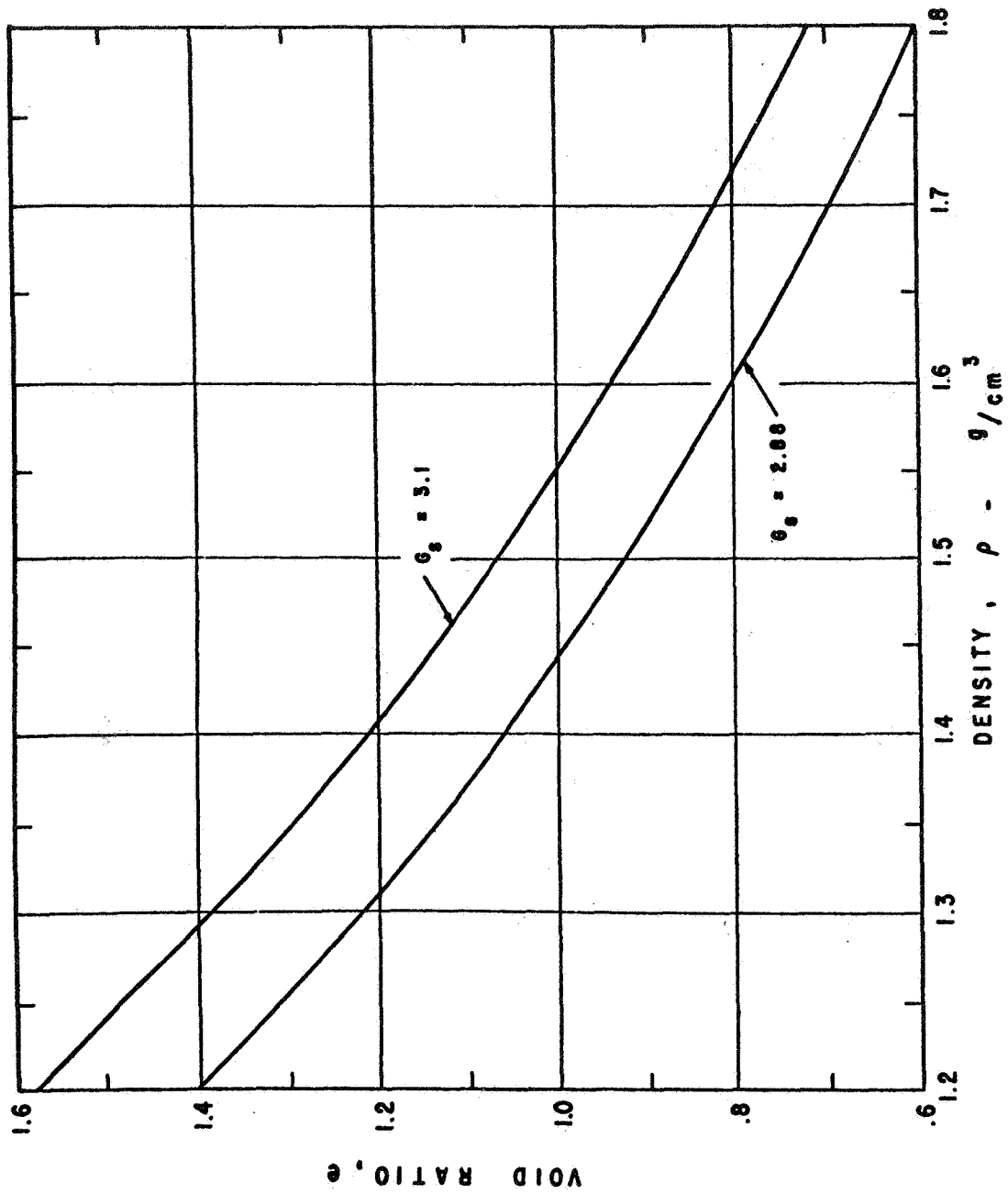


Fig. 1-1. Relationship between void ratio and density for lunar soil ($G_s = 3.1$, Costes et al., 1970) and lunar soil simulants ($G_s = 2.88$).

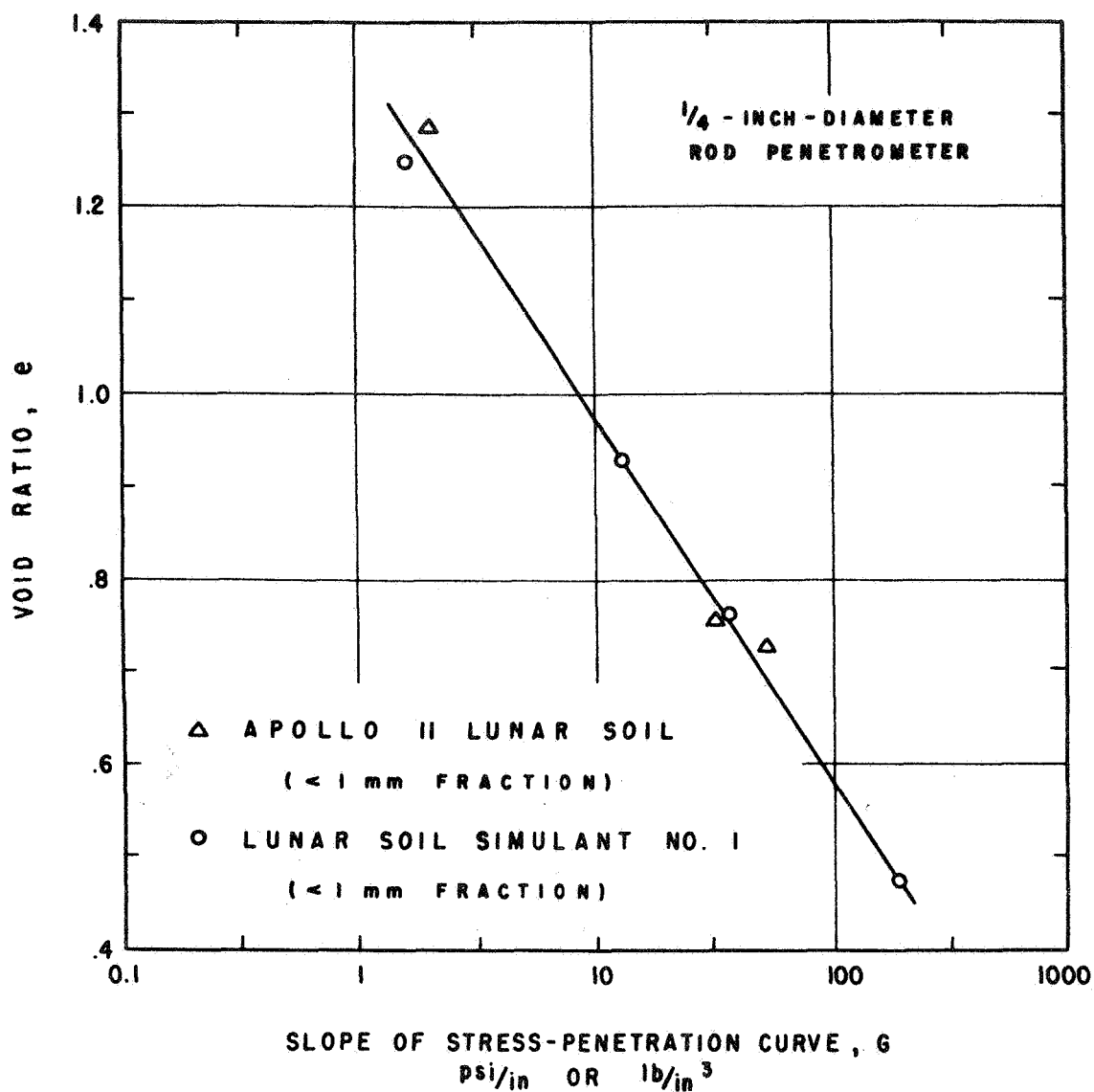


Fig. 1-2. Relationship between G and void ratio for Apollo 11 lunar soil, Costes et al. (1970), and for Lunar Soil Simulant No. 1.

large-scale model testing, it was necessary to sieve and mix some additional stock material, as was done in the preparation of LSS No. 1. The sieving and mixing operations were accomplished as described in the Final Report of January 1970 (Mitchell and Houston, Vol. I). Reprocessing and preparation were accomplished over a period of about 4 months and the modified gradation obtained is shown in Figure 1-3 as Lunar Soil Simulant No. 2 (LSS No. 2).

Subsequently, a more reliable gradation curve for the soil returned by Apollo 11 was obtained, and the gradation for the Apollo 12 core tube samples became available. These curves are shown in Figure 1-3.

STRENGTH AND STRESS-STRAIN CHARACTERISTICS

Vacuum plane strain shear tests were conducted on specimens representing a range of different initial void ratios. Plane strain tests were used because plate load deformation, boot imprints, trench wall failures, and most foundation deformations are closer to plane strain than the triaxial loading conditions. The tests were conducted at a constant rate of deformation of 0.03 inch per minute on specimens with confining pressures ranging from 0.05 to 0.4 kg/cm². Specimen dimensions before the application of confining pressure were 11.5 cm in length, 4.6 cm in width, and about 15 cm in height. The deviator load applied to the specimen was measured with a load cell; the axial deformation was measured with a dial gage. The volume change during the duration of the test was monitored by the movement of a water bubble in the vacuum line. A confining pressure of about 0.05 kg/cm² was found to be about the lowest value which could be used, because for lower values membrane corrections became too large relative to the strength. A constant water content of 1.9% was used for the test series discussed in the following paragraphs. Corresponding values of the various parameters were determined for a second test series at $w = 1.0\%$. These values are presented at the end of this section.

The preparation of specimens such that they would have the same void ratio under different confining pressures was attempted but found to be nearly impossible without repeated trials. Therefore, specimens were

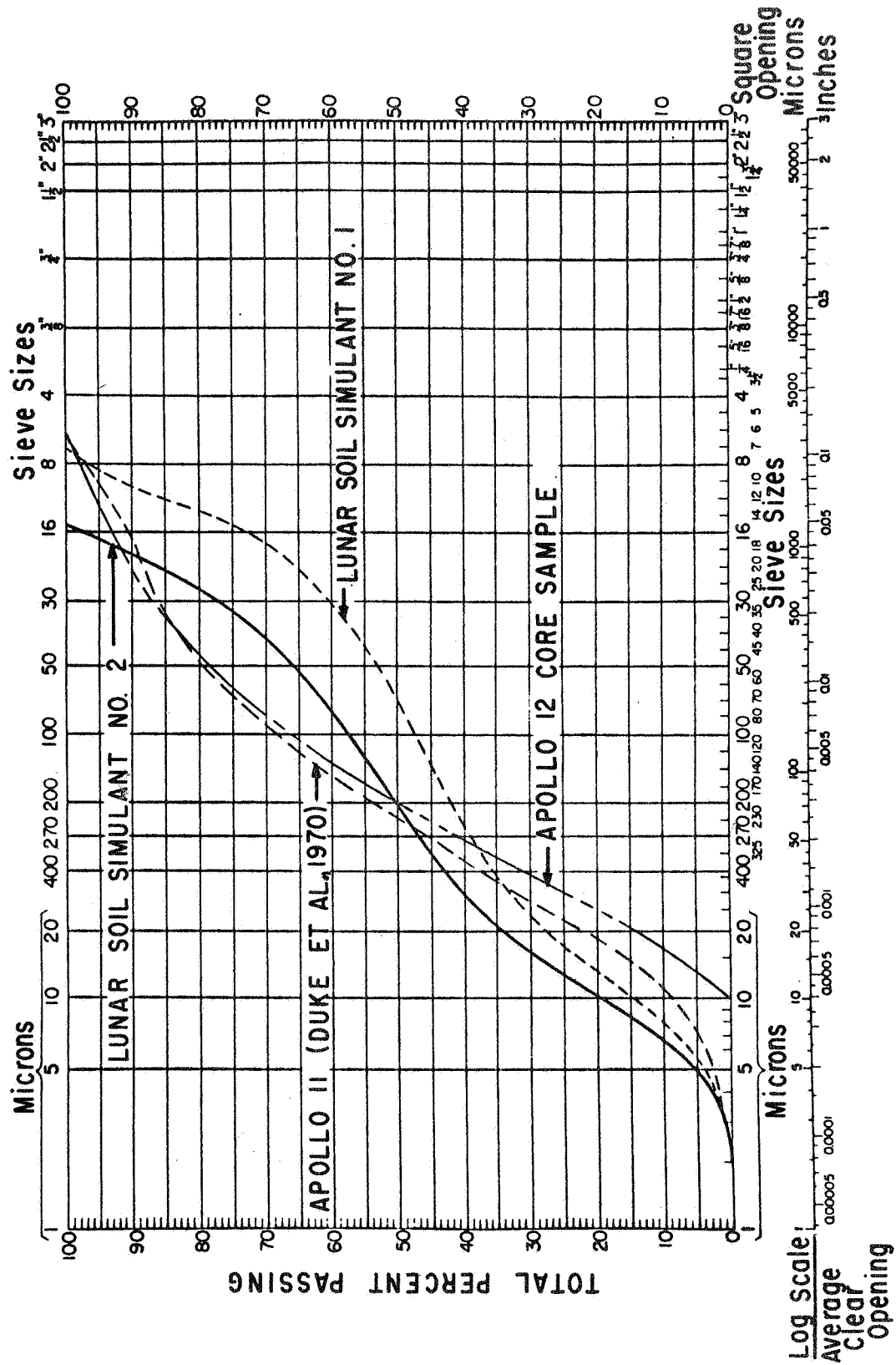


Fig. 1-3. Gradation curves for Lunar Soil Simulants Nos. 1 and 2 and Apollo 11 and 12 material.

prepared over a range of void ratios for each confining pressure, thus enabling determination of results for any void ratio by interpolation. Due to changing membrane correction during each test and from test to test, it was also found impossible to hold the confining pressure precisely constant during the shear test. These difficulties made it necessary to develop a series of cross-plots so as to relate the strength and stress-strain parameters of interest to void ratio. The procedures used are described in the following paragraphs.

Principal Stress Difference at Failure σ_{df}

The test data indicated that the principal stress ratios at failure $(\sigma_1/\sigma_3)_f$, varied linearly with the log of e_c (the void ratio after the application of confining pressure but before shear) for different values of the minor principal stress at failure, σ_{3f} . Figure 1-4a shows this relationship for LSS No. 2 at a water content of 1.9%. The lines shown in Figure 1-4a were located on the basis of both the data points indicated and previous experience and test results which indicated that curves of this type do not cross. The principal stress difference at failure, σ_{df} , for constant values of e_c but at different values of σ_{3f} , could be determined from Figure 1-4a. The relationship between $\log \sigma_{df}$ and e_c for different values of σ_{3f} was found to be linear, as shown in Figure 1-4b. Values of σ_{df} and σ_{3f} from Figure 1-4 were used to generate the linear relationship for any void ratio between $\log \sigma_{df}$ and $\log \sigma_{3f}$, shown in Figure 1-5. A linear relationship between $\log \sigma_{df}$ and $\log \sigma_{3f}$ has been found for other granular soils. This relationship can be expressed mathematically as a parabola:

$$\sigma_{df} = I \left(\frac{\sigma_{3f}}{0.1} \right)^{G_f} \quad (\text{for } \sigma_{3f} \text{ and } \sigma_{df} \text{ in kg/cm}^2), \quad (1-1)$$

where

I = intercept, a function of e_c at $\sigma_{3f} = 0.1 \text{ kg/cm}^2$

G_f = slope of the relationship between $\log \sigma_{df}$ and $\log \sigma_{3f}$
 = 0.875 (a constant for all values of e_c).

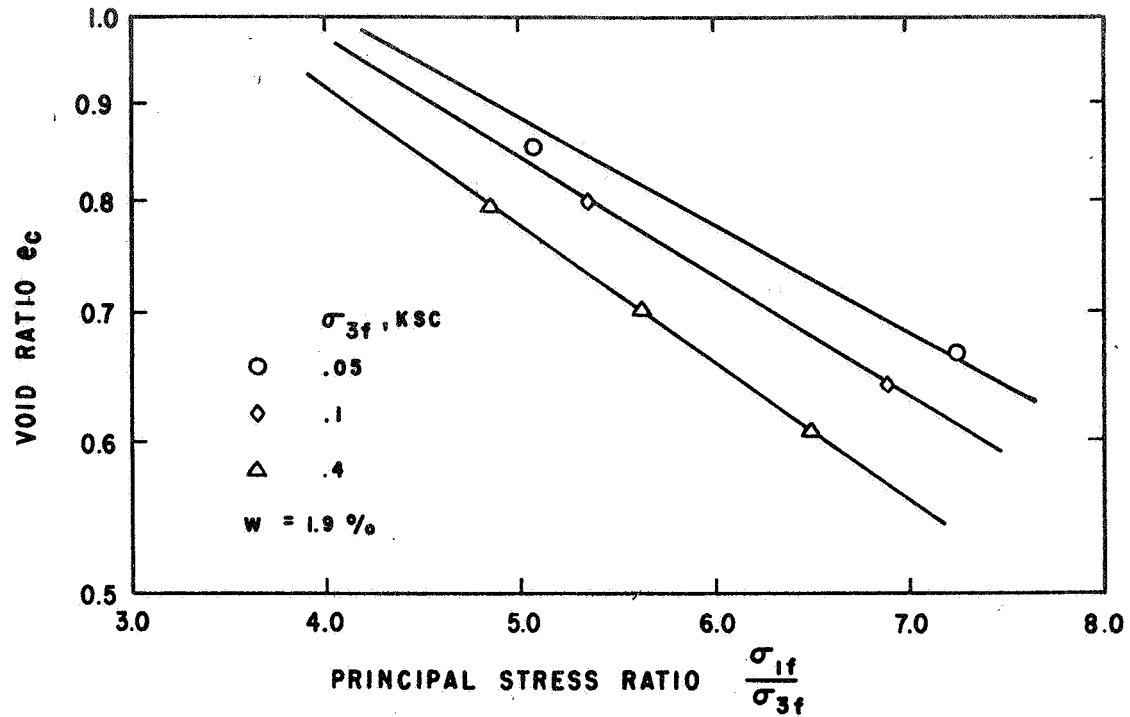


Fig. 1-4a. Variation of principal stress ratio at failure with void ratio for various values of confining pressure.

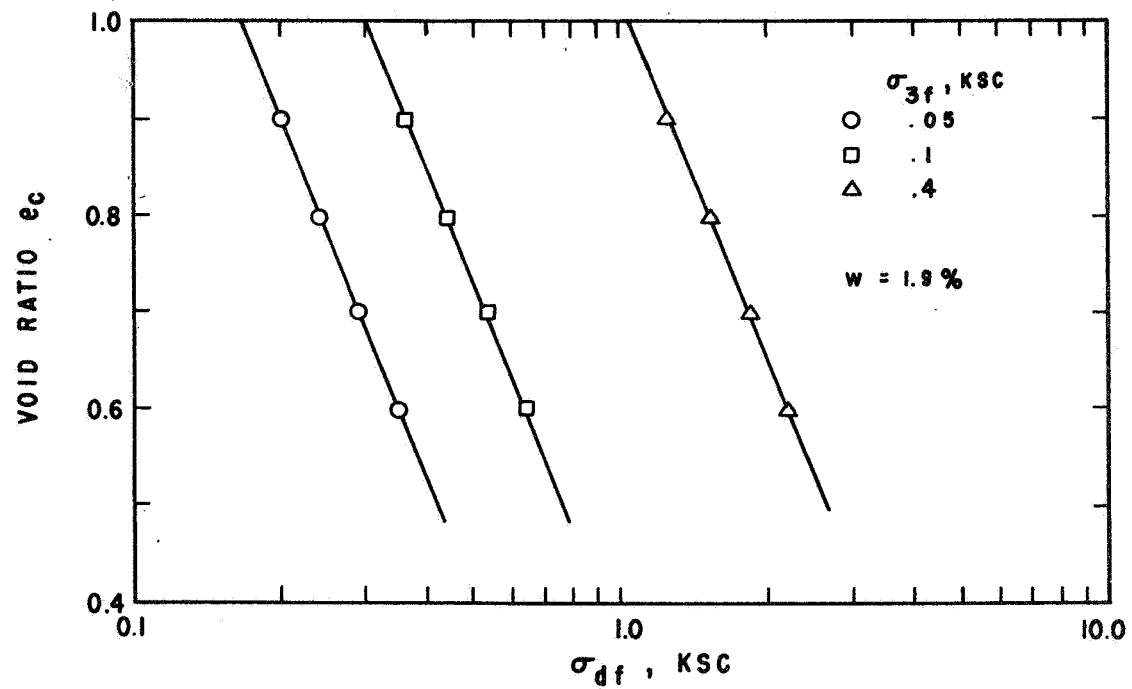


Fig. 1-4b. Variation of principal stress difference at failure with void ratio.

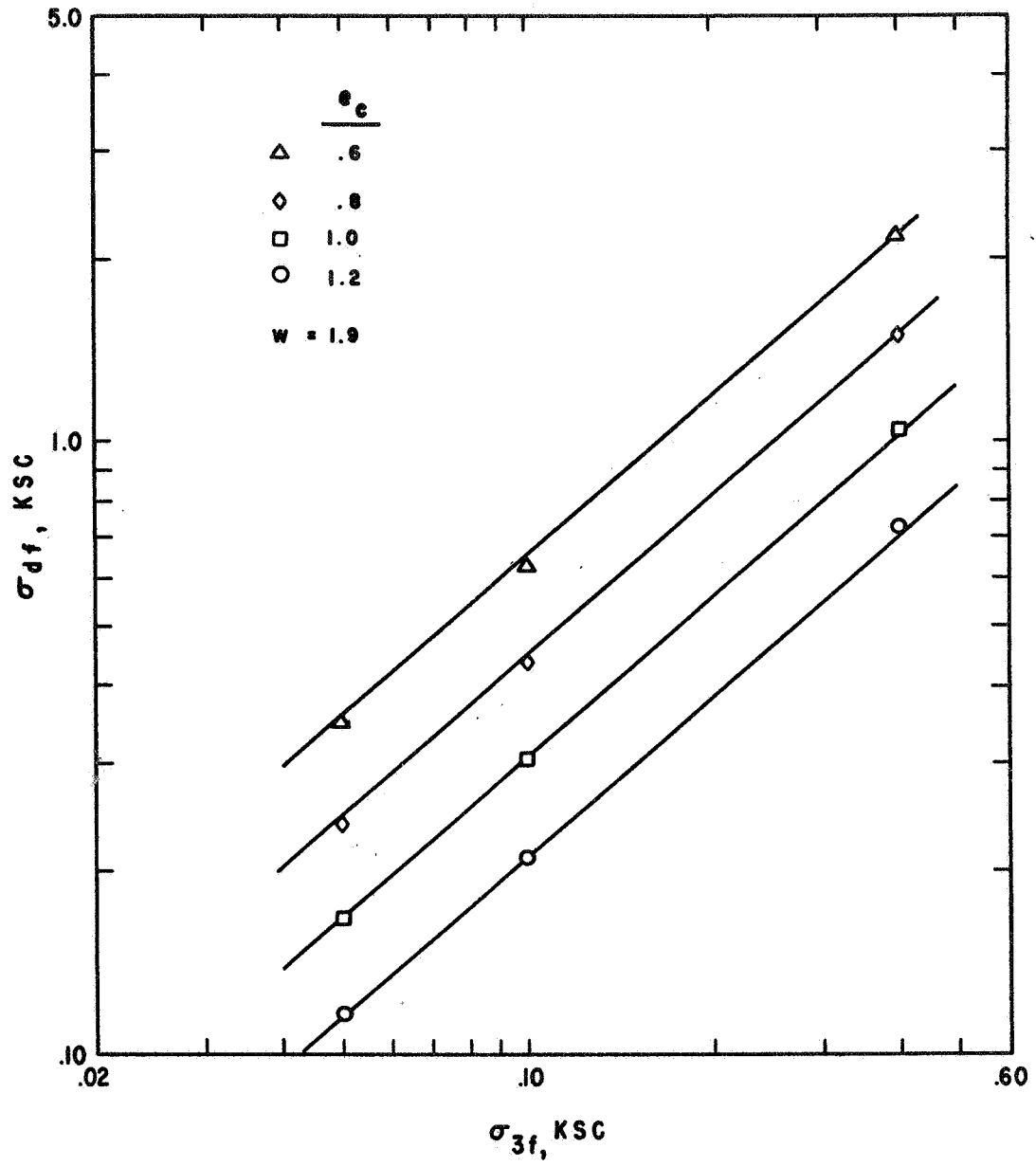


Fig. 1-5. Variation of principal stress difference at failure with confining pressure.

Equation (1-1) was chosen to relate σ_{df} and σ_{3f} rather than the usual $c - \tan \phi$ relationship, because ϕ was found to vary slightly with confining pressure.

It was found that $\log I$ varies linearly with e_c , as shown in Figure 1-6. This variation is described by the following equation:

$$I = \frac{L_0}{M e_c^{(10)}} \quad (1-2)$$

where $L_0 = 1.99$

and $M = 0.815$

for LSS No. 2 at $w = 1.9\%$.

Hence, the value of the principal stress difference at failure, σ_{df} , can readily be determined for any void ratio and confining pressure using Equation (1-1).

It is important to note, however, that while Equation (1-1) indicates that, for $\sigma_{3f} = 0$, $\sigma_{df} = 0$, the LSS does have a finite cohesion (as discussed in following paragraphs). Therefore, the lower limiting value of σ_{df} is $2c$, where c = cohesion.

Cohesion, c .

The variation of cohesion, c , with void ratio, e , has been determined by excavating trenches with vertical walls in the lunar soil simulant as previously described in detail (Mitchell and Houston, Jan. 1970, Final Report, Vol. I). Figure 1-7 shows the values obtained. It was found that the variation of cohesion with void ratio was about the same for LSS No. 2 as for LSS No. 1, with the values of cohesion for LSS No. 2 at $w = 2.0\%$ about the same as those for LSS No. 1 at $w = 1.8\%$.

The relationship between cohesion (c) and void ratio for LSS No. 2 ($w = 2.0\%$) can be represented mathematically, within the range of void ratios of interest, as follows:

$$c = \frac{333}{(10)^{2.22 e}} \quad (1-3)$$

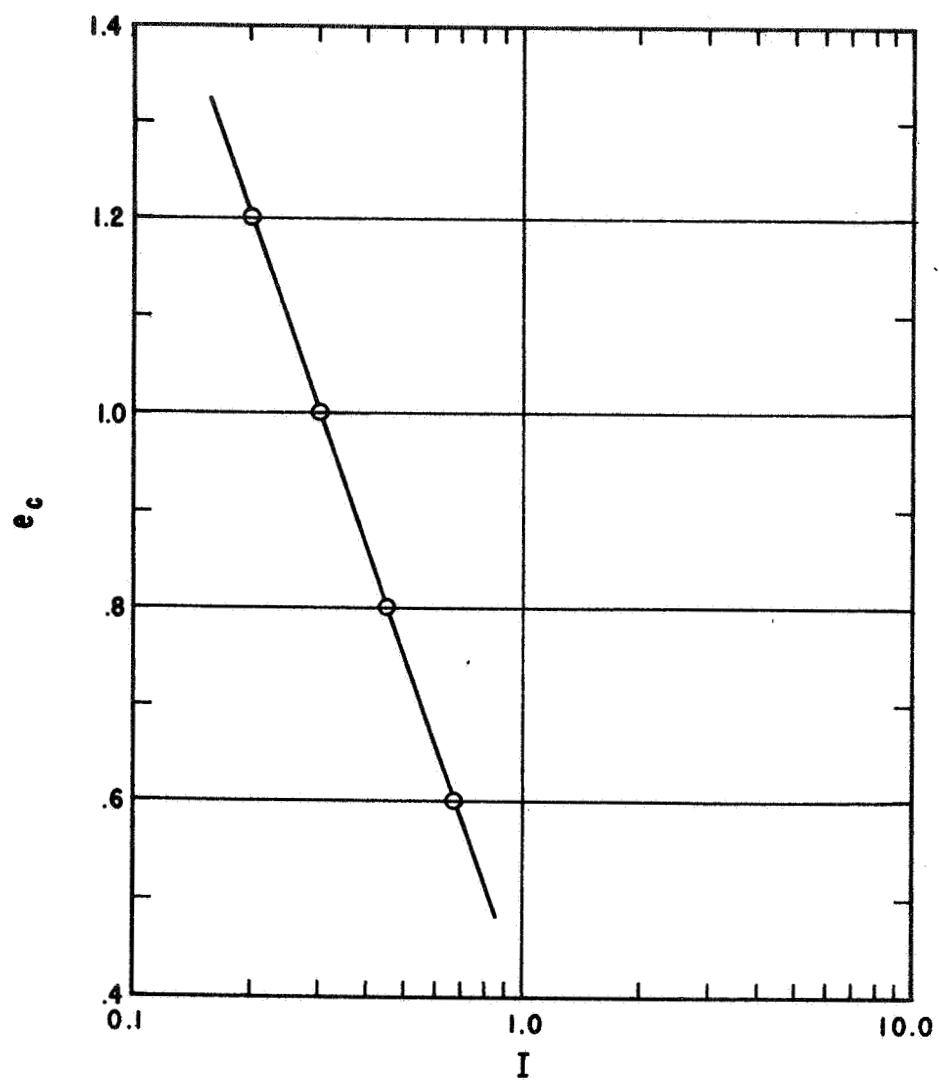


Fig. 1-6. Relationship between I and pre-shear void ratio, e_c .

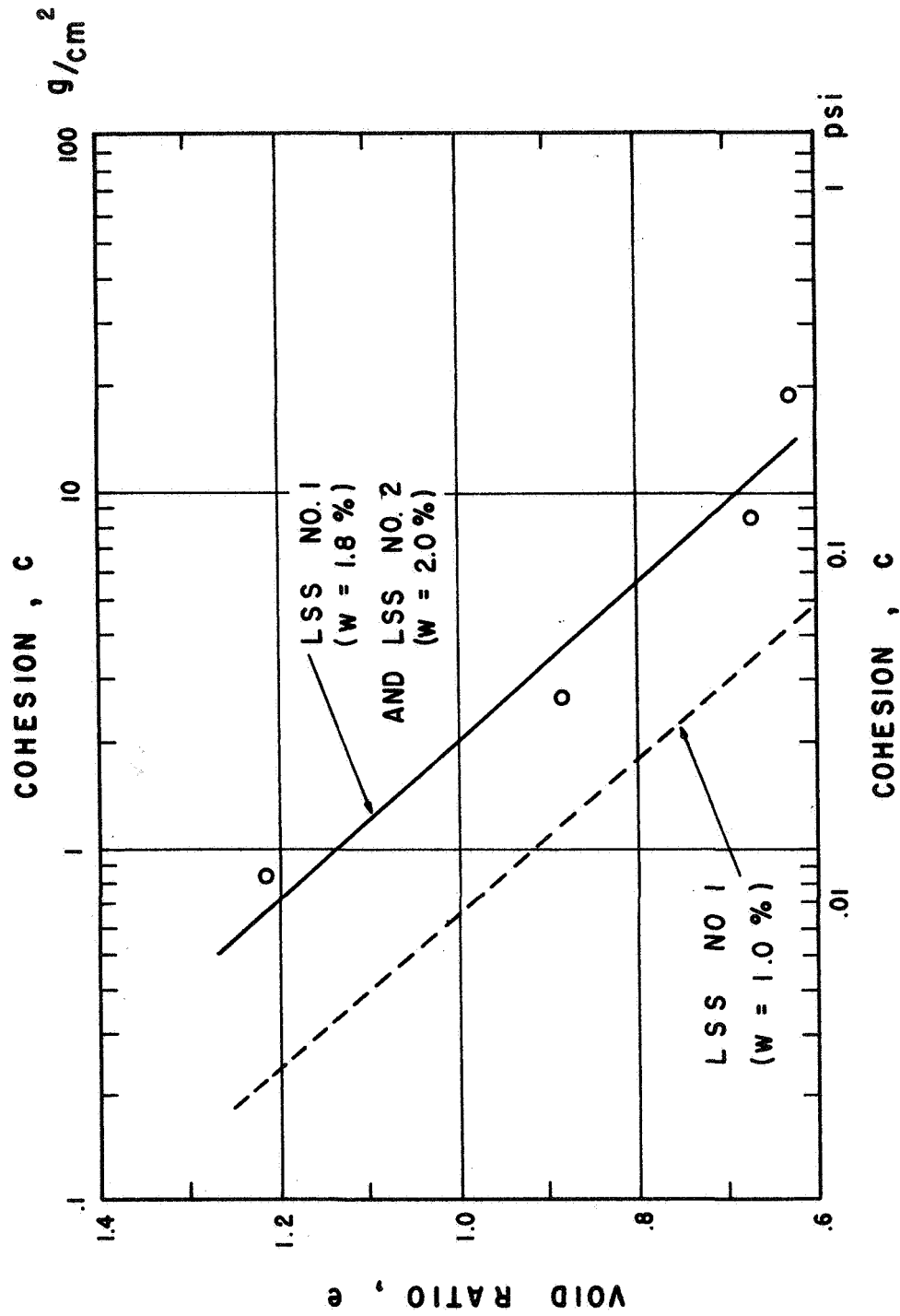


Fig. 1-7. Relationship between cohesion, c, and void ratio, e, for LSS No. 1 and LSS No. 2.

where c = cohesion, gm/cm^2

e = void ratio.

Cohesion values at other water contents may be estimated from Figure 1-7 by interpolation.

Friction Angle, ϕ

Equation (1-1) was used to compute σ_{df} for different void ratios at σ_{3f} values ranging from 0.05 to 0.4 kg/cm^2 . This allowed the determination of the friction angle, ϕ , for several values of void ratio before shear, e_c . Figure 1-8 shows the obtained relationship between $\tan \phi$ and $1/e_c$. Although the data showed a small decrease in ϕ value with confining pressure, which is usual, the single line shown on Figure 1-8 provides a suitable average value for the range of confining pressures considered. The slope of the line in Figure 1-8 is slightly greater than was found for LSS No. 1.

Axial Strain at Failure, ϵ_{af}

The test data indicate that the relationship between axial strain at failure, ϵ_{af} , and pre-shear void ratio, e_c , can best be approximated by straight lines on a semilog plot for different values of σ_{3f} . Figure 1-9 shows this relationship. Considerable scatter in the ϵ_{af} values for LSS No. 2 was observed, but this has been observed for several other granular soils as well. Fortunately, analyses have shown that the tangent to the stress-strain curve, an important parameter whose development is described in following paragraphs, is not highly sensitive to the strain at failure. Values of ϵ_{af} were then crossplotted with values of σ_{3f} . Linear relationships were found between $\sigma_{3f}/\epsilon_{af}$ and σ_{3f} for different values of e_c , as shown in Figure 1-10. This relationship can be described by the hyperbolic equation:

$$\epsilon_{af} = \frac{\sigma_{3f}}{a + b \sigma_{3f}} \quad , \quad (1-4)$$

(for σ_{3f} in kg/cm^2 and ϵ_{af} in percent)

where a = intercept at $\sigma_{3f} = 0$

b = slope of the line in Figure 1-10.

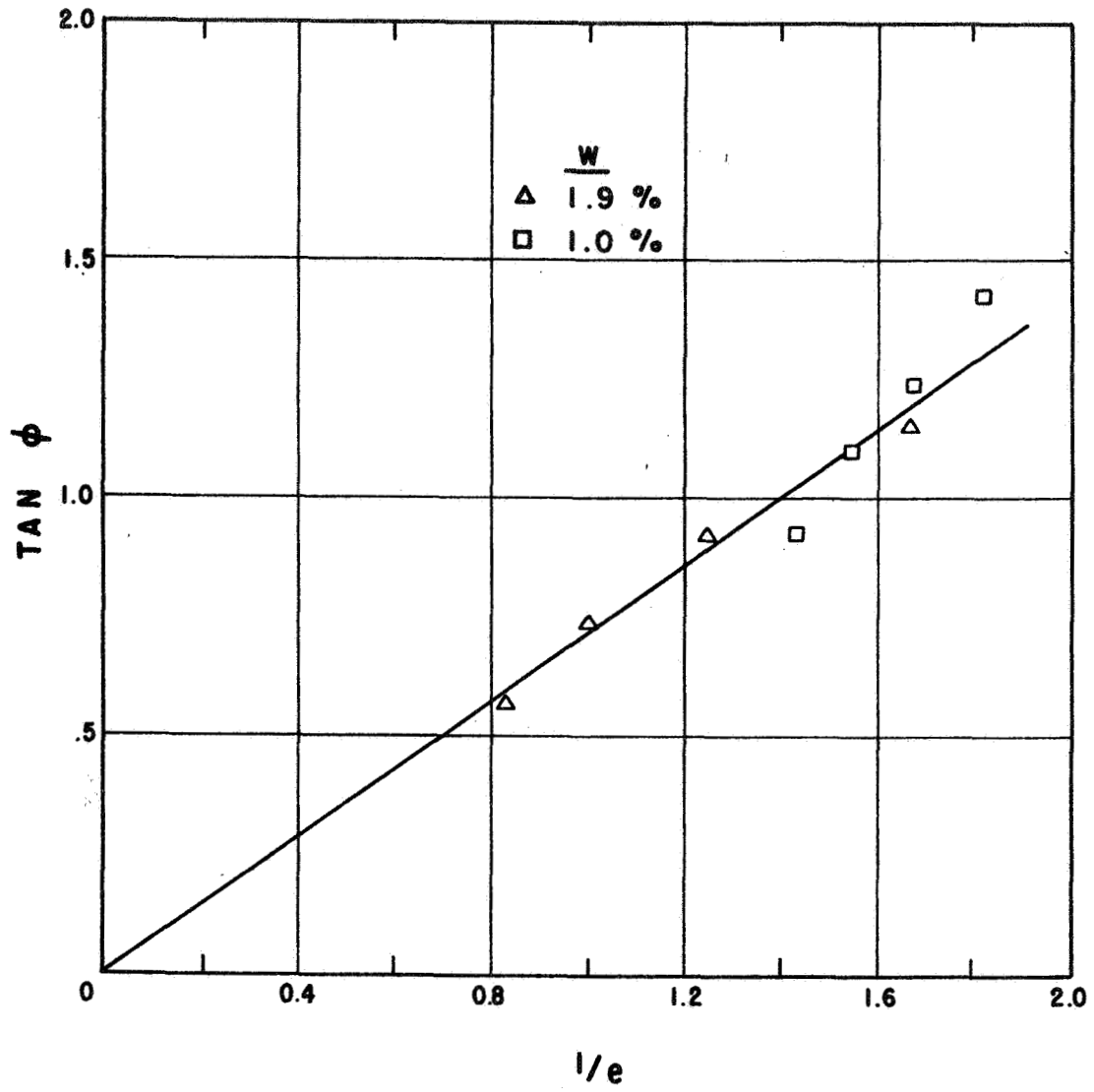


Fig. 1-8. Relationship between ϕ and void ratio for LSS No. 2.

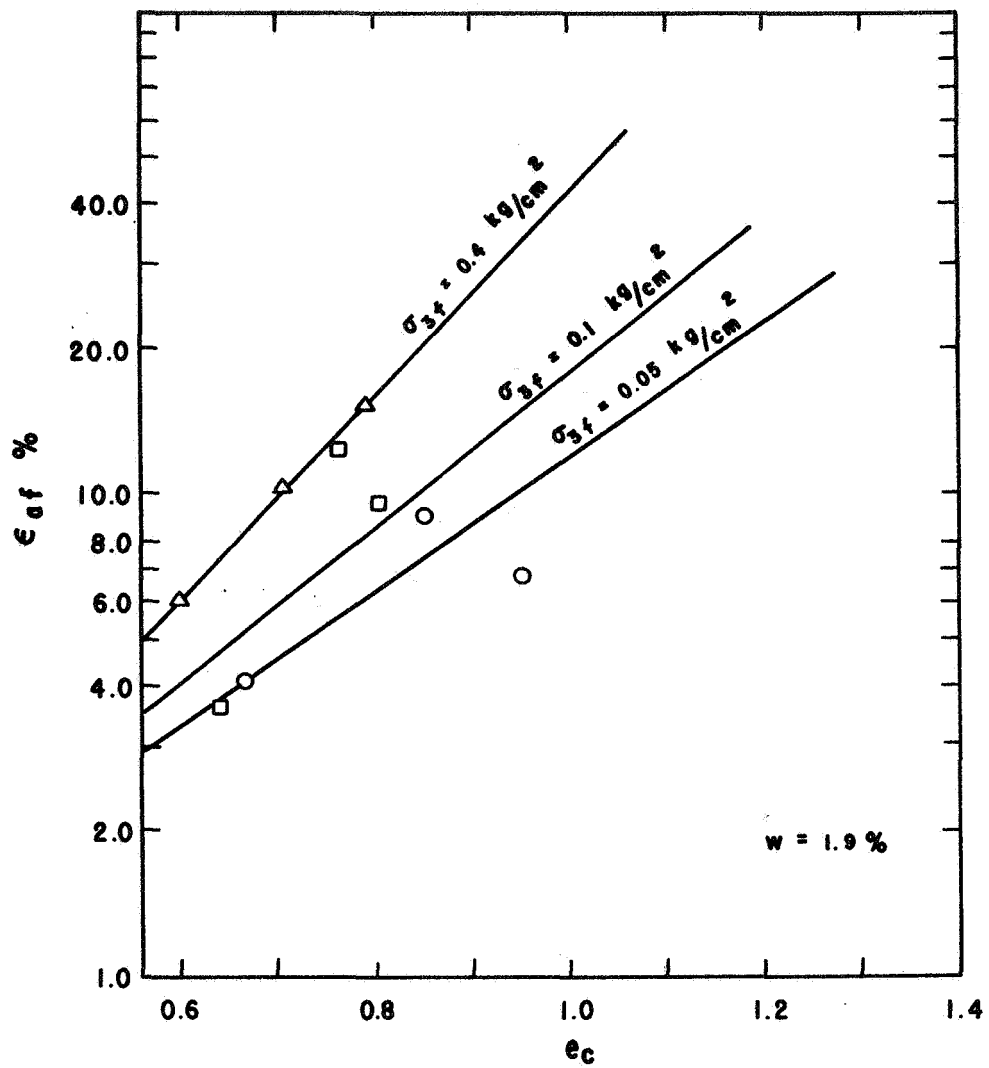


Fig. 1-9. Relationship between axial strain at failure and void ratio.

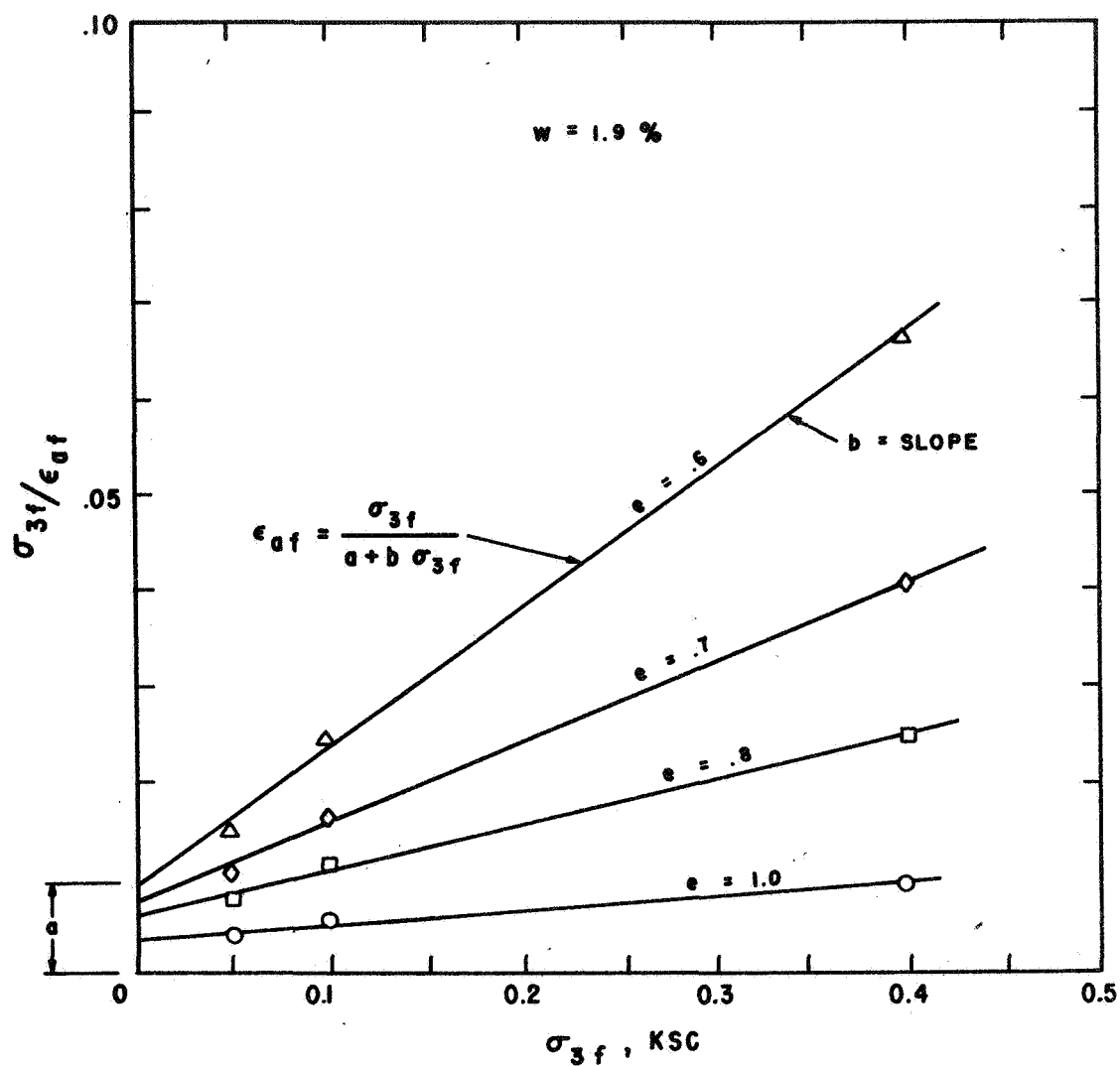


Fig. 1-10. Transformed plot of hyperbolic relationship between axial strain at failure and confining pressure.

The variations of a and b with void ratio are shown in Figures 1-11 and 1-12, respectively. These relations can be described mathematically as follows.

From Figure 1-11,

$$a = \frac{F}{(10)^h e_c}, \quad (1-5)$$

and from Figure 1-12,

$$b = \frac{P}{(10)^q e_c}. \quad (1-6)$$

Tangent Modulus for Plane Strain, E_{tps}

As is the case for almost all soils, the relationship between the principal stress difference, σ_d , and the axial strain, ϵ_a , is nonlinear. The relationship between σ_d and ϵ_a at any stress level ($\sigma_d/\sigma_{df} = \bar{D}$, where σ_{df} is the principal stress difference at failure) may be described in terms of a tangent modulus, E_{tps} . The tangent modulus for plane strain can be defined as:

$$E_{tps} = \frac{d\sigma_d}{d\epsilon_a} \quad (1-7)$$

The procedure for determination of E_{tps} is as follows.

The stress level, \bar{D} , was plotted versus the normalized axial strain ($\epsilon_a/\epsilon_{af} = \bar{\epsilon}_a$). The data are shown in Figures 1-13, 1-14, and 1-15. The plots indicate that the relationship between \bar{D} and $\bar{\epsilon}_a$ can reasonably be assumed to be independent of e_c , for $\sigma_3 = \text{constant}$. The three normalized stress-strain curves from Figures 1-13, 1-14, and 1-15 are replotted in Figure 1-16, which shows that a single, normalized stress-strain curve can be used with only small sacrifice in accuracy. The advantage of using the single solid curve shown in Figure 1-16 is that the relationship between \bar{D} and $\bar{\epsilon}_a$ is independent of confining pressure.

The normalized stress-strain curve can be represented reasonably well by a hyperbola. Hyperbolas have been found by several investigators, (Konder and Zelasko 1963; Duncan and Chang, 1969; and Kulhawy and

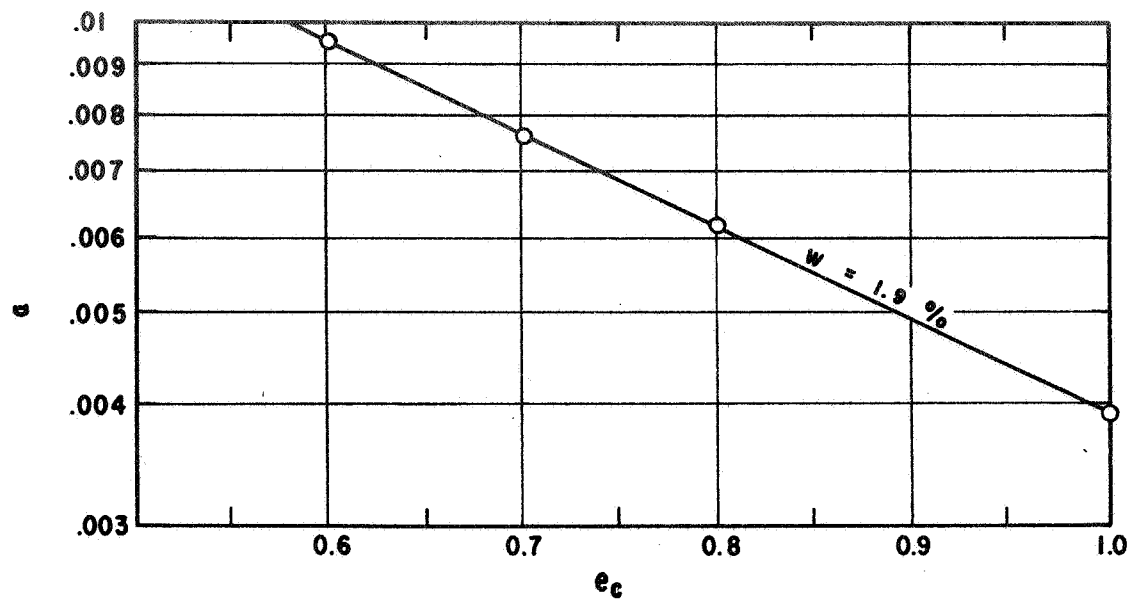


Fig. 1-11. Relationship between intercept, a , and void ratio.

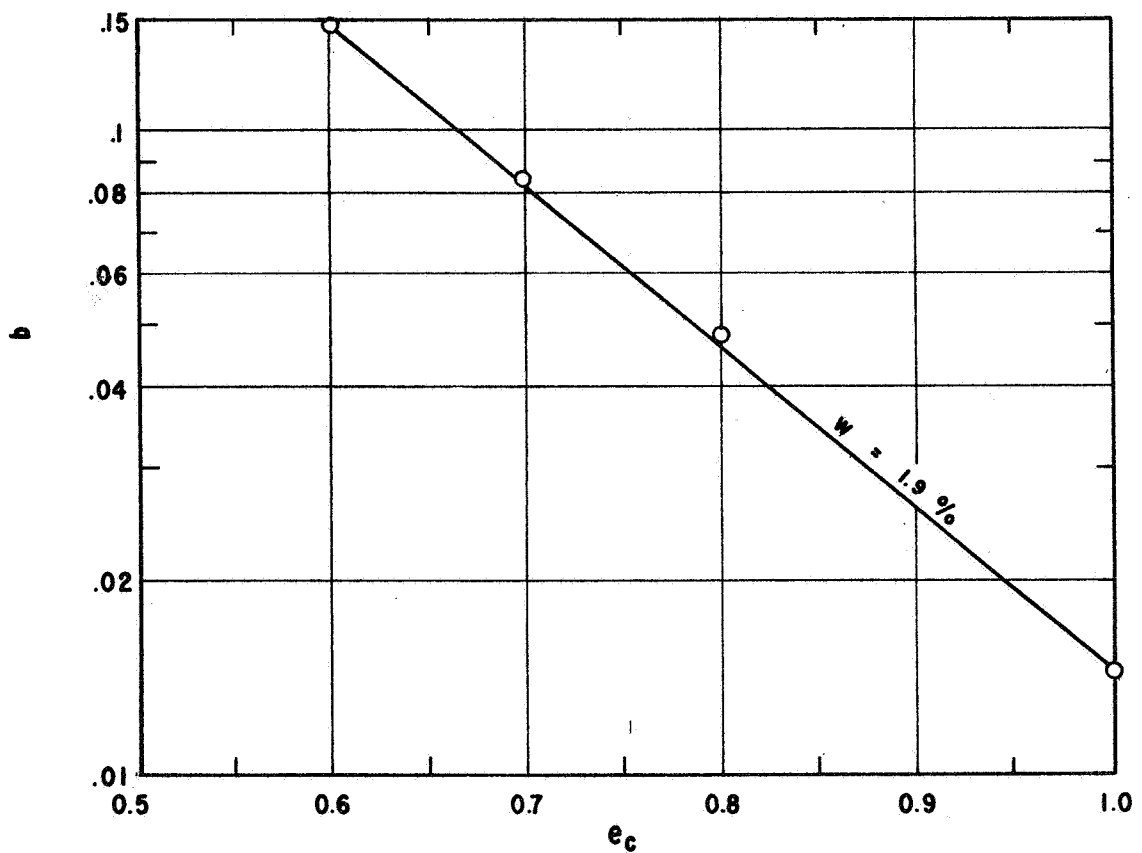


Fig. 1-12. Relationship between slope, b , and void ratio.

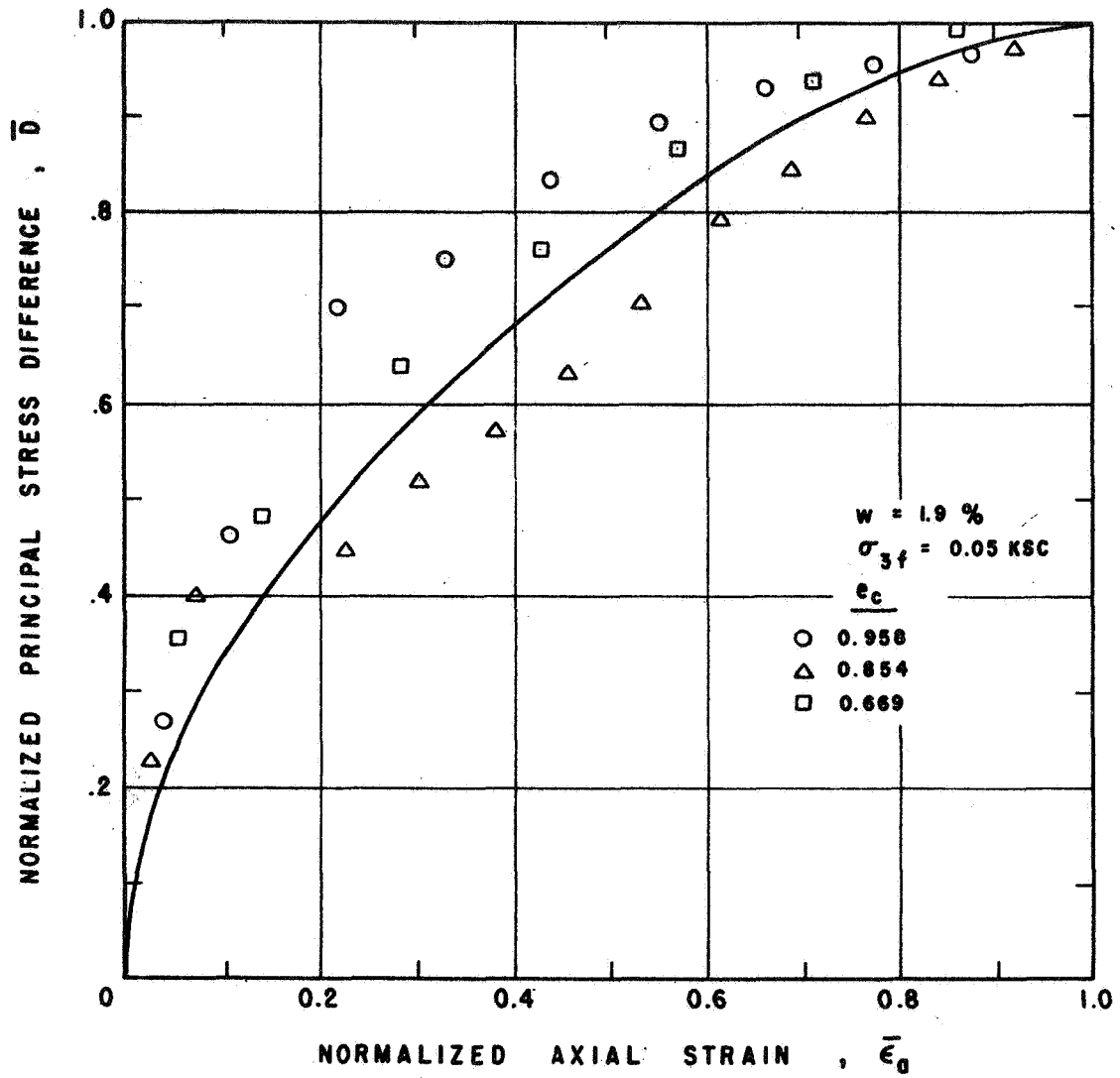


Fig. 1-13. Normalized stress-strain curve for confining pressure = 0.05 kg/cm².

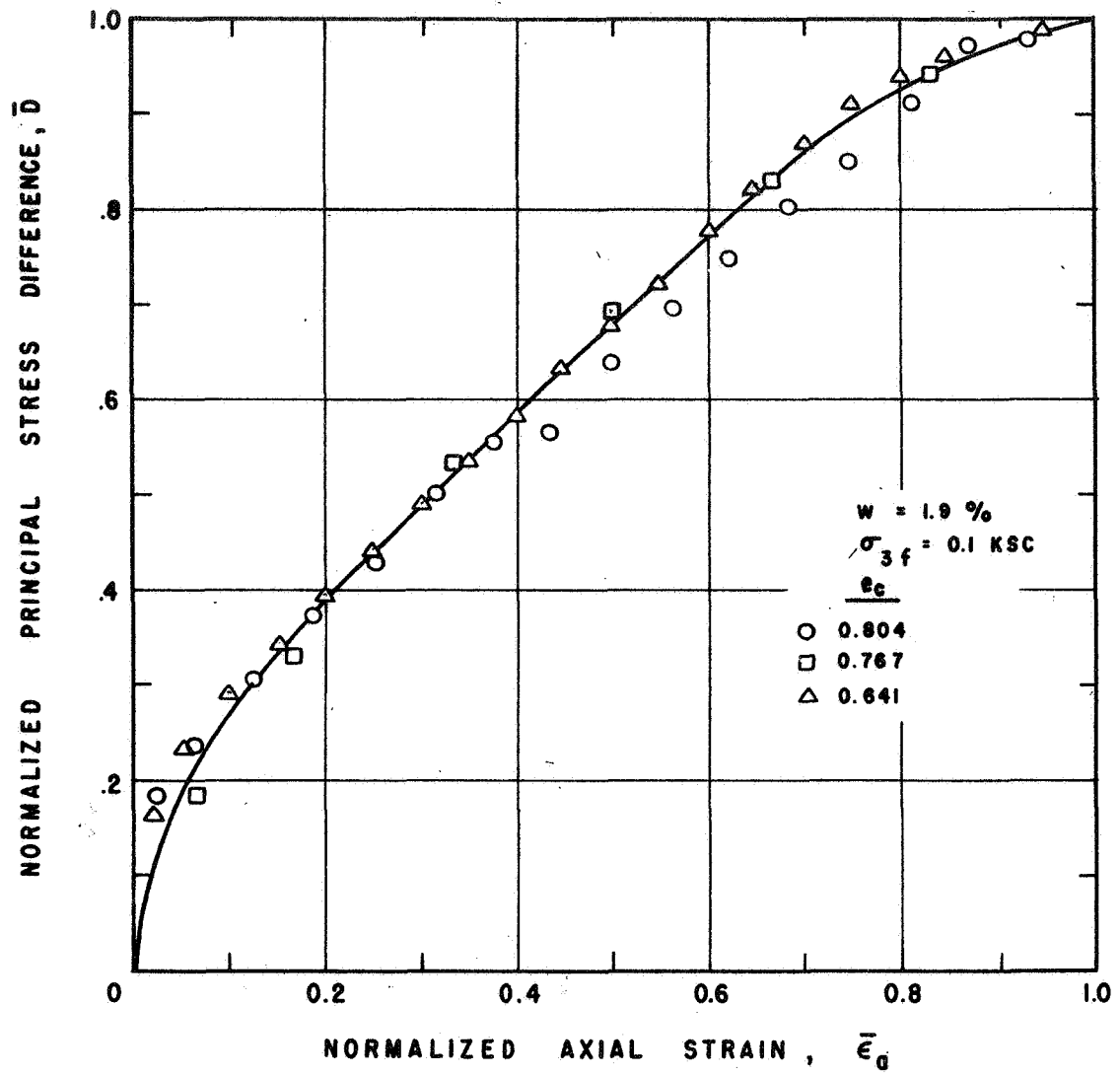


Fig. 1-14. Normalized stress-strain curve for confining pressure = 0.1 kg/cm².

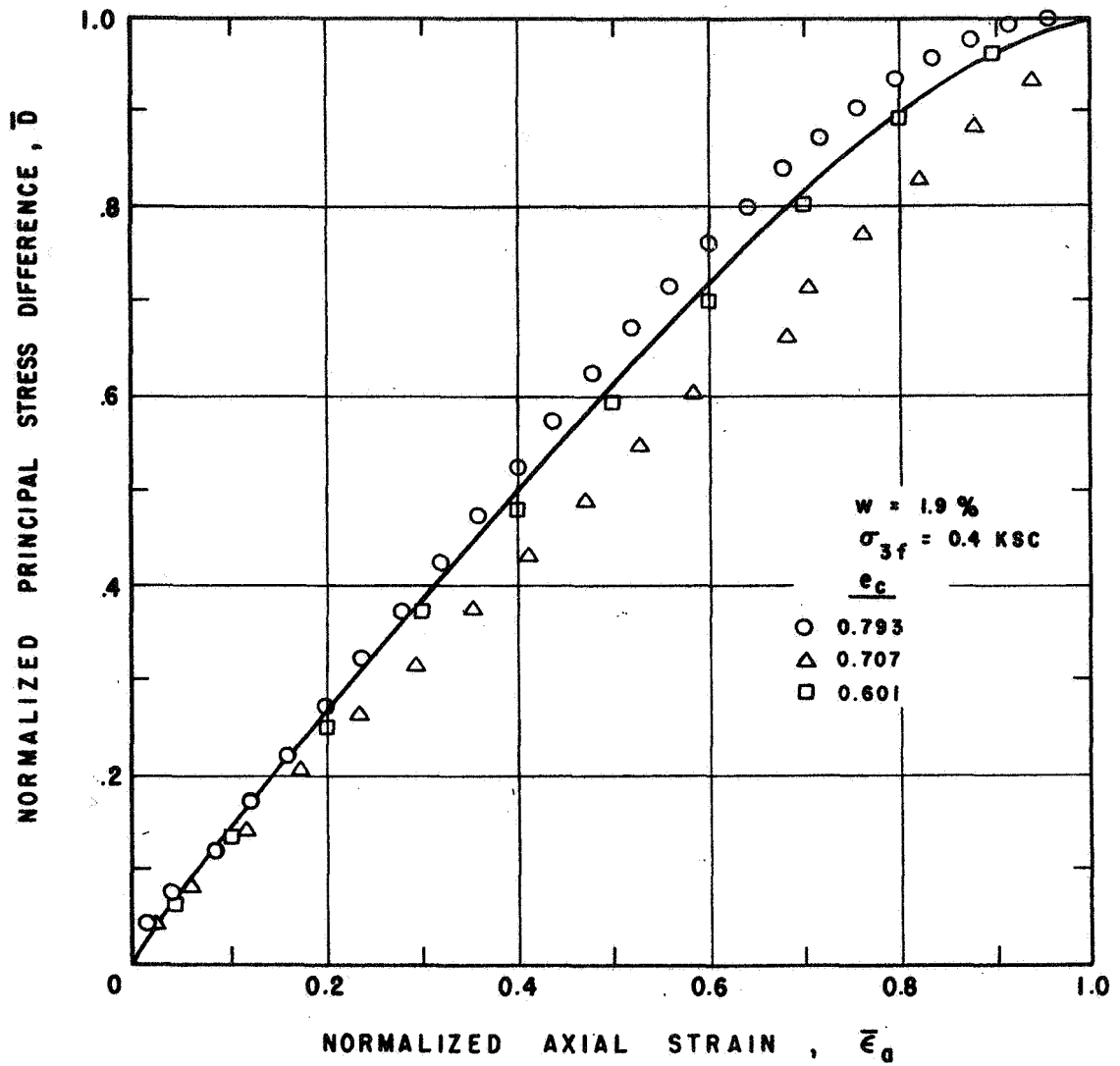


Fig. 1-15. Normalized stress-strain curve for confining pressure = 0.4 kg/cm².

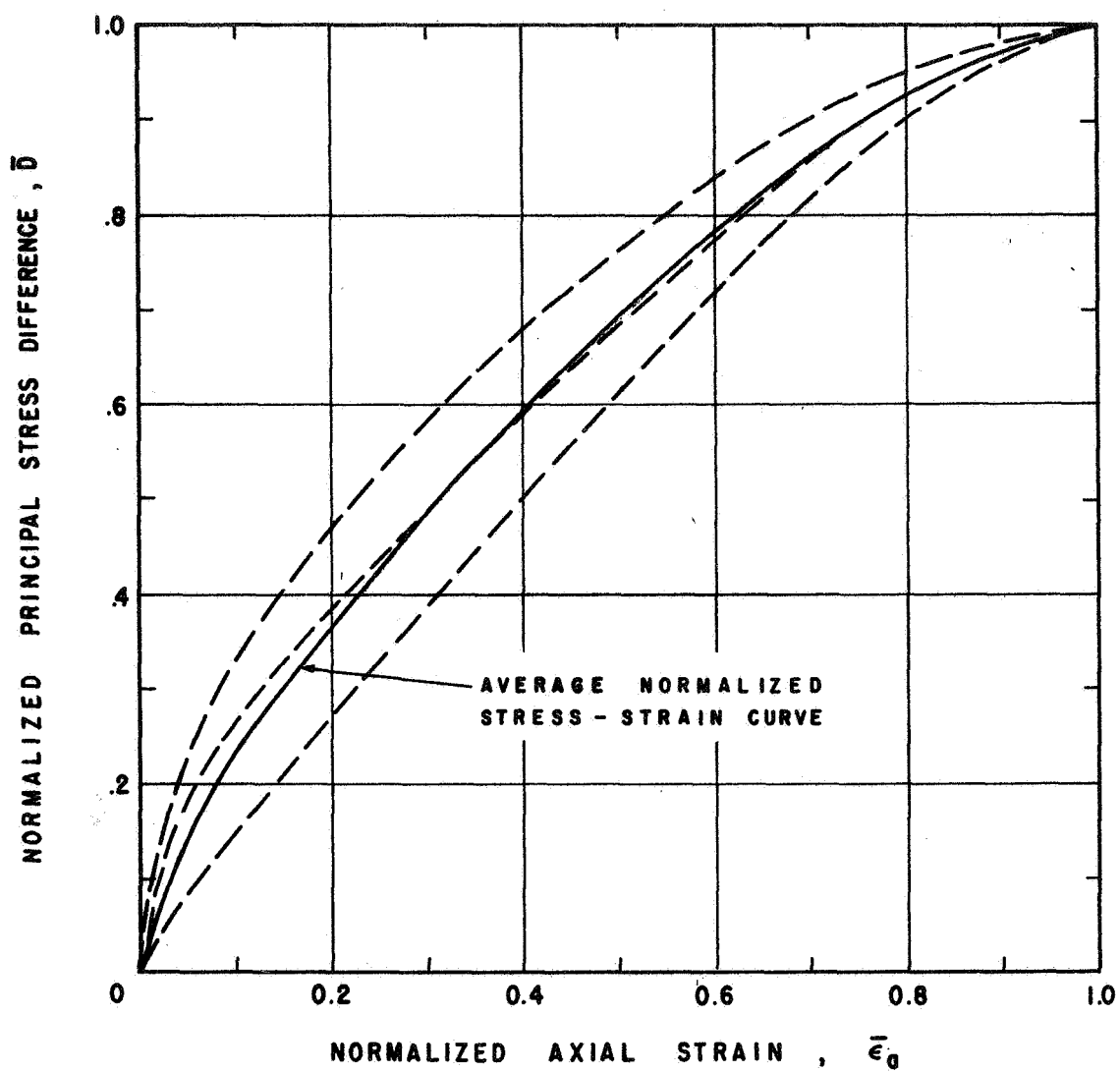


Fig. 1-16. Average normalized stress-strain curve.

Duncan, 1970) to represent stress-strain curves quite satisfactorily up to the point of peak deviator stress. The equation of the hyperbola is

$$\bar{D} = \frac{\bar{\epsilon}_a}{\bar{a} + \bar{b} \bar{\epsilon}_a} \quad , \quad (1-8)$$

where \bar{a} and \bar{b} are the intercept and slope, respectively, of the transformed plot shown in Figure 1-17 which indicates that $\bar{\epsilon}_a/\bar{D}$ varies linearly with $\bar{\epsilon}_a$.

From Figure 1-17, $\bar{a} = 0.485$ and $\bar{b} = 0.475$. Since $1/\bar{a}$ represents the ratio of stress to strain at zero strain, it is analogous to an initial tangent modulus, E_i , for an ordinary stress-strain curve. Since the stress-strain curve has been normalized in Figure 1-17, the actual value of E_i is given by:

$$E_i = \frac{\sigma_{df}}{\epsilon_{af}} \bar{E}_i \quad (1-9)$$

where $\bar{E}_i = \frac{1}{\bar{a}}$.

It is important to note that the stress-strain parameters described herein were developed for loading conditions where the confining pressure is held constant during application of shear stress. Thus, the value of confining pressure at failure, σ_{3f} , is equal to the value of σ_3 at the beginning of shear. Because σ_{df} and ϵ_{af} are both influenced by σ_{3f} to differing degrees, the influence of σ_{3f} on the initial tangent modulus, E_i , is not immediately apparent when normalized stress-strain curves are used. As an example, to show the variation of E_i with confining pressure, a typical value of void ratio, $e_c = 0.8$ was selected and values of E_i were computed using Equation (1-9). These values were plotted versus σ_{3f} , in a log-log plot as shown in Figure 1-18. The equation of this line is

$$E_i = k p_a \left(\frac{\sigma_{3f}}{p_a} \right)^n \quad (1-10)$$

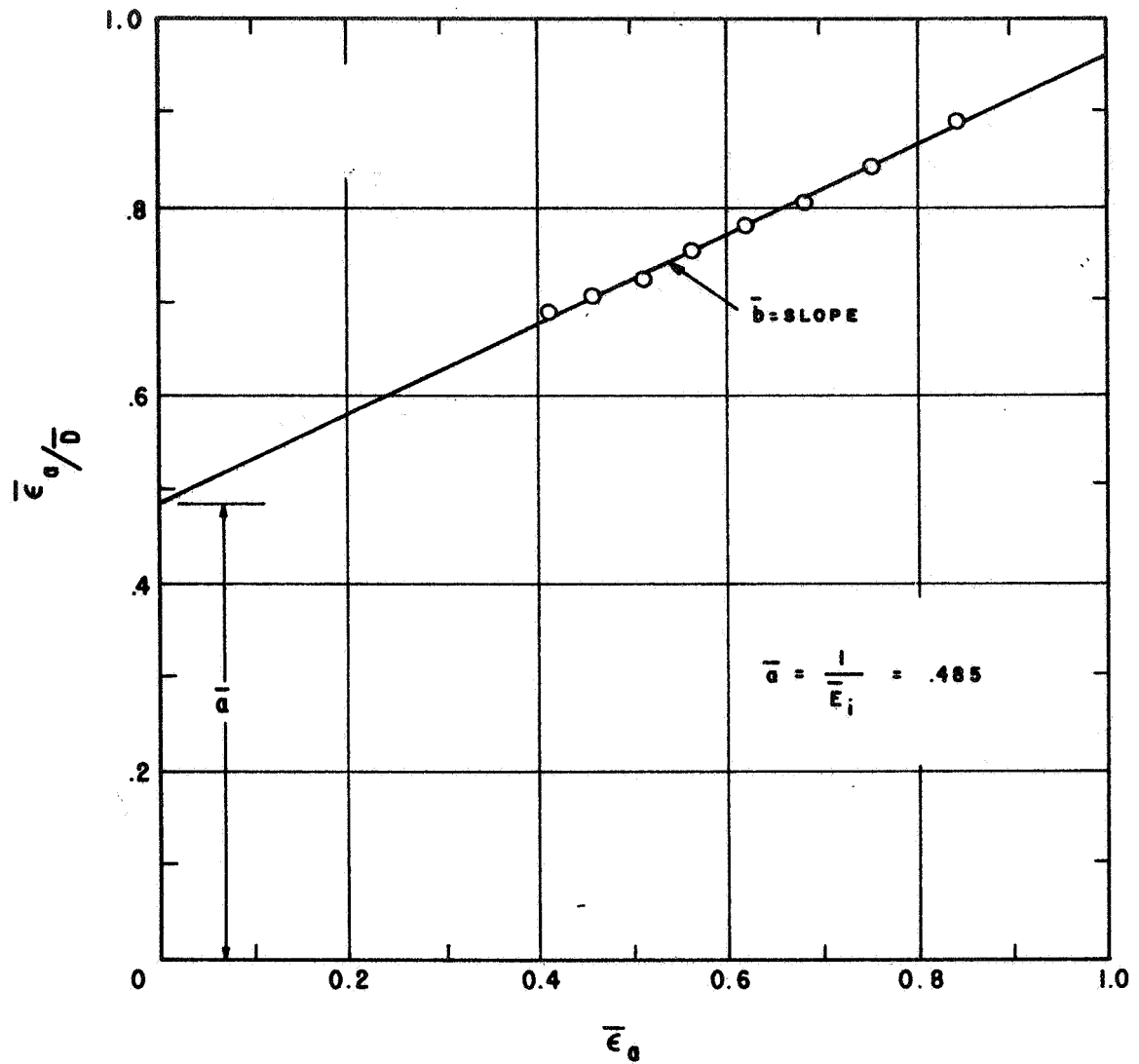


Fig. 1-17. Transformed plot of hyperbolic relationship between normalized axial strain and normalized principal stress difference at failure.

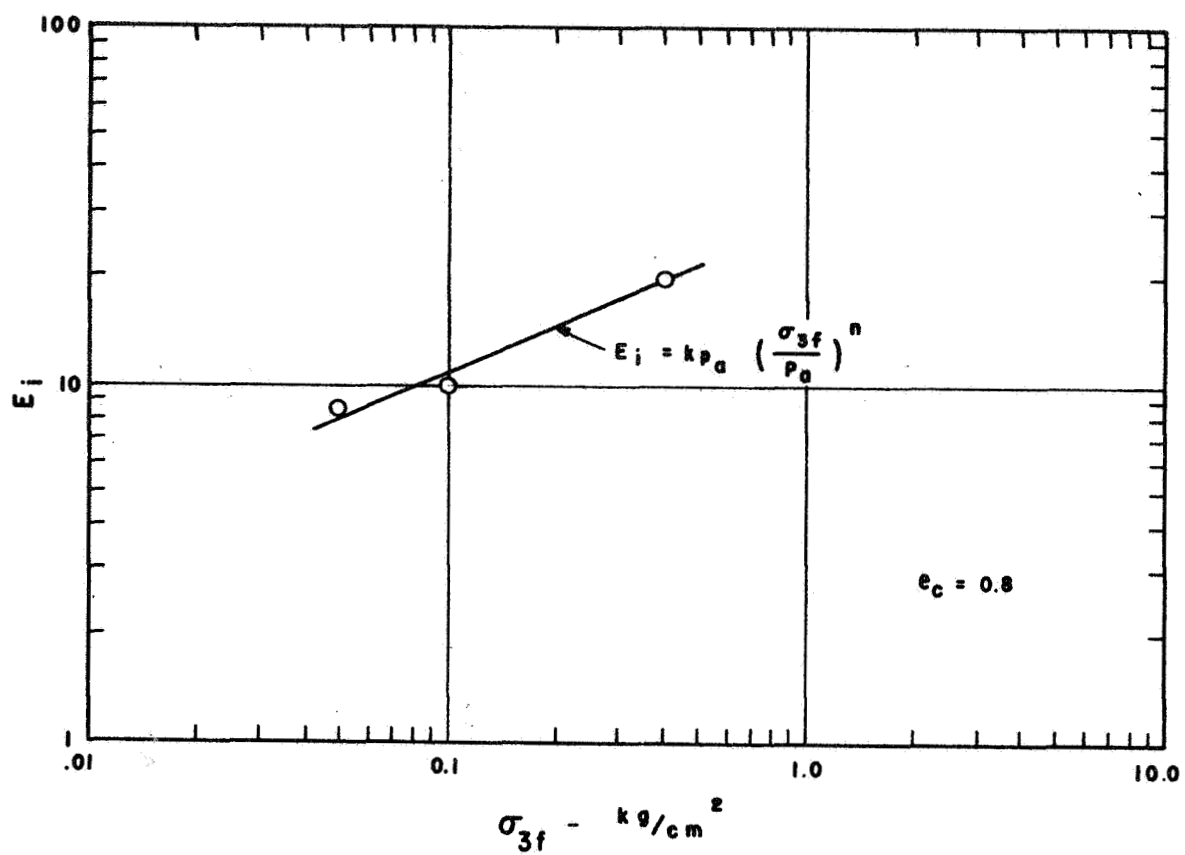


Fig. 1-18. Relationship between E_i and confining pressure for $e_c = 0.8$.

where p_a is atmospheric pressure and k and n are constants. The average value of n for the pressure range shown in Figure 1-18 is about 0.45.

The value of \bar{b} in Equation (1-8) is the inverse of the value of the horizontal asymptote that \bar{D} approaches as the strain becomes infinitely large. The value of this horizontal asymptote may be called the hyperbolic failure-stress level, \bar{D}_{fh} , and is useful in describing stress-strain curves. Values of \bar{D}_{fh} greater than 1 indicate that the hyperbola used to represent the stress-strain curve continues to rise after \bar{D} reaches 1. This presents no particular problem, however, since real values of \bar{D} cannot exceed unity, and no computations are made using greater values of this parameter. The failure ratio, R_f , is defined as

$$R_f = \bar{D}_f / \bar{D}_{fh} = 1 / \bar{D}_{fh}$$

and is commonly used in describing hyperbolic stress-strain curves. It can be evaluated from Figure 1-17.

$$R_f = \frac{1}{\bar{D}_{fh}} = \bar{b} \quad (1-11)$$

The value of the plane strain tangent modulus, E_{tps} , is the slope of the stress-strain curve.

$$E_{tps} = \frac{d\sigma_d}{d\epsilon_a}.$$

If the stress-strain curve is represented as a hyperbola, differentiation yields the following result:

$$E_{tps} = \left(1 - \frac{\sigma_d}{\sigma_{dfh}}\right)^2 E_i \quad (1-12)$$

where σ_d = principal stress difference

σ_{dfh} = hyperbolic principal stress difference at failure

E_i = initial tangent modulus.

In terms of stress levels, Equation (1-12) becomes

$$E_{tps} = \left(1 - \frac{\bar{D}}{D_{fh}}\right)^2 \left(\frac{\sigma_{df}}{\epsilon_{af}}\right) \bar{E}_i$$

or

$$E_{tps} = \left(1 - R_f \bar{D}\right)^2 \left(\frac{\sigma_{df}}{\epsilon_{af}}\right) \bar{E}_i \quad (1-13)$$

Equation (1-13) can be used in an incremental nonlinear elastic analysis to compute the plane strain tangent modulus for any void ratio, confining pressure, or stress level.

The variation of Poisson's ratio with stress level is also needed for such an incremental nonlinear elastic analysis. The variation of Poisson's ratio may be evaluated with knowledge of the ratio of lateral strain to axial strain, as discussed in the following section.

Ratio of Lateral Strain to Axial Strain at Failure, $(\epsilon_l/\epsilon_a)_f$

The test data indicate that the ratio $(\epsilon_l/\epsilon_a)_f$ varies linearly with e_c for different values of σ_{3f} , as shown in Figure 1-19. For convenience, ϵ_l was assumed positive for extension. Values of $(\epsilon_l/\epsilon_a)_f$ and σ_{3f} were taken from Figure 1-19, and a linear relationship was obtained when $(\epsilon_l/\epsilon_a)_f$ was plotted vs $\log \sigma_{3f}$, for $e_c = \text{constant}$, as shown in Figure 1-20. This relationship may be expressed by the equation

$$\left(\epsilon_l/\epsilon_a\right)_f = I_R + S \log \left(\sigma_{3f}/0.1\right), \quad (1-14)$$

where I_R = intercept at $\sigma_{3f} = 0.1 \text{ kg/cm}^2$

and S = change in $\epsilon_{lf}/\epsilon_{af}$ for 1 log-cycle of σ_{3f} , which is in kg/cm^2 slope.

The intercept I_R as well as the slope S were found to be linearly related to e_c , as shown in Figures 1-21 and 1-22, respectively. Hence,

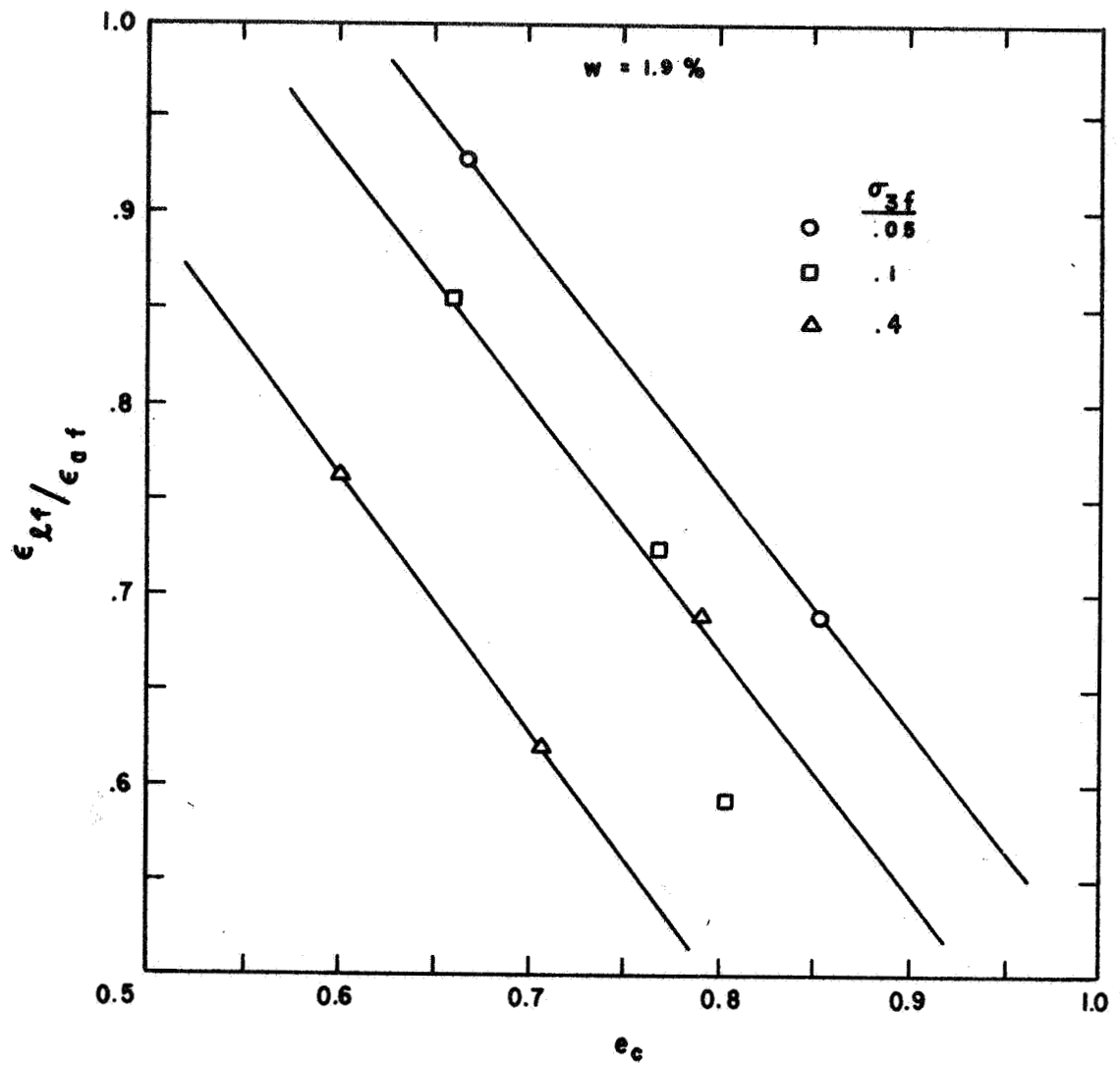


Fig. 1-19. Variation of ratio of lateral strain to axial strain with pre-shear void ratio.

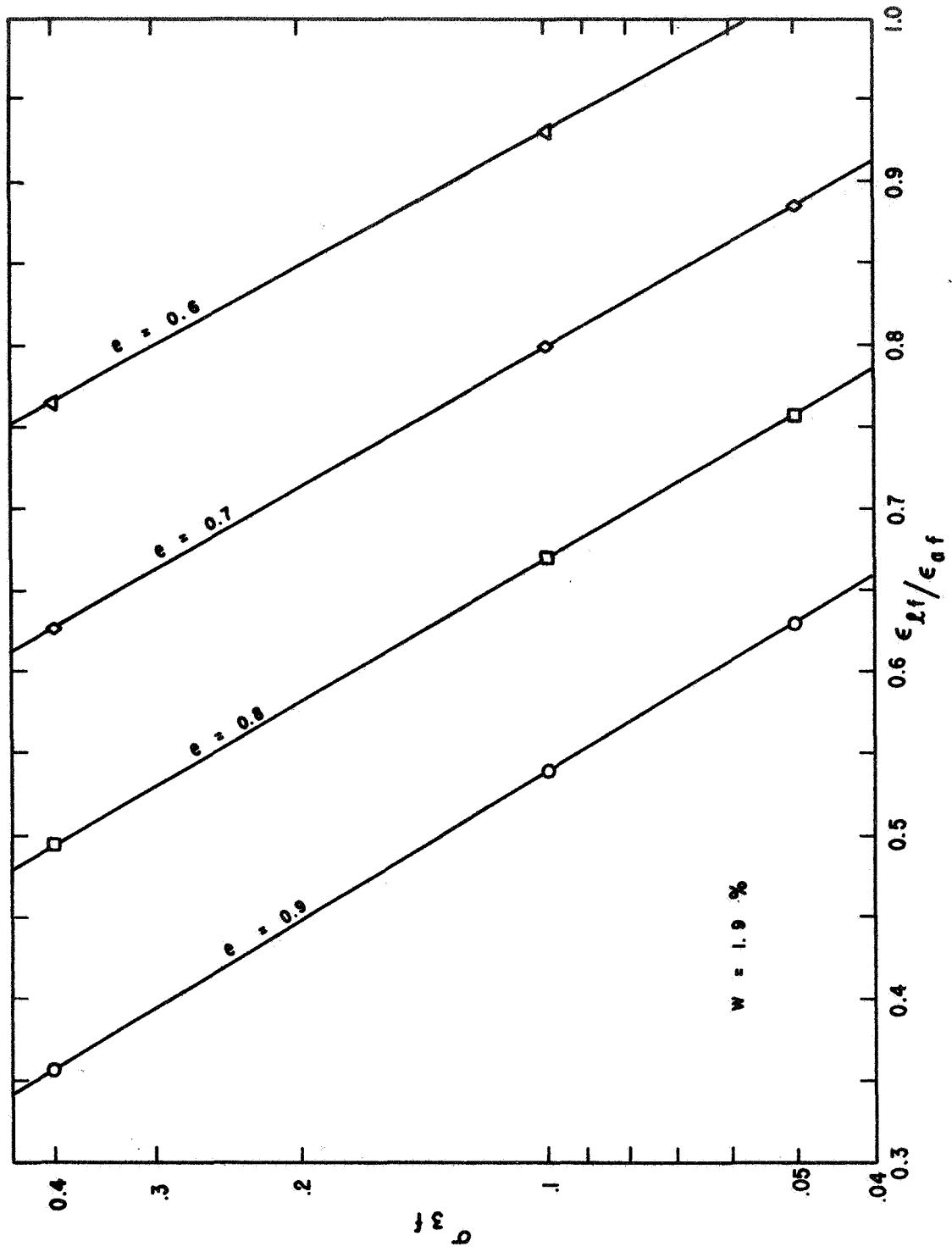


Fig. 1-20. Variation of ratio of lateral strain to axial strain with confining pressure.

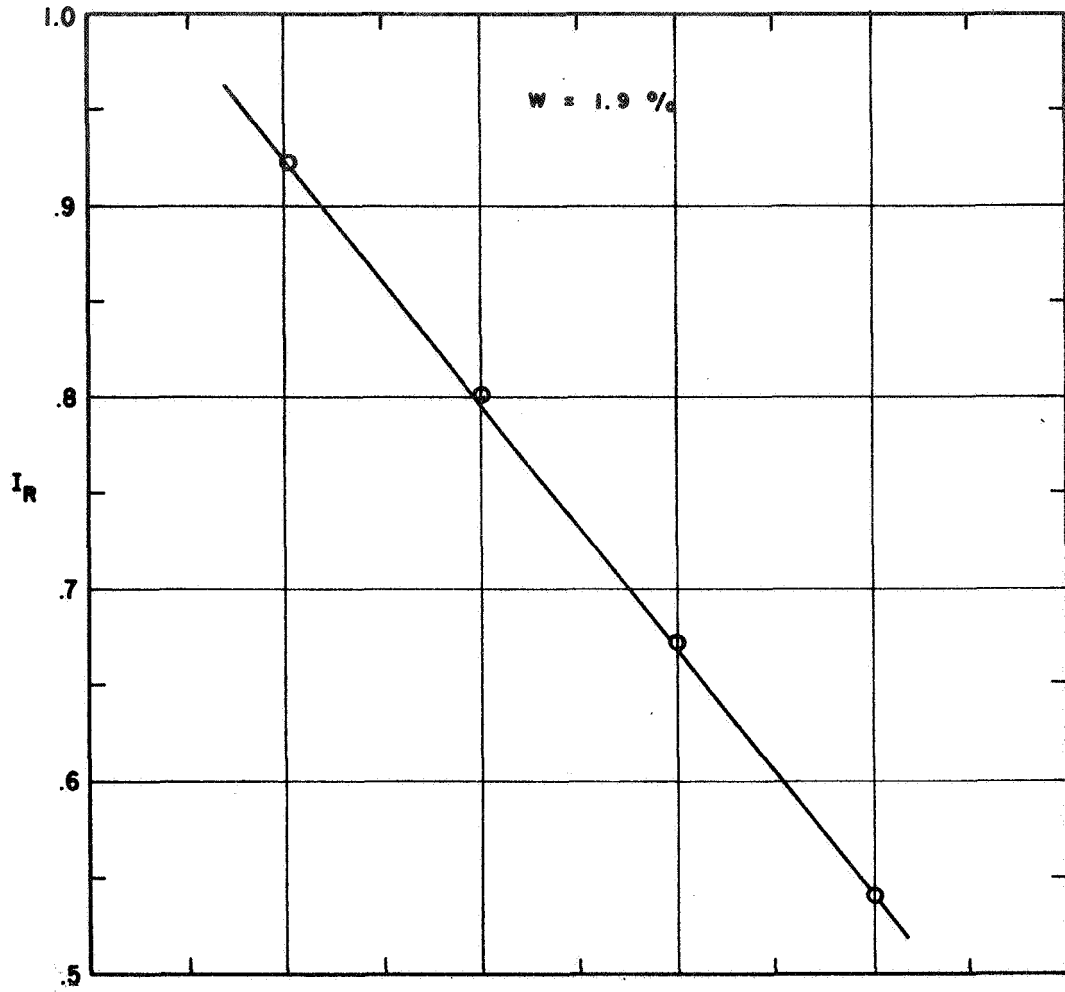


Fig. 1-21. Relationship between I_R and void ratio.

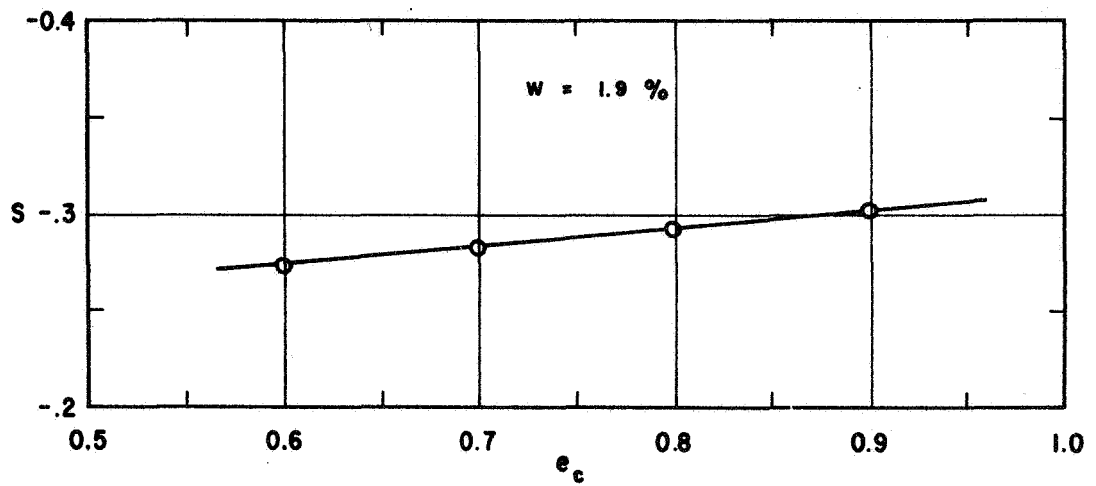


Fig. 1-22. Relationship between S and void ratio.

the following equations may be used to express their values:

$$I_R = U + V e_c \quad (1-15)$$

and

$$S = Y + Z e_c \quad (1-16)$$

where

U = intercepts at $e_c = 0$

Y = intercepts at $e_c = 0$

V = slopes

Z = slopes .

Tangential Lateral Strain Ratio for Plane Strain, $(\epsilon_\ell/\epsilon_a)_{tps}$

The volume changes associated with shear may be described by the ratio of ϵ_ℓ/ϵ_a , at any stress level, \bar{D} , or axial strain, ϵ_a . This ratio, ϵ_ℓ/ϵ_a , is not constant, nor does it vary linearly with \bar{D} or ϵ_a . The instantaneous change in ϵ_ℓ with respect to ϵ_a may be defined as:

$$\left(\frac{\epsilon_\ell}{\epsilon_a} \right)_{tps} = \frac{d\epsilon_\ell}{d\epsilon_a} \quad (1-17)$$

An equation allowing the computation of $(\epsilon_\ell/\epsilon_a)_{tps}$ at any stress level, \bar{D} , was developed as follows.

The normalized axial strains, $\epsilon_a/\epsilon_{af} = \bar{\epsilon}_a$, were plotted versus the normalized lateral strains, $\epsilon_\ell/\epsilon_{\ell f} = \bar{\epsilon}_\ell$, as shown in Figures 1-23, 1-24, and 1-25 for $\sigma_{3f} = 0.05, 0.1, 0.4 \text{ kg/cm}^2$, respectively.

The relationship between $\bar{\epsilon}_\ell$ and $\bar{\epsilon}_a$ is essentially independent of e_c , as can be observed from the plots. Hyperbolic representations of these curves were made in a manner similar to that used for the stress-strain curves discussed previously. Hyperbolas have been used for lateral-strain variation by other investigators (Kulhawy and Duncan, 1970). The transformed plots of the hyperbolic representation are shown in Figure 1-26. All lines can reasonably be passed through $(\bar{\epsilon}_\ell/\bar{\epsilon}_a) = \bar{\epsilon}_\ell = 1.0$.

Values of the inverse of the intercepts, (\bar{I}_ϵ) , at $\epsilon_\ell = 0$ are related linearly to $\log \sigma_{3f}$, as shown by Figure 1-27.

Therefore, the hyperbolic relationship between $\bar{\epsilon}_a$ and $\bar{\epsilon}_\ell$ may be expressed as follows:

$$\bar{\epsilon}_a = \frac{\bar{\epsilon}_\ell}{\bar{I}_\epsilon + \bar{d} \bar{\epsilon}_\ell} \quad (1-18)$$

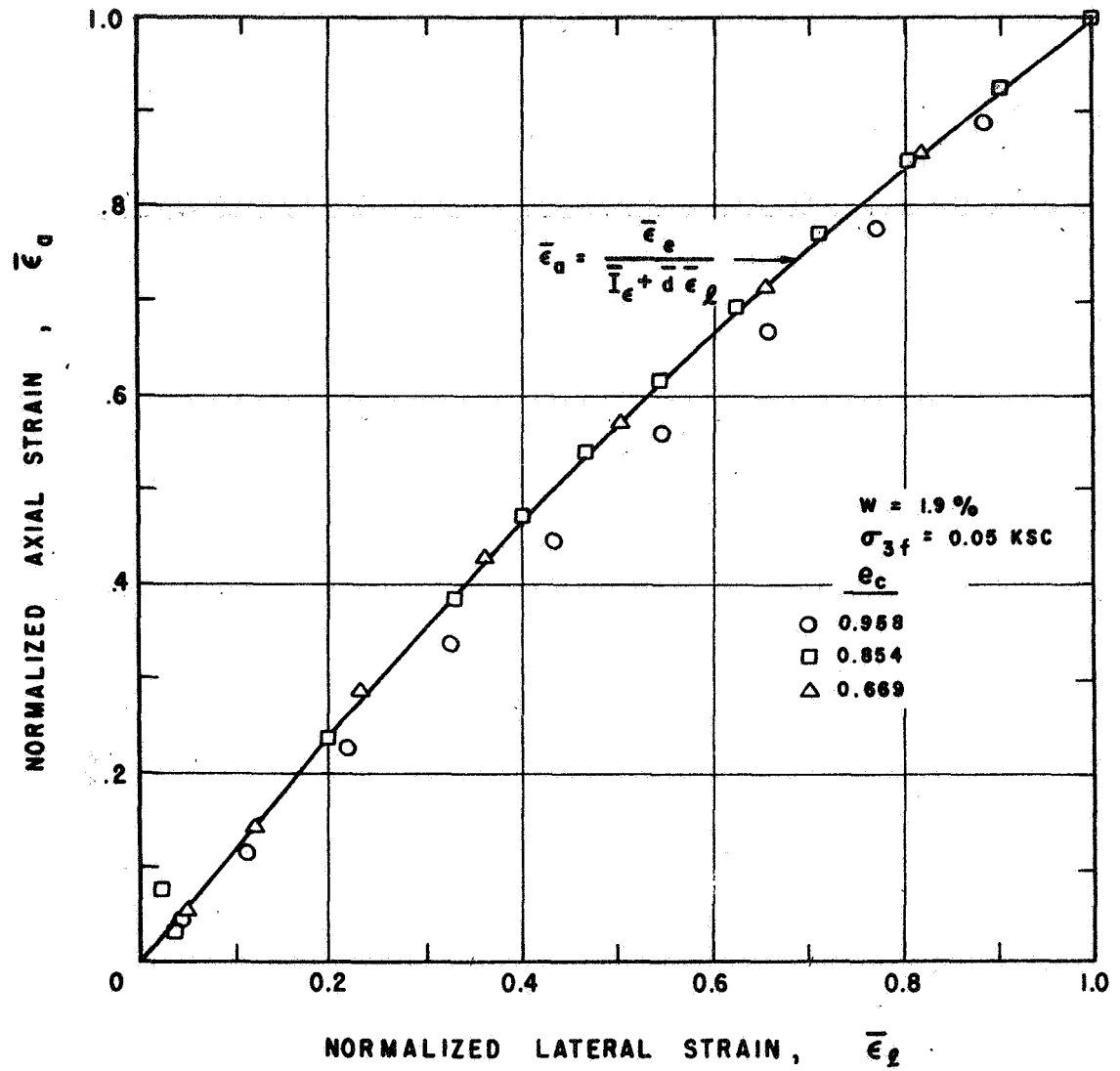


Fig. 1-23. Variation of normalized lateral strain with normalized axial strain for $\sigma_{3f} = 0.05 \text{ kg/cm}^2$.

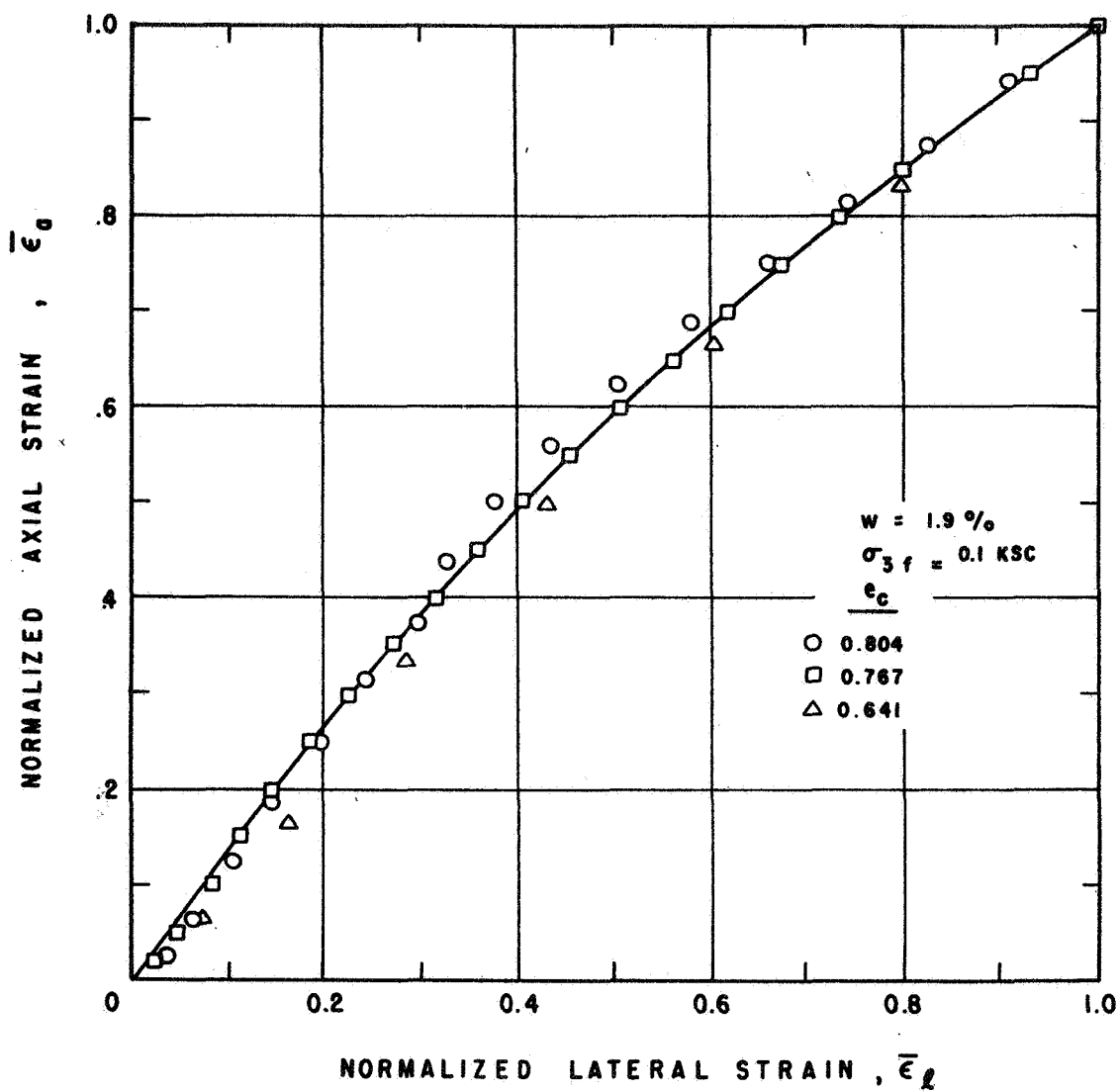


Fig. 1-24. Variation of normalized lateral strain with normalized axial strain for $\sigma_{3f} = 0.1 \text{ kg/cm}^2$.

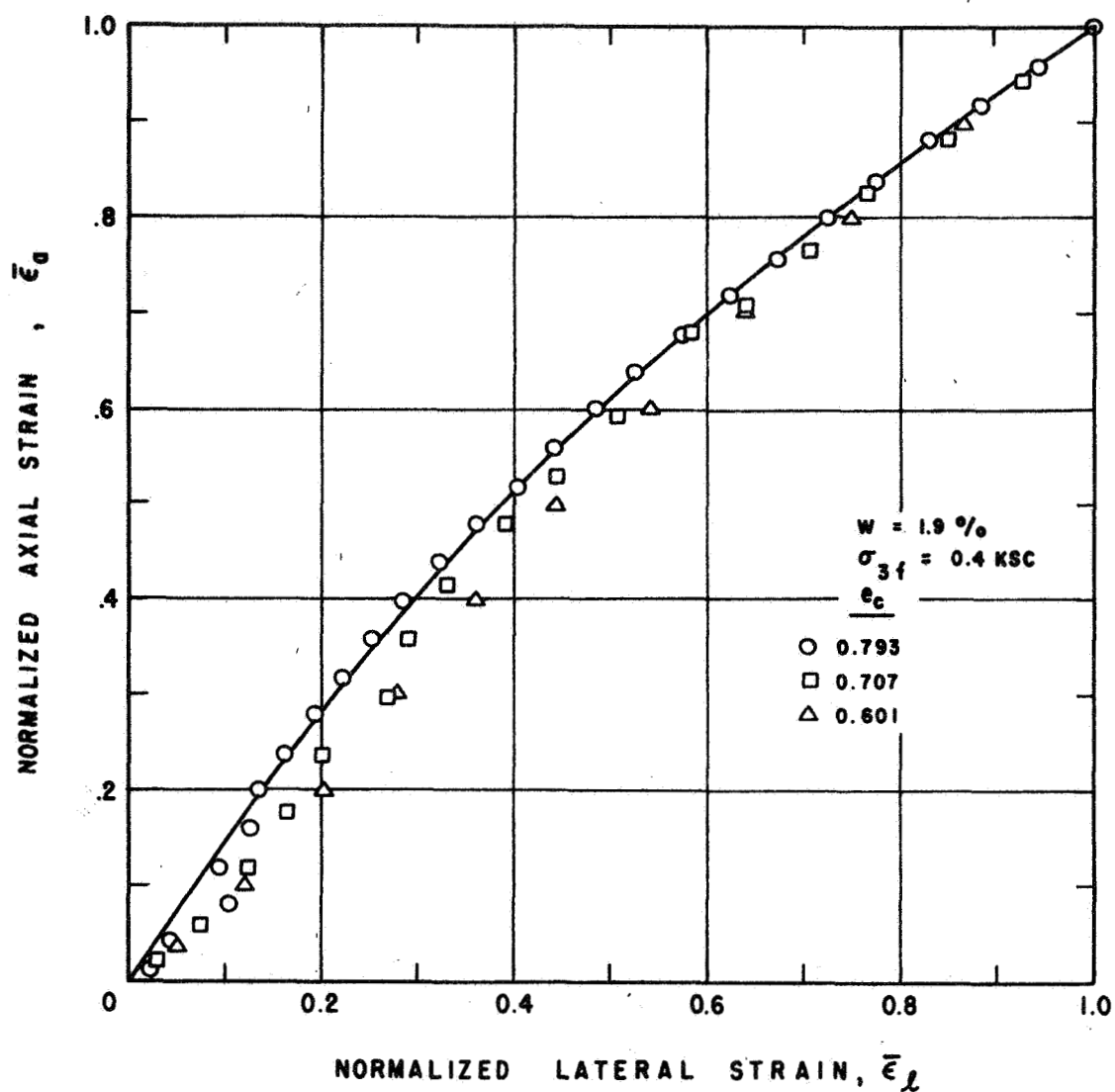


Fig. 1-25. Variation of normalized lateral strain with normalized axial strain for $\sigma_{3f} = 0.4 \text{ kg/cm}^2$.

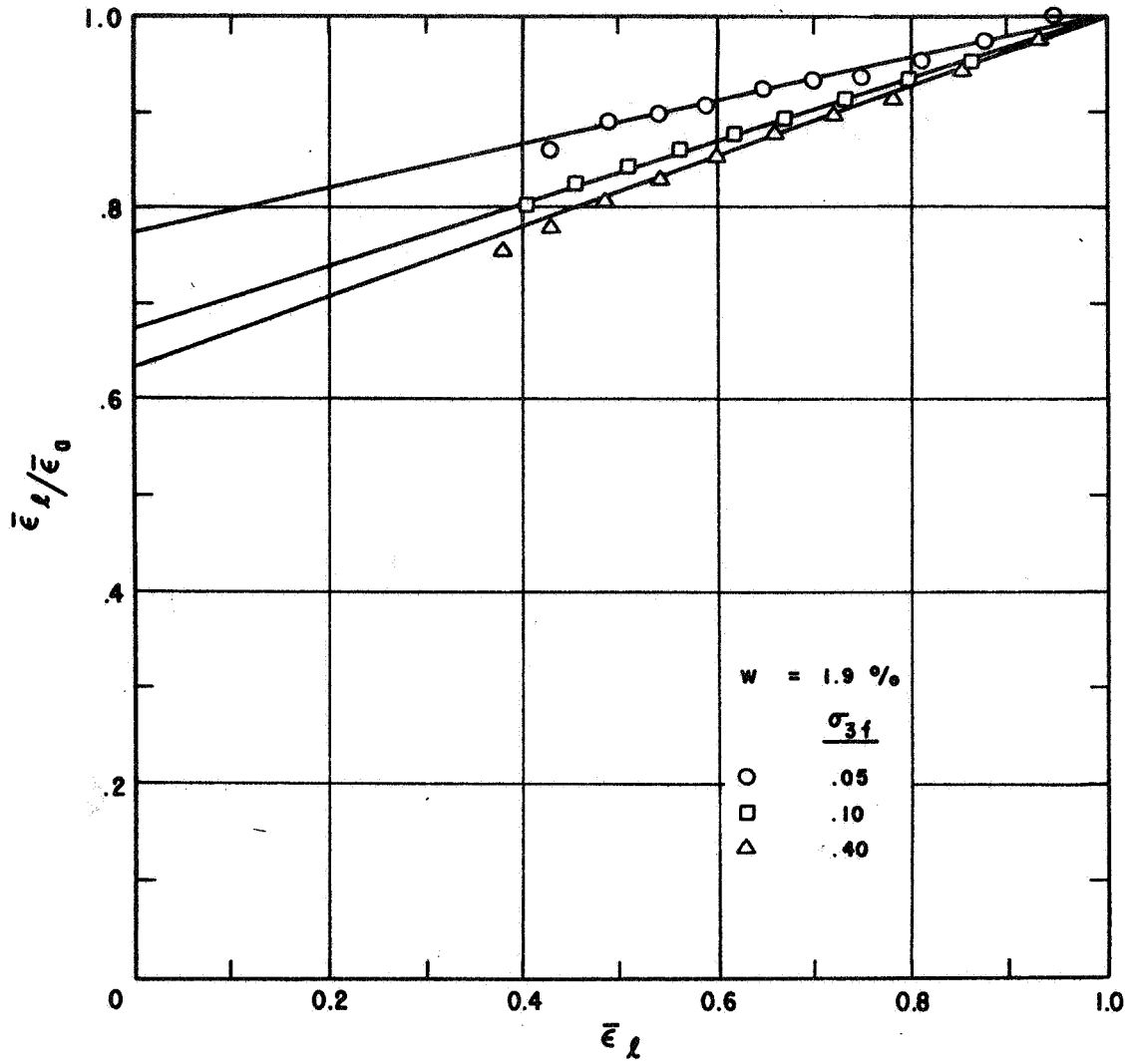


Fig. 1-26. Transformed hyperbolic plot for normalized lateral strain.

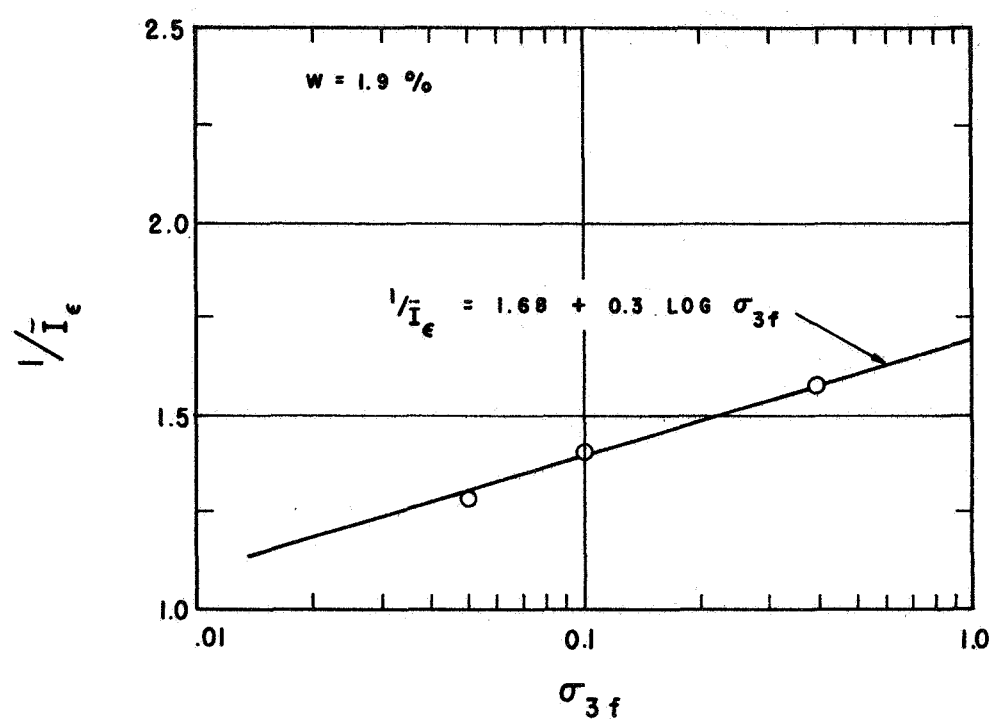


Fig. 1-27. Relationship between inverse of intercept, I_{ϵ} , and σ_{3f} .

where $\bar{I}_\epsilon = \text{intercept at } \bar{\epsilon}_\ell = 0$

and $\bar{d} = \text{slope of the line from Figure 1-26.}$

From Figure 1-27,

$$\frac{1}{\bar{I}_\epsilon} = J + N \log(\sigma_{3f})$$

$$\text{or } \bar{I}_\epsilon = \frac{1}{J + N \log_{10} \sigma_{3f}} \quad (1-19)$$

where $J = \text{intercept at } \sigma_{3f} = 1 \text{ kg/cm}^2$

$N = \text{slope} = \text{change in } 1/\bar{I}_\epsilon \text{ for 1 log cycle of } \sigma_{3f}, \text{ which is}$
in kg/cm^2 ,

and from Figure 1-26,

$$\bar{d} = \frac{1.0 - \bar{I}_\epsilon}{1.0} \quad (1-20)$$

Equation (1-18) may be solved for $\bar{\epsilon}_\ell$ and differentiated to obtain:

$$\left(\frac{\epsilon_\ell}{\epsilon_a} \right)_{\text{tps}} = \frac{d\epsilon_\ell}{d\epsilon_a} = \left(\frac{\epsilon_\ell}{\epsilon_a} \right)_f \frac{\bar{\epsilon}_\ell}{\bar{\epsilon}_a} = \left(\frac{\epsilon_\ell}{\epsilon_a} \right)_f \frac{\bar{I}_\epsilon}{(1 - \bar{d} \bar{\epsilon}_a)^2}$$

or

$$\left(\frac{\epsilon_\ell}{\epsilon_a} \right)_{\text{tps}} = \left(\frac{\epsilon_\ell}{\epsilon_a} \right)_f \frac{\bar{I}_\epsilon}{[1 - (1 - \bar{I}_\epsilon) \bar{\epsilon}_a]^2} \quad (1-21)$$

Equation (1-8) may be used to eliminate $\bar{\epsilon}_a$ from Equation (1-21), after first substituting

$$\bar{a} = \frac{1}{\bar{E}_i}$$

$$\text{and } \bar{b} = R_f.$$

Thus:

$$\left(\frac{\epsilon_l}{\epsilon_a}\right)_{\text{tps}} = \left(\frac{\epsilon_l}{\epsilon_a}\right)_f \left[\frac{\bar{I}_\epsilon}{1 - \frac{(1 - \bar{I}_\epsilon)\bar{D}}{\bar{E}_i(1 - R_f\bar{D})}} \right]^2 \quad (1-22)$$

The values of E_{tps} and $(E_l/\epsilon_a)_{\text{tps}}$ from Equations (1-13) and (1-22) may be used in an incremental nonlinear elastic analysis to compute the corresponding values of the incremental Young's modulus, E_t , and Poisson's ratio, ν_t , from Equations (1-23) and (1-24), which were obtained by simplifying Hooke's law for plane strain.

$$\nu_t = \frac{(\epsilon_l/\epsilon_a)_{\text{tps}}}{1 + (\epsilon_l/\epsilon_a)_{\text{tps}}} \quad (1-23)$$

$$E_t = E_{\text{tps}} (1 - \nu_t^2) \quad (1-24)$$

These values of E_t and ν_t may then be used in finite element analyses or other analytical methods to solve problems related to lunar surface loadings, such as plate load tests, boot imprints, and trench wall failures.

The preceding analyses were made using data obtained from a plane-strain test series on LSS No. 2 at a water content of 1.9%. A similar test series was performed for a water content of 1.0% to determine the effect of cohesion (see Figure 1-7) on the stress-strain parameters, and the same analyses were made. Many of the parameters turned out to be the same for both water contents, but some varied significantly. The data showed that the shift in a stress-strain curve due to a moisture content variation of only 0.1% is negligible.

The stress-strain parameters for both $w = 1.9\%$ and $w = 1.0\%$ are summarized in Table 1-1. The equations relating stress and strain are summarized below.

Principal Stress Difference at Failure, σ_{df}

$$I = \frac{L_0}{10^{Me}_c} \quad (1-2)$$

$$\sigma_{df} = I \left(\frac{\sigma_{3f}}{0.1} \right)^{G_f} \quad (1-1)$$

(for σ_{3f} and σ_{df} in kg/cm^2)

Axial Strain at Failure, ϵ_{af}

$$a = \frac{F}{(10)^h e_c} \quad (1-5)$$

$$b = \frac{P}{(10)^{Qe}_c} \quad (1-6)$$

$$\epsilon_{af} = \frac{\sigma_{3f}}{a + b \sigma_{3f}} \quad (1-4)$$

(for σ_{3f} in kg/cm^2)

Tangent Modulus for Plane Strain, E_{tps}

$$R_f = \bar{b} \quad (1-11)$$

$$E_{tps} = \left(1 - R_f \bar{D} \right)^2 \left(\frac{\sigma_{df}}{\epsilon_{af}} \right) \bar{E}_i \quad (1-13)$$

Ratio of Lateral Strain to Axial Strain at Failure, $(\epsilon_l/\epsilon_a)_f$

$$I_R = U + V e_c \quad (1-15)$$

$$S = Y + Z e_c \quad (1-16)$$

$$\left(\frac{\epsilon_l}{\epsilon_a}\right)_f = I_R + S \log_{10} \left(\frac{\sigma_{3f}}{0.1} \right) \quad (1-14)$$

(for σ_{3f} in kg/cm^2)

Tangential Lateral Strain Ratio, $\left(\frac{\epsilon_l}{\epsilon_a}\right)_{tps}$

$$1/\bar{I}_\epsilon = J + N \log_{10} \left(\frac{\sigma_{3f}}{0.1} \right) \quad (1-19)$$

(for σ_{3f} in kg/cm^2)

$$\left(\frac{\epsilon_l}{\epsilon_a}\right)_{tps} = \frac{\left(\frac{\epsilon_l}{\epsilon_a}\right)_f \bar{I}_\epsilon}{\left[1 - \frac{(1 - \bar{I}_\epsilon)\bar{D}}{\bar{E}_i(1 - R_f\bar{D})} \right]^2} \quad (1-22)$$

Table 1-1. Summary of stress-strain parameters for LSS No. 2 at water contents of 1.9 and 1.0 %.

Parameter	w(%)		Parameter	w(%)	
	1.0	1.9		1.0	1.9
L	3.128	1.99	\bar{b}	0.475	0.475
M	1.165	0.815	U	1.713	1.713
G_f	0.964	0.875	V	-1.303	-1.303
F	0.360	0.0362	Y	-0.218	-0.218
h	2.301	0.9675	Z	-0.0933	-0.0933
P	2.97	4.58	J	1.78	1.68
Q	2.21	2.50	N	0.45	0.30
\bar{E}_i	2.06	2.06			

ONE-DIMENSIONAL COMPRESSION CHARACTERISTICS

One-dimensional compression tests (confined compression) were performed on specimens with different initial densities. A series with water content, $w = 1.0\%$ and a series with $w = 1.9\%$ were performed so that the influence of cohesion variations could be determined. The specimens were compressed in 2.8-inch-diameter, 1-inch-high, teflon-lined consolidation rings.

The compression data obtained from these tests were plotted as conventional e - $\log \sigma$ plots. Two example compression curves are shown in Figure 1-28. For both the 1.0% and 1.9% water contents it was found that, for mathematical description, the compression curves could be represented adequately by two straight lines and occasionally by one straight line in the case of high initial void ratio specimens.

A total of nine specimens were tested at various initial densities. For each specimen the value of void ratio at compressive stresses of $\sigma = 1, 10, 40, 100$, and 1000 g/cm^2 were observed and crossplotted to generate compression curves for specimens of intermediate initial density by interpolation. The compression curves thus obtained are shown in Figures 1-29 and 1-30. Each curve is identified by its initial void ratio, e_i , which corresponds to the void ratio of the specimen in the compression ring immediately after placement. The equations of the straight-line segments of the compression curves are

$$e = e_1 - c_a \log \sigma \quad (\text{for } 1 < 10 \text{ g/cm}^2). \quad (1-25)$$

and

$$e = e_{10} - c_b \log \sigma/10 \quad (\text{for } \sigma > 10 \text{ g/cm}^2). \quad (1-26)$$

The applicability of Equation (1-25) is limited to stresses greater than 1 g/cm^2 as indicated, but this presents no serious problem because compression under stresses less than 1 or 2 g/cm^2 was found to be negligible.

For a limited number of computations it is probably most practical to determine the change in the void ratio that accompanies a given change in stress by entering Figures 1-29 and 1-30 directly. The curves for intermediate values of e_i can be interpolated graphically. The stress

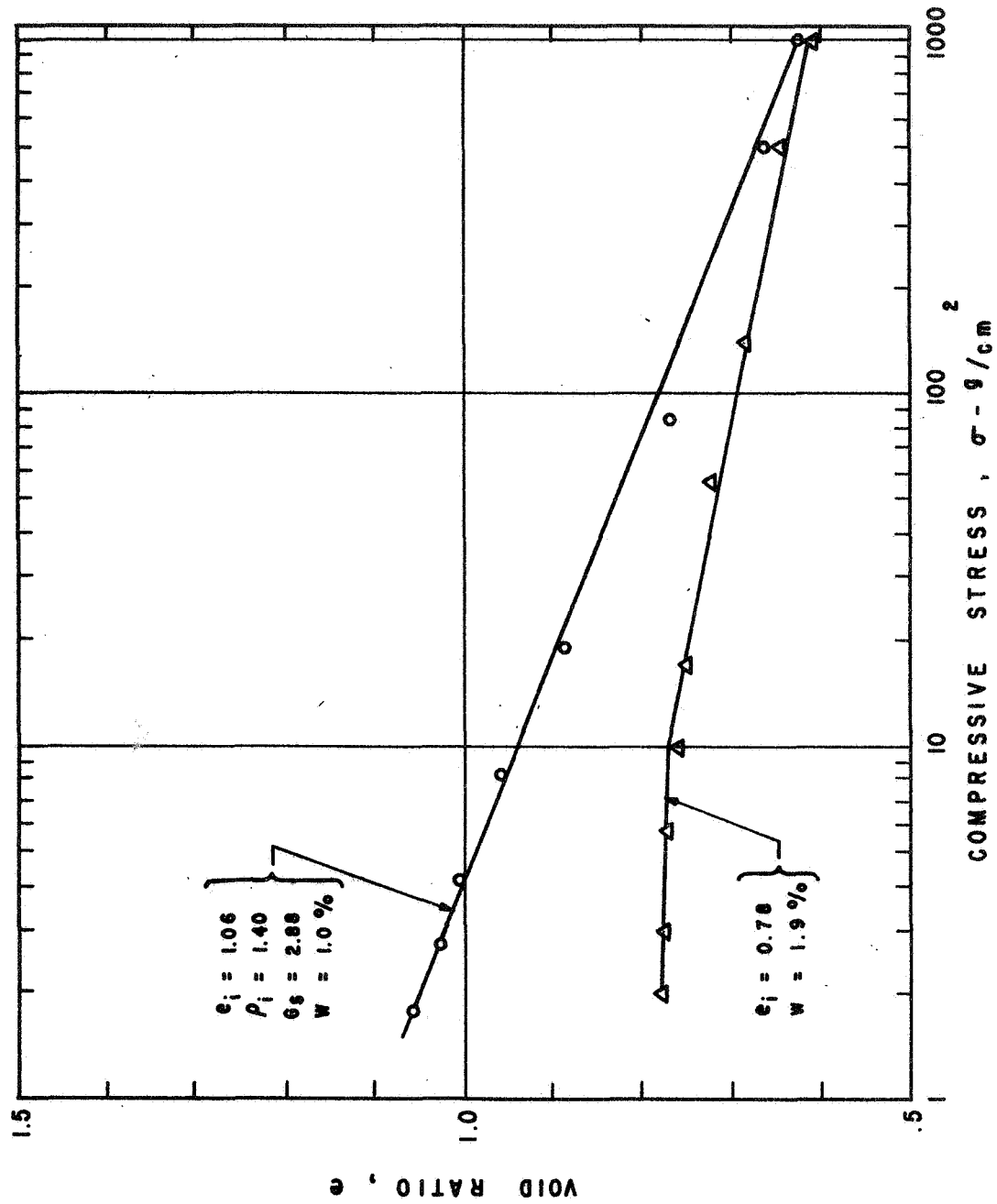


Fig. 1-28. Example 1-D compression curves for LSS No. 2.

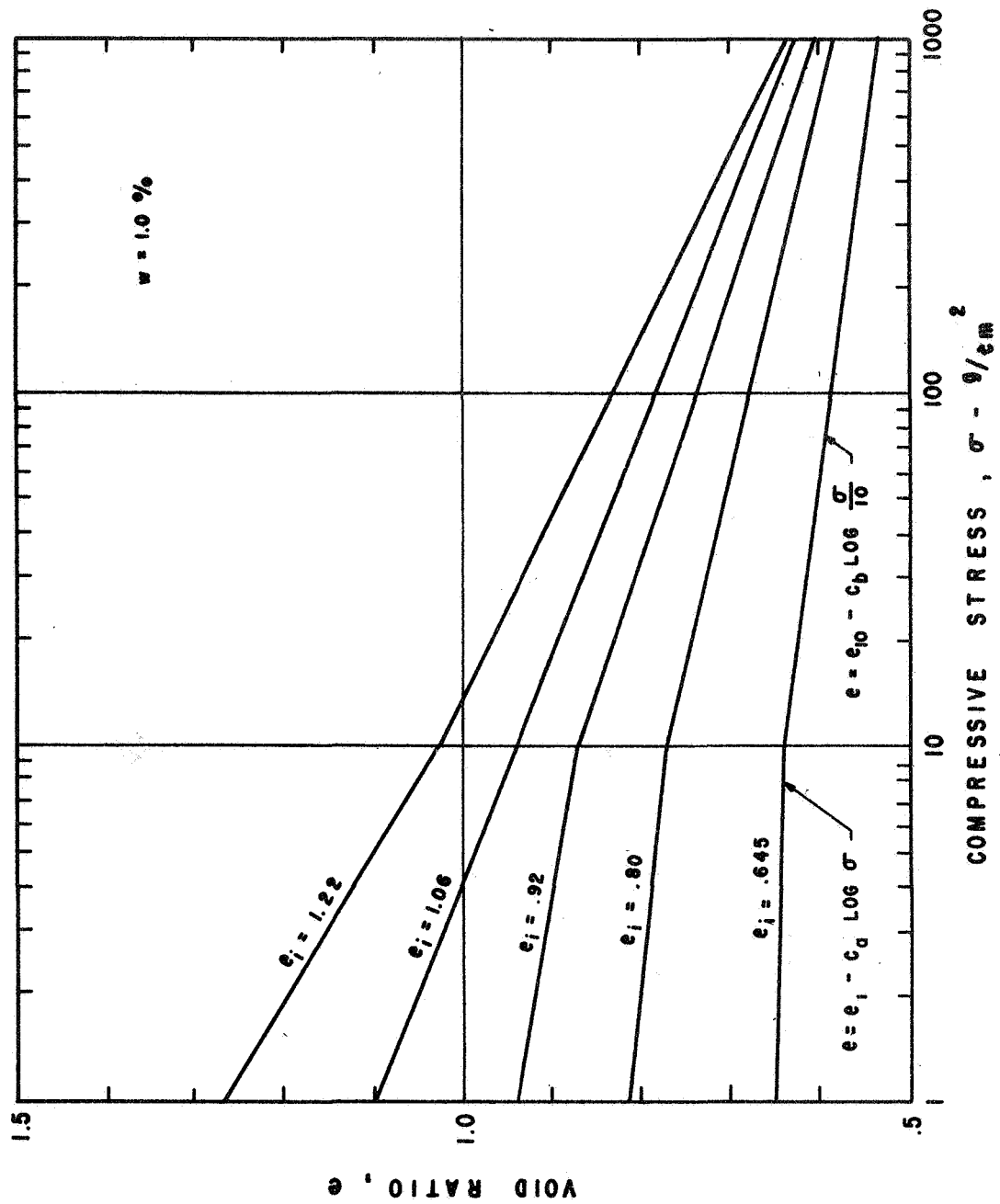


Fig. 1-29. One-dimensional compression curves for LSS No. 2 at 1.0% water content.

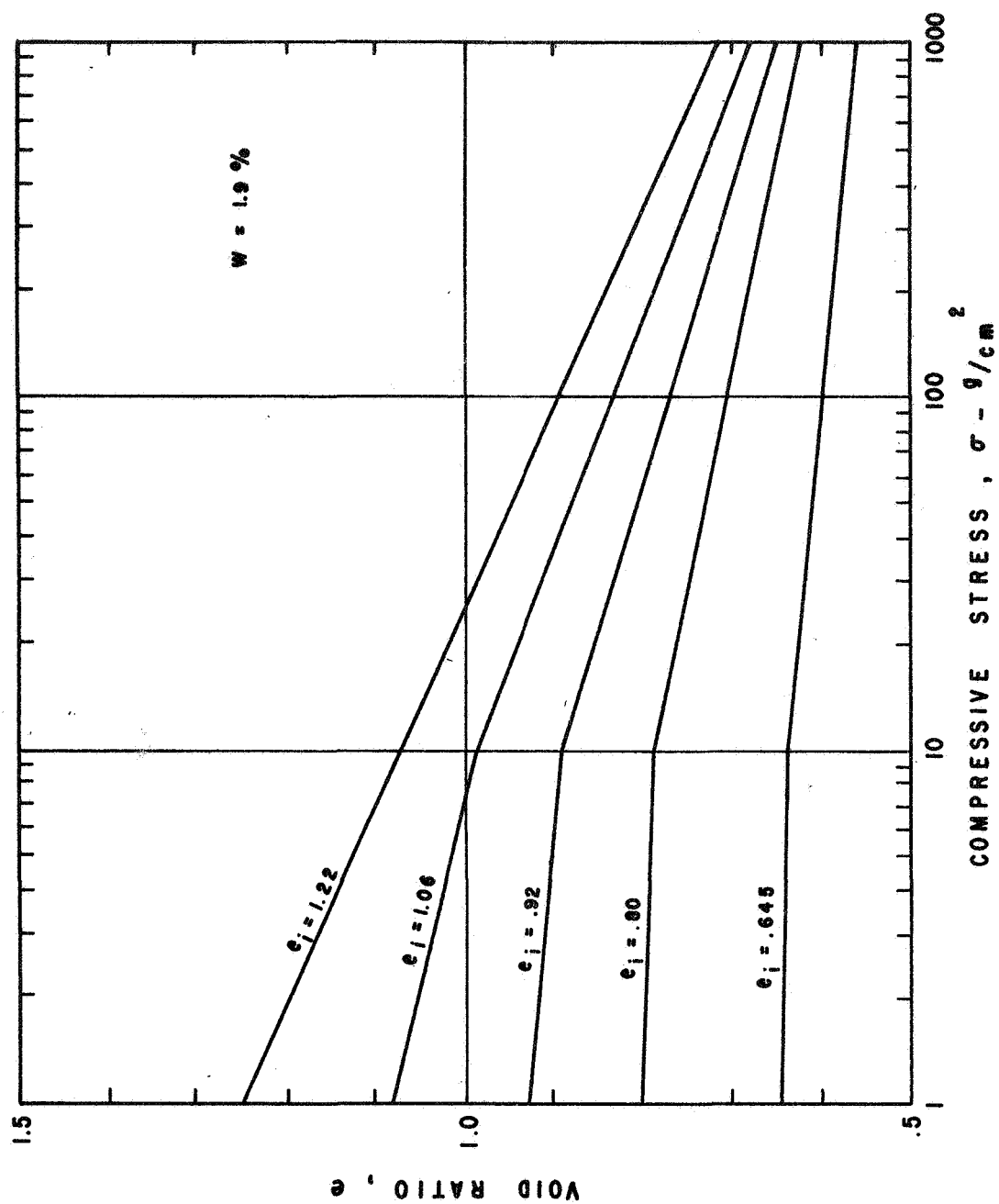


Fig. 1-30. One-dimensional compression curves for LSS No. 2 at 1.9% water content.

corresponding to e_i is the average gravity stress on the compression specimen at mid-depth before application of external load. This initial stress averages about 2 g/cm^2 .

For more numerous computations, it may be more practical to compute void ratio changes with a computer program. For programming, the parameters e_i , c_a , e_{10} , and c_b must be evaluated and related to the initial void ratio, e_i , and water content, w .

$$\begin{aligned} e_i &= \text{void ratio at } \sigma = 1 \text{ g/cm}^2 \text{ (obtained by extrapolation)} \\ c_a &= \Delta e \text{ between } \sigma = 1 \text{ and } \sigma = 10 \\ e_{10} &= \text{void ratio at } \sigma = 10 \\ c_b &= \Delta e \text{ between } \sigma = 10 \text{ and } \sigma = 100. \end{aligned}$$

Of course only three of the parameters are independent since

$$e_{10} = e_i - c_a \quad (1-27)$$

It was found that the relationship between e_1 and e_i could be satisfactorily represented as a straight line on an arithmetic plot, as shown in Figure 1-31. The equation of the line is

$$e_1 = m_1 e_i + r_1 \quad (1-28)$$

The values of m_1 and r_1 for $w = 1.0\%$ and 1.9% are shown on Figure 1-31.

The relationship between c_a and e_i was best represented as a straight line on a log-log plot, as shown in Figure 1-32. The equation expressing this relationship is

$$c_a = K_a e_i^{n_a} \quad (1-29)$$

The values of K_a and n_a for $w = 1.0\%$ and 1.9% are shown on Figure 1-32.

Because the value of e_{1000} , the void ratio at $\sigma = 1000 \text{ g/cm}^2$, is much less variable than c_b , it is useful to relate e_{1000} and e_i and calculate c_b by

$$c_b = \frac{e_{10} - e_{1000}}{2} \quad (1-30)$$

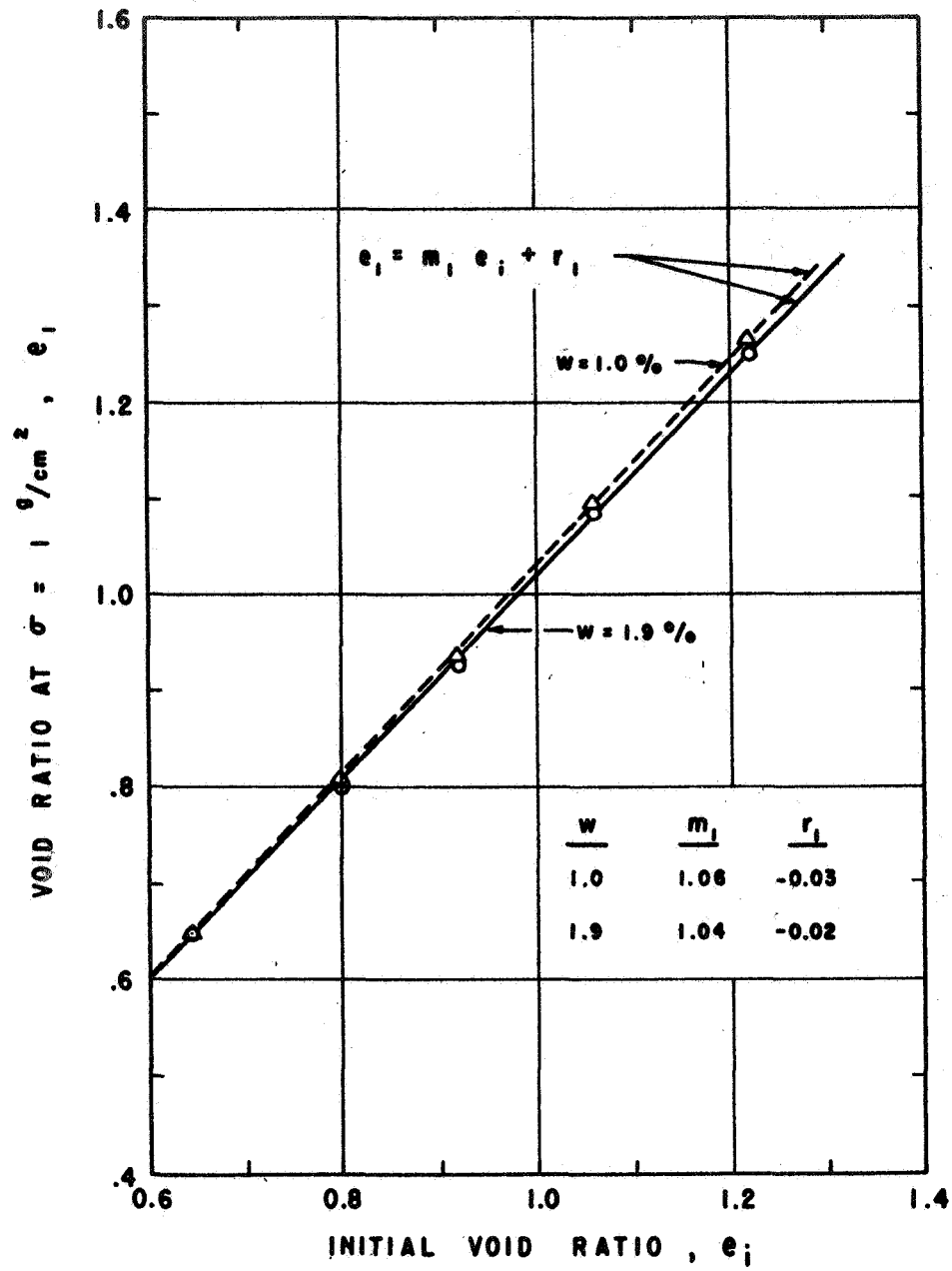


Fig. 1-31. Relationship between e_1 and e_i .

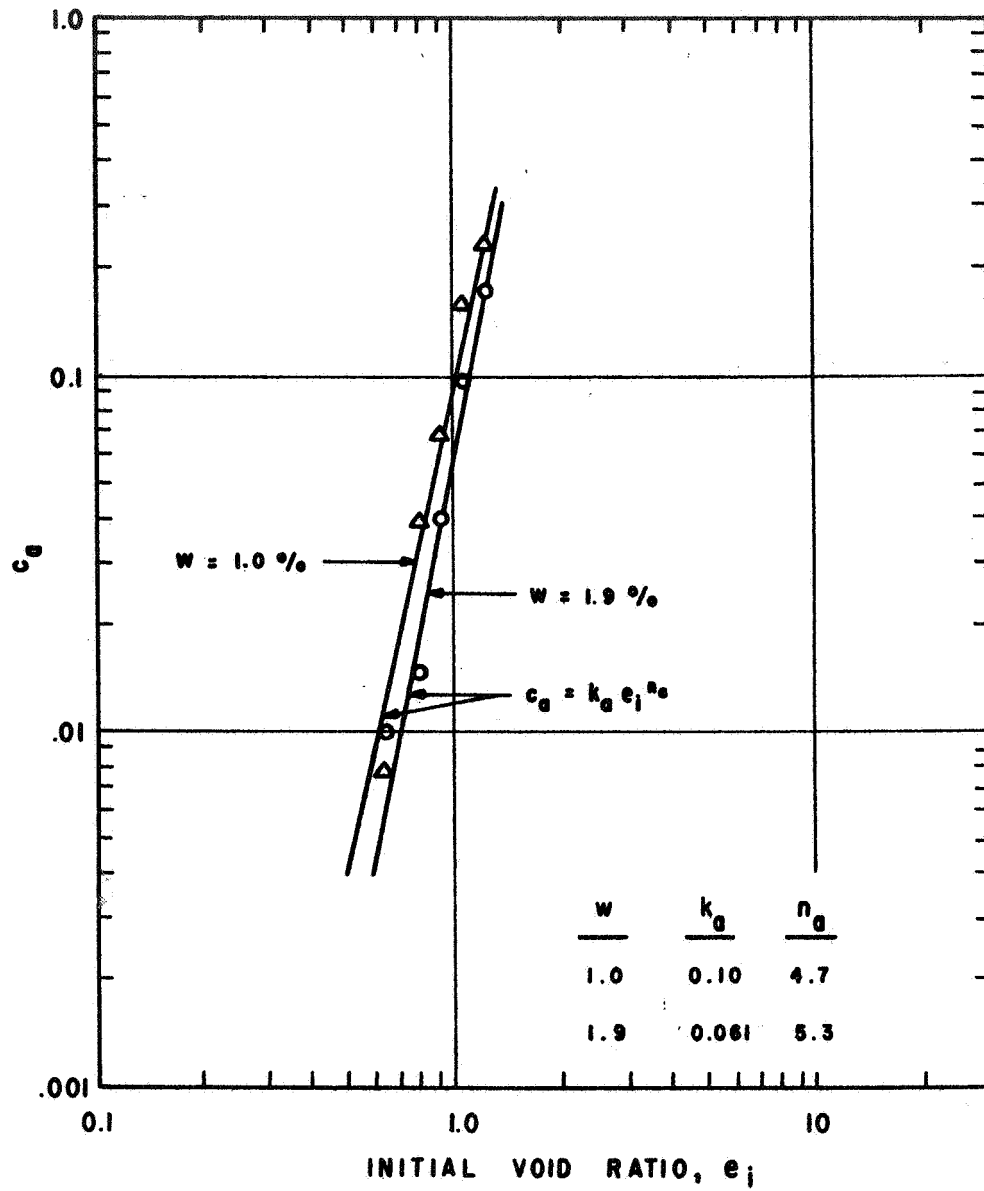


Fig. 1-32. Variation of c_a with e_i for 1-D compression tests.

The relationship between e_{1000} and e_i was found to give the best straight line when e_i/e_{1000} was plotted versus e_i on an arithmetic plot as shown in Figure 1-33. The equation is

$$\frac{e_i}{e_{1000}} = c_{1000} e_i + d_{1000}$$

or

$$e_{1000} = \frac{e_i}{c_{1000} e_i + d_{1000}} \quad (1-31)$$

The values of c_{1000} and d_{1000} for $w = 1.0\%$ and 1.9% are shown on Figure 1-33.

In view of the fact that the influence of water content on the compression parameters is relatively small, it is recommended that interpolations and small extrapolations for values of w other than 1.0% and 1.9% be made on a straight-line basis. Accordingly,

$$m_i = 1.06 - 0.02 \left(\frac{w - 1.0}{1.9 - 1.0} \right) = 1.082 - 0.022 w. \quad (1-32)$$

Similarly,

$$r_1 = 0.011 w - 0.041 \quad (1-33)$$

$$k_a = 0.1433 - 0.0433 w \quad (1-34)$$

$$n_a = 4.033 + 0.667 w \quad (1-35)$$

$$c_{1000} = 1.442 - 0.267 w \quad (1-36)$$

$$d_{1000} = 0.32 + 0.122 w. \quad (1-37)$$

The one-dimensional compression curves defined above are expected to represent the void ratio-stress relationship for both the lunar soil simulant and the actual lunar soil. One of the uses of such curves is to compute the change in void ratio which occurs as a result of compression of a soil layer under its own weight. The occurrence of gravity-induced compression implies that the soil deposit was built up in small layers and that each layer was subsequently compressed by the weight of overlying soil.

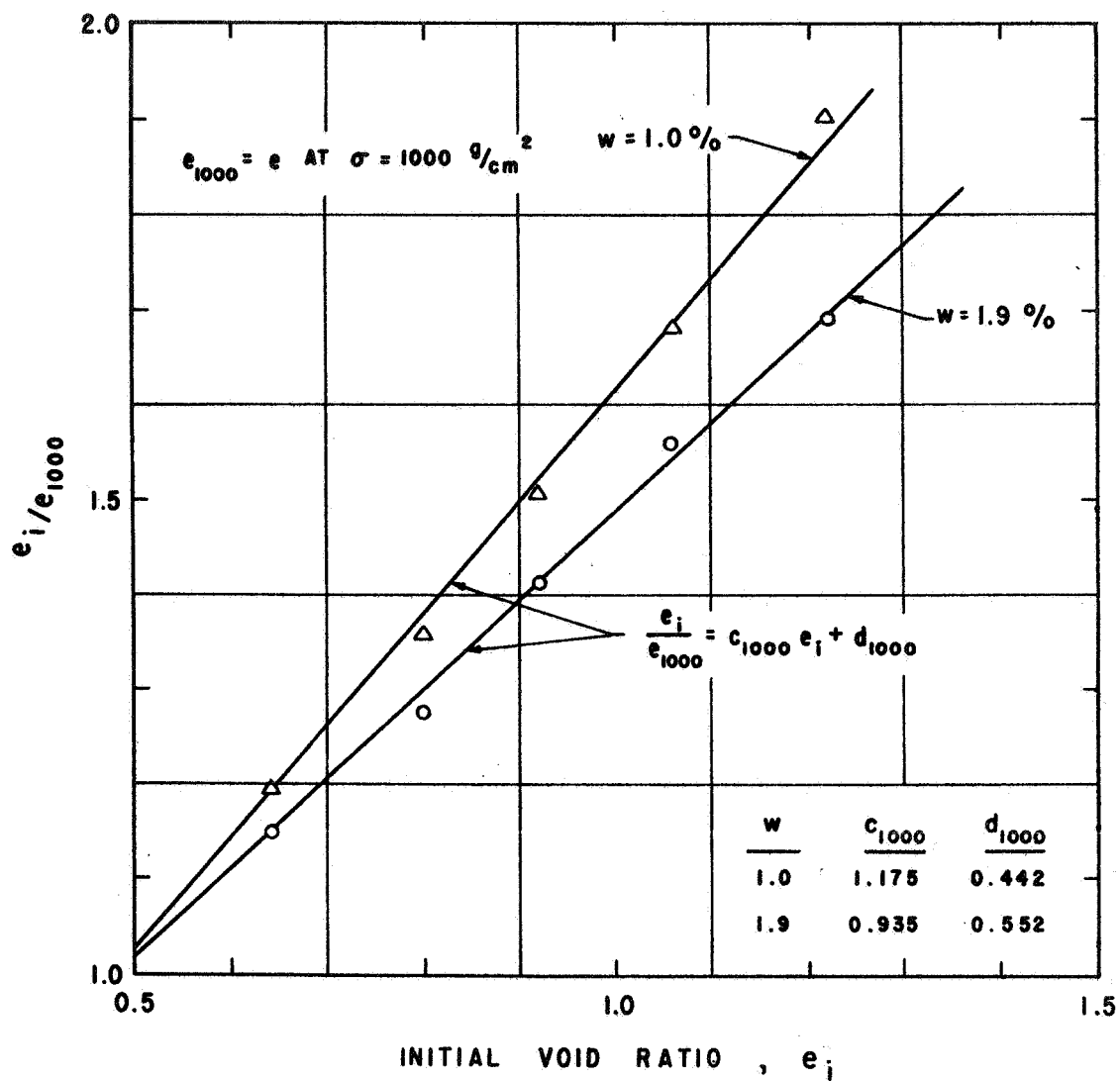


Fig. 1-33. Hyperbolic representation of relationship between e_i and e_{1000} for 1-D compression tests.

The void ratio-stress relationship for gravity-induced compression can be computed for a known value of water content, w , and initial void ratio at the surface of the deposit, e_i , by the following series of steps.

1. Compute values of m_1 , r_1 , k_a , n_a , c_{1000} , and d_{1000} from Equations (1-32) through (1-37).

2. Compute e_1 from Equation (1-28)

$$e_1 = m_1 e_i + r_1$$

3. Compute c_a from Equation (1-29)

$$c_a = K_a e_i^{n_a}$$

4. Compute e_{1000} from Equation (1-31)

$$e_{1000} = \frac{e_i}{c_{1000} e_i + d_{1000}}$$

5. Compute e_{10} from Equation (1-27)

$$e_{10} = e_1 - c_a$$

6. Compute c_b from Equation (1-30)

$$c_b = \frac{e_{10} - e_{1000}}{2}$$

7. Compute the final void ratio corresponding to any desired stress by Equations (1-25) and (1-26).

$$e = e_1 - c_a \log \sigma \quad (\text{for } 1 < \sigma < 10 \text{ g/cm}^2)$$

$$e = e_{10} - c_b \log \left(\frac{\sigma}{10} \right) \quad (\text{for } \sigma > 10 \text{ g/cm}^2).$$

The values of e_i and w are needed to generate the compression curve as outlined in the preceding steps. Although e_i is frequently known, in the more general case, an element of soil may be known to exist at some void ratio, e_0 , and some stress σ_0 . The value of e_0 , may be significantly less than e_i . The computation of subsequent compression requires the determination of the compression curve on which the point (σ_0, e_0) lies. Again, this determination is most easily made by entering Figures (1-29) and (1-30) with the values σ_0 and e_0 and graphically interpolating to find the right compression curve and the corresponding value of e_i . For values of w other than 1.0% and 1.9%, graphical interpolation can be made using both Figures (1-29) and (1-30) and straight-line interpolation can be used. It may be noted that for relatively small changes in stress satisfactory accuracy can be obtained by ignoring water content.

For the case in which the solution is to be obtained using a computer program, the interpolation described in the preceding paragraph may be accomplished as follows:

1. Compute values of m_1 , r_1 , k_a , n_a , c_{1000} , and d_{1000} from Equations (1-32) through (1-37) as in Step 1 above.
2. Solve the following six equations simultaneously for the unknown parameters e_1 , c_a , e_{10} , c_b , e_i , e_{1000} .

$$e_1 = m_1 e_i + r_1$$

$$c_a = k_a e_i^{n_a}$$

$$e_{1000} = \frac{e_i}{c_{1000} e_i + d_{1000}}$$

$$e_{10} = e_1 - c_a$$

$$c_b = \frac{e_{10} - e_{1000}}{2}$$

$$e_0 = e_1 - c_a \log \sigma_0 \quad (\text{for } \sigma_0 < 10)$$

or

$$e_0 = e_{10} - c_b \log \left(\sigma_0 / 10 \right) \quad (\text{for } \sigma_0 > 10) .$$

The parameters thus obtained may be used in Equations (1-25) and (1-26) to compute the decrease in void ratio due to increasing the stress above the existing value, σ_0 .

The preceding development of compression parameters facilitates the computation of the densification caused by any one-dimensional loading of the LSS starting from any reasonable values of initial density and compressive stress. The same parameters can be used for similar computations for the actual lunar soil. The accuracy of these computations is expected to be consistent with the degree to which the LSS matches the actual lunar soil.

DETERMINATION OF DENSITY VARIATION WITH DEPTH

Stress-strain relationships for the LSS depend very heavily on initial density or void ratio. Therefore, any detailed analysis of the stress-deformation behavior of the LSS or the actual lunar soil requires knowledge of the variation of initial density with depth for the soil deposit.

If densification of a soil deposit has occurred due to the weight of overlying soil, the one-dimensional compression parameters developed in the preceding section can be used to relate void ratio to depth. It is possible to derive analytical relationships between average density and depth as was done for Lunar Soil Simulant No. 1 and reported in the detailed Technical Report (Mitchell and Houston, 1970) submitted to MSFC in January 1970. However, the description of the e - $\log \sigma$ curves as two straight lines instead of one makes the relationships to be derived much too cumbersome. Instead, Figures 1-29 and 1-30 were used to graphically develop the density profiles shown in Figures 1-34 and 1-35.

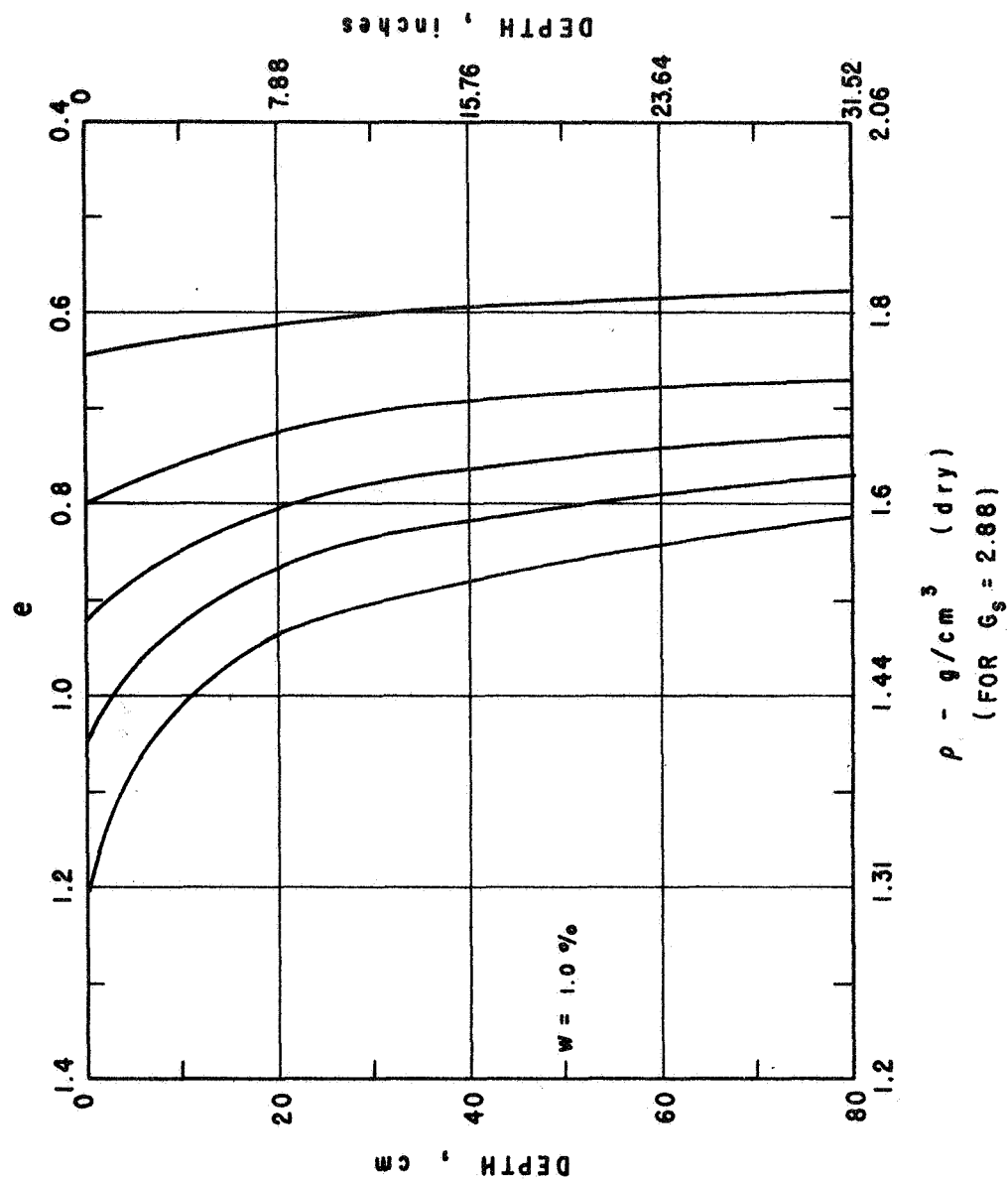


Fig. 1-34. Variation of void ratio with depth for LSS No. 2 at $w = 1.0\%$ with terrestrial gravity.

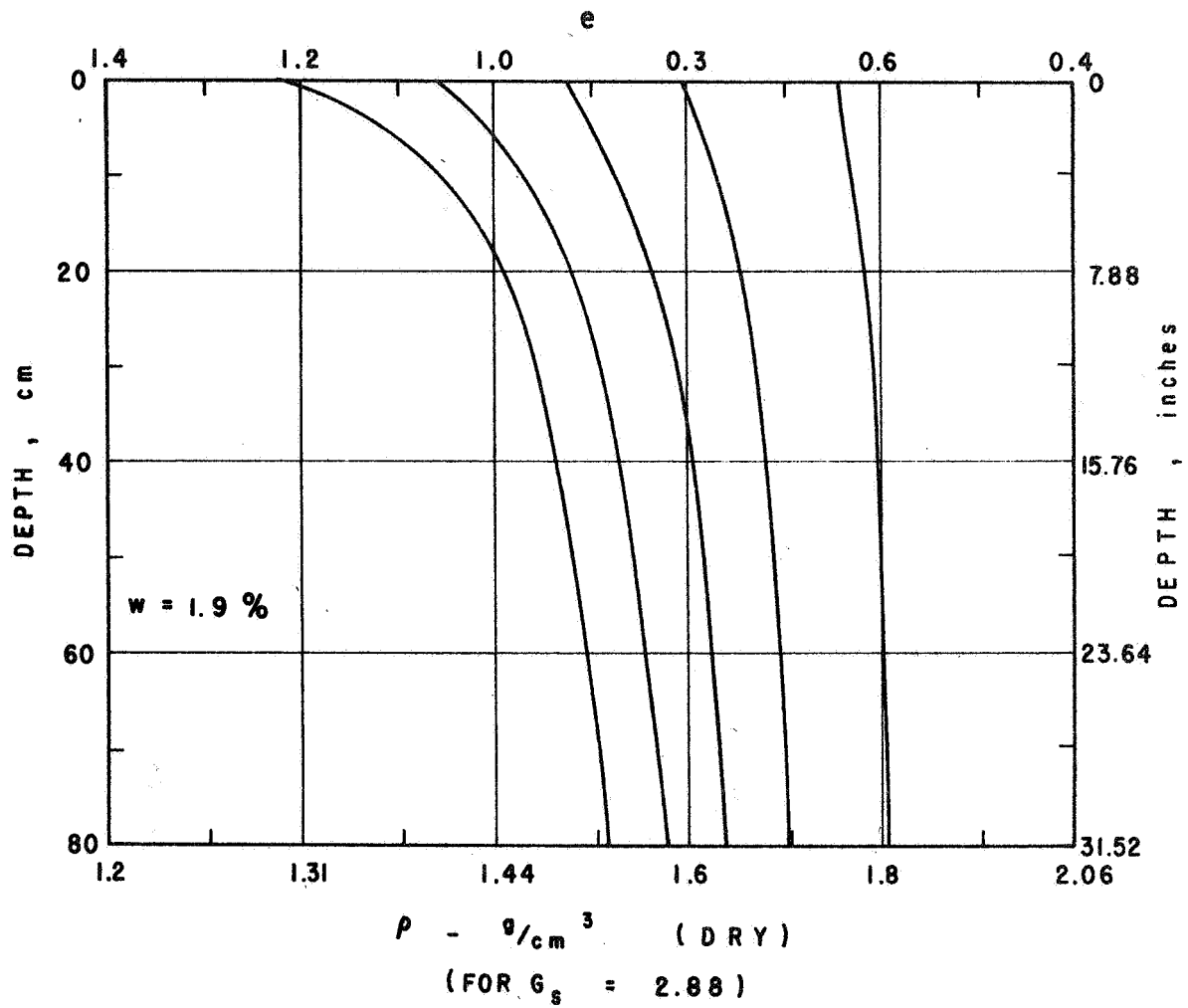


Fig. 1-35. Variation of void ratio with depth for LSS No. 2 at $w = 1.9\%$ with terrestrial gravity.

The void ratio at the surface ($z = 0$) represents the value of e_i for each profile. Profiles for intermediate values of e_i may be obtained by interpolation.

Figures 1-36 and 1-37 show how the average void ratio, e_{ave} , depends on the initial void ratio, e_i . Because void ratio varies with depth, the value of e_{ave} depends on the total depth of deposit. The average void ratio for the top 15 cm (≈ 6 inches) was adopted for comparison of depths of footprints and penetration resistances discussed in later sections.

The top 6 inches was chosen because it is expected to exert the strongest influence on the footprint depth and penetration resistance. Through interpolation, Figures 1-36 and 1-37 may be used to determine the value of e_{ave} for the top 15 cm of any deposit of LSS No. 2, provided that e_{ave} is known for any depth between 15 and 80 cm and that compression has occurred due to the weight of overlying soil. Figures 1-36 and 1-37 facilitate easy conversion of average void ratio for one depth to average void ratio for another depth.

Similar charts were prepared for the actual lunar soil under lunar gravity (Figures 1-38 and 1-39). These profiles were developed by assuming that the compressibility parameters of the actual lunar soil are most closely matched by those of LSS No. 2 at $w = 1.9\%$. A water content of 1.9% was chosen because cohesion studies have indicated that the cohesion of LSS No. 2 at this water content is closest to the best estimates thus far obtained for the actual lunar soil. Since the weight of overlying material on the moon is only about one-sixth of the corresponding stress under terrestrial gravity, densification with depth is less pronounced on the lunar surface than on earth.

PLATE LOAD TESTS

Plate load tests were conducted on the lunar soil simulant in a test bin 3.5 feet wide, 4 feet deep, and 7 feet long. The wooden test bin is made up of two 2-foot-high removable rectangular sections. These sections may be used separately. Separate use of these sections allows the tests to be conducted on any depth of soil and reduces the effort of emptying and filling the test bin. The details of the equipment and the testing procedures are discussed below.

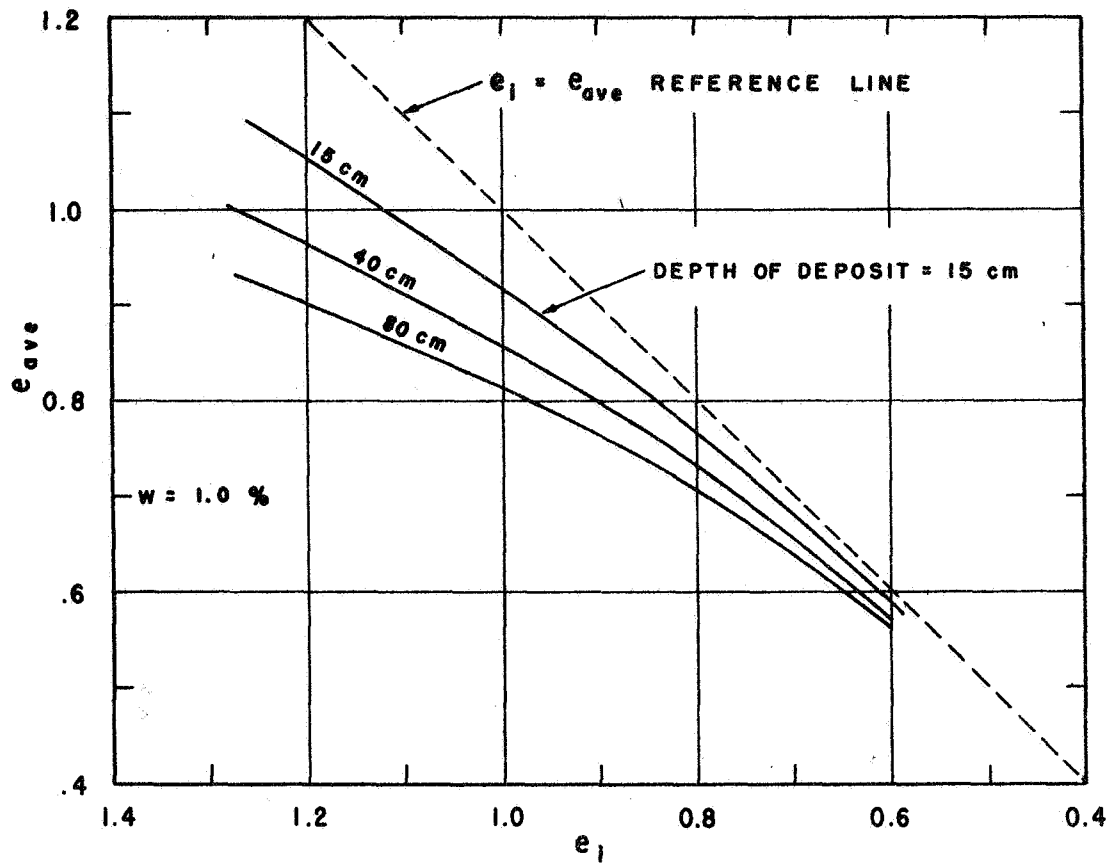


Fig. 1-36. Variation of average void ratio with initial void ratio for LSS No. 2 at $w = 1.0\%$ with terrestrial gravity for various depths of deposit.

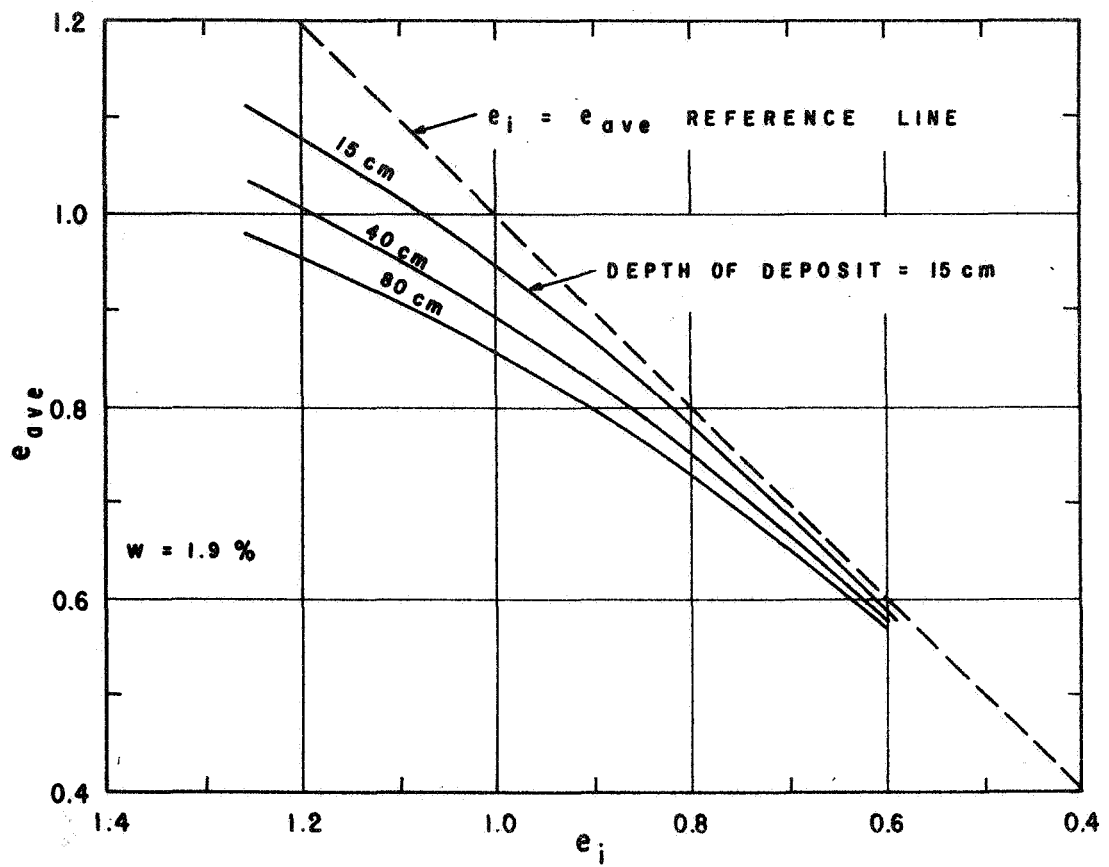


Fig. 1-37. Variation of average void ratio with initial void ratio for LSS No. 2 at $w = 1.9\%$ with terrestrial gravity for various depths of deposit.

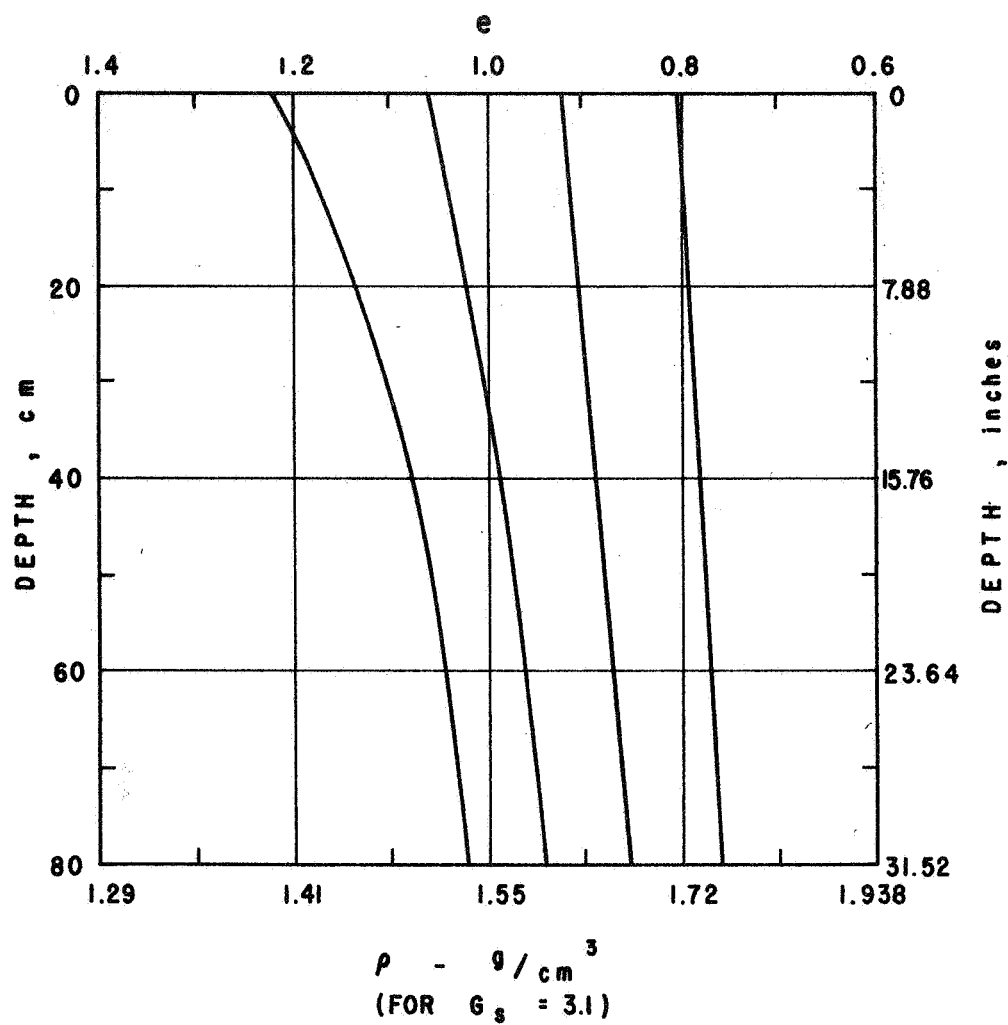


Fig. 1-38. Predicted variation of void ratio with depth for actual lunar soil under lunar gravity (compression parameters correspond to $w = 1.9\%$).

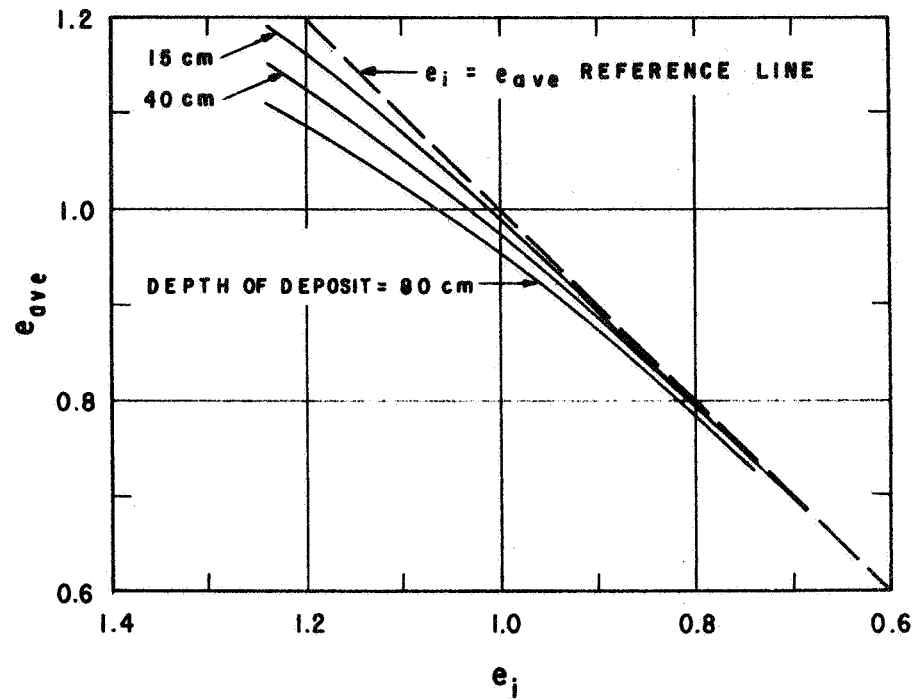


Fig. 1-39. Predicted variation of average void ratio with initial void ratio for actual lunar soil under lunar gravity (compression parameters correspond to $w = 1.9\%$).

Soil Placement

As reported earlier (Mitchell and Houston, 1970), the placement density depends on the height of drop, other factors being constant. This fact was utilized in the development of the placement technique. The soil placement equipment is shown in Figures 1-40a, 1-40b, 1-41, and 1-42. Briefly, the placement technique is as follows. The lunar soil simulant is placed in a large spreader box (Figures 1-40a and 1-40b) with a triangular cross section (Figure 1-40b). A cylindrical steel shaft occupies an opening in the bottom of the box. This shaft is capable of rotation about its long axis, thus facilitating the removal of the soil from the spreader box. The shaft is driven by an electric motor mounted on the side of the spreader box (Figure 1-40a). A wooden board is suspended from the spreader box immediately under the rotating shaft to absorb the kinetic energy of the soil particles by breaking their height of drop, thus yielding uniform low-density deposits. This board is raised or removed when medium to dense deposits are required.

The spreader box is suspended from a gantry by adjustable cables. The gantry is chain-driven by an electric motor. This frame can be moved forward and backward, thus allowing the spreader box to deposit soil along the full width of the test bin. As the soil deposit builds up, the spreader box is elevated to maintain a constant height of drop. It was found that some vibration of the spreader box is required for a continuous downflow of soil. For this purpose, an electric vibrator is connected to the spreader box by a chain extending from one end of the box to the other.

The electric motors are operated from one conveniently located control panel.

The loading equipment includes a hydraulically activated loading apparatus (Figures 1-43 and 1-44), consisting of three bellofram loading pistons in series. The load is transmitted to the plate by a shaft that extends through and is rigidly connected to the three pistons. The two lower pistons apply a load downward. The effective areas of these two bellofram pistons are different. The smaller piston (cylinder No. 1

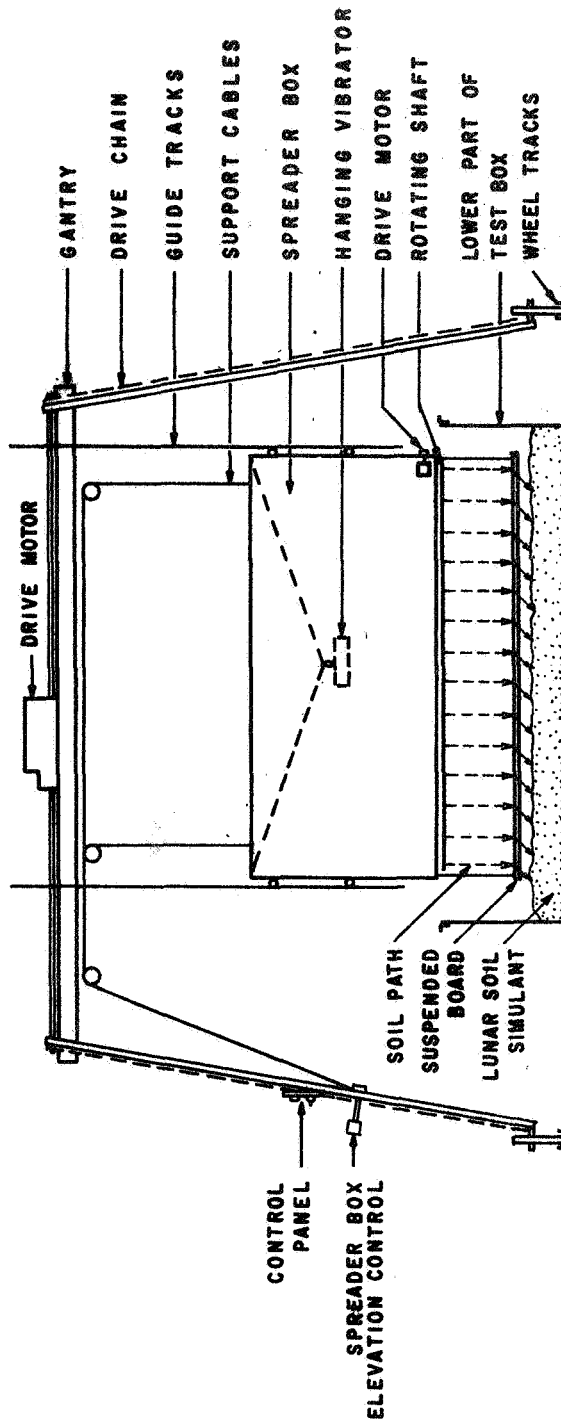


Fig. 1-40a. Schematic diagram of equipment used for the placement of the lunar soil simulant.

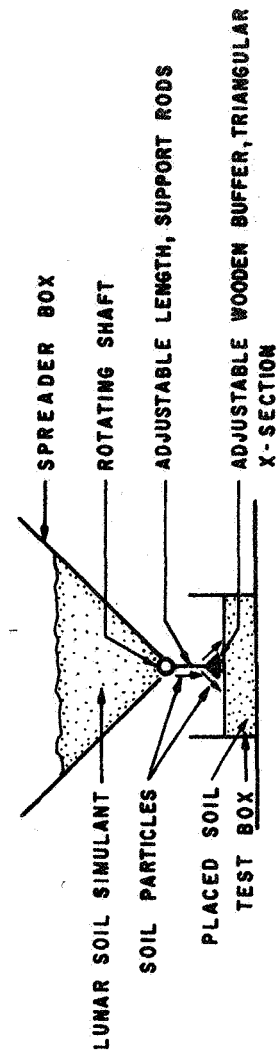


Fig. 1-40b. Schematic diagram of spreader box side view.

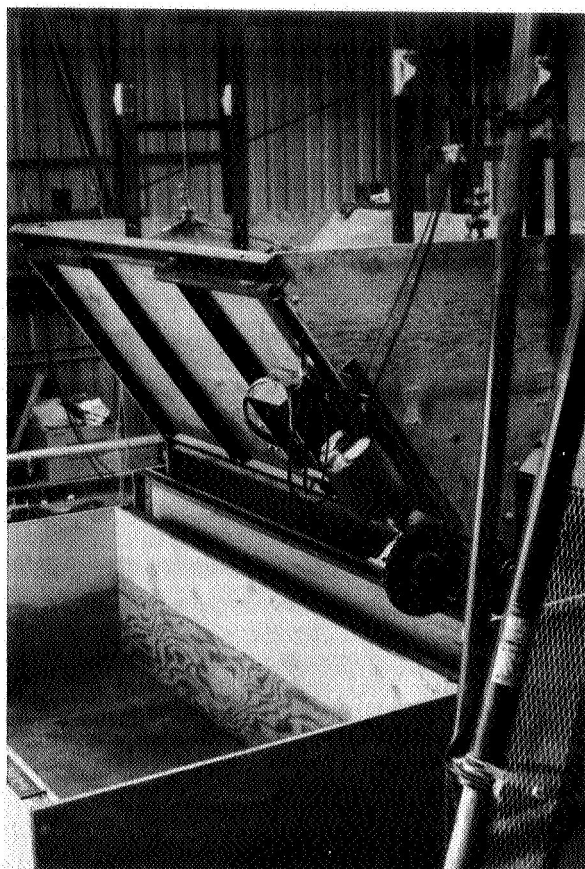


Fig. 1-41. Soil placement equipment.

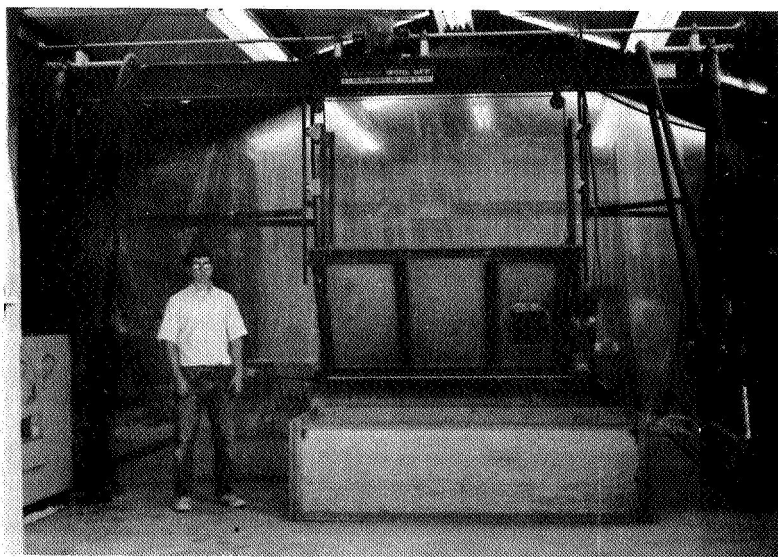


Fig. 1-42. Soil placement equipment.

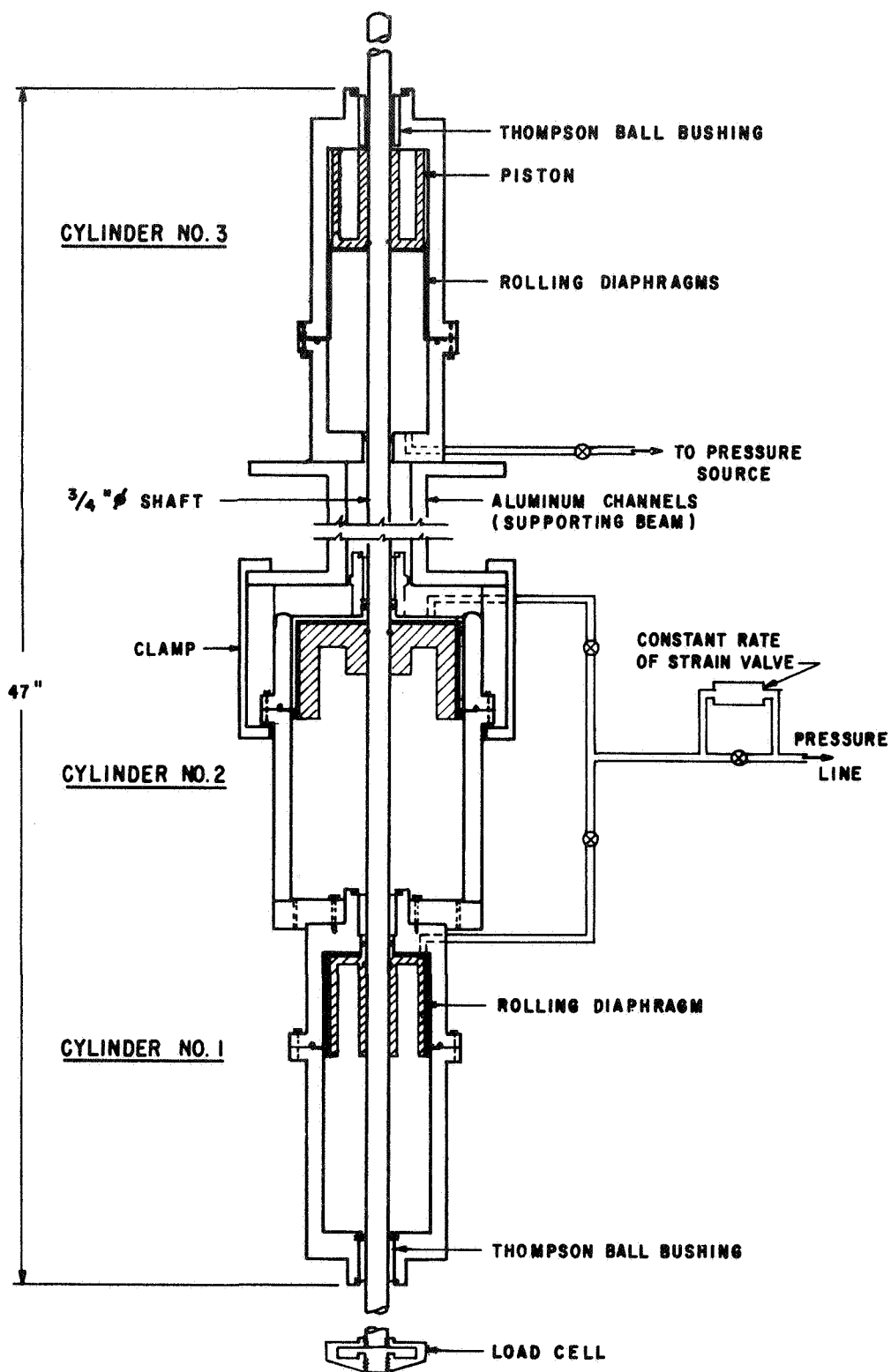


Fig. 1-43. Schematic diagram for plate loading device.

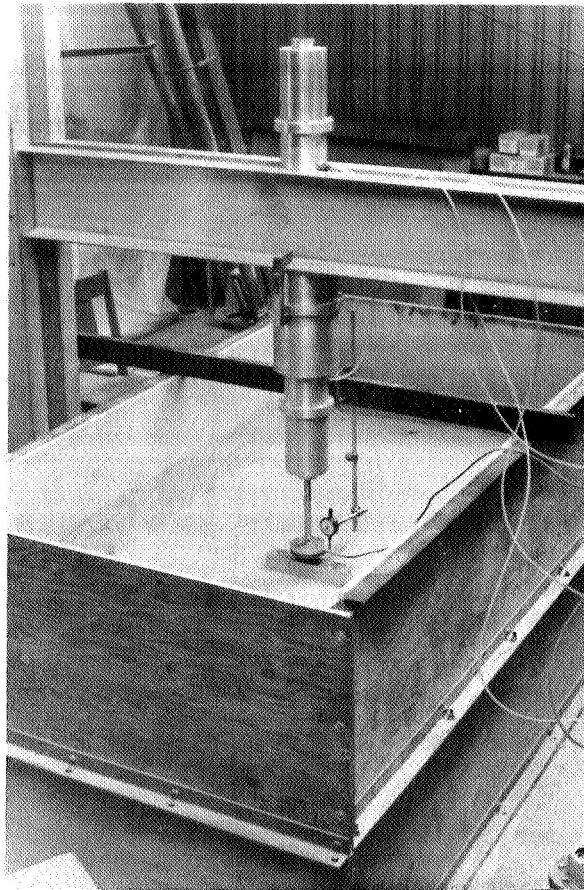


Fig. 1-44. Plate loading device.

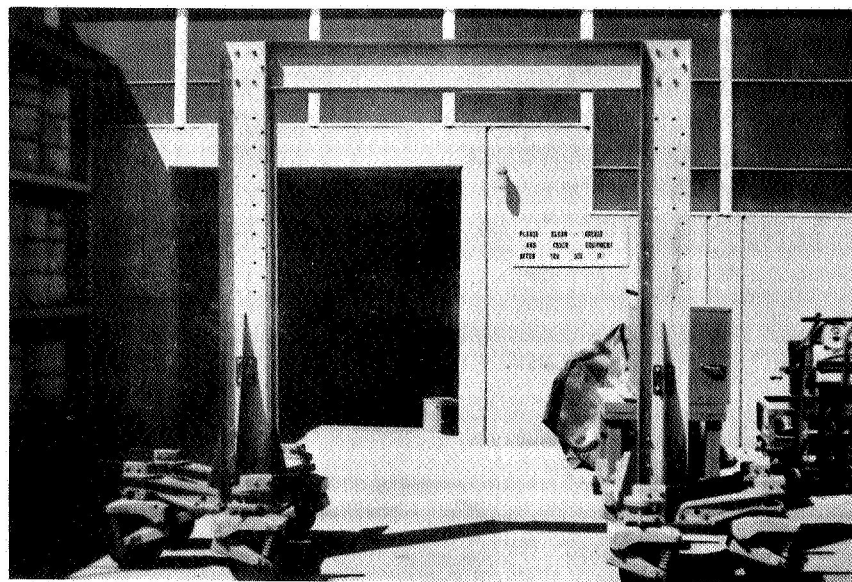


Fig. 1-45. Supporting frame.

in Figure 1-43) is activated in the low load range to obtain higher sensitivity, and the larger piston (in cylinder No. 2) is activated for higher loads. Maximum loading capacity is obtained by activating both pistons simultaneously. The third piston (in cylinder No. 3) is in a reversed position and applies an upward load. It can be used to balance the weight of any size plate and facilitates zeroing the load and positioning the plate. For loose soils, plate penetration would be excessive if the full weight of a heavy plate were applied. The third piston allows the gradual application of the full weight of any plate.

The versatility of the apparatus is improved by the provision of a relatively large piston stroke (6.25 inches). Furthermore, the hydraulic system allows for the application of the load either incrementally or continuously at any desired loading rate or at a constant deformation rate.

The plate load test equipment also includes a supporting frame, which consists of two aluminum channels spanning across the test box. The heavy supporting frame acts as a reaction for the loading piston. The supporting beam for the cylinder is connected by bolts to two channeled aluminum columns, which are individually supported on wheels and are therefore easily moveable. The supporting beam elevation is easily adjusted to allow testing any depth of soil deposited in the test bin (Figure 1-45).

Test Plates

Three different size aluminum plates were used. All plates have a length-to-width ratio of 5:1, and the following dimensions:

- 1 × 5 inches, 1 inch thick
- 2 × 10 inches, 2 inches thick
- 4 × 20 inches, trussed plates 12 inches thick at center, tapering to 2 inches thick at the ends.

Test Procedure

Three different soil densities ranging from loose to dense were used for the plate load tests.

The low-density soil deposit was obtained using a soil free-fall of about 2 inches. The free-fall for the medium density soil deposit was 26 inches. The dense soil deposit was obtained by first depositing the soil using a 26-inch free-fall in 4-inch lifts. Then a 3.5-by-2.0-ft board 1-inch thick, was placed on the surface of each lift. The soil was densified by vibration using a rotary vibrator placed on the board for a period of 2 minutes.

Vibration rather than static load alone was used for densification for the following reason. If a static vertical stress large enough to achieve the same densification as for vibration had been applied, the upper layer of soil would have been effectively over-consolidated when the stress was removed. Abnormally high horizontal normal stresses would have been "locked in" if this procedure had been followed. The "locked in" stresses are expected to be lower for vibratory compaction than for static compaction. Figures 1-46 and 1-47 show the void ratio and the moisture content vs depth for three test bins.

Each test bin was large enough to allow testing of all three plates. For each test series, at least three tests were performed with the smallest plate and two tests with the medium plate. In general, the plates were aligned perpendicular to the long axis of the test bin and spaced so as to minimize test bin side effects and the influence of other test plates. The degree of reproducibility for tests with the same plate at different locations within the test bin indicates that side effects were negligible and that horizontal variations in soil density were negligible. The load applied to each plate was measured with a very sensitive load cell, and the vertical settlement was measured by a 1/1000-inch dial gage. A typical test setup is pictured in Figure 1-48. Figure 1-49 shows the imprint in the loose soil deposit of the 4-by-20-inch test plate.

Basic Test Data

The results of the duplicated tests for each test series were in very good agreement. Figures 1-50, 1-51, and 1-52 show the results of each test series.

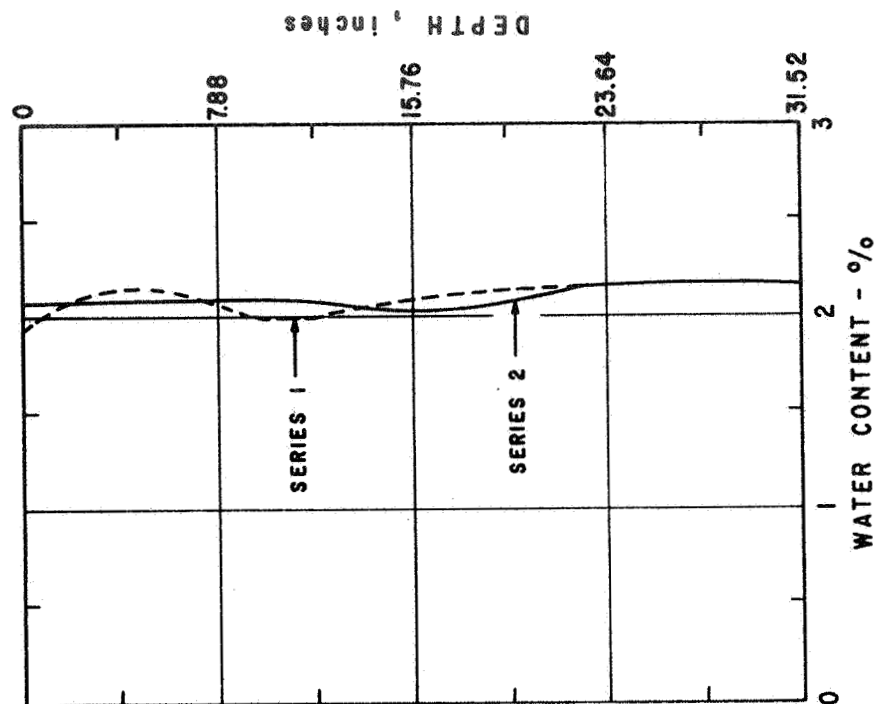
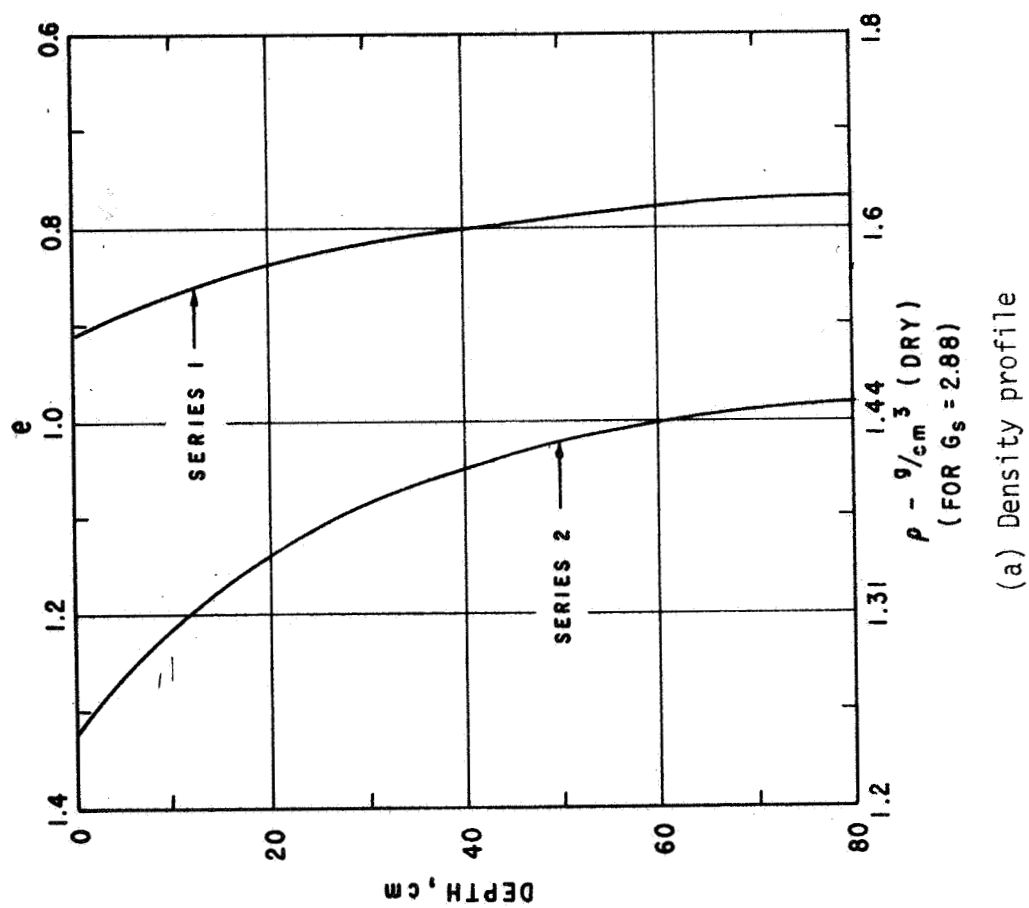
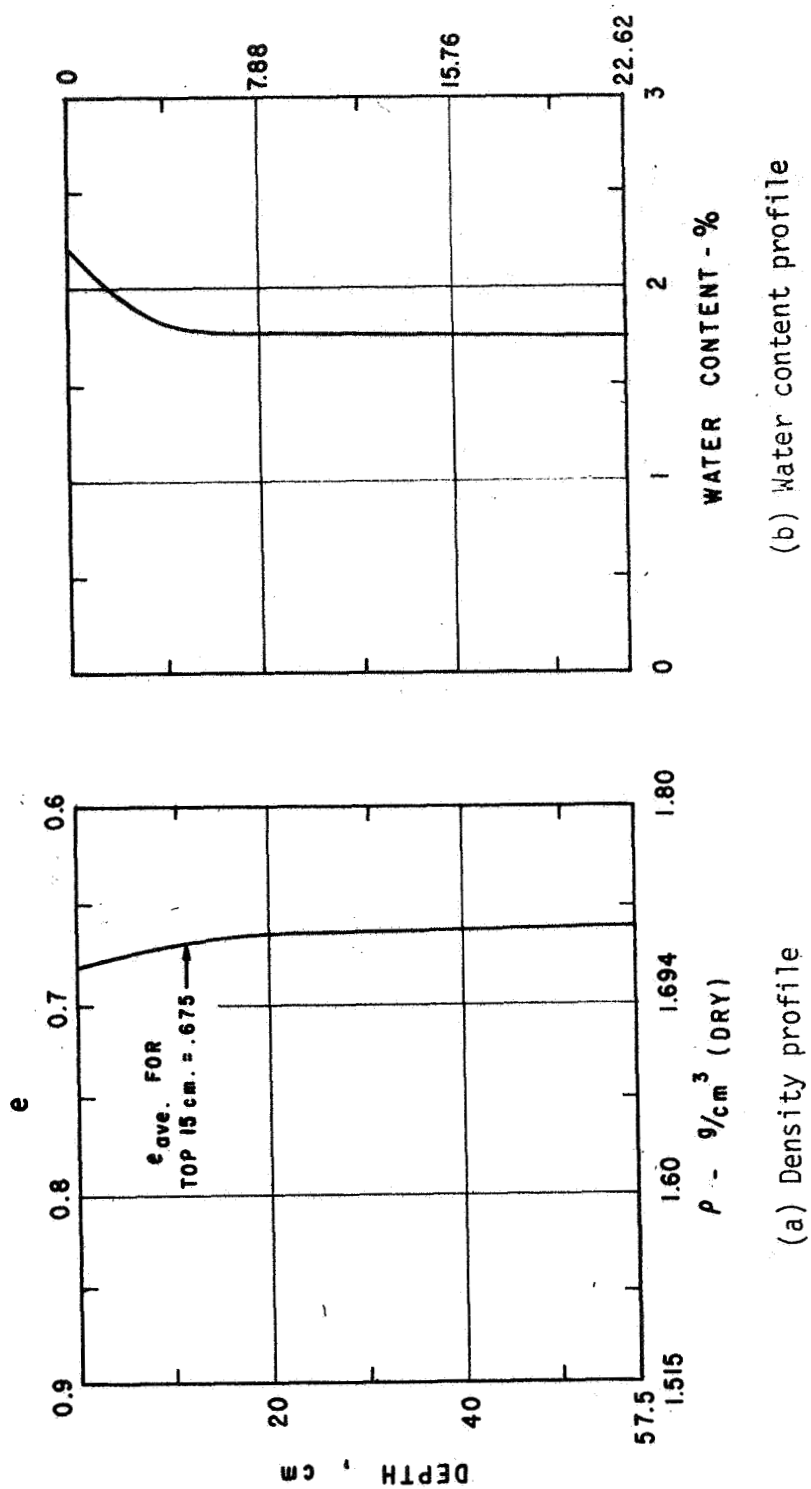


Fig. 1-46. Density and water content profiles for model test series Nos. 1 and 2.



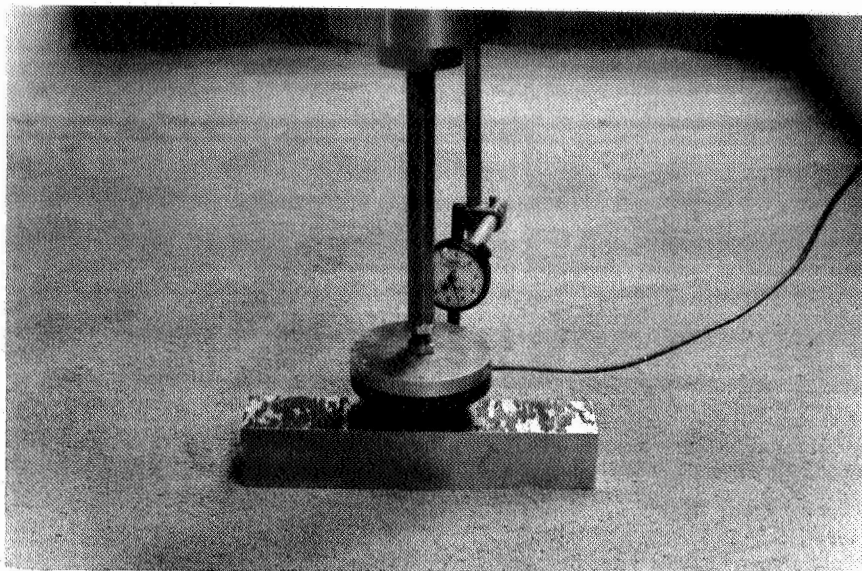


Fig. 1-48. Test setup.

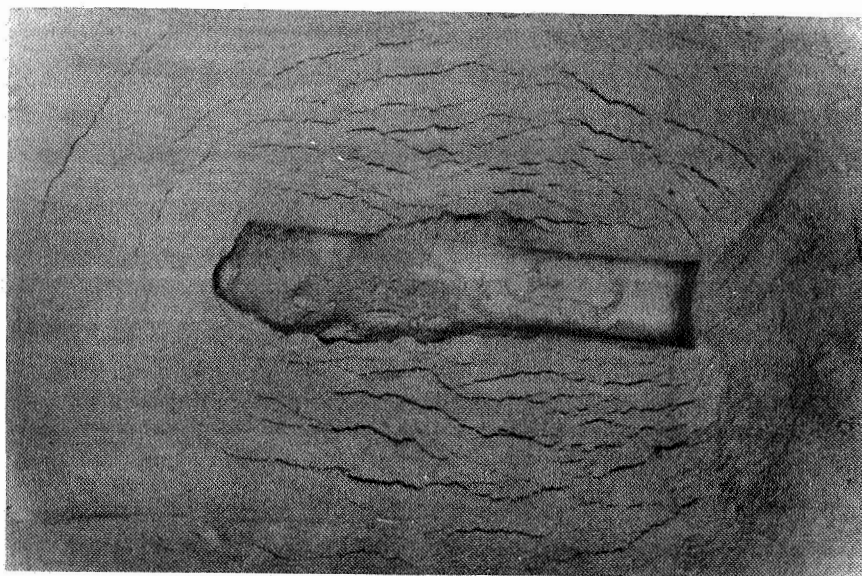


Fig. 1-49. Imprint of the 4 x 20 inches plate
in test series 2 (Loose deposit).

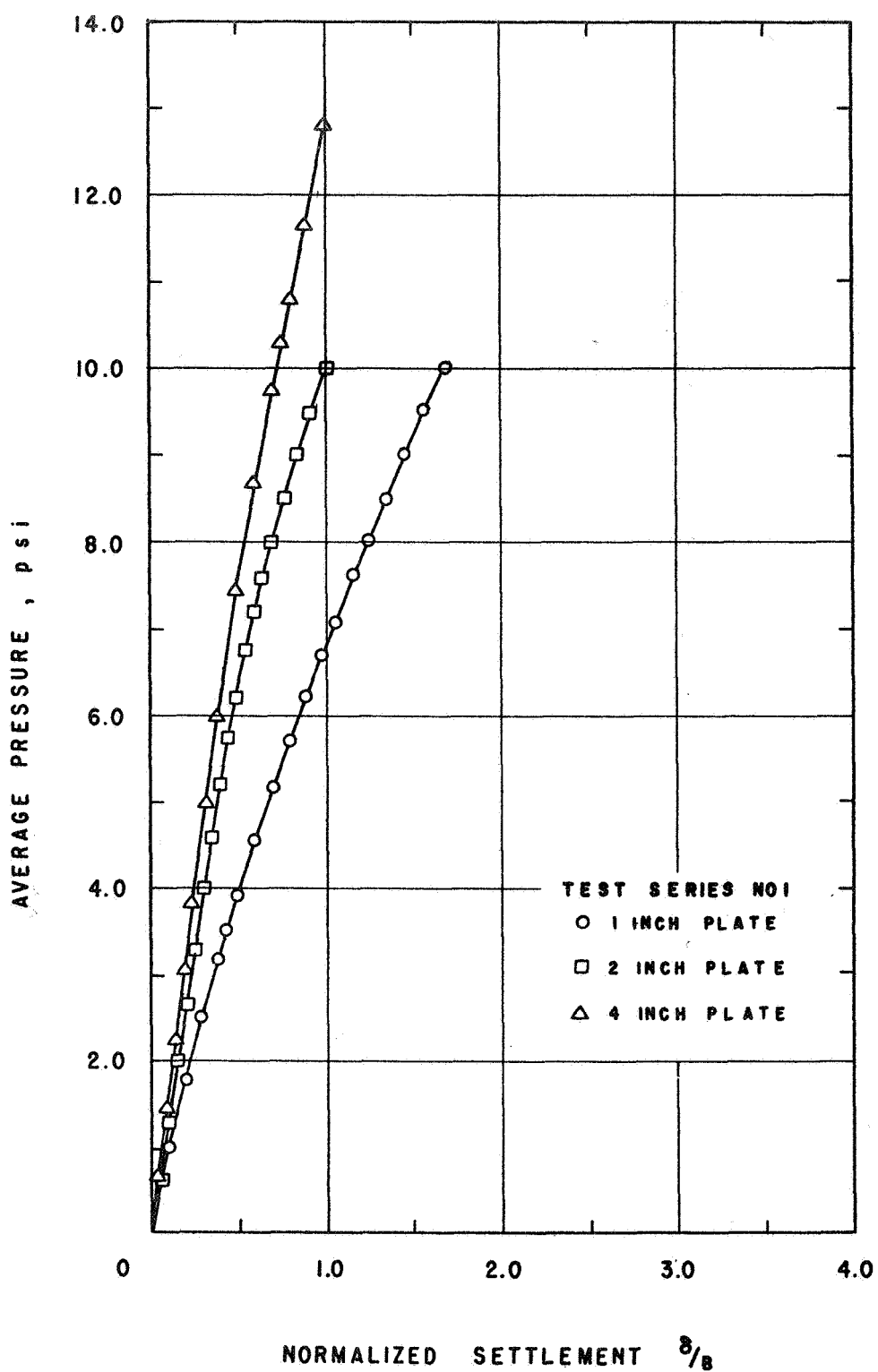


Fig. 1-50. Plate load test results for test series No. 1 (Medium dense).

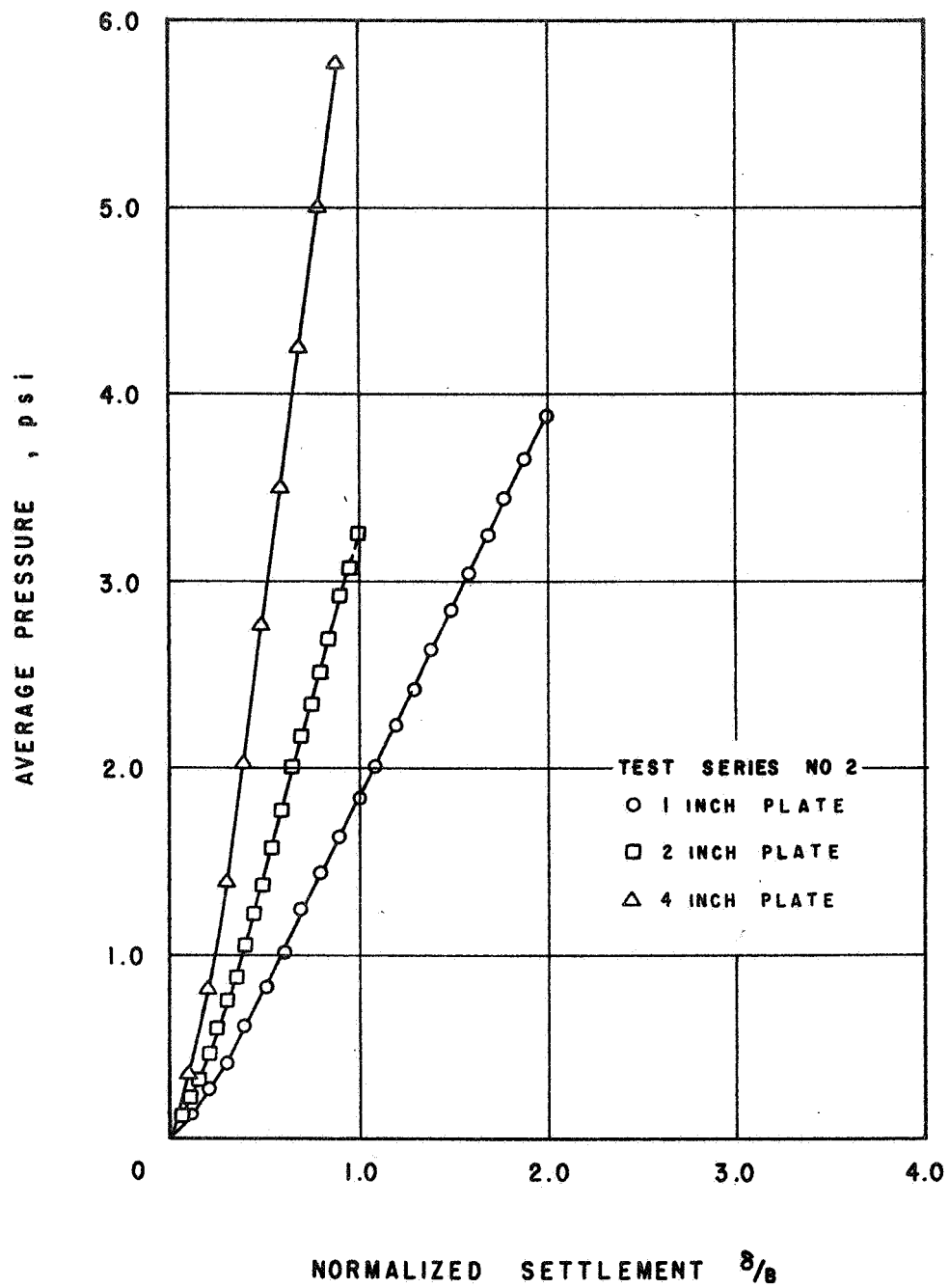


Fig. 1-51. Plate load test results for test series No. 2 (Loose).

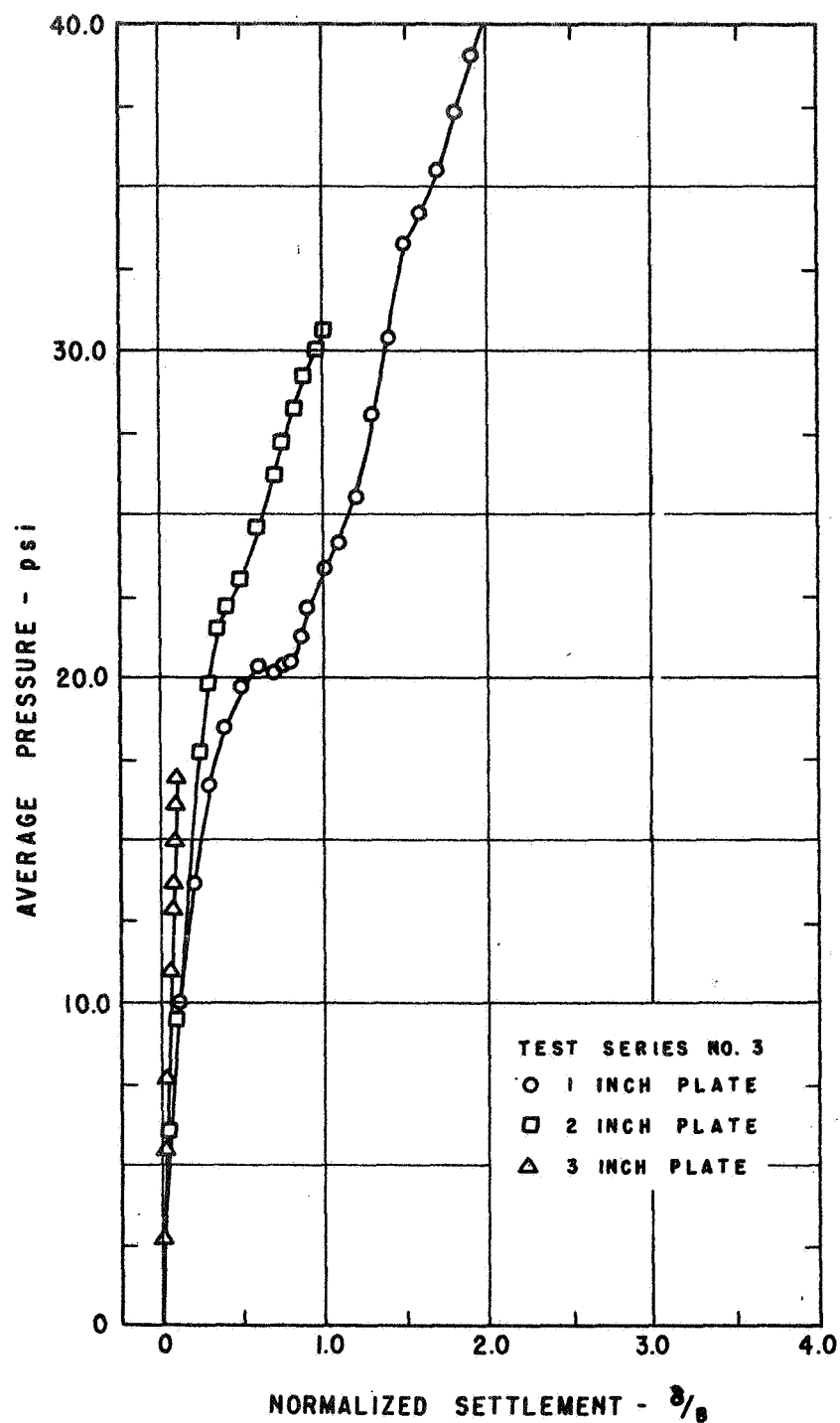


Fig. 1-52. Plate load test results for test series No. 3 (Dense).

The most striking feature of these data is the large deformation that occurred because of the high compressibility of the soil. The near-linearity of the stress-deformation curves and estimates of bearing capacity indicate that the bearing capacity was not exceeded, although deformation as high as one to two plate-widths was observed before loading was discontinued. A significant discontinuity in the curve for the 1-inch plate at about 20 psi on the dense soil deposit of Series No. 3 was observed. This discontinuity corresponded to the development of some bulging around the plate. Plate load test data can be used as a basis for evaluating the applicability of different analytical methods for the description of the stress-deformation behavior of lunar soil. The deformations of the plates on the LSS and on the actual lunar surface may be computed by several methods, including the Finite Element Method and the Stress Path Method (SPM) (Lambe and Whitman, 1969).

As a first step in the analysis of the plate load test data, soil deformations under the 4-inch plate were computed by the SPM for various initial soil densities. The major steps in the SPM computation are as follows.

The zone beneath the plate was subdivided into five elements as shown in Figure 1-53. The bottom of Element 5 was taken at a depth of 10B or at the bottom of the test bin, whichever was smaller. The vertical strains were computed at the center of each element and multiplied by the element thickness to obtain the total settlement under the plate.

The increases in vertical and horizontal normal stresses at various points under the plate were computed using a theory of elasticity computer program entitled HSPACE (Lysmer and Duncan, 1969). The results of these computations are shown in Figure 1-54. The average of the centerline and one/sixth point stresses from Figure 1-54 were used in the computations.

Each element was assumed to exist under K_0 conditions before plate loading, with $K_0 = 0.5$. Schematically, the initial stress state of each element is represented by point A in Figure 1-55. Point A is the point at the top of the stress circle which represents the stress state for each element. The increases in vertical and horizontal normal stresses

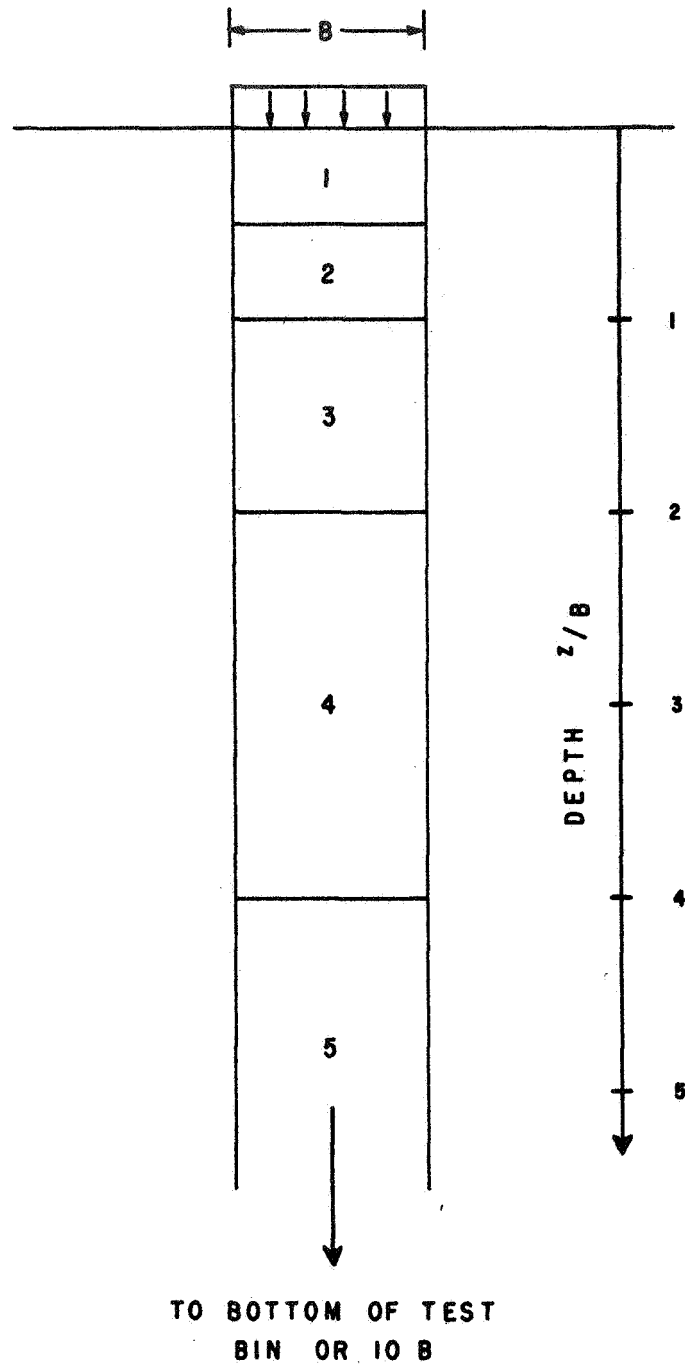


Fig. 1-53. Configuration of elements for stress path computations.

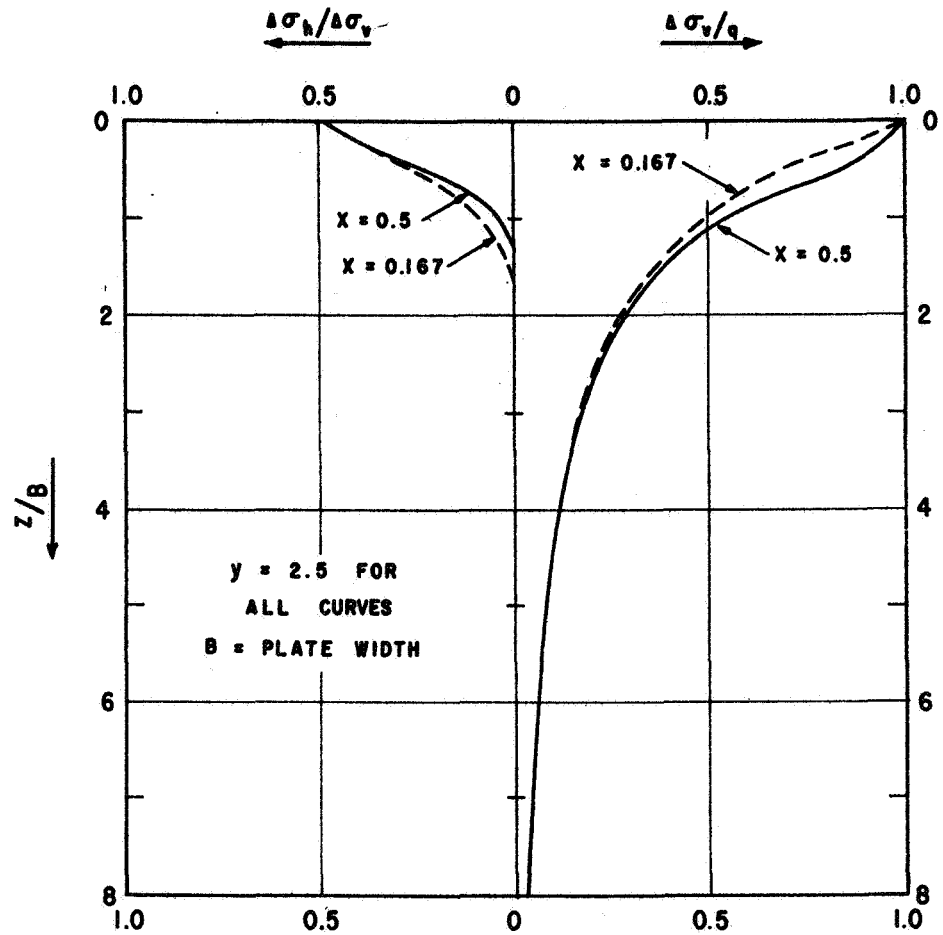
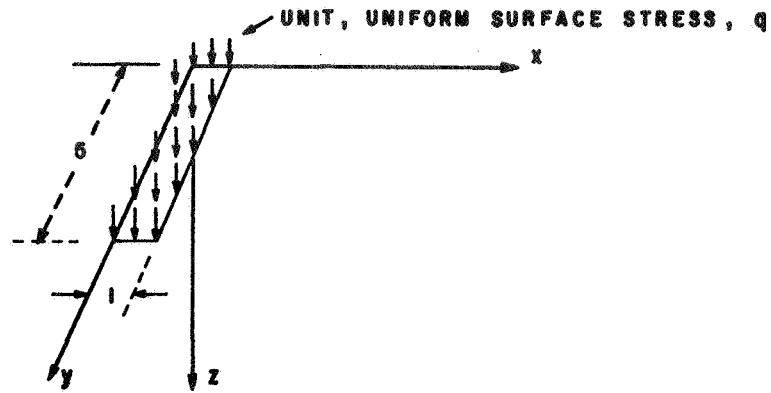


Fig. 1-54. Stress distribution with depth according to Theory of Elasticity for a rectangular, unit, uniform, surface stress.

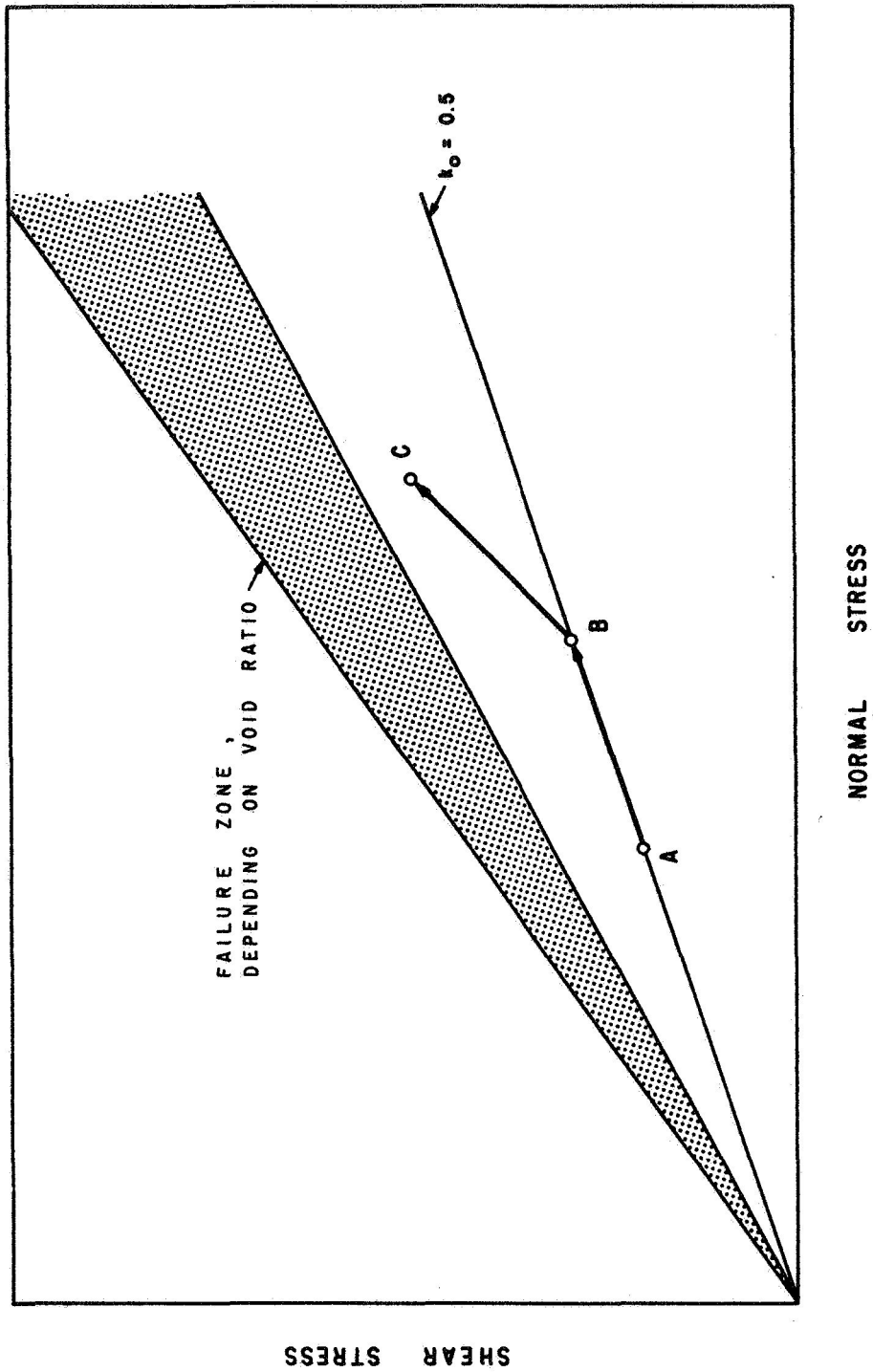


Fig. 1-55. Schematic representation of stress path method computations.

from Figure 1-54 were used as changes in major and minor principal stresses, and a new final stress state, represented by point C in Figure 1-55, was determined for each element. The vertical strain for each element corresponding to stress path A-B-C- was computed. Path A-B is along the K_0 -line and the compression is therefore one-dimensional for this segment. The vertical strain for path A-B was computed using the one-dimensional compression parameters presented in an earlier section. Path B-C represents loading under constant continuing pressure. Therefore, the plane strain stress-strain parameters presented in an earlier section were used to compute the vertical strain for this segment of the stress path.

A comparison between the measured and computed plate deformations is shown in Figure 1-56. The agreement is fairly good, especially in the range of void ratio of interest for the lunar surface (from about 0.7 to 1.0).

The SPM was also used to compute the plate deformation for the same contact stress under reduced gravity for various densities. The effect of reduced gravity is to lower the initial vertical and horizontal normal stresses, which results in significantly higher stress levels in some elements. The ratio of the deformation under full gravity to the deformation under $1/6$ g, is plotted in Figure 1-57. The curve in Figure 1-57 indicates, for example, that for an average void ratio of 0.8, the 4-inch plate deformation under 1 psi and full gravity would be about 85 percent of the plate sinkage for the same stress and same soil on the lunar surface.

The data in Figures 1-56 and 1-57 have several applications. For example, if a plate load test were performed on the lunar surface, the deformation could be multiplied by a value of R_Δ from Figure 1-57 to obtain the estimated deformation for the same soil under full gravity. A first-trial estimate of void ratio would be used to enter Figure 1-57 to get a value of R_Δ . This value of R_Δ could then be used to calculate plate sinkage under full gravity. The value thus determined could be used to enter a correlation between plate load sinkage and void ratio (e.g., the solid line in Figure 1-56) to obtain the corresponding void ratio. If the void ratio thus estimated differed significantly from the assumed void ratio used to enter Figure 1-57, the procedure could be

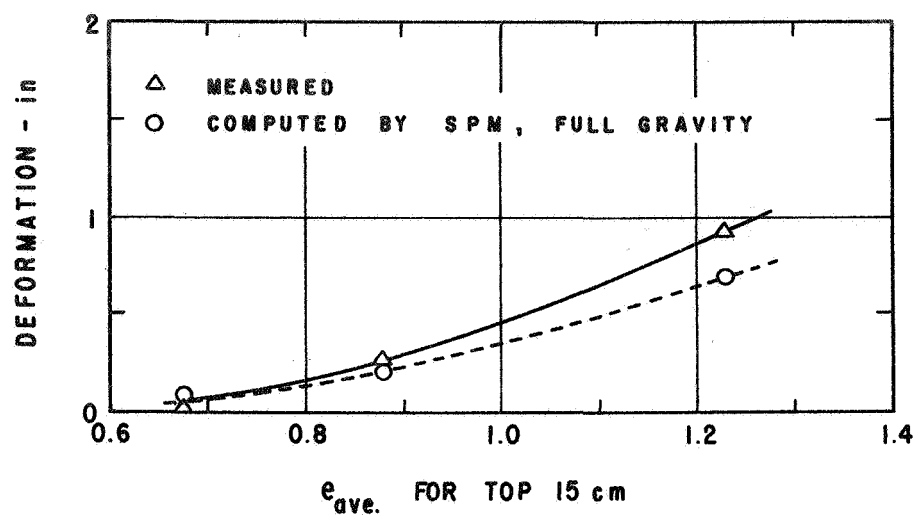


Fig. 1-56. Comparison measured and computed plate load test deformations for 4-inch plate under 1-psi contact stress.

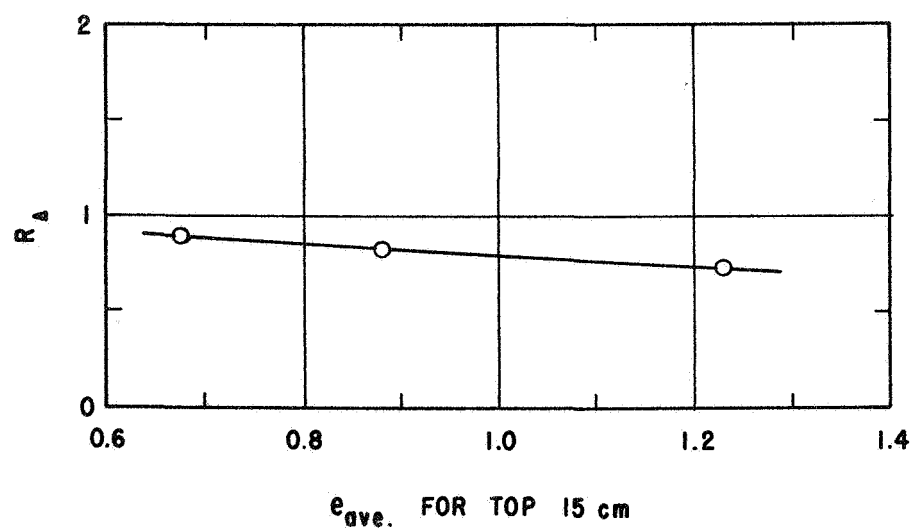


Fig. 1-57. Variation of gravity reduction factor, R_{Δ} , with void ratio.

repeated with an improved estimate of void ratio. From the void ratio, other parameters such as strength, stress-strain, and compression could be estimated as described in the preceding sections.

A similar analysis, although considerably less precise, can be made from astronaut boot imprint data, as described in the next section.

BOOT IMPRINT TESTS

A series of boot imprint tests were performed on LSS No. 2. It was anticipated that footprints made by astronauts during Apollo missions might be analyzed in a manner similar to that of the plate load tests.

The boot imprint tests were performed using the same procedure as was used for LSS No. 1 and described in detail by Mitchell and Houston (1970). Test results obtained using the new large test bin (3.5×7 inches) did not appear to differ significantly from those obtained in earlier tests using a smaller test bin (2×2 inches).

The relationships between void ratio and depth of footprint for contact stresses of 4 psi and 1 psi are shown in Figure 1-58. The contact stress for a suited astronaut with his full weight on one foot is about 1 psi in the lunar gravitational field. In Figure 1-59, the 1-psi curve is replotted as a dashed line and the predicted curve for the actual lunar surface appears as a solid line. The predicted curve was determined by applying values of the plate-load reduction factor, R_{Δ} , from Figure 1-57. The R_{Δ} values from Figure 1-57 were for a 4-inch-wide plate with a contact stress of 1 psi.

While precise determination of footprint depths from Apollo 11 and 12 photographs is difficult, a statistical survey was made from available photographs and, although a few footprints greater than an inch in depth were observed, most of the values fell between 0.1 and 0.5 inch with an average of about 0.25 inch.

If Figure 1-59 is entered using a footprint depth of 0.25 inch, an estimated value of e_{ave} for the top 15 cm of 0.85 is obtained. The range in e_{ave} for footprints ranging from 0.1 to 0.5 inch is from 0.74 to 0.94

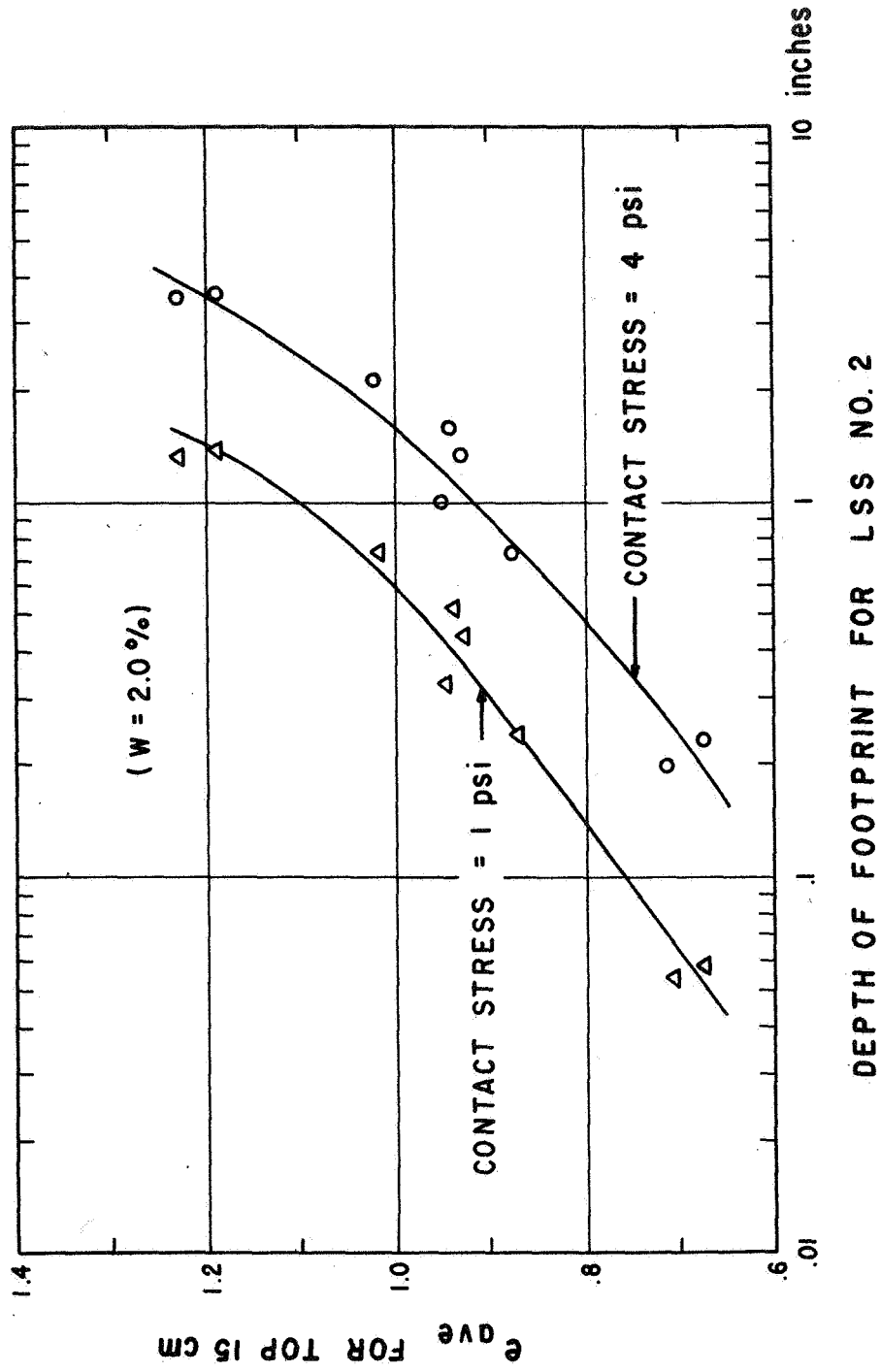


Fig. 1-58. Variation of footprint depth with void ratio for LSS No. 2.

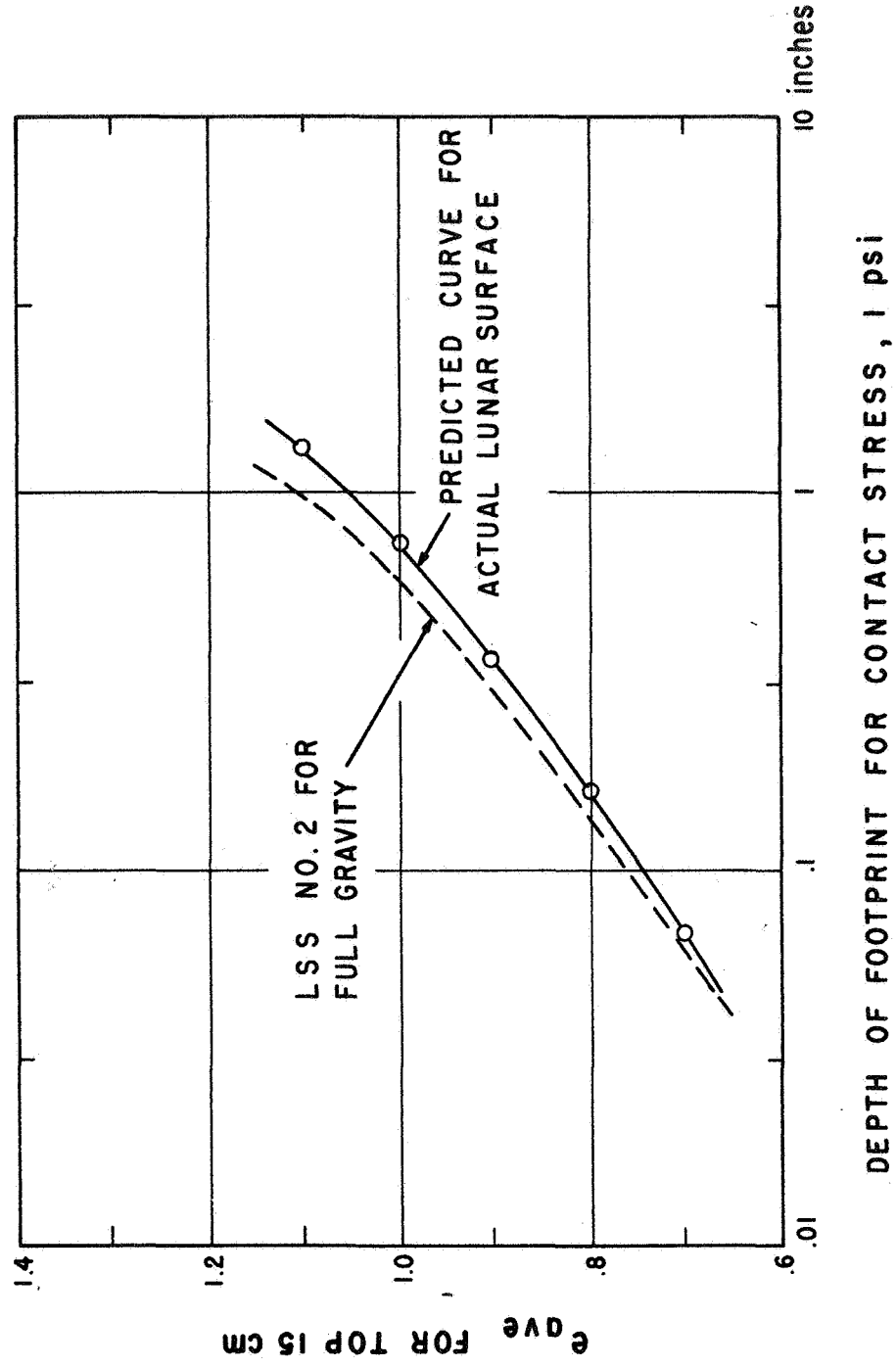


Fig. 1-59. Predicted variation of footprint depth with void ratio for actual lunar surface.

A comparison of this void ratio estimate and these obtained from Apollo 11 and 12 core tubes is given in Table 1-2.

Table 1-2. Comparative void ratios.

Data Source	Best estimate or average value of void ratio	Density for $G_s = 3.1$	Corresponding range in void ratio	Corresponding range in density for $G_s = 3.1$
Apollo 11 core tubes*	0.94	1.60	1.00 to 0.88	1.55 to 1.65
Apollo 12 core tubes**	0.72	1.80	0.94 to 0.55	1.60 to 2.0
SPM footprint analysis described herein	0.85	1.677	0.94 to 0.74	1.60 to 1.78

*Costes et al. (1970)

**Scott et al. (1971)

The comparison shows that the density estimate obtained from the SPM-plate load analysis is well within the wide range obtained from Apollo 12 core tubes and is slightly higher than the Apollo 11 core tube range.

PENETROMETER TESTS

Penetration resistance tests are likely to be an efficient and effective means by which astronauts may gather data leading to the assessment of lunar surface soil properties. Such tests are planned for future Apollo missions.

An important application of penetration resistance data may be in the trafficability analyses needed for range prediction for lunar roving vehicles. It is also anticipated that penetration resistance can be correlated with density. In addition, abrupt changes in the slope of the stress-penetration curve may be used as indicators of nonhomogeneities in the soil profile. An example of this type of indication is shown in Figure 1-60. The curve in Figure 1-60 was obtained with the standard WES cone penetrometer.

Considerable effort was devoted to the development of a penetrometer which could be used on the lunar surface. The cone and shaft size and configuration chosen were that of the Waterways Experiment Station, a cone penetrometer shown in Figure 1-61. The alternate black and white sections on the shaft were added to provide a visual measure of the depth of penetration, either by direct observations or from photographs.

A proving ring and dial gage were chosen for load measurement. The proving ring was mounted in an extension-type handle [Figure 1-62(a)]. The plate is 1 inch wide, 5 inches long, and 1/4 inch thick. All attachments can be used with the extension handle and the proving ring dial gage can be used to measure force.

The 1/4-inch-diameter rod protruding out of the top of the extension handle passes through the hollow extension handle and behind the dial gage to the bottom of the proving ring. This rod may be used for hammering, if necessary, without damaging the dial gage. The assembled penetrometer [Figure 1-62(b)] is shown in testing position in Figure 1-63.

It was proposed that data be obtained by the astronauts on the lunar surface by performing the test in front of a sequence camera. From the photos, the depth of penetration and the dial gage can be read for determination of the load. This method of data acquisition was investigated in the laboratory by taking a rapid series of snapshots (rather than continuous photography by sequence camera) during the penetration test. The stress-penetration curves obtained in this way were equally as consistent and reproducible as were the curves obtained by direct observation.

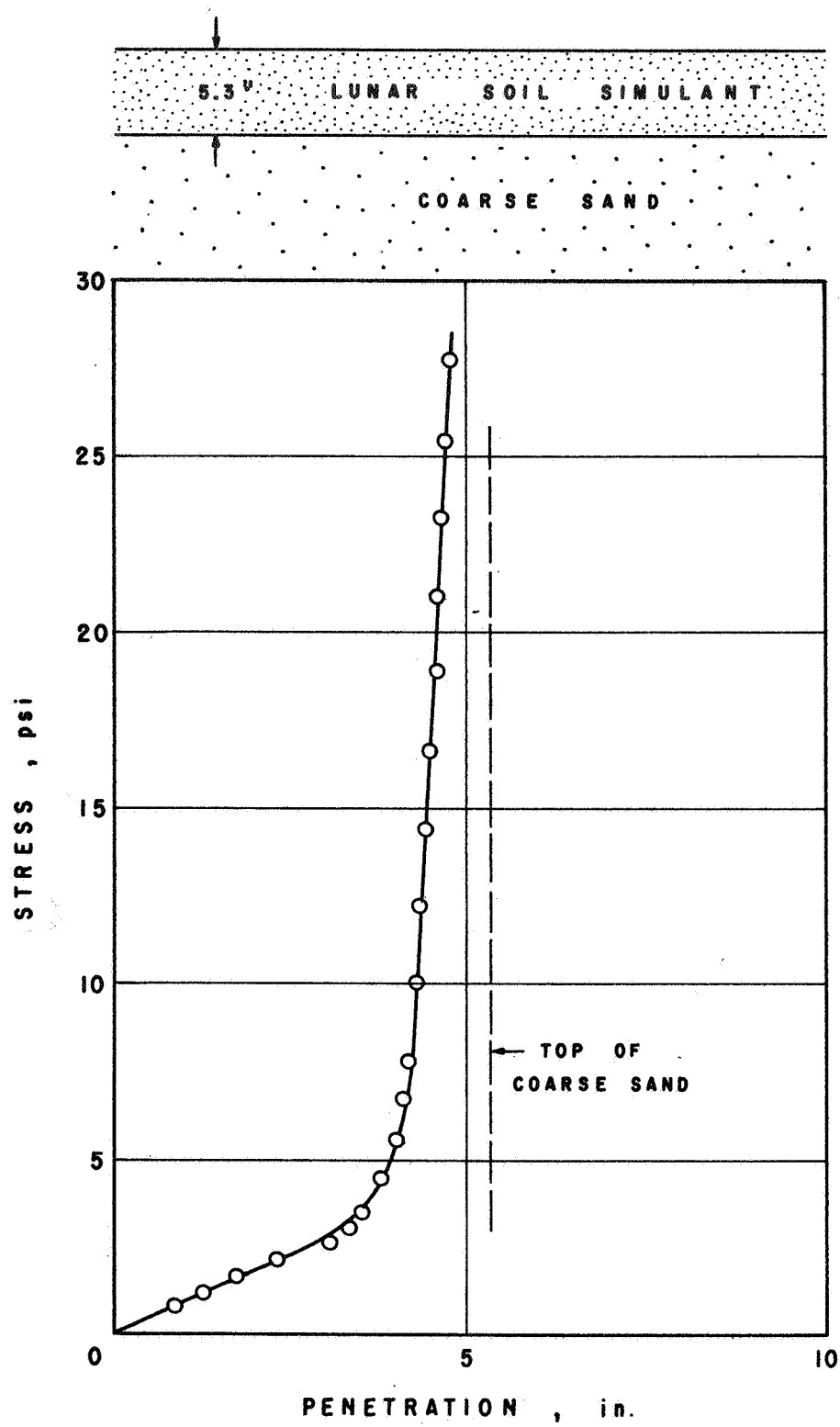


Fig. 1-60. Stress-penetration curve for two-layer profile.

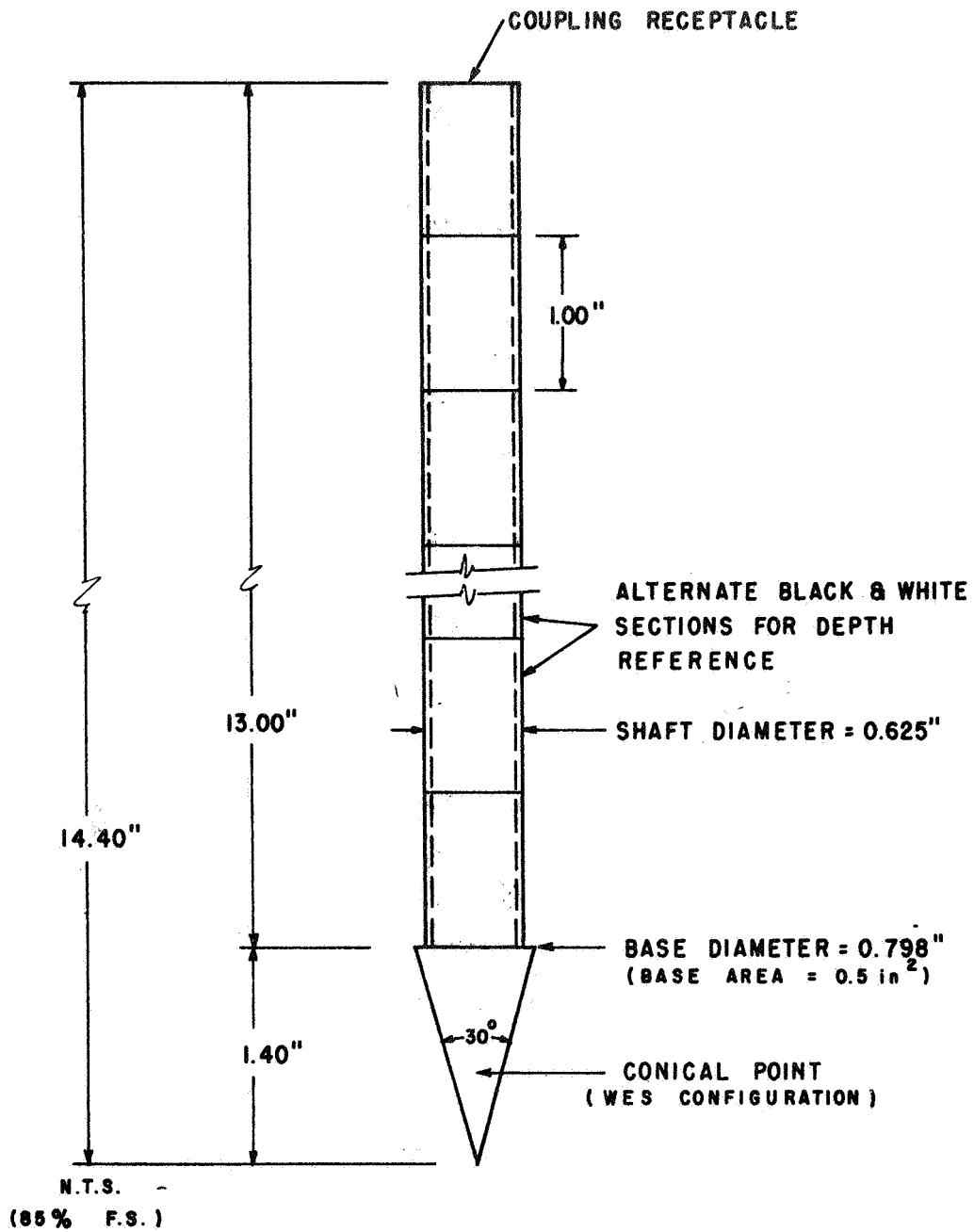
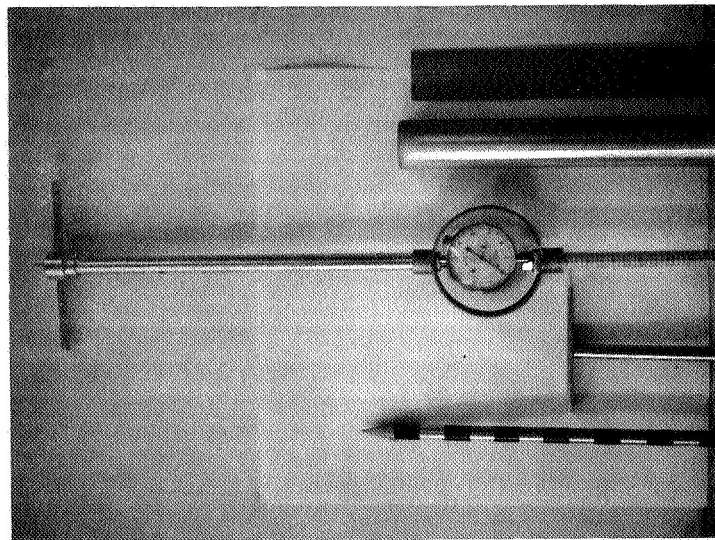
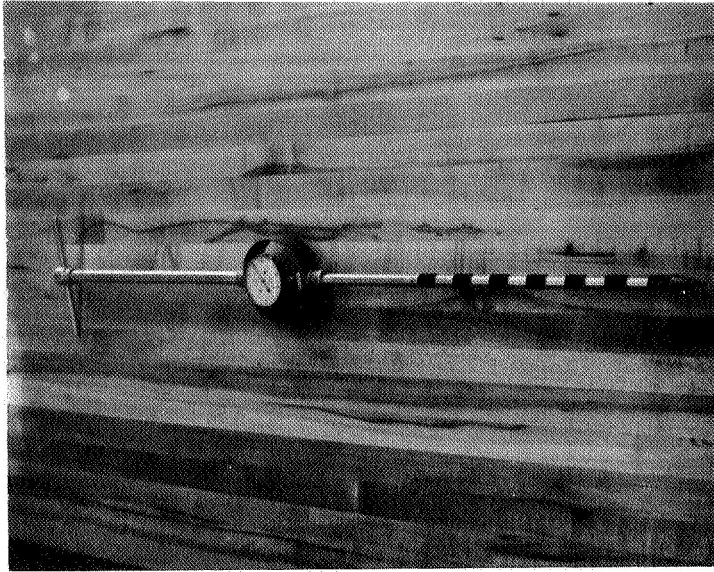


Fig. 1-61. Penetrometer cone and shaft.



(a)



(b)

Fig. 1-62. Proving ring extension handle with attachments.

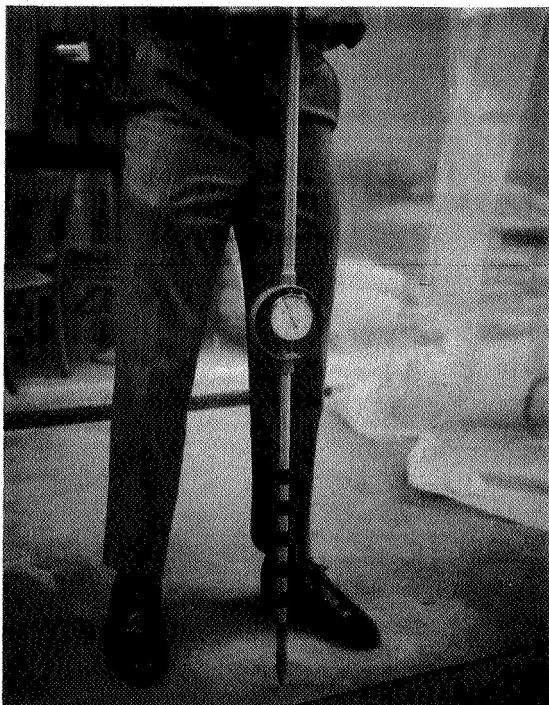


Fig. 1-63. Penetrometer in testing position.

An example stress-penetration curve is shown in Figure 1-64. The position of the feet of the man performing the test with respect to the penetrometer has an effect on the results. Therefore, the position indicated in the upper left corner of Figure 1-64 has been adapted as standard. The penetrometer was advanced at the rate of about 1 inch per 5 seconds to avoid the development of pore air pressures; however, a penetrometer on the lunar surface would be advanced at a greater rate.

A series of penetration resistance tests was performed on LSS No. 2 using the cone penetrometer. The slope of the stress-penetration curve, G , is plotted versus the average void ratio for the top 15 cm in Figure 1-65. One of the uses of the data in Figure 1-65, in connection with trafficability studies, is that of comparing the G - e_{ave} relationship of any new proposed lunar soil simulant to that of LSS No. 2. Because available data indicate that LSS No. 2 is a good simulant of the actual lunar soil, Figure 1-65 can be used as an indicator of the suitability of any new soil that might be used for LRV simulation studies.

Figure 1-65 provides the relationship between G and e_{ave} for terrestrial gravity. The variation of G with e_{ave} for lunar gravity is also of great interest for trafficability analyses and other property studies. An estimate of the effect of reduced gravity on G value was obtained by applying the following bearing capacity equation to the penetrometer.

$$q_{ult} = \frac{b\gamma}{2} N_{\gamma} s_{\gamma} + c N_c s_c + q' N_q s_q \quad , \quad (1-38)$$

where q_{ult} = unit ultimate bearing capacity

γ = soil unit weight

b = width of loaded area

c = soil cohesion

q' = surcharge, $d\gamma$

s_{γ} = shape factor $(1 - 0.3 b/L)$

s_c = shape factor $(1 + 0.2 b/L)$

s_q = shape factor $(1 + 0.2 b/L)$

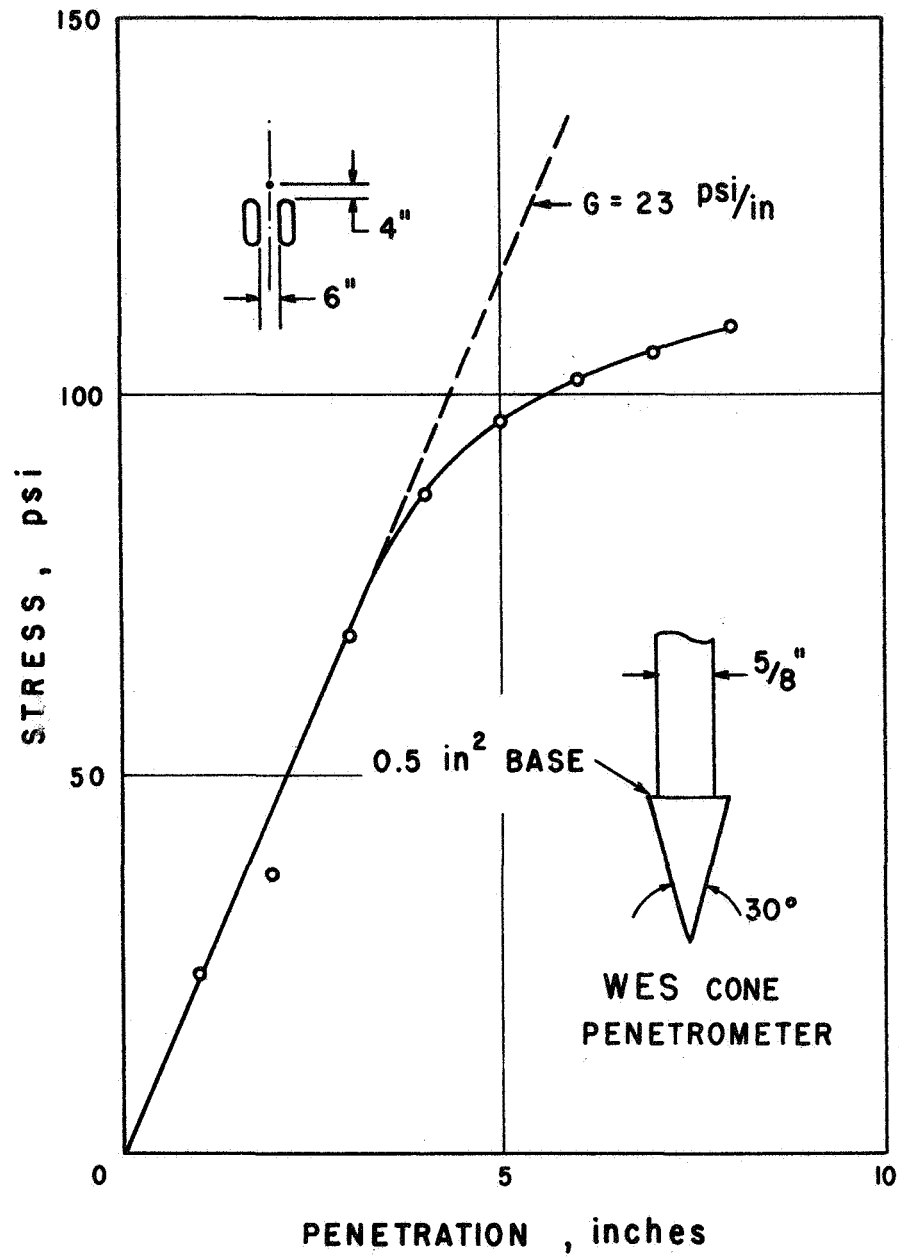


Fig. 1-64. Example stress-penetration curve.

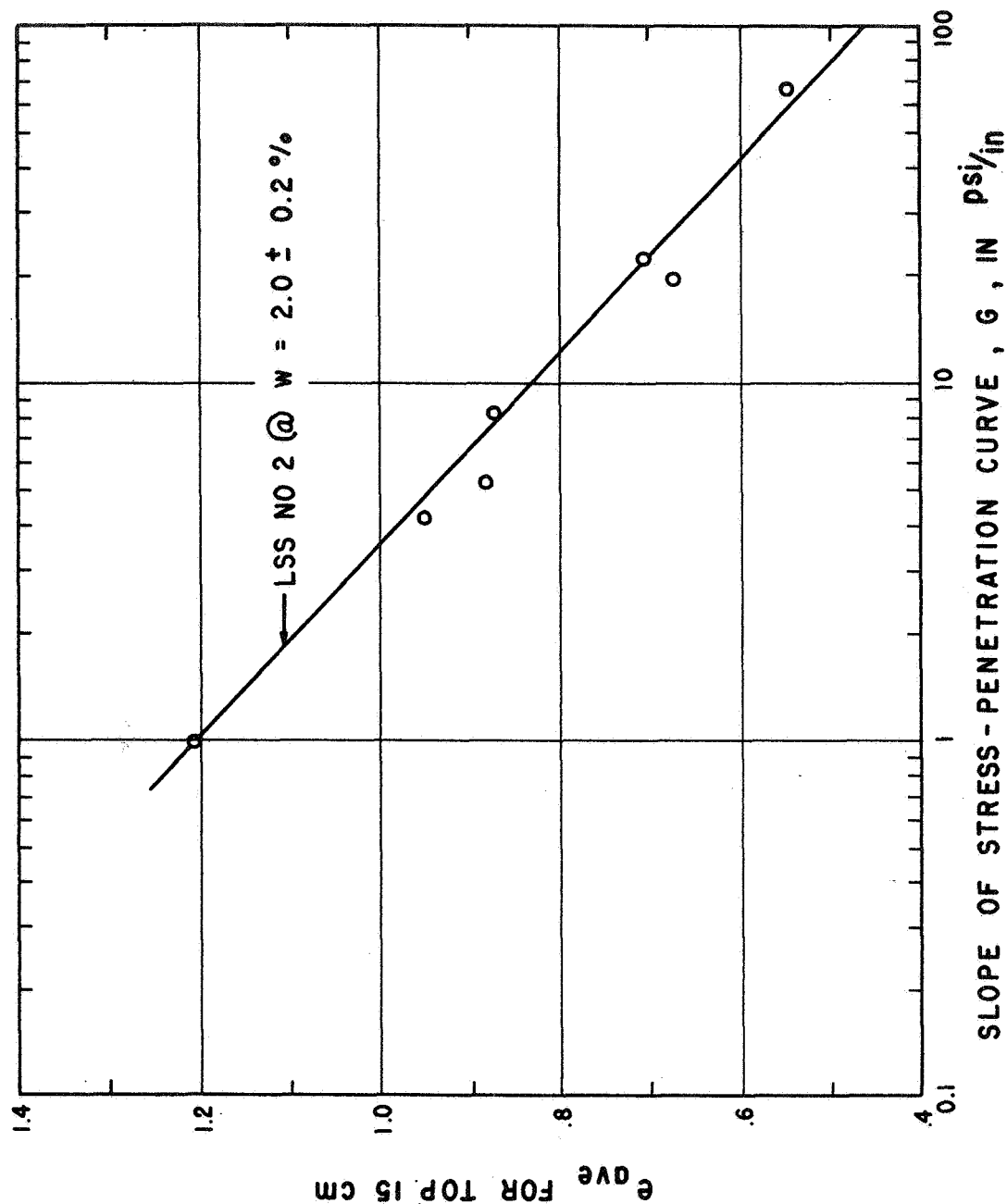


Fig. 1-65. Relationship between G and void ratio for LSS No. 2 under full gravity.

N_γ, N_c, N_q = bearing capacity factors, dependent on the
soil friction angle, ϕ

d = depth of loaded area

L = length of loaded area.

The penetrometer has a diameter of about 0.8 inch which was used for b . A value of $b/L = 1$ was used for all computations. For each set of computations a soil profile consistent with terrestrial gravity was chosen from Figure 1-35. The bearing capacity was computed for a depth, d , equal to 0 and 15 cm. The void ratio for $d = 0$ and $d = 15$ cm were taken from Figure 1-35 and used to enter Figures 1-7 and 1-8 to obtain values for c and ϕ . Meyerhof's (1951) charts were used for the bearing capacity factors.

For a compressible soil that may experience local shear, the bearing capacity is usually computed by using reduced strength parameters c_r and ϕ_r , so that.

$$c_r = k_{\ell s} c \quad (1-39)$$

$$\phi_r = \text{Arc tan}(k_{\ell s} \tan \phi) \quad (1-40)$$

The value of $k_{\ell s}$ varies from 1 to 0.67, depending on soil compressibility. A value close to 0.67 is indicated for LSS No. 2 because no bulging was observed around the penetrometer during testing. A value of $k_{\ell s} = 0.75$ was used for all computations.

The stress-penetration gradient, G , was taken as the change in q_{ult} between $d = 0$ and $d = 15$ cm divided by 15 cm. Values of G obtained in this way were plotted versus e_{ave} for the top 15 cm.

The results are shown in Figure 1-66, where measured and computed values are compared. The close agreement indicates that the bearing capacity Equation (1-38) provides a basis for estimating G values. If so, then the same relationship may be used to investigate the probable influence of gravity on G value.

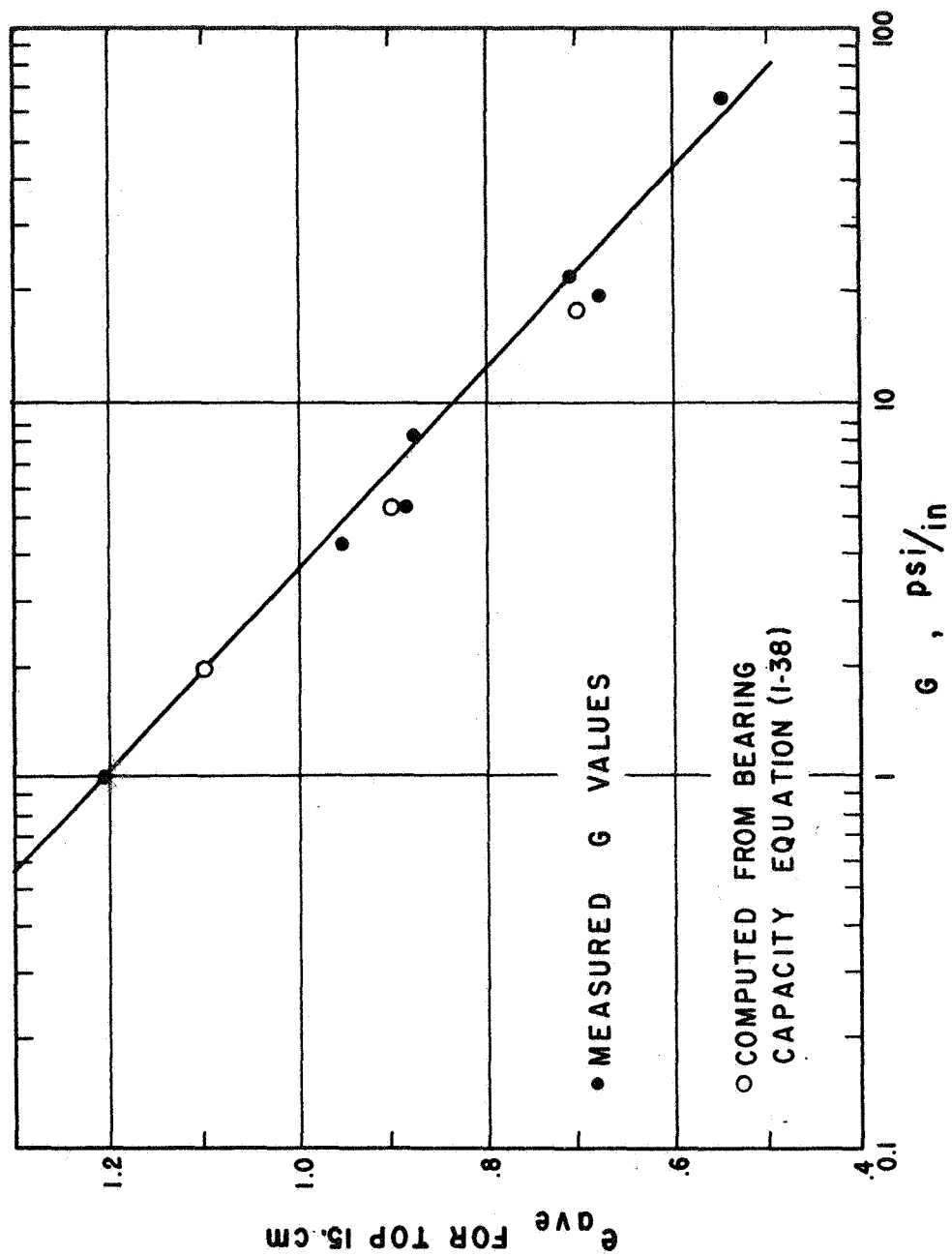


Fig. 1-66. Comparison of measured and computed G values for LSS No. 2 under full gravity.

The bearing capacity computations were repeated for reduced gravity using the same factors, except that $\gamma/6$ was used instead of γ for the density. A void ratio-depth profile more consistent with the lunar surface (as given in Figure 1-38) was used.

The G values obtained in this way were used to determine the ratio, R_p , of G under reduced gravity to G under terrestrial gravity with the result shown in Figure 1-67. These values of the reduction factor, R_p , from Figure 1-67 were then applied to the measured terrestrial G values (shown by the lines in Figures 1-65 and 1-66) to obtain the predicted G values for the lunar surface shown in Figure 1-68.

It is of interest to note that the estimate of $e_{ave} = 0.85$ from the boot imprint analysis discussed in the previous section yields a G value of 2.5 psi/inch. On the other hand, Apollo 12 core tube data analysis by Scott et al. (1970) gave a density estimate of $1.8 \pm 0.2 \text{ g/cm}^3$ for the top 30 cm, which corresponds to an e_{ave} (top 15 cm) of about 0.722 with a range of 0.55 to 0.94. A value of $e_{ave} = 0.722$ indicates a $G = 5.5 \text{ psi/inch}$. Thus, a range $2.5 \leq G \leq 5.5 \text{ psi/inch}$ is indicated by these two estimates of average density.

CORE TUBE STUDIES

Core tube tests were performed to investigate the efficiency of the core tube sampler used on Apollo 11 and 12 landings and to compare the results to those obtained using a newly designed thin-wall tube. The tests were conducted in a 2 by 2 by 3 inch bin using LSS No. 2 placed at various densities.

The sampler used on Apollo 11 and 12 has a split core barrel with an inside diameter of 0.75 inch and a wall thickness of 0.125 inch. The split barrel is held together at top and bottom, respectively, by a threaded handle attachment and the bit (see Figure 1-69). This sampler was originally supplied with two interchangeable bits. The least efficient of these bits (Figure 1-69) has a 15-degree inward flare, thus compressing the soil as it enters the core tube. The better of the two bits flares outwards, thus maintaining the 0.77-inch inside diameter of the tube.

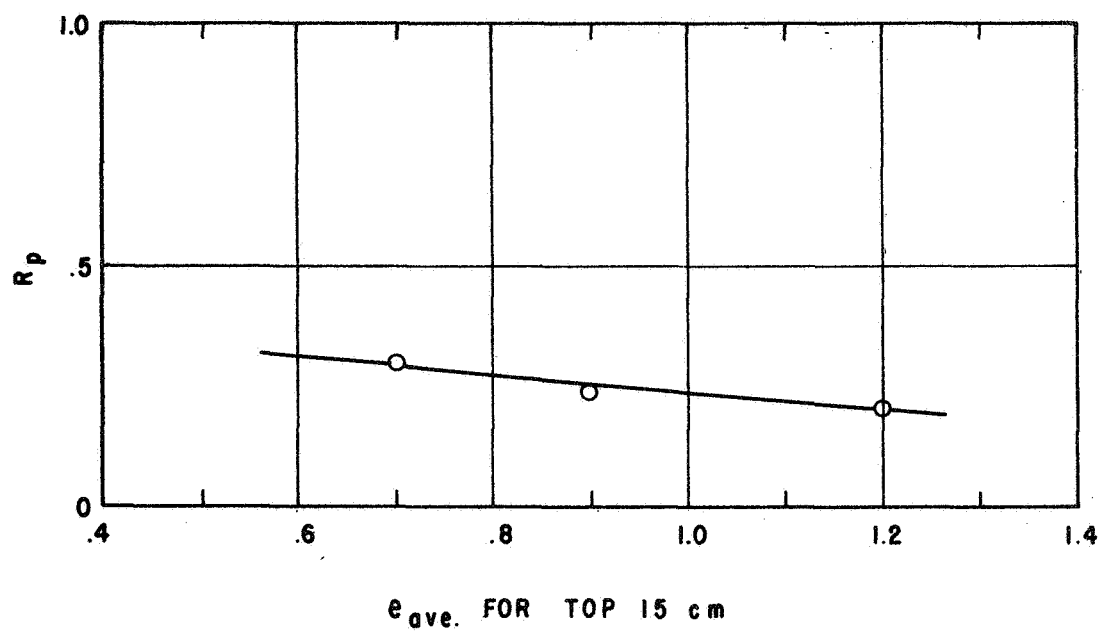


Fig. 1-67. Variation of G-value reduction factor, R_p , with void ratio.

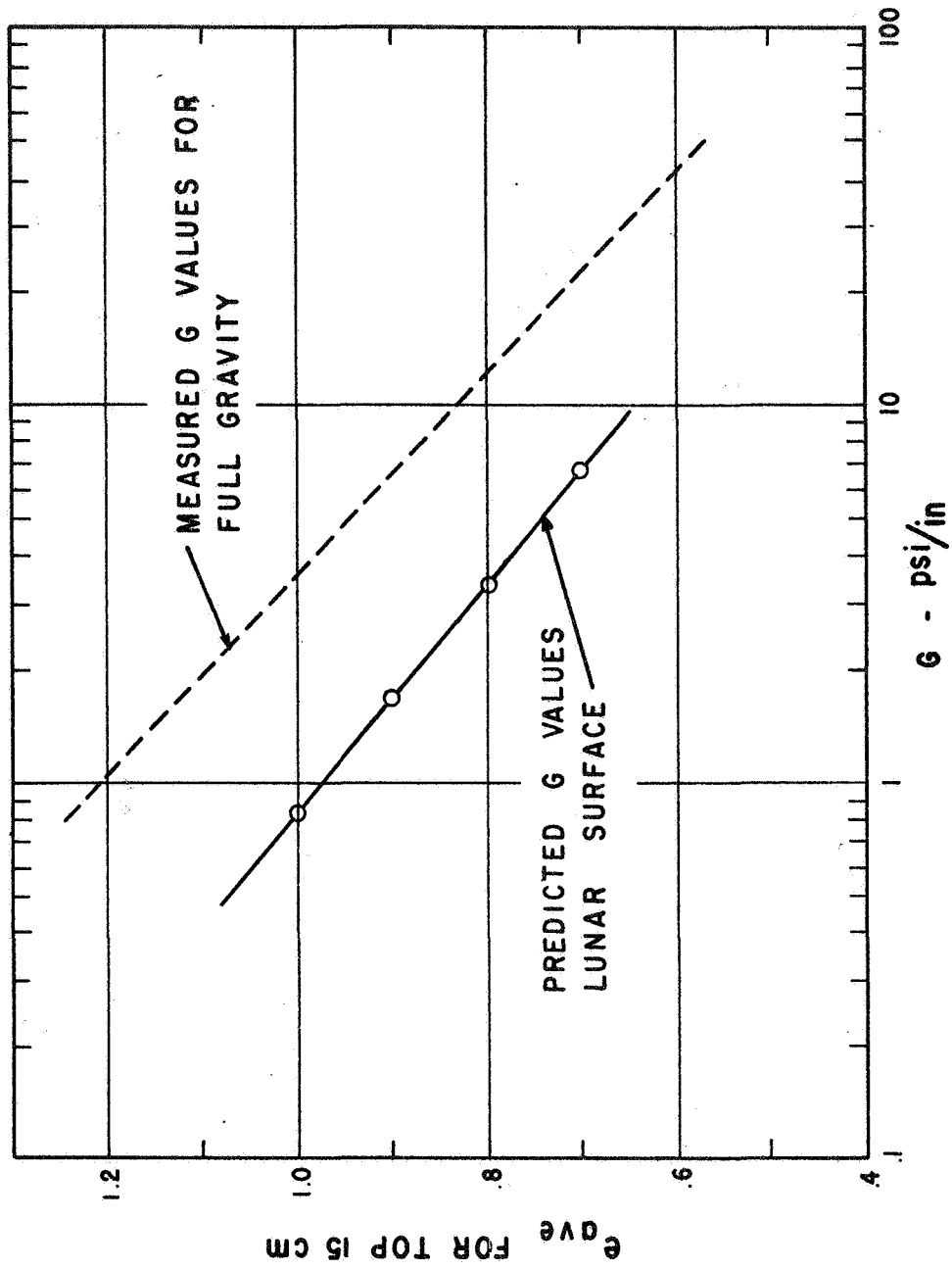


Fig. 1-68. Predicted variation of G value with void ratio for actual lunar surface.

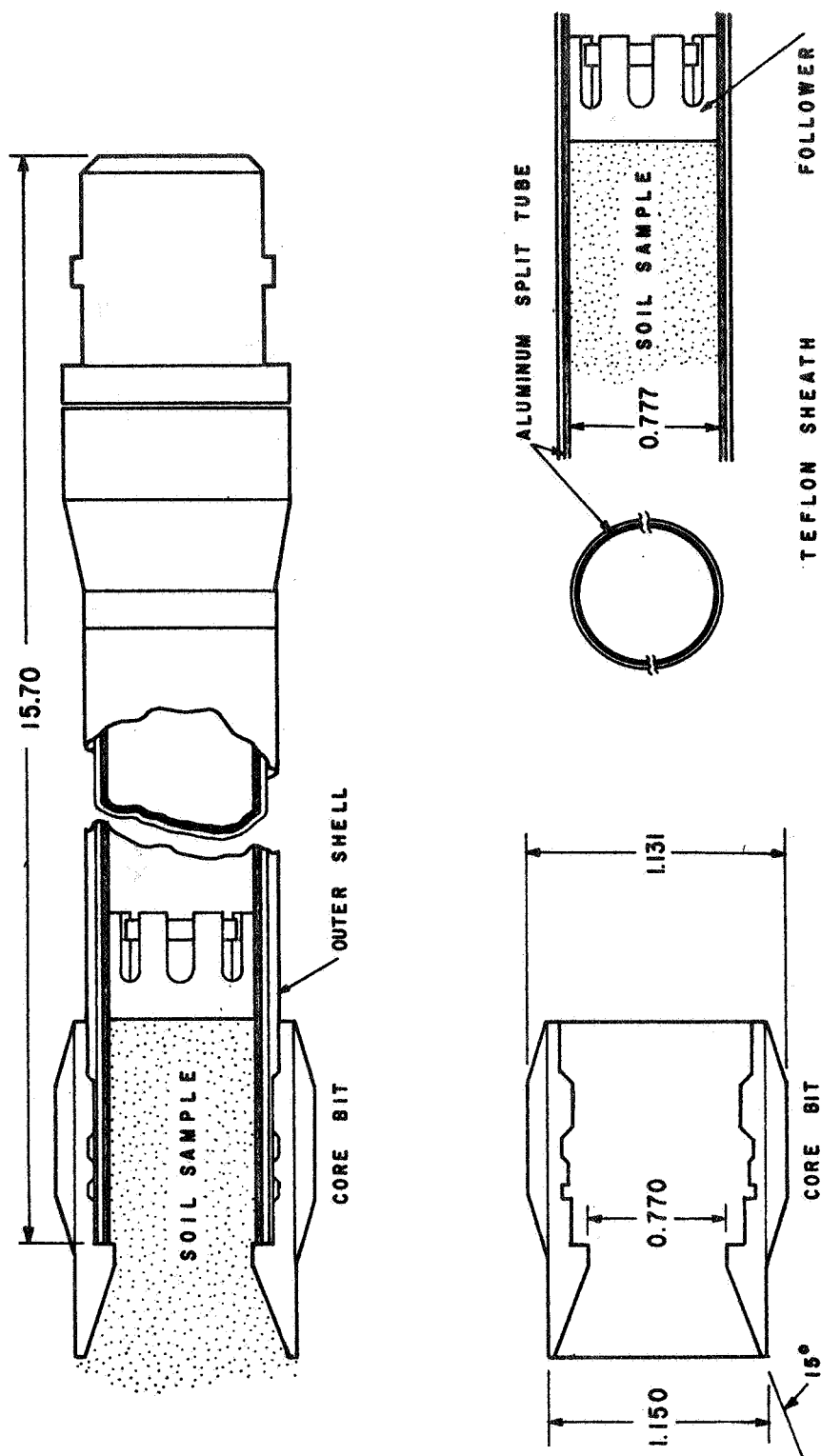


Fig. 1-69. Core-tube sampler and bit used in the Apollo 11 mission. Dimensions are given in inches. (Costes and Mitchell, 1970)

The revised sampler is of solid-shell thin-wall design with the bit being the sharpened leading edge of the core tube wall. It has an inside diameter of 1.92 inches and a wall thickness of 0.04 inch. The barrel length is about 12 inches. The revised core tube sampler is shown in Figures 1-62(a) and 1-70.

This sampler was driven into the soil by pushing as shown on Figure 1-71. The original samplers were advanced by pushing, augering, and hammering. After inserting the samplers a given distance (typically 10 to 11- $\frac{1}{2}$ inches), the amount of soil in the tube was measured prior to withdrawing the sampler. The ratio of the amount of soil present in the tube after insertion to the depth of sampling as measured from the original soil surface was used as the standard of comparison between the sampler types. This ratio is termed the "sampling ratio" and is expressed as a percentage.

The values of sampling ratio obtained during testing are summarized in Table 1-3. The values for the less efficient inward flare bit are listed first for the four methods of sampler advancement. The sampling ratios for the inward flare bit range from about 7 to 58 per cent, depending mainly on the method of advancement. For this bit, hammering yields the highest sampling ratio.

The tabulated sampling ratios for the more efficient outward flare bit as listed in Table 1-3 range from 63 to 84 per cent, depending mainly on the dry unit weight of the lunar soil simulant tested. It is obvious from these values that this type of bit yields more satisfactory results than those for the inward flare bit.

The sampling ratio values for the thin-wall sampler range from 85 to greater than 99 per cent. These values are significantly better than those obtained using the Apollo samplers, and can be attributed to the greatly reduced ratio of sampler cross section area to sample cross section area because of the thinner walls.

It should be mentioned that some difficulties were encountered in retaining the sample in the sampler upon withdrawal, using both the Apollo and the thin-wall samplers. This difficulty is ascribed to the differences between the lunar and terrestrial environment (vacuum, reduced gravity).

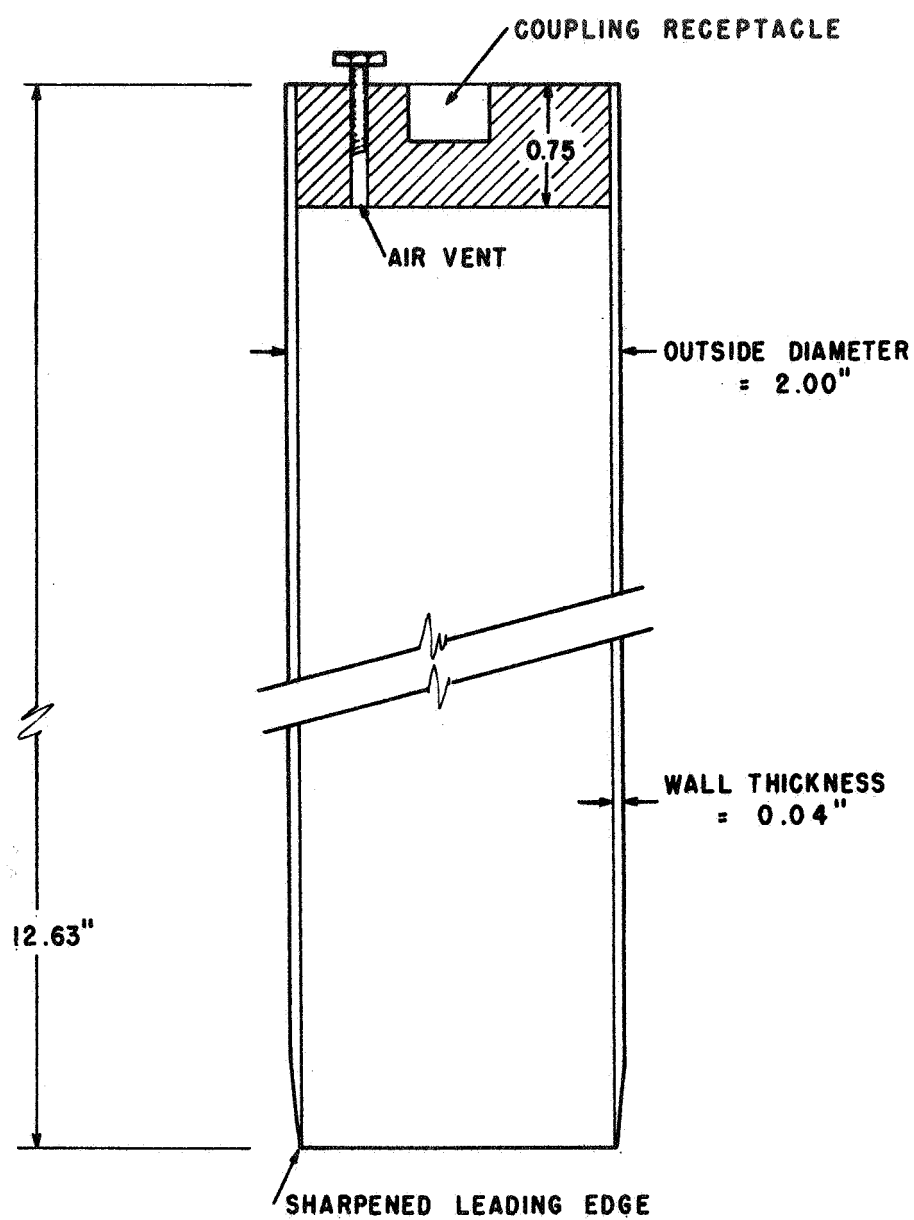


Fig. 1-70. Proposed new thin-wall core tube sampler.

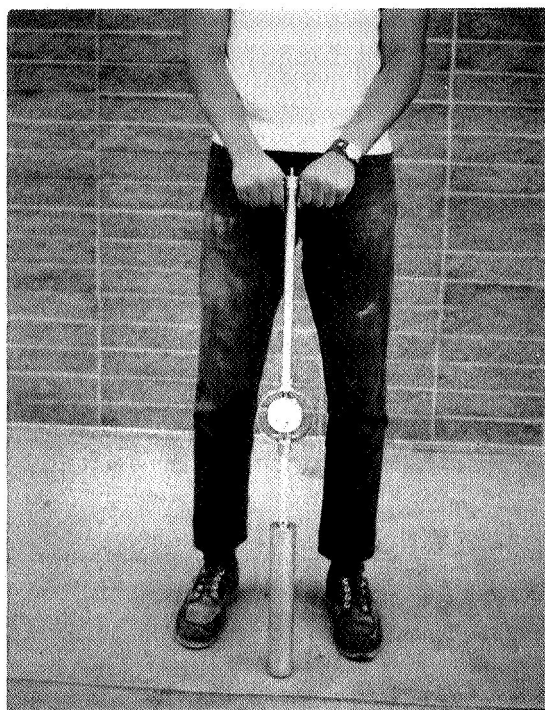


Fig. 1-71. Sampling tube in position.

Table 1-3. Summary of "sampling ratios" (%) for LSS No. 2.

Apollo core sampler			
Dry unit weight, g/cc	1.67	1.79	1.88
Moisture content, %	1.24	1.43	1.23
Void ratio	0.725	0.61	0.53
<i>Inward flare bit</i>			
1. push	9.1	7.5	11.4
2. push & auger	9.6	7.3	14.9
3. hammer	58.2	42.3	55.7
4. hammer & auger	44.8	38.0	55.9
<i>Outward flare bit</i>			
1. push	63.2	64.6	84.4
2. push & auger	66.6	59.0	78.7
3. hammer	73.3	69.2	78.2
4. hammer & auger	69.8	66.0	82.5
Thin-wall sampler			
Dry unit weight, g/cc	1.51	1.75	1.88
Moisture content, %	1.30	1.30	1.30
Void ratio	0.905	0.642	0.53
<i>Integrally-cast bit</i>			
push	85.0	97.3	99+

It was therefore impossible to measure reliably the dry unit weight of the sampled soil in order to evaluate the compression during sampling.

It should also be noted that the force required to push the core tube sampler into the soil became quite large for very dense soil deposits. For this reason, a sampler somewhat smaller than the 2-inch-O.D. sampler described herein has been recommended.

Based partly on the recommendations derived from this study, the Apollo Spacecraft Program Office has authorized the redesign of the Apollo 11-12 core tube for subsequent Apollo missions. Requirements for the new sampler are as follows (from MSC Configuration Control Board Directive, May 14, 1970):

Requirements

1. Area ratio 10%
2. Integral bit
3. Area of bit: 1 to 2% less than inner area
4. Piston type follower
 - No resistance during sampling
 - Lock capability after sampling
5. Core extraction compatible LRL processing
6. Interface with existing HTC with minimum impact
7. Capability of retrieving double core

Note:

Methods of core sample removal; i.e., extrusion, split-tube must be prototyped for evaluation to establish most satisfactory method.

CONCLUSIONS

1. Lunar Soil Simulant No. 2 appears to be a good match for the actual lunar soil in terms of gradation, penetration resistance, and other physical properties.
2. The conclusion reported in the Final Report of January 1970 (Mitchell and Houston, Vol. I) regarding the sensitivity of lunar soil properties to void ratio is reinforced by studies on LSS No. 2. These studies indicate that most soil properties of interest can be predicted from knowledge of the void ratio.
3. Strength, stress-strain, and one-dimensional compression parameters of the lunar soil simulant have all been related to void ratio in both equation and graphic form. One-dimensional compression parameters have been used to estimate density profiles for both terrestrial gravity and lunar gravity conditions. These profiles show that the increase in density with depth should be less pronounced for the lunar surface than for the same soil on earth.
4. One-dimensional compression parameters and plane strain stress-strain parameters were used in a stress path method of analysis to compute the soil deformations under a 4-inch by 20-inch plate acted on by a 1-psi vertical stress for several initial void ratios. The computed values were compared with the measured plate load sinkage and the agreement was fairly good, as shown in Figure 1-56. The stress path computations were repeated for reduced gravity, and the gravity reduction factors shown in Figure 1-57 were obtained. These factors were used to relate footprint depth to void ratio in Figure 1-59. Estimates of footprint depths from Apollo 11 and 12 photos gave a range of 0.1 to 0.5 inch for most values, with an average value of about 0.25 inch. This footprint depth corresponds to an estimate of e_{ave} for the top 15 cm of 0.85 on the lunar surface. This corresponds to an in situ density of about 1.7 gm/cm^3 , for $G_s = 3.1$.

An estimated value of $e = 0.85$ corresponds to the following strength and stress-strain properties.

$$c = 4.3 \text{ g/cm}^2 = 0.06 \text{ psi}$$

$$\phi = 40^\circ \text{ (average value for a range in confining pressures)}$$

$$\sigma_{df} = 0.41 \left(\frac{\sigma_{3f}}{0.1} \right)^{0.875} \quad \text{for } \sigma_{3f} \text{ in kg/cm}^2$$

$$\epsilon_{af} = \frac{\sigma_{3f}}{0.00548 + 0.0348 \sigma_{3f}} \quad \text{for } \sigma_{3f} \text{ in kg/cm}^2$$

$$E_{tps} = \left(1 - 0.475 \bar{D} \right)^2 \left(\frac{\sigma_{df}}{\epsilon_{af}} \right) 2.06$$

$$\left(\frac{\epsilon_l}{\epsilon_a} \right)_f = 0.606 - 0.297 \log_{10} \left(\frac{\sigma_{3f}}{0.1} \right) \quad \text{for } \sigma_{3f} \text{ in kg/cm}^2$$

$$\bar{I}_\epsilon = \frac{1}{1.68 + 0.30 \log_{10} \sigma_{3f}} \quad \text{for } \sigma_{3f} \text{ in kg/cm}^2$$

$$\left(\frac{\epsilon_l}{\epsilon_a} \right)_{tps} = \frac{\left(\epsilon_l / \epsilon_a \right)_f \bar{I}_\epsilon}{\left[1 - \frac{(1 - \bar{I}_\epsilon) \bar{D}}{2.06(1 - 0.475 \bar{D})} \right]^2}$$

5. The plate load test results indicated that no general shear failure occurred, except perhaps in the case of loading by the 1-inch plate on the very dense soil. However, the data showed (see Figures 1-50, 1-51, and 1-52) that the sinkages were quite large, ranging up to 1 and 2 plate-widths.
6. A bearing capacity equation was used to estimate the G value for LSS No. 2 under full gravity and yielded good agreement with values measured directly with a penetrometer when local shear strength parameters were used, as shown in Figure 1-66. A similar set of computations for reduced gravity led to the penetrometer reduction factors, R_p , shown in Figure 1-67, and the predicted relationship between G and void ratio for the

lunar surface shown in Figure 1-68. Figure 1-68 indicates that G may range from 2.5 psi/inch (for the estimated $e_{ave} = 0.85$ from the boot imprint analysis) to 5.4 psi/inch (for the estimated $e_{ave} = 0.73$ from Apollo 12 core tube density analysis).

RECOMMENDATIONS

1. Good measurements of in-place density on the lunar surface soil are needed. The core tube sampler should be modified by greatly reducing the area ratio in an effort to obtain samples with less disturbance and more representative density. Other types of in-place density tests should also be considered.
2. Measurements of G value by the astronauts during Apollo missions are needed as soon as possible. These penetration resistance measurements should be made using either a penetrometer of the type described herein, or with another type of load and penetration measurement device. The cone and shaft should be the standard WES configuration (i.e., 30-degree apex angle and 0.5-square-inch base area), and a standard placement of feet and penetrometer for testing should be adopted.
3. Plate load tests should be performed on an Apollo mission as soon as possible. The studies reported herein indicate that useful information pertaining to void ratio and other mechanical properties can be derived from plate load tests. The plate load tests could be performed by attaching a plate to the penetrometer extension handle, or by having the astronaut lower a large (4-inch) plate to the surface and step on it with his full weight. Photos should be taken before and after loading.
4. Analyses of the plate load test results reported herein should be continued using both the stress path method and the finite element method. Analysis by the finite element method, though not complete, is well under way at present.

5. Values of G should be determined for a good lunar soil simulant under conditions of reduced gravity. Although the penetrometer reduction factors, R_p , obtained in this study by the bearing capacity equation appear to be reliable, a high degree of certainty can only be obtained by making measurements in a $1/6$ g aircraft simulation.
6. Additional strength and stress-strain tests should be performed with confining pressures as low as 0.01 kg/cm^2 , if possible. The lowest confining pressure that could be used in the study described herein was 0.05 kg/cm^2 . Although the extrapolation to lower confining pressures used may well be reliable, the extent of extrapolation necessary was quite large. Very small specimens will probably be required because the weight of specimens of conventional size produces significant internal stress.

SYMBOLS

a	Intercept of $e_c = \text{constant}$ lines at $\sigma_{3f} = 0 \text{ kg/cm}^2$ in $\sigma_{3f}/\epsilon_{af} - \sigma_{3f}$ plot
\bar{a}	Intercept of $\bar{\epsilon}_a/\bar{D} - \bar{\epsilon}_a$ curve at $\bar{\epsilon}_a = 0$
B	Width
b	Slope of $e_c = \text{constant}$ lines in $\sigma_{3f}/\epsilon_{af} - \sigma_{3f}$ plot
\bar{b}	Slope of $\bar{\epsilon}_a/\bar{D} - \bar{\epsilon}_a$ curve
c	Cohesion, gm/cm^2 or lb/in.^2
c_a	Change in e between $\sigma = 1$ and $\sigma = 10 \text{ gm/cm}^2$ for confined compression curves
c_b	Change in e between $\sigma = 10$ and $\sigma = 100 \text{ gm/cm}^2$ for confined compression curves
c_r	Reduced cohesion value, gm/cm^2 or lb/in.^2
c_{1000}	Slope of $e_i/e_{1000} - e_i$ curve
d	Depth
\bar{d}	Slope of $\sigma_{3f} = \text{a constant}$ lines in $\bar{\epsilon}_l/\bar{\epsilon}_a - \bar{\epsilon}_l$ plot for σ_{3f} in kg/cm^2
d_{1000}	Intercept at $e_i = 0$ of $e_i/e_{1000} - e_i$ plot
\bar{D}	Stress level, σ_d/σ_{df}
\bar{D}_f	Stress level at failure = 1
\bar{D}_{fh}	Principal stress difference at failure of hyperbolic, normalized stress-strain curve
e, e_0	Void ratio
e_c	Pre-shear void ratio
e_i	Initial void ratio
e_1	Void ratio at $\sigma = 1 \text{ gm/cm}^2$
e_{10}	Void ratio at $\sigma = 10 \text{ gm/cm}^2$
e_{1000}	Void ratio at $\sigma = 1000 \text{ gm/cm}^2$
E_i	Initial tangent modulus of stress-strain curve
\bar{E}_i	Initial tangent modulus of normalized hyperbolic stress-strain curve = $1/\bar{a}$
E_t	Incremental Young's modulus
E_{tps}	Tangent modulus of stress-strain curve for plain strain condition

F	Value of a at $e_c = 0$ in $\log a - e_c$ plot
G	Slope of stress-penetration curve, psi/in for cone penetrometer tests
G_f	Slope of $e_c = \text{constant}$ lines in $\log \sigma_{df} - \log \sigma_{3f}$ plot
G_s	Specific gravity
h	Slope of $\log a - e_c$ curve
I	Intercept of $e_c = \text{constant}$ lines at $\sigma_{3f} = 0.1 \text{ kg/cm}^2$ in $\log \sigma_{df} - \log \sigma_{3f}$ plot
I_R	Intercept of $e_c = \text{constant}$, lines at $\sigma_{3f} = 0.1 \text{ kg/cm}^2$ in $(\epsilon_\ell/\epsilon_a)_f - \log \sigma_{3f}$ plot
\bar{I}_e	Intercepts of $\sigma_{3f} = 0$ lines at $\bar{\epsilon}_\ell = 0$, in $\bar{\epsilon}_\ell/\bar{\epsilon}_a - \bar{\epsilon}_\ell$ plot, for σ_{3f} in kg/cm^2
J	Intercept of $1/\bar{I}_e - \sigma_{3f}$ curve at $\sigma_{3f} = 1 \text{ kg/cm}^2$
k	Value of E_i at $\sigma_3 = 1.0 \text{ kg/cm}^2$
k_a	Intercept at $e_i = 1$ of $\log c_a - \log e_i$ plot
$k_{\ell s}$	Reduction factor
L_0	Value of I at $e_c = 0$ in $e_c - \log I$ plot
L	Length of loaded area
LSS	Lunar soil simulant
M	Slope of $e_c - \log I$ curve
m_1	Slope of $e_1 - e_i$ curve
N	Slope of $1/\bar{I}_e - \sigma_{3f}$ curve
N_Y, N_c, N_q	Bearing capacity factors
n	Slope of $\log E_i - \log \sigma_{3f}$ curve
n_a	Slope of $\log c_a - \log e_i$ curve
P	Value of b at $e_c = 0$ in $\log b - e_c$ plot
p_a	Atmospheric pressure
Q	Inverse of the change in e_c for one log cycle change in b
q_{ult}	Unit ultimate bearing capacity
q^1	Surcharge
R_f	Failure ratio: \bar{D}_f/\bar{D}_{fh}
R_p	Penetrometer G-value reduction factor for reduced gravity
R_Δ	Gravity reduction factor, for plate loading
r_1	Intercept at $e_i = 0$ of $e_1 - e_i$ curve
S	Change in $(\epsilon_\ell/\epsilon_a)_f$ for one log cycle change in σ_{3f} where σ_{3f} is in kg/cm^2

S_γ, S_c, S_q	Shape factors for bearing capacity equations
U	Intercept at $e_c = 0$ of $I_R - e_c$ curves
V	Slope of $I_R - e_c$ curves
w	Water content
WES	Waterway experiment station
Y	Intercept at $e_c = 0$ of $S - e_c$ curves
Z	Slope of $S - e_c$ curves
δ	Settlement
ϵ_a	Axial strain
ϵ_{af}	Axial strain at failure
$\bar{\epsilon}_a$	Normalized axial strain, ϵ_a/ϵ_{af}
ϵ_ℓ	Lateral strain
$\bar{\epsilon}_\ell$	Normalized lateral strain, $\epsilon_\ell/\epsilon_{\ell f}$
$\epsilon_{\ell f}$	Lateral strain at failure
γ	Unit weight lb/in ³ , gm/cm ³
ν_t	Incremental Poisson's ratio
ϕ	Friction angle, degrees
ρ	Density gm/cm ³
σ, σ_0	Stress gm/cm ² , kg/cm ² , lb/in ²
σ_1	Major principal stress, kg/cm ²
σ_3	Minor principal stress, kg/cm ²
σ_{df}	Principal stress difference at failure, kg/cm ²
σ_{3f}	Minor principal stress at failure, kg/cm ²
$(\sigma_1/\sigma_3)_f$	Principal stress ratio at failure

REFERENCES

- Costes, N. C., Carrier, W. D. II, Mitchell, J. K., and Scott, R. F. (1970), "Apollo 11: Soil Mechanics Results," *Journal of the Soil Mechanics and Foundations Division, ASCE*, Vol. 96, No. SM6, pp. 2045-2080.
- Costes, N. C., and Mitchell, J. K. (1970), "Apollo 11 Soil Mechanics Investigation," *Proc. Apollo 11 Lunar Sciences Conf.*, Vol. 3, pp. 2025-2044.
- Duke, M. B., Woo, C. C., Bird, M. L., Sellers, G. A., and Finkelman, R. B. (1970), "Lunar Soil: Size Distribution and Mineral Constituents," *Science*, Vol. 167, No. 3918, 30 Jan. 1970, pp. 648-650.
- Duncan, J. M., and Chang, C-Y (1969), "Nonlinear Analysis of Stress and Strain in Soils," submitted to ASCE for publication, 1969.
- Konder, R. L., and Zelasko, J. S. (1963), "A Hyperbolic Stress-Strain Formulation for Sands," *Proc. Second Pan-American Conf. Soil Mechanics & Foundation Engr.*, Vol. 1, Rio de Janeiro, 1963, pp. 289-324.
- Kulhawy, F. H., and Duncan, J. M. (1970), "Nonlinear Finite Element Analysis of Stresses and Movements in Oroville Dam," *Geotechnical Engineering Res. Report*, Depart. Civil Engr., University of California, Berkeley.
- Lambe, T. W., and Whitman, R. V. (1969), *Soil Mechanics*, John Wiley and Sons, New York, 1969, p. 216.
- Lysmer, J., and Duncan, J. M., *Stresses and Deflections in Foundations and Pavements*, 4th ed., 1969, University of California, Berkeley.
- Meyerhof, G. G., (1951) "The Ultimate Bearing Capacity of Foundations," *Geotechnique*, Vol. 11, 1951, p. 301.
- Mitchell, J. K., and Houston, W. N. (1970), "Lunar Surface Engineering Properties Experiment Definition," *Final Report: Vol. I: Mechanics and Stabilization of Lunar Soils*, prepared for George C. Marshall Space Flight Center, NASA Contract NAS 8-21432, Jan. 1970.

REFERENCES (Cont'd)

Scott, R. F., Carrier, W. D., Costes, N. C., and Mitchell, J. K. (1970),
"Apollo 12 Soil Mechanics Investigations," *Geotechnique*, Vol. 21,
No. 1, pp. 1-14.

Chapter 2. DETERMINATION OF IN SITU SOIL PROPERTIES UTILIZING AN IMPACT PENETROMETER

J. B. Thompson and J. K. Mitchell

INTRODUCTION

Due to the widespread distribution of major deposits of soil and "soil-like" material both terrestrially and on extraterrestrial bodies, such as the moon and probably Mars, soil mechanics and foundation engineering aspects of space explorations must be considered early in mission planning. The solution process of the majority of soil mechanics problems can be divided into two phases:

1. The determination of the in situ properties of the soil deposit, and
2. The engineering analysis of the probable effects of operations to be performed on the soil.

Both phases of this solution process have been given considerable study by workers in soil mechanics and foundation engineering and numerous solution techniques have been developed.

The present study is concerned with the determination of in situ soil properties by remote means. Perhaps the simplest technique for accomplishing this goal is the educated interpretation of visual or photographic observations of the soil surface. An evaluation of several variations of this technique has been presented by Mitchell et al. (1969, 1970a, 1970b) including some estimates of lunar soil properties determined in this manner. With reference to the moon, the two surface features that seem to be most promising for this type of study are the boulder tracks and secondary impact craters. The in situ soil properties considered in the method of analysis of boulder tracks presented by Mitchell et al. (1970b) are the cohesion, friction angle, and density. The magnitude of one of these properties can be calculated after assuming values for the other two. The analysis of secondary impact craters (Mitchell et al., 1969) does not include commonly recognized soil properties but other parameters to which these soil properties can be correlated. Many of the limitations on the analysis of secondary impact craters apply

equally to the analysis of impact penetration tests. The interpretation of secondary impact craters, however, does require several additional assumptions. The second technique for determining in situ soil properties is the deployment of equipment designed to test the soil deposit. Several such devices have been considered for use on the lunar surface including:

1. An automated soil scoop,
2. Static penetrometers of various shapes and sizes,
3. Soil corers and samplers,
4. Various types of static shear devices, and
5. Impact penetrometers of various shapes and sizes.

Although the present study has not progressed to the point at which a comparison of the relative merits of the impact penetration test and the other techniques and devices can be made, the impact penetration test possesses two obvious advantages which should be mentioned.

First, the unit would not necessarily require provisions for a soft landing on the moon. Only the impact penetrometer need contact the soil surface and telemetry could be used for data transmission. The second advantage is that the penetrometer along with any necessary instrumentation would likely compose a relatively small, inexpensive package economically allowing extensive deployment of these units over the area or areas of concern.

Since the value of the impact penetration test lies in its ability to determine in situ soil properties, the primary purpose of this investigation is to evaluate which soil properties can be determined from the penetrometer output and to what accuracy. It would be impossible to study all combinations of penetrometer, environmental, and soil variables influencing impact penetration within reasonable time and monetary constraints. Consequently, this investigation is limited to cone-tipped right circular cylinders impacting normally at velocities up to 200 fps onto a dry granular soil target.

The organization of the body of this report generally follows the approach we have taken to the problem. First, an extensive literature

review was conducted to determine the state of the art of impact penetration and to provide a basis for planning the remainder of the study. Following this literature review, the feasibility of approaching this problem theoretically was evaluated. It was concluded that a theoretical approach is not justified at this time. Next, an examination of the existing empirical analytical expressions relating the dependent and independent variables of the impact penetration problem was conducted. This examination emphasized an evaluation of the relative and absolute merits of these expressions and the determination of probable independent variables requiring additional experimental investigation to allow extrapolation of terrestrial test results to the lunar environment. After identifying the independent variables requiring further experimental study, an experimental program was designed. At the present time, a conceptual design of all equipment necessary for conducting the testing has been completed.

LITERATURE REVIEW

An extensive review of the published literature on impact penetration has been completed. A rather detailed summary of this literature review is presented below because we believe that prior evaluations of the state of the art are lacking in both scope and detail.

Considerable effort has been devoted to the study of impact penetration problems involving a broad spectrum of projectile and target materials and shapes. A major portion of this research dealing with armor penetration by projectiles travelling at ballistic velocities is not relevant to the problem under consideration and will not be discussed in this report. In this presentation, previous research on the dynamic penetration of soils will be divided into three categories.

1. Theoretical studies designed to develop theoretical, analytical relationships between the dependent and independent variables of the impact penetration problem, and
2. Experimental investigations instigated primarily to develop a qualitative understanding of impact penetration (considerable test data and some analytical expressions have also resulted from these studies), and

3. Statistical studies designed to develop empirical, analytical relationships from the combined test results of several experimental programs.

Theoretical Investigations

Investigations of this type have been conducted to develop analytical expressions relating the dependent and independent variables of the impact penetration problem. These relationships are based on the concepts of theoretical mechanics and appropriate assumptions. The investigations of this type are summarized in Table 2-1, which indicates the author(s), theoretical bases, the resultant equation(s), and the assumptions and conclusions of each investigation.

Experimental Investigations

Investigations of this type have usually been designed to develop a qualitative understanding of impact penetration for a certain limited combination of penetrometer and soil variables. In a few of these studies, analytical expressions have also been developed. Previous investigations of this type are summarized in Tables 2-2 and 2-3. In Table 2-2, the author(s), soil(s), penetrometer shape(s) and dimensions, impact velocity(ies), impact angle(s) (the acute angle between the normal to the soil surface and the velocity vector of the penetrometer), and the air pressure (measured at the soil surface) of each study are given. All penetrometers had zero rotational velocity and moved in a plane normal to the soil surface. The principal conclusions from each study are summarized in Table 2-3.

Statistical Investigations

Statistical investigations have been conducted to develop empirical, analytical relationships between the dependent and independent variables of the impact penetration problem. These studies utilized the extensive test results generated by the experimental programs presented above. Previous investigations of this type are summarized in Tables 2-4 and 2-5. In Table 2-4 the author(s), soil(s), penetrometer shape(s) and dimensions, impact velocity(ies), impact angle (s), and the air pressures of the experimental programs from which the test results were taken are presented. The equations derived from these studies are shown in Table 2-5 along with the significant conclusions of each study.

Table 2-1. Theoretical investigations.

AUTHORS: Robins (1742), Euler (1745)

THEORETICAL BASIS: Newton's Second Law of Motion

EQUATIONS: (1) $a = -\frac{c_0}{m}$ (2) $z = -\frac{c_0^2 t^2}{2m} + V_0 t$ (3) $V = -\frac{c_0^2 t}{m} + V_0$

ASSUMPTIONS AND CONCLUSIONS:

- (1) The weight of the penetrometer and the soil moving with the penetrometer is negligible.
- (2) The soil resistance is a constant, c_0 .
- (3) Any consistent set of units may be used.

AUTHOR: Poncelet (1829)

THEORETICAL BASIS: Newton's Second Law of Motion

EQUATIONS: (1) $a = -\frac{(c_0 + c_2 V^2)}{m}$ (2) $V = \left(\frac{\frac{c_0}{c_2} + V_0^2}{\frac{z}{2c_2 m}} - \frac{c_0}{c_2} \right)^{1/2}$ (3) $P = \frac{m}{2c_2} \ln \left(1 + \frac{c_2}{c_0} V_0^2 \right)$

ASSUMPTIONS AND CONCLUSIONS:

- (1) The weight of the penetrometer and the soil moving with the penetrometer is negligible.
- (2) The soil resistance is given by $c_0 + c_2 V^2$ where c_0 and c_2 are constants.
- (3) Any consistent set of units may be used.

Table 2-1. (Cont'd)

AUTHOR: Resal (1895)

THEORETICAL BASIS: Newton's Second Law of Motion

$$(1) \quad a = - \frac{(c_1 v + c_2 v^2)}{m}$$

$$(2) \quad v = \frac{\frac{c_1}{c_2} + v_0}{\frac{z}{c_2 m}} - \frac{c_1}{c_2}$$

$$(3) \quad P = \frac{m}{c_2} \ln \left(1 + \frac{c_2}{c_1} v_0 \right)$$

EQUATIONS:

ASSUMPTIONS AND
CONCLUSIONS:

- (1) The weight of the penetrometer and the soil moving with the penetrometer is negligible.
- (2) The soil resistance is given by $c_1 v + c_2 v^2$ where c_1 and c_2 are constants.
- (3) Any consistent set of units may be used.

AUTHOR: Petry (1910)

THEORETICAL BASIS: Newton's Second Law of Motion

$$P = \frac{W}{A} K \log_{10} \left(1 + \frac{v_0}{215,000} \right)$$

EQUATION:

ASSUMPTIONS AND
CONCLUSIONS:

- (1) Same assumptions as Poncelet (1829).
- (2) K is a constant.
- (3) For this equation:

W - lbs A - sq in P - ft v_0 - fps

Table 2-1. (Cont'd)

AUTHORS:

McCarty and Carden (1962)

THEORETICAL BASES:

Solution 1

(a) Newton's Second Law of Motion

(b) Theory of Elasticity (Hertz Law of Contact)

Solution 2

(a) Newton's Second Law of Motion

(b) Theory of Plasticity (Meyer's Law)

EQUATIONS:

Solution 1

$$(a) \quad F = k\alpha^{3/2}$$

$$(b) \quad a_{\max} = \left(\frac{125 DV_0^6}{72\pi^2 m^2 [\delta_p + \delta_t]^2} \right)^{1/5}$$

$$(c) \quad t_m = 5.208 \left(\frac{[\delta_p + \delta_t]_m}{\sqrt{DV_0}} \right)^{2/5} = \text{total contact time}$$

$$(d) \quad \alpha = \left(\frac{15\pi V_0^2 [\delta_p + \delta_t]_m}{8\sqrt{2} D} \right)^{2/5} = \text{maximum relative approach}$$

$$(e) \quad k = \frac{2}{3} \sqrt{\frac{2D}{\pi}} \left[\frac{1}{\delta_p + \delta_t} \right]$$

$$(f) \quad \delta_p = \frac{1 - \mu_p^2}{\pi E_p}$$

$$(g) \quad \delta_t = \frac{1 - \mu_t^2}{\pi E_t}$$

Table 2-1. (Cont'd)

AUTHORS:

McCarty and Carden (1962) Cont'd

EQUATIONS:

Solution 2

$$(a) \quad F = \pi D z p$$

$$(d) \quad t_m = \frac{1}{2} \sqrt{\frac{\pi m}{D p}}$$

$$(b) \quad z = V_0 \sqrt{\frac{m}{\pi D p}} \sin \left(\sqrt{\frac{\pi D p}{m}} t \right)$$

$$(c) \quad p = V_0 \sqrt{\frac{m}{\pi D p}}$$

$$(e) \quad a_{\max} = -V_0 \sqrt{\frac{\pi D p}{m}}$$

ASSUMPTIONS AND
CONCLUSIONS:

Solution 1

(1) Assumptions

(a) The penetrometer is an elastic sphere having the moduli E_p , μ_p .(b) The soil target is an elastic, massive plane surface having the moduli E_t , μ_t .

(c) The penetrometer impacts normal to the soil surface.

(2) Conclusions

(a) This solution is not applicable to soils.

Solution 2

(1) Assumptions

(a) The soil resistance is a constant, p .

(b) The penetrometer is a sphere.

(c) $p < \frac{D}{2}$.

(2) Conclusions

(a) This solution is applicable in some cases for $\frac{D}{10} < p < \frac{D}{2}$.

(b) Penetrometers impacted at low velocity into soil seem to follow this equation.

Table 2-1. (Cont'd)

AUTHOR: Scott (1962)

THEORETICAL BASES: Solution 1

Newton's Second Law of Motion

Solution 2

(a) Newton's Second Law of Motion

(b) Mohr-Coulomb Failure Theory

EQUATIONS:

Solution 1

$$(a) \quad \bar{V}^2 = \frac{1}{\left(\frac{CM}{\pi} + z\right)^2} \left\{ \left(\frac{CM}{\pi}\right)^2 \left[\bar{V}_0^2 + \frac{CM}{\pi} \left(p_0 - \frac{2}{3}\right) \right] - \left[\frac{CM}{\pi} p_0 - \frac{2}{3} \left(\frac{CM}{\pi} + z\right) \right] \left(\frac{CM}{\pi} + z\right)^2 \right\}$$

$$- \frac{2CM}{\pi} \frac{p_1}{c^n} \frac{z^{n+1}}{(n+2)} \left[\frac{CM}{\pi} \frac{(n+2)}{(n+1)} + z \right]$$

$$(b) \quad A' = - \left[\frac{1}{\left(\frac{CM}{\pi} + z\right)^3} \left\{ \left(\frac{CM}{\pi}\right)^2 \left[\bar{V}_0^2 + \frac{CM}{\pi} \left(p_0 - \frac{2}{3}\right) \right] - \left[\frac{CM}{\pi} p_0 - \frac{2}{3} \left(\frac{CM}{\pi} + z\right) \right] \left(\frac{CM}{\pi} + z\right)^2 \right\} \right.$$

$$\left. - \frac{2CM}{\pi} \frac{p_1}{c^n} \frac{z^{n+1}}{(n+2)} \left[\frac{CM}{\pi} \frac{(n+2)}{(n+1)} + z \right] \right\} + \frac{1}{\left(\frac{CM}{\pi} + z\right)} \left\{ \frac{CM}{\pi} p_0 - \frac{2}{3} \left(\frac{CM}{\pi} + z\right) + \frac{CM}{\pi} \frac{p_1}{c^n} z^n \right\} - \frac{1}{3}$$

Table 2-1. (Cont'd)

AUTHOR: Scott (1962) Cont'd

EQUATIONS: Solution 2

(a) Case 1: for $z \leq 2r$

$$\bar{V}^2 = \left(\frac{1}{p + qz} \right)^2 \left[p^2 V_{ic}^2 + 2 puZ + (qu - pw)Z^2 - \frac{2}{3} qwZ^3 \right]$$

(b) Case 2: for $z \geq 2r$

$$\bar{V}^2 = \left(\frac{1}{p + qz} \right)^2 \left[2pRZ + (qR - ps')Z^2 - \frac{2(qs' + pt)}{3} Z^3 - Z^4 + b_9 \right]$$

(c) Where for Solutions 1 and 2

$$i. \quad b_1 = 6.5, \quad b_2 = \frac{\pi}{3}, \quad b_3 = 9\pi, \quad b_4 = 2\pi, \quad b_5 = 6\pi, \quad b_6 = 40.8, \quad b_7 = 37.7, \quad b_8 = 3\pi$$

$$ii. \quad b_9 = \bar{V} @ Z = 2r$$

$$x. \quad R = M + b_2 - B(b_4H + b_6)$$

$$iii. \quad \bar{V} = \frac{V}{\sqrt{rg}}, \quad V_{ic} = \left(\frac{M}{M + \frac{\pi}{3}} \right) \bar{V}_0, \quad \bar{V}_0 = \frac{V_0}{\sqrt{rg}}$$

$$xi. \quad M = \frac{m}{\rho_1 r^3}$$

$$xii. \quad B = \frac{c}{\rho_1 rg} \quad xvi. \quad P_0 = \frac{P_0 \pi r^2}{mg}$$

$$iv. \quad Z = \frac{z}{r}$$

$$xvii. \quad A' = \frac{a}{g}$$

$$v. \quad p = M + b_1$$

$$xiii. \quad H = \frac{h}{r}$$

$$vi. \quad u = M + b_2 - \pi N_C B - \pi N_Y$$

$$xiv. \quad q = \frac{9}{8\pi} \quad xviii. \quad P_1 = \frac{b\pi r^{n+2}}{mg}$$

$$vii. \quad w = b_3 + \pi N_q$$

$$viii. \quad s' = b_3 + Bb_5 + \pi K_0 \tan \phi (2H + 1) + b_7 \tan \phi$$

$$ix. \quad t = b_8 K_0 \tan \phi$$

$$xv. \quad C = \frac{\rho_2 - \rho_1}{\rho_2}$$

Table 2-1. (Cont'd)

AUTHOR:	Scott (1962) Cont'd
ASSUMPTIONS AND CONCLUSIONS:	<p>(1) Assumptions common to both Solution 1 and Solution 2.</p> <ul style="list-style-type: none"> (a) The soil deposit is homogeneous, having a mass density ρ_1, and semi-infinite in depth. (b) The penetrometer is a short, cylindrical prism of length h having a blunt tip. (c) The soil surface is normal to the gravitational acceleration and the penetrometer velocity vectors. (d) The axis of revolution and velocity vector of the penetrometer are coincident. (e) The penetrometer is rigid. <p>(2) Solution 1 assumptions.</p> <ul style="list-style-type: none"> (a) The penetration mechanism is as shown in Figure 2-1. (b) The zone of soil affected is limited to a soil plug of height s and width $2r$ formed directly beneath the penetrometer. (c) The soil mass density, ρ_2, in the soil plug is uniform. (d) Side friction between the soil plug, the penetrometer and the surrounding soil is assumed to be negligible. (e) The soil plug moves at the same velocity as the penetrometer. (f) The soil pressure acting on the base of the soil plug is given by: $p = p_0 + bz^n$ where b and n are constants and p_0 is the initial soil resistance. <p>(3) Assumptions common to both Case 1 and Case 2 of Solution 2.</p> <ul style="list-style-type: none"> (a) Soil is an incompressible material. (b) Soil is a rigid plastic material.

Table 2-1. (Cont'd)

AUTHOR:	Scott (1962) Cont'd
ASSUMPTIONS AND CONCLUSIONS:	<p data-bbox="397 532 430 1893">(4) Solution 2 - Case 1 assumptions.</p> <p data-bbox="430 532 673 1893">(a) A soil cone directly beneath the penetrometer is formed instantaneously on contact with the soil surface and moves at the same velocity as the penetrometer. A corrected impact velocity is determined by assuming that the momentum of the penetrometer and the soil cone immediately after impact is equal to the momentum of the penetrometer immediately before impact.</p> <p data-bbox="673 532 803 1893">(b) The soil resistance can be calculated from the static bearing capacity equations by adding inertial forces resulting from soil particle accelerations derived from the velocity field shown in Figure 2-2.</p> <p data-bbox="803 532 1047 1893">(c) Although the author notes that in frictional soil the included angle of the cone shown in Figure 2-2 would be $\pi/2 - \phi$ (smooth base) or greater than $\pi/2 - \phi$ (rough base) and that the circular segment of the failure surface would be a logarithmic spiral (approximately), he states that the mechanism shown in Figure 2-2 should be adequate.</p> <p data-bbox="1047 532 1096 1893">(5) Solution 2 - Case 2 assumptions.</p> <p data-bbox="1096 532 1161 1893">(a) The penetration mechanism is as shown in Figure 2-2.</p> <p data-bbox="1161 532 1274 1893">(b) The initial velocity condition is given from Solution 2 - Case 1 at a depth of $z = 2r$.</p> <p data-bbox="1274 532 1307 1893">(c) In the Mohr-Coulomb equation, σ on bcd in Figure 2-2 is ρ_1gz.</p> <p data-bbox="1307 532 1404 1893">(d) Except for the above exception, $\sigma_1 = \rho_1gz$ and acts vertically, and $\sigma_3 = K_0\sigma_1$ and acts horizontally at all points in the soil mass.</p> <p data-bbox="1404 532 1471 1893">(6) Any consistent set of units may be used.</p>

Table 2-1. (Cont'd)

AUTHOR: Philco (1966a, 1966b)

THEORETICAL BASIS: Newton's Second Law of Motion

EQUATIONS: (1) Solution 1

(a) Case 1: for $z \leq \frac{D}{2}$

$$V^2 = \exp \left[\frac{\pi \rho_t}{10D^2 m} (4z^5 - 10Dz^4 + 10D^2z^3 - 5D^3z^2) \right] \left\{ V_0^2 + \frac{20\pi}{m} \right. \\ \times \left[\frac{z^3}{3} + \frac{\pi \rho_t}{10D^2 m} \left(-\frac{1}{2} z^8 + 2Dz^7 - \frac{10D^2}{3} z^6 + 3D^2z^5 - \frac{5D^4z^4}{4} \right) \right. \\ \left. + \frac{1}{2} \left(\frac{\pi \rho_t}{10D^2 m} \right)^2 \frac{16}{13} (z^{13} - 8Dz^{12} + \frac{260}{11} D^2z^{11} - 42D^3z^{10} + \frac{440}{9} z^9 \right. \right. \\ \left. \left. - \frac{300}{8} D^5z^8 + \frac{125}{7} D^6 - \frac{25}{6} D^7z^6) - \frac{D}{2} z^2 \right] \right\}$$

(b) Case 2: for $z \geq \frac{D}{2}$

$$V^2 = V_i^2 + \frac{4\sigma}{\rho_t} \exp \left[-\frac{\pi D^2}{8m} \rho_t \left(z - \frac{D}{2} \right) \right] - \frac{4\sigma}{\rho_t}$$

V_i = penetrometer velocity at $z = \frac{D}{2}$ determined from Solution 1 - Case 1

Table 2-1. (Cont'd)

AUTHOR:	Philco (1966a, 1966b) Cont'd
EQUATIONS:	<p>(2) Solution 2</p> <p>Similar to Solution 1 except that the system of differential equations cannot be solved in closed form.</p>
ASSUMPTIONS AND CONCLUSIONS:	<p>(1) Solution 1 assumptions.</p> <ul style="list-style-type: none"> (a) The penetrometer is a rigid sphere. (b) The inertial soil resistance is contributed to only by the soil in direct contact with the penetrometer. (c) The soil target has a constant yield stress, σ, and mass density, ρ_t, with depth. <p>(2) Solution 1 conclusions.</p> <p>This solution yields poor agreement with experimental test results. In some cases the signature shape was incorrect and in all cases the maximum deceleration was underestimated.</p> <p>(3) Solution 2 assumptions.</p> <ul style="list-style-type: none"> (a) The penetrometer is a rigid sphere. (b) Soil yield stress, $\sigma = a_0 + a_1z + a_2z^2 + a_3z^3$ where a_0, a_1, a_2, and a_3 are constants. (c) Soil mass density, $\rho = b_0 + b_1z + b_2z^2$ where b_0, b_1, and b_2 are constants. (d) A soil wedge moves with the penetrometer and its mass is given by $K_1(\pi D^2/4)\rho_t z$ where K_1 is a constant. (e) The inertial term derived in Solution 1 is multiplied by a constant, K_2, to account for the larger mass being affected.

Table 2-1. (Cont'd)

AUTHOR:	Philco (1966a, 1966b) Cont'd.
ASSUMPTIONS AND CONCLUSIONS:	(4) Solution 2 conclusions In some cases this solution seems to be adequate. However, this solution generally underestimated total penetration. (5) Any consistent set of units may be used.

AUTHOR:	Schmid (1966)
THEORETICAL BASES:	(1) Solution 1 and Solution 2 are the same as McCarty and Carden (1962). (2) Solution 3 (a) Newton's Second Law of Motion (b) Theory of Elasticity (Hertz Law of Contact)
EQUATIONS:	(1) Solution 1 and Solution 2 are the same as McCarty and Carden (1962). (2) Solution 3

$$\sqrt{z^3 \left(r - \frac{z}{4} \right)} = \frac{3F_{\max}}{8G_1} \left\{ \left[\frac{1 + 4\Gamma}{1 + \Gamma} + \frac{k\omega_2^2}{\omega^2 + \omega_2^2} + \frac{\beta_1\omega_3}{\omega^2 + \omega_3^2} + \frac{\beta_2\omega_4}{\omega^2 + \omega_4^2} \right] \sin \omega t \right.$$

$$\left. - \left[\frac{\omega_1}{\omega} + \frac{k\omega\omega_2}{\omega^2 + \omega_2^2} + \frac{\beta_1\omega}{\omega^2 + \omega_3^2} + \frac{\beta_2\omega}{\omega^2 + \omega_4^2} \right] \cos \omega t \right\}$$

$$+ \frac{\omega_1}{\omega} + \frac{k\omega\omega_2}{\omega^2 + \omega_2^2} e^{-\omega_2 t} + \frac{\beta_1\omega}{\omega^2 + \omega_3^2} e^{-\omega_3 t} + \frac{\beta_2\omega}{\omega^2 + \omega_4^2} e^{-\omega_4 t} \left\}$$

Table 2-1. (Cont'd)

AUTHOR: Schmid (1966) Cont'd

EQUATIONS: (3) Where for Solution 3

$$(a) \quad \Gamma = \frac{G_1}{6K} \qquad (b) \quad k = \frac{G_1}{G_2}$$

$$(c) \quad \omega_1 = \frac{G_1}{\eta_1} \qquad \omega_2 = \frac{G_2}{\eta_2}$$

$$\omega_3 = \frac{1}{2} \left\{ \omega_2 + \frac{1}{1 + \Gamma} (\omega_1 + k\omega_2) \right\} \pm \frac{1}{2} \left\{ \left[\omega_2 + \frac{1}{1 + \Gamma} (\omega_1 + k\omega_2) \right]^2 - \frac{4}{1 + \Gamma} \omega_1 \omega_2 \right\}^{\frac{1}{2}}$$

$$(d) \quad \beta_1 = \frac{1}{1 + \Gamma} \alpha_1 \left\{ \frac{1 + 2\Gamma + 4\Gamma^2}{1 + \Gamma} + \frac{k\omega_2}{\omega_2 - \omega_3} - \frac{\omega_1}{\omega_3} \right\}$$

$$\beta_2 = \frac{1}{1 + \Gamma} \alpha_2 \left\{ \frac{1 + 2\Gamma + 4\Gamma^2}{1 + \Gamma} + \frac{k\omega_2}{\omega_2 - \omega_4} - \frac{\omega_1}{\omega_4} \right\}$$

$$(e) \quad \alpha_1 = \frac{\omega_1 \omega_2 - \omega_1 \omega_3 - k\omega_2 \omega_3}{\omega_4 - \omega_3} \qquad \alpha_2 = \frac{\omega_1 \omega_2 - \omega_1 \omega_4 - k\omega_2 \omega_4}{\omega_3 - \omega_4}$$

(f) K = soil bulk modulus

ASSUMPTIONS AND
CONCLUSIONS:

(1) Assumptions and conclusions for Solution 1 and Solution 2 are the same as
McCarty and Carden (1962).

Table 2-1. (Cont'd)

AUTHOR:	Schmid (1966) Cont'd
ASSUMPTIONS AND CONCLUSIONS:	(2) Solution 3 assumptions.
	(a) Soil can be represented by the rheological model shown in Figure 2-3.
	(b) The penetrometer is a sphere or is tipped with a hemisphere.
	(c) Soil resistance has a sinusoidal variation of frequency ω with time.
	(d) Total penetration $\leq D/2$.
	(e) The product of the penetration and the contact radius (at the penetrometer-soil surface boundary) is assumed to be linear with the contact force, F .
	(3) Solution 3 conclusions.
	(a) Whereas simple elastic and plastic solutions neglect time effects on impact penetration, this rheological model accounts for this variable.
	(b) A unique set of rheological constants may not exist and several combinations of these parameters may exhibit the observed behavior.
	(c) Sinusoidal acceleration-time signatures have been observed in tests in clay, silt, and loose sands.
	(4) Any consistent set of units may be used.
AUTHOR:	Thompson (1966)
THEORETICAL BASES:	(1) Newton's Second Law of Motion
	(2) Conservation of Mass
	(3) Mohr-Coulomb Failure Theory

Table 2-1. (Cont'd)

AUTHOR:	Thompson (1966) Cont'd
EQUATIONS:	<p>This investigation yielded a lengthy set of partial differential equations involving numerous assumptions. It would be impractical to present these equations and assumptions herein. However, it should be pointed out that the approach followed in this study is one of the most rigorous published on impact penetration. These equations cannot be solved in closed form and, unfortunately, it appears that they are too highly nonlinear to be solved numerically.</p>
ASSUMPTIONS AND CONCLUSIONS:	
AUTHOR:	
THEORETICAL BASIS:	Moore (1967) Conservation of Energy
EQUATION:	$\frac{P}{L} = K \left(\frac{\rho}{\rho_t} \right)^{\frac{1}{2}} \frac{1}{g^{\frac{1}{2}}} \frac{V_0}{L^{\frac{1}{2}}} \quad K = \text{constant}$
ASSUMPTIONS AND CONCLUSIONS:	<p>(1) Assumptions.</p> <ul style="list-style-type: none"> (a) The soil penetration resistance is proportional to the soil density. (b) The soil penetration resistance is proportional to the acceleration of gravity. (c) The soil penetration resistance is proportional to the depth of penetration. (d) The energy available for penetration is proportional to the kinetic energy of the penetrometer immediately before impact. (e) The soil penetration resistance is independent of the instantaneous penetrometer velocity. (f) The penetrometer is assumed to be tipped with a blunt nose. <p>(2) Any consistent set of units may be used.</p>

Table 2-1. (Cont'd)

AUTHOR:

Shipley (1967)

THEORETICAL BASES: (1) Newton's Second Law of Motion

(2) Mohr-Coulomb Failure Theory

EQUATIONS:

$$(1) \quad F = \pi r^2 (A' + Bz) + \left[(C' + Ez) \frac{d^2 z}{dt^2} + E \left(\frac{dz}{dt} \right)^2 \right] \pi r^2$$

$$(2) \quad \frac{d^2 z}{dt^2} = \frac{mg - \pi r^2 (A' + Bz) - \pi r^2 E \left(\frac{dz}{dt} \right)^2}{m + [C' + Ez] \pi r^2}$$

(3) Where for this study

$$(a) \quad A' = 1.3c N_c + \rho_t g + 0.6N_\gamma$$

$$(b) \quad B = \rho_t g N_q$$

$$(c) \quad C' = -0.83 \rho_t r$$

$$(d) \quad E = 0.14 \rho_t$$

ASSUMPTIONS AND

CONCLUSIONS:

(1) Assumptions

Similar to Scott (1962) -- Solution 2-Case 1

(2) Any consistent set of units may be used.

Table 2-1. (Cont'd)

AUTHOR: Tsai (1967)

THEORETICAL BASES: Same as Schmid (1966) — Solution 3

EQUATIONS: (1) Solution 1

$$(a) \quad \sqrt{z^3 \left(r - \frac{z}{4} \right)} = \frac{3F_{\max}}{8} \left[C_1 \sin \omega t - (C_2 + C_3) \cos \omega t + C_2 + C_3 e^{-\omega_2 t} \right]$$

$$(b) \quad C_1 = \frac{1}{G_1} + \frac{G_2}{\eta_2^2} \left(\alpha^2 + \frac{G_2^2}{\eta_2^2} \right) C_2 = \frac{1}{\eta_1 \omega} C_3 = \frac{\omega}{\eta_2 \left(\omega^2 + \frac{G_2^2}{\eta_2^2} \right)}$$

(2) Solution 2

$$(a) \quad \sqrt{z^3 \left(r - \frac{z}{4} \right)} = C'_1 \sin \omega t + C'_2 (1 - \cos \omega t)$$

$$(b) \quad C'_1 = \frac{3 \text{ ma}_{\max}}{8G_1} \quad C'_2 = \frac{3 \text{ ma}_{\max}}{\omega \eta}$$

ASSUMPTIONS AND
CONCLUSIONS:

(1) Solution 1 assumptions.

Same as Schmid (1966) — Solution 3 except that the soil bulk modulus $K = \infty$.

(2) Solution 2 assumptions.

Same as Schmid (1966) — Solution 3 and Tsai (1967) — Solution 1 except that a new rheological model shown in Figure 2-4 is evaluated.

(3) Any consistent set of units may be used.

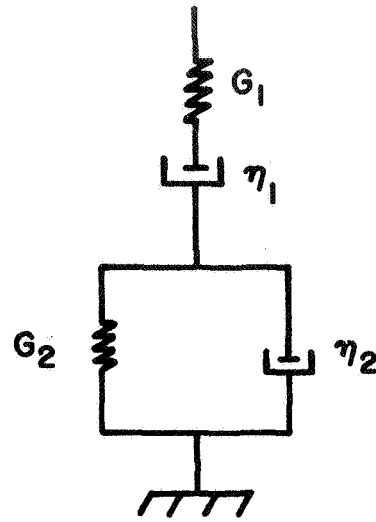


Fig. 2-3. Soil rheological model proposed by Schmid (1966) (G_1 , G_2 , η_1 , and η_2 are soil spring and dashpot constants).

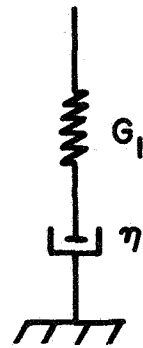


Fig. 2-4. Soil rheological model proposed by Tsai (1967) (G_1 and η are soil spring and dashpot constants).

Table 2-1. (Cont'd)

AUTHOR:

Schmid (1969)

THEORETICAL BASIS: Newton's Second Law of Motion

EQUATIONS:

(1) Solution 1

(a) Case 1: for $\beta^2 < 4\alpha\gamma$

$$z = \frac{m}{2\gamma} \ln \frac{\gamma V_0^2 + \beta V_0 + \alpha}{\gamma V^2 + \beta V + \alpha} - \frac{m\beta}{\gamma} A' (4\alpha\gamma - \beta^2)^{-\frac{1}{2}} @ t = 2 A' m (4\alpha\gamma - \beta^2)^{-\frac{1}{2}} - \frac{1}{2}$$

(b) Case 2: for $\beta^2 > 4\alpha\gamma$

$$z = \frac{m}{2\gamma} \ln \frac{\gamma V_0^2 + \beta V_0 + \alpha}{\gamma V^2 + \beta V + \alpha} - \frac{m\beta}{\gamma} B (\beta^2 - 4\alpha\gamma)^{-\frac{1}{2}} @ t = 2Bm (\beta^2 - 4\alpha\gamma)^{-\frac{1}{2}}$$

(c) Case 3: for $\beta^2 = 4\alpha\gamma$

$$z = \frac{m}{\gamma} \ln \frac{\beta + 2\gamma V_0}{\beta + 2\gamma V} - \frac{\beta}{\gamma} C m @ t = 2Cm$$

(d) Where for Solution 1 ..

$$i. A' = \tan^{-1} (2\gamma V_0 + \beta) (4\alpha\gamma - \beta^2)^{-\frac{1}{2}} - \tan^{-1} (2\gamma V + \beta) (4\alpha\gamma - \beta^2)^{-\frac{1}{2}}$$

$$ii. B = \frac{1}{2} \ln \left\{ \frac{[2\gamma V + \beta + (\beta^2 - 4\alpha\gamma)^{\frac{1}{2}}] [2\gamma V_0 + \beta - (\beta^2 - 4\alpha\gamma)^{\frac{1}{2}}]}{[2\gamma V + \beta - (\beta^2 - 4\alpha\gamma)^{\frac{1}{2}}] [2\gamma V_0 + \beta + (\beta^2 - 4\alpha\gamma)^{\frac{1}{2}}]} \right\}$$

$$iii. C = (2\gamma V + \beta)^{-1} - (2\gamma V_0 + \beta)^{-1}$$

Table 2-1. (Cont'd)

AUTHOR:	Schmid (1969) Cont'd
EQUATIONS:	(2) Solution 2
	$z = \frac{V_0^m}{2\pi r\mu} \left(1 - e^{-2\pi r\mu t/m} \right)$
ASSUMPTIONS AND CONCLUSIONS:	(1) Solution 1 assumptions.
	(a) The weight of the penetrometer and the soil moving with the penetrometer is negligible.
	(b) The soil resistance is given by $\alpha + \beta v + \gamma v^2$ where α , β , and γ are constants.
	(2) Solution 2 assumptions.
	(a) The soil resistance is viscous in nature and is given by $2\pi r\mu v$ where μ is a constant (the soil viscosity).
	(b) The penetrometer is a solid of revolution.
	(c) The contact area between the penetrometer and the soil at the nose of the penetrometer is constant.
	(3) Any consistent set of units may be used.

Table 2-2. Experimental investigations.

Author(s)	Soil(s) investigated	Penetrometer(s) utilized	Impact velocity (ft/sec)	Impact angle* (°)	Air press. at soil surface (Torr)
USAE-WES (1957, 1958)	1. WES lean clay 2. Heavy clay 3. Silt	0.125 ft diameter right circular cylinder tipped with a nose consisting of two cones and a cylinder. Overall length = 2.54-3.0 ft Overall weight = 1.19 lbs	72-169	0-15	760
McCarthy and Carden (1962)	1. Low velocity tests a) Sod b) Dry No. 000 sand 2. High velocity tests a) Layered profile consisting of sod, silty sand, and sandy clay b) Peat moss	1. Low velocity tests Right circular cylinder tipped with a hemispherical nose. Diameter = 0.0834-0.25 ft Weight = 0.965-9.87 lbs 2. High velocity tests 0.25 ft diameter right circular cylinder tipped with a hemispherical or 60° apex included angle cone. Weight = 8.89-17.4 lbs	1. Low velocity tests 5-30 2. High velocity tests 190-900	0	760

* The acute angle between the normal to the soil surface and the velocity vector of the penetrometer.

Table 2-2. (Cont'd)

Author(s)	Soil(s) investigated	Penetrometer(s) utilized	Impact velocity (ft/sec)	Impact angle (°)	Air press. at soil surface (Torr)
Roddy, Rittenhouse and Scott (1962)	Fresh, crushed olivine basalt having the gradations between 1. $D_{10} = 0.006$ mm $D_{60} = 0.047$ mm and 2. $D_{10} = 0.27$ mm $D_{60} = 0.35$ mm	0.16 ft long right circular cylinder tipped with a blunt nose on one end and a 60° apex included angle on the other. Diameter = 0.02-0.033 ft Weight = 0.025-0.061 lbs	5.8	0	10^{-5} - 760
Rowe and Selig (1962)	Finely ground silica flour (85% of particles 2 to 40 microns)	0.05 ft diameter right circular cylinder.	≈4	0	5×10^{-8} - 760
Clark and McCarty (1963)	1. Uniform sized aluminum oxide Average size = 0.003-0.6 mm. 2. Silicon carbide Average size = 0.016 mm	Sphere. Diameter = 0.05-0.08 ft Weight = 0.027-0.147 lbs	3.2-15	0	10^{-5} - 760

Table 2-2. (Cont'd)

Author(s)	Soil(s) investigated	Penetrometer(s) utilized	Impact velocity (ft/sec)	Impact angle (°)	Air press. at soil surface (Torr)
Vey and Nelson (1965, 1966)	1. Quartz silt and sand 2. Enstatite silt and sand 3. Silicic and ferro-magnesium silicate olivine silts 4. Limonite silt	1. Instrumented penetrometer 0.06 ft diameter right circular cylinder tipped with either a blunt nose or a 60° apex included angle nose. 2. Sphere Diameter = 0.0416-0.125 ft	1. Instrumented penetrometer 2.0-5.0 2. Sphere 11-40	0	2×10^{-9} -760
Hanks and McCarty (1966)	1. Aluminum oxide having gradations between a) $D_{10} = 0.86$ mm $D_{60} = 0.95$ mm and b) $D_{10} = D_{60} = 0.005$ mm 2. Ground pumice $D_{10} = 0.046$ mm $D_{60} = 0.072$ mm	Sphere. Diameter = 0.167-0.33 ft Weight = 0.773-1.0 lbs	5-30	0	760

Table 2-2. (Cont'd)

Author (s)	Soil(s) investigated	Penetrometer(s) utilized	Impact velocity (ft/sec)	Impact angle (°)	Air press. at soil surface (Torr)
Philco (1966a, 1966b)	1. Nevada sand 2. Crushed basalt agglomerate, sand, and silt 3. Silica powder (Cabosil) Diameter = 0.000015 mm	Sphere. Diameter = 0.33-1.0 ft Weight = 2.205-5.01 lbs	19-250	0-60	10^{-5} - 760
Schmid (1966)	1. Beach sand 2. Fine sand 3. Crushed rock 4. Silty sand 5. Sandy clay 6. Clay	0.247 ft diameter right circular cylinder tipped with a conical, hemispherical, or blunt nose Weight = 3.47 lbs	14-39	0	760
Thompson (1966)	1. Moist bulked silt 2. Dry Ottawa sand size: - #20 + #30 3. Clayey sand 4. Layered soil profiles consisting of silty sand, silty clay, and clay	1. Square parallelepiped tipped with a blunt nose Width = 0.0625-0.125 ft Weight = 0.51 lbs 2. 0.75 ft diameter right circular cylinder tipped with: a) Blunt nose Weight = 636-1200 lbs b) Tangent ogive nose CRH = 2.2-9.25 Weight = 900-1100 lbs	50-1100	0-5	760

Table 2-2. (Cont'd)

Author (s)	Soil(s) investigated	Penetrometer(s) utilized	Impact velocity (ft/sec)	Impact angle (°)	Air press. at soil surface (Torr)
Carden (1967)	1. Angular fine sand 2. Subangular coarse sand 3. Rounded aluminum oxide 4. Gravel	Hemisphere. Diameter = 0.164 ft Weight = 0.26-29 lbs	4-12	0	760
Caudle et al. (1967)	1. Loose to dense moist sands 2. Dense cemented sands and gravels 3. Soft estuarine muds 4. Stiff moist to saturated clays 5. Hard dry silty clays 6. Loessial permafrost	Long slender penetrometers.	wide range	0	760
Moore (1967)	Sand	Right circular cylinder tipped with a blunt nose. Also one sphere.	1-21	0	760
Reichmuth (1967)	1. Clay 2. Ottawa sand 3. Subangular well graded sand	1. 60° and 120° included angle wedges. Length = 0.468-1.38 ft Weight = 34-134 lbs			

Table 2-2. (Cont'd)

Author(s)	Soil(s) investigated	Penetrometer(s) utilized	Impact velocity (ft/sec)	Impact angle (°)	Air press. at soil surface (Torr)
Reichmuth (1967) (Cont'd)		2. 1.66-ft-diameter right circular cylinder. Weight = 50-150 lbs 3. 1.66-ft-diameter sphere. Weight = 40-94 lbs	10-40	0	760
Womack and Cox (1967)	1. Clay 2. Ottawa sand 3. Subangular well-graded sand 4. Subangular poorly graded sand 5. Crushed stone	0.096-ft-diameter circular plate. Weight = 5.384 lbs	14-16	0	760
Woodward, Clyde, Sherard, and Associates (1962-1967)	Wide range	Long slender penetrometers tipped with blunt to very sharp noses.	Wide range	0	760
Awoshika and Cox (1968)	1. Ottawa sand 2. Subangular well graded sand	60° apex included angle cone. Length = 1.0 ft Weight = 43-130 lbs	10-23	0	760

Table 2-2. (Cont'd)

Author(s)	Soil(s) investigated	Penetrometer(s) utilized	Impact velocity (ft/sec)	Impact angle (°)	Air press. at soil surface (Torr)
Colp (1968)	1. Bay mud 2. Playa lake 3. Quartz sand 4. Permafrost	Long slender penetrometers tipped with blunt to very sharp noses. Diameter = 0.083-1.5 ft	60-2750	0	760
McCarty and Carden (1968)	Study based entirely on the data obtained by Philco (1966a, 1966b): see above.				
Mitchell et al. (1969)	Silty clay	Spheres. Diameter = 0.05-0.06 ft Weight = 0.005-0.015 lbs	20-84	0-60	760
Thompson et al. (1969)	1. Clay 2. Ottawa sand	0.13-ft-diameter right circular cylinder tipped with: 1. a blunt nose 2. 22.6° apex included angle cone Weight = 3.7-8 lbs	170-360	0	760
Scott (1970)	Seabottom deposits	Several types of box and cylindrical corers.	10-40	0	

Table 2-3. EXPERIMENTAL INVESTIGATIONS.

Author (s)	Principal Conclusions
USAF - WES (1957, 1958)	<ol style="list-style-type: none"> 1. The impact penetrometer can be utilized to determine soil relative cone index (RCI), a parameter used for predicting trafficability. 2. For soils having a given WES cone index, total penetration is a linear function of the impact velocity and decreases with increasing cone index. 3. Penetration caused some softening or remolding of the soil in the immediate vicinity of the penetrometer up to a distance of 1.0 feet below the tip of the penetrometer and 0.5 feet radially from the edge of the penetrometer.
McCarty and Carden (1962)	<ol style="list-style-type: none"> 1. The acceleration-time signature of an impact penetrometer can be characterized by the maximum deceleration, rise time (time to reach the maximum deceleration), total duration time, and the general shape of the curve. 2. A generalized acceleration-time signature would have the following shape:

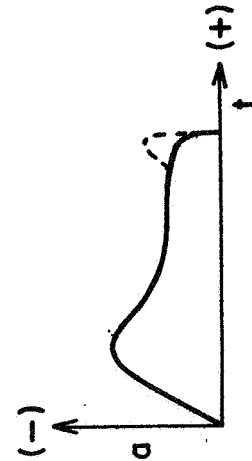


Fig. 2-5. Generalized acceleration-time signature.

Table 2-3. (Cont'd)

Author(s)	Principal Conclusions
McCarty and Carden (1962, Cont'd)	<p>For the time up to the initial peak deceleration, the forces acting on the penetrometer are associated with target inertial forces and elastic compression of target material just ahead of the partially embedded projectile which, upon expansion, forms the crater associated with such material. For the time following this initial peak, the forces acting on the penetrometer are associated with the drag or friction forces on the projectile caused by shear and compressive forces exerted on the target material. The double peak (dashed line) was noticed in loose material.</p> <p>3. High frequency vibrations about the average signature are characteristic of granular material and are due to frictional forces inherent in such target material.</p> <p>4. A penetrometer instrumented with an accelerometer is sufficiently sensitive to indicate layering in nonhomogeneous soil deposits.</p> <p>5. The empirical equations derived from this investigation are:</p>

a) Low impact velocity tests in sand:

$$a_{\text{first peak}} = -1.24 \times 10^{-3} \frac{D^{5/3} V^{5/3}}{m} \quad a_{\text{second peak}} = -23.16 \frac{D^{4/3} V^0}{m^{2/5}}$$

$$P = 2.6 \frac{m^{1/2} V^{2/3}}{D}$$

Table 2-3. (Cont'd)

Author(s)	Principal Conclusions
<p>McCarty and Carden (1962, Cont'd)</p>	<p>b) High impact velocity tests (for both nose shapes):</p> $a_{\max} = -6.8 \times 10^{-2} \frac{V_0^{3/2}}{m} \quad P = 0.005 m V_0^{3/2}$ <p>where for this study:</p> $a - \text{in./sec}^2 \quad D - \text{in}$ $V_0 - \text{in./sec} \quad m - \text{lb sec}^2/\text{in.}$ $P - \text{in}$ <p>6. Crater characteristics may also prove useful. In the low impact velocity tests in sand, the ratio of the blast crater diameter to the projectile diameter was independent of the penetrometer mass but increased with increasing impact velocity and decreasing penetrometer diameter.</p>
<p>Roddy, Rittenhouse and Scott (1962)</p>	<p>1. Impact penetration is a function of the physical characteristics of the soil, not of the mineralogical characteristics except as they may be interrelated.</p> <p>2. Maximum total penetration occurs in tests conducted at 760 Torr with the soil in the loosest state. Minimum penetration occurs in tests conducted at 760 Torr with the soil in the densest state. Total penetration in tests conducted in vacuum for the loosest and densest soil lies between the results of penetration</p>

Table 2-3. (Cont'd)

Author(s)	Principal Conclusions
Roddy, Rittenhouse and Scott (1962) (Cont'd)	<p>tests conducted at 760 Torr for the same state of packing. These observations can be explained in terms of the tendency of a soil to expand or compress during shear and the resultant excess pore air pressures.</p> <ol style="list-style-type: none"> 3. At air pressures greater than $1. \times 10^{-1}$ Torr, all total penetration values approach those for a pressure of 760 Torr. 4. Larger apparent craters were formed in the denser soils, and crater size appeared to increase with decreasing particle size. 5. Splashing action, or ejection, increased with decreasing particle size and was greater in air than vacuum and was greatest in the loosest soils. 6. The density of packing is by far the most dominant factor affecting total penetration. Penetrometer weight and nose shape appeared to be relatively unimportant.
Rowe and Selig (1962)	<ol style="list-style-type: none"> 1. The soil penetration resistance increases with a decrease in air pressure at the soil surface. 2. The development of excess pore air pressure gradients was noticed. When the air pressure was 760 Torr, a mound of dust pushed up around the penetrometer. This did not occur under vacuum conditions.

Table 2-3. (Cont'd)

Author(s)	Principal Conclusions
Vey and Nelson (1965, 1966)	<ol style="list-style-type: none"> 1. The effects of vacuum in fine granular soil will be: a) to eliminate pore air pressure yielding either an increase or decrease in soil penetration resistance depending on the initial soil void ratio, b) to increase c, ϕ, and penetration resistance due to the increased strength of asperity bonding, and c) to increase inertial forces due to an increase in c, ϕ, and the resulting soil stiffness and shear strength causing a larger soil mass to be affected. In coarse granular soil, the effects are similar except that bonds at asperities are less important. 2. The initial rapid rise in the acceleration-time signature is due to forces required to accelerate the soil. Subsequent deceleration of the penetrometer is due to forces required to cause progressive shear failure in the soil. 3. In loosely packed fine granular soil, the total duration time and the total penetration decrease while the maximum deceleration increases with decreasing air pressure as a result of excess pore air pressures.
Hanks and McCarty (1966)	<ol style="list-style-type: none"> 1. The acceleration-time signature can be characterized by the maximum deceleration, the rise time, and the total duration time. 2. An increase in target density yields an increase in the maximum deceleration. 3. Total duration time is only slightly affected by the impact velocity. Effects occur primarily in the low impact velocity region where an increase in impact velocity yields an increase in total duration time.

Table 2-3. (Cont'd)

Author(s)	Principal Conclusions
Hanks and McCarty (1966, Cont'd)	<p>4. The rise time increases with decreasing impact velocity and is independent of penetrometer weight and diameter at high impact velocities.</p> <p>5. The ratio of the explosive crater diameter to the penetrometer diameter increases with increasing impact velocity and decreasing penetrometer diameter and is independent of penetrometer weight.</p> <p>6. The empirical equations derived from this investigation are:</p> $a_{\max} = \frac{K' V_0^n D^2}{m}$ $P = K'' \frac{m^{1/2}}{D} V_0^{2/3}$ <p>where for this study:</p> <p>a - g units P - in V₀ - in/sec D - in. m - lb sec²/in.</p> <p>K', K'', n, n₁, n₂ are constants varying with particle size.</p>
Philco (1966a, 1966b)	<p>1. The maximum deceleration increases with increasing impact velocity, penetrometer diameter, and penetrometer weight and decreases with increasing impact angle.</p> <p>2. The rise time increases as the hardness of the target decreases.</p>

Table 2-3. (Cont'd)

Author (s)	Principal Conclusions
Philco (1966a, 1966b, Cont'd)	<p>3. Up to a certain penetration, the dynamic force required to reach that penetration is greater than the static force and vice versa beyond this penetration.</p>
Schmid (1966)	<p>1. The most important soil properties influencing the penetrometer output are dry density and water content.</p> <p>2. For clay soils with a water content higher than optimum, the acceleration-time signatures are smooth, monotonously increasing then decreasing.</p> <p>3. In sand, gravel, or crushed stone a definite peak soil resistance occurs which drops off rapidly and is followed by another increase followed by a logarithmic decay. This behavior is due to the fact that initially a small number of grains are affected and they become liquefied behaving as a fluid. Upon further penetration, more grains are affected and there is no liquefaction. Thus the signature is stabilized and deceleration decreases beyond this point.</p> <p>4. The energy dissipated in stress waves during the penetration process is negligible.</p>
Thompson (1966)	<p>1. For stability during penetration, a penetrometer length to diameter ratio of at least 7-8 is required.</p> <p>2. A soil nose nearly conical in shape was observed on blunt, hemispherical, and short ogive tipped penetrometers. For long ogive tipped penetrometers, ablation of the penetrometer nose was observed.</p> <p>3. The shape of the penetrometer nose and the angle of impact markedly affects the penetrometer deceleration.</p>

Table 2-3. (Cont'd)

Author (s)	Principal Conclusions
Thompson (1966) (Cont'd)	<ol style="list-style-type: none"> 4. In tests in sand, comminution of the sand grains was observed and in some cases the soil was "hot to touch" following penetration. 5. Radial cracks were noticed on the soil surface following tests in a dry playa lake. 6. The area of paint removed from the penetrometer directly behind the nose increases as the nose length is increased. 7. In many instances soil was observed to stick to the sides of the penetrometer. 8. Total penetration increases as the sharpness of the penetrometer nose increases.
Carden (1967)	<ol style="list-style-type: none"> 1. The acceleration-time signature can be characterized by the maximum deceleration, rise time, total duration time, and the overall shape of the curve. 2. An increase in the static bearing strength of the soil target results in an increase in the peak deceleration and a decrease in both the rise time and the total duration time. 3. The total duration time is only slightly affected by the impact velocity but increases with increasing penetrometer weight. 4. An increase in penetrometer weight yields an increase in the rise time.

Table 2-3. (Cont'd)

Author (s)	Principal Conclusions
Carden (1967) (Cont'd)	<p data-bbox="446 510 479 1553">5. The empirical equations derived from this investigation are:</p> $a_{\max} = -K' \frac{V_0^{n_1}}{m^2}$ $p = K'' m^{\frac{1}{2}} V_0^{2/3}$ <p data-bbox="755 1138 787 1478">where for this study:</p> $m - \text{kg} \quad V_0 - \text{m/sec}$ $a - g \quad p - \text{cm}$ <p data-bbox="917 574 950 1415">K', K'', n_1, n_2 are constants varying with soil type.</p>
Caudle et al. (1967)	<ol style="list-style-type: none"> <li data-bbox="974 244 1006 1553">1. An impact penetrometer can detect layering in a nonhomogeneous soil deposit. <li data-bbox="1031 180 1112 1553">2. For stability during penetration, the penetrometer length to diameter ratio must be greater than 8 to 10. <li data-bbox="1144 148 1226 1553">3. The deceleration of penetrometers impacting soils is on the order of a few hundred g's. <li data-bbox="1258 670 1291 1553">4. The penetration event can be described as follows: <ol style="list-style-type: none"> <li data-bbox="1323 223 1404 1478">a) During initial penetration, a small crater is formed with a minor amount of ejecta.

Table 2-3. (Cont'd)

Author(s)	Principal Conclusions
Caudle et al. (1967, Cont'd)	<p>b) After this initial penetration, a thin zone of soil is sheared and compressed around the penetrometer.</p> <p>c) While velocities are still high, soil is pushed away from the penetrometer with sufficient velocity that the soil and the afterbody barely contact. The soil does, however, rebound and the hole diameter decreases after the penetrometer has passed.</p> <p>d) As the penetrometer slows, the soil "grabs" it resulting in a terminal deceleration peak. For many penetration events, this terminal deceleration peak is the highest value of the entire record.</p> <p>e) After reaching the maximum penetration, the soil-projectile system often oscillates for a cycle or two.</p> <p>5. If a soil deposit is homogeneous, the deceleration should increase with depth as more soil "grabbing" occurs.</p> <p>6. An increase in impact velocity yields an increase in total penetration and deceleration.</p> <p>7. Total penetration and deceleration decrease with increasing penetrometer weight and nose sharpness and with decreasing penetrometer diameter.</p> <p>8. The impact angle is not very significant if kept reasonably small.</p>

Table 2-3. (Cont'd)

Author (s)	Principal Conclusions
Caudle et al. (1967) (Cont'd)	<p>9. The sensitivity of a penetrometer to soil properties is greatest for low weights (can't be too low or decelerations will be excessive), large diameters, moderately sharp noses (can't be too blunt or initial deceleration spike will obscure data), and intermediate impact velocities.</p> <p>10. Some characteristic soil responses include:</p> <ul style="list-style-type: none"> a) Clay — Generally small decelerations. b) Sand — low frequency mild variations about the average signature in uniform sand and relatively large decelerations in dense sand. Nonhomogeneity in sand deposits will be indicated by jumps in the acceleration curve. c) Gravel — will exhibit larger decelerations than sand and also larger variations about the average signature. <p>11. The accuracy of the impact penetrometer in evaluating in situ soil properties is about the same as the standard penetration test.</p>
Moore (1967)	<p>1. The equation derived from this investigation is:</p> $P = K \left(\frac{\rho_p}{\rho_t} \right)^{\frac{1}{2}} \frac{L^{\frac{1}{2}} V_0}{g^{\frac{1}{2}}}, \quad K = \text{constant.}$

Table 2-3. (Cont'd)

Author (s)	Principal Conclusions
Reichmuth (1967)	<ol style="list-style-type: none"> 1. The target density is the most important parameter influencing total penetration. Soil viscosity is important but static soil strength has only a minor effect. 2. Sand shows considerable fluid-like flow (ejecta). In unsaturated sand, considerable ejecta was observed but in saturated sands, little ejecta was observed. 3. Clay behaves more like an elastic material. 4. The shape of the acceleration-time signature is greatly affected by the soil type and the moisture content. The greatest variation occurs between saturated and unsaturated soils. 5. Soil impact forces will increase considerably as the percent solids increases and will increase to a lesser degree as the percent water increases. 6. Either one or two soil force peaks in the force-time curve were noticed. The first force peak is not a reproducible phenomenon. 7. Penetrometer size effects were noticeable, particularly in sand. In clay, an increase in the characteristic length of the penetrometer causes an increase in the measured decelerations and vice versa in sands. 8. A noticeable rise in the ground level due to pore air pressure was observed.

Table 2-3. (Cont'd)

Author(s)	Principal Conclusions
Womack and Cox (1967)	<ol style="list-style-type: none"> 1. Static test results are quite limited as a basis for predicting impact penetration. They seem to correlate best for dry sands but poorly for moist sands. 2. The Coulombic soil shearing resistance was concluded to be the main factor influencing impact penetration although target density was also felt to be quite important. 3. In cohesionless soil, the percent by volume of air and water are very important parameters whereas cohesive soils appear to be insensitive to percent by volume of air and water. 4. Sand exhibits two force peaks in the force-penetration curve and clays only one. 5. The initial force peak, when observed in sands, could not be correlated to other parameters. 6. Possible evidence of air blast in dry sands was observed. 7. For a plate diameter greater than 1.0 feet, equal total penetrations were observed if the ratio $\frac{4m}{\pi D^2}$ was a constant along with all other variables.

Table 2-3. (Cont'd)

Author (s)	Principal Conclusions
Woodward, Clyde, Sherard, and Associates (1962 - 1967)	<p>1. The following impact penetration mechanisms may occur:</p> <ul style="list-style-type: none"> a) Soil compaction. <ul style="list-style-type: none"> i) Occurs in loose sands or inefficiently packed soils. ii) A soil nose consisting of soil at a density greater than the free field density is formed. b) Soil shearing. <ul style="list-style-type: none"> i) Occurs in efficiently packed soils such as dense sands. ii) Impact penetration is accomplished mainly by mobilizing plastic fields and shearing large wedges of soil laterally out of the path of the penetrometer. iii) If soil compaction occurs before soil shearing, only partial development of shear planes will result. c) Combinations of soil compaction and shearing. <p>2. Important in situ soil properties influencing impact penetration are compressibility, dynamic shearing strength, angle of internal friction, and density.</p> <p>3. During penetration, excess pore air pressure dissipates upward along an annular ring around the penetrometer thereby reducing the soil resistance. This phenomenon should be a function of the instantaneous penetrometer velocity. In situ soil properties which may be pertinent to this flow of air are a) soil-air or soil-water drag coefficient, b) viscosity of the fluid entrained around the penetrometer,</p>

Table 2-3. (Cont'd)

Author(s)	Principal Conclusions
Woodward, Clyde, Sherard, and Associates (1962-1967) (Cont'd)	<p>and c) soil particle velocity of a characteristic radial deformation front which propagates away from the penetrometer and creates a "breathing" action around the fast moving penetrometer.</p> <ol style="list-style-type: none"> 4. A smooth acceleration-time signature is characteristic of a fine grained soil and a rough signature is characteristic of a coarse grained soil. 5. Total penetration increases with increasing penetrometer W/A, nose sharpness, and impact velocity. 6. A given soil layer will produce higher decelerations at higher instantaneous penetrometer velocities. 7. In those cases in which terminal oscillation of the penetrometer was noticed, the period of oscillation was longer in soft soils than in hard soils.
Awoshika and Cox (1968)	<ol style="list-style-type: none"> 1. During penetration, some energy is lost to heat, sound, and surface waves. 2. Soil particle comminution occurs in sand and gravel but not in silt and clay. 3. The penetration mechanism is a function of the soil shear strength. 4. Considerable ejecta was observed in dry sand. 5. The maximum deceleration and minimum total duration time occurred in saturated dense sand and vice versa in loose sand. Dry dense sand exhibited intermediate values.

Table 2-3. (Cont'd)

Author (s)	Principal Conclusions
Colp (1968)	<ol style="list-style-type: none"> 1. Radial cracks were observed on the soil surface. 2. Upon excavation, soil drawdown, a soil nose, and horizontal bedding distortions were observed. 3. The amount of soil-afterbody contact increases with increasing soil stiffness.
McCarty and Carden (1968)	<ol style="list-style-type: none"> 1. The acceleration-time signature can be characterized by the maximum deceleration, the rise time, the total duration time, and the overall shape of the curve. 2. The general shape of the signature is a sharp peak followed by a long duration of low-level decelerations. The sharp peak is due to the rapid compression of the target ahead of the partially embedded penetrometer which, upon expansion, is responsible for the crater forming ejecta. The low-level decelerations are attributed to drag forces. 3. An increase in the target static bearing strength yields an increase in the maximum deceleration and a decrease in the rise time and total duration time. 4. The total penetration increases with an increase in the impact velocity and the penetrometer weight and with a decrease in penetrometer diameter. For the larger and heavier penetrometers, the effect of the impact velocity becomes negligible after a penetration of about one penetrometer diameter.

Table 2-3. (Cont'd)

Author (s)	Principal Conclusions
McCarty and Carden (1968) (Cont'd)	<p>5. The effect of increasing the impact angle is to decrease the maximum deceleration and to increase the rise time and total duration time.</p> <p>6. The effect of vacuum, when noticeable, is to decrease the total penetration, rise time, and total duration time and to increase the maximum deceleration. The effect of air pressure is a function of soil grain size.</p> <p>7. An empirical equation derived from this investigation is:</p> $a_{\max} = - \frac{K V_0^2 D^2}{n_1 m}$ <p>where for this study:</p> <p>m - kg a - g units</p> <p>V_0 - m /sec K, n_1, n_2 are constants varying with soil type.</p> <p>D - cm</p>
Mitchell et al. (1969)	<p>1. The empirical equation derived from this investigation is:</p> $P = K n Q^{\frac{1}{2}} V_0 + P_0$ <p>V_0 - impact velocity component normal to the soil surface in this case</p> <p>K - soil constant</p>

Table 2-3. (Cont'd)

Author(s)	Principal Conclusions
Mitchell et al. (1969) (Cont'd)	<ol style="list-style-type: none"> 1. The effect of increasing the impact angle (from 0° to 60°) is to cause the total penetration to be less than that predicted by the above equation. However, the error is negligible.
Thompson et al. (1969)	<ol style="list-style-type: none"> 1. Radial cracks on the surface of soil targets having a smooth, relatively dry surface were observed. 2. The soil in the soil nose is densified relative to free field conditions. 3. Soil drawdown was observed.
Scott (1970)	<ol style="list-style-type: none"> 1. A lack of sensitivity of the penetrometer to the instant of soil contact can be due to a) instrumentation sensitivity, b) excessive penetrometer weight, c) too small a penetrometer diameter, and c) softness of the soil surface. 2. For a successful impact test, vertical stability of the penetrometer during penetration is required.

Table 2-4. Statistical studies.

Author (s)	Soil(s) investigated	Penetrometer(s) utilized	Impact velocity (ft/sec)	Impact angle* (°)	Air press. at soil surface (Torr)
Woodward, Clyde, Sherard, and Associates (1962-1967)	Wide range	Long, slender penetrometers tipped with blunt to very sharp noses.	Wide range	0	760
Mitchell et al. (1969)	1. Dry, silty clay 2. Layered (soft over stiff) silty clay 3. Soft saturated clay 4. Soft bay mud 5. Air dried silty clay 6. Ground pumice 7. Silt to gravel-sized aluminum oxide 8. Loose to medium dense, moist sand 9. Angular fine sand 10. Dense fine sand 11. Dry No. 000 sand 12. Subangular coarse sand	1. 0.37-ft-diameter right-circular cylinder tipped with a blunt nose Weight = 223 lbs 2. Right-circular cylinder tipped with a tangent ogive nose CRH = 2.2-9.5 Diameter = 0.26-0.75 ft Weight = 220-1100 lbs 3. Spheres Diameter = 0.05-0.33 ft Weight = 0.005-28.6 lbs 4. Right-circular cylinder tipped with a hemispherical nose Diameter = 0.08-0.25 ft Weight = 0.97-9.87 lbs	4-198	0-60	760

* The acute angle between the normal to the soil surface and the velocity vector of the penetrometer.

Table 2-4. (Cont'd)

Author(s)	Soil(s) investigated	Penetrometer(s) utilized	Impact velocity (ft/sec)	Impact angle (°)	Air press. at soil surface (Torr)
Young (1969)	1. Stiff, moist clay 2. Dry, hard, dense clayey silt and silty clay 3. Bay mud 4. Varved, soft, plastic clay 5. Very stiff silty clay 6. Soft silty clay 7. Dense silty, clayey sand 8. Dry, well cemented, very dense silty sand 9. Moist, loose to medium sand	1. 0.37-ft-diameter right-circular cylinder tipped with a flat nose Weight = 223 lbs 2. Right circular cylinders tipped with a tangent ogive nose CRH = 2.2-12.5 Diameter = 0.26-0.75 ft Weight = 220-5720 lbs 3. 0.7-ft-diameter right-circular cylinder tipped with a conical nose L/D (nose) = 2-3 Weight = 300 lbs 4. 0.7-ft-diameter right-circular cylinder tipped with a biconic nose Weight = 300 lbs	110-1065	0	760

Table 2-5. Results of statistical studies.

Author (s)	Equation(s) evaluated	Significant conclusions
Woodward, Clyde, Sherard, and Associates (1962-1967)	<p>1. $P = \frac{1}{\alpha} \ln(1 + \beta V_o)$</p> <p>2. $P = \frac{1}{d} \ln(1 + bV_o^2)$</p> <p>where for this study:</p> <p>$V_o = \text{fps}$ $\rho_t = \text{lb sec}^2/\text{ft}^4$</p> <p>$P = \text{ft}$ $\alpha, \beta, d, \text{ and } b = \text{constants}$</p> <p>$g = \text{ft/sec}^2$</p> <p>$Q = \text{psi}$ $A = \text{sq in}$</p>	<p>1. The constants α and β of Equation(1) (reported by Resal, 1895) and d and b of Equation(2) (reported by Poncelet, 1829) are functions of in situ soil properties and the penetrometer characteristics. The following relationships were found:</p> $\alpha = \frac{(80 + N) \rho_t g C}{625,000 \ell Q}$ $\beta = 1.26A \times 10^{-6}$ $d = \frac{(85 + N) (1.29 - 3.5V_o \times 10^{-4}) \rho_t g C}{14,000 \ell Q}$ $b = 4.31A \times 10^{-7}$ $\ell = 0.042(\text{CRH}) + 0.942$ $C = 1 + 1.5 \operatorname{sech} \left(\frac{N}{10} \right) - 2.5 \exp \left(- \frac{N^2}{52} \right)$
Mitchell et al. (1969)	<p>1. $P = K_n Q^{\frac{1}{2}} V_o + P_o$</p> <p>2. $P = 0.53 \operatorname{Sn} Q^{\frac{1}{2}} \ln(1 + 2 \times 10^{-5} V_o^2)$</p> <p>3. $P = K_1 \operatorname{Sn} Q^{\frac{1}{2}} \ln(1 + K_2 V_o^2)$</p>	<p>1. Of Equation(2) (reported by Young, 1969), Equation(4), and Equation(6) (the latter two reported by Woodward, Clyde, Sherard and Associates, 1962-1967), Equation(2) best fits the experimental data. Equations(4) and (6) both underestimate total penetration.</p>

Table 2-5. (Cont'd)

Author (s)	Equation(s) evaluated	Significant conclusions
Mitchell et al. (Cont'd)	<p>4. $P = \frac{1}{\alpha} \ln(1 + \beta V_o)$</p> <p>$\alpha = \frac{(80 + N) \rho_t g C}{625,000 \ell Q}$</p> <p>$\beta = 1.26A \times 10^{-6}$</p> <p>$\ell = 0.042(CRH) + 0.942$</p> <p>$C = 1 + 1.5 \operatorname{sech}\left(\frac{N}{10}\right) - 2.5 \exp\left(-\frac{N^2}{52}\right)$</p> <p>5. $P = K_3 \operatorname{Sn} Q \ln\left(1 + K_4 A V_o\right)$</p> <p>6. $P = \frac{1}{d} \ln(1 + bV_o^2)$</p> <p>$d = \frac{(85 + N)(1.29 - 3.5V_o \times 10^{-4}) \rho_t g C}{14,400 \ell Q}$</p> <p>$b = 0.431A \times 10^{-6}$</p> <p>7. $P = K_5 \operatorname{Sn} Q \ln\left(1 + K_6 A V_o^2\right) / \left(1 - K_7 V_o\right)$</p> <p>where for this study:</p> <p>$P, P_o = \text{ft} \quad Q = \text{psi} \quad A = \text{sq in}$ $V_o = \text{fps} \quad \rho_t = \text{lb sec}^2/\text{ft}^4$ $g = \text{ft/sec}^2$ $K_1, K_2, K_3, K_4, K_5, K_6, K_7 = \text{constants.}$</p>	<p>2. Of Equations (3), (5), and (7), Equation (3) best fits the experimental data and Equation (7) worst fits the experimental data.</p> <p>3. Of Equations (1) through (3), Equation (1) best fits the experimental data and is therefore the equation favored by this study. A major drawback of Equations (2) and (3) is that the soil constant, S, in these equations appears to be extremely sensitive to impact velocity.</p> <p>4. Some factors not evaluated in this study which may influence impact penetration are:</p> <p>a) Although K in Equation (1) is primarily a soil constant, it will also be a function of the air pressure at the soil surface.</p> <p>b) The effect of gravity is unknown.</p> <p>c) The effect of nonhomogeneity in the soil deposit is not known.</p> <p>5. Equation (1) applies to cases in which the impact angle is not zero if V_o is taken as the component of the impact velocity normal to the soil surface.</p>

Table 2-5. (Cont'd)

Author (s)	Equation(s) evaluated	Significant conclusions
Young (1969)	<p>1. $P = 0.53 \text{ Sn}(W/A)^{\frac{1}{2}} \ln(1 + 2 \times 10^{-5} V_o^2)$ for $V_o < 200 \text{ fps}$</p> <p>2. $P = 0.0031 \text{ Sn} \left(\frac{W}{A} \right)^{\frac{1}{2}} (V_o - 100)$ for $V_o \geq 200 \text{ fps}$</p> <p>3. $P = W/A K \log_{10} \left(1 + \frac{V_o^2}{215,000} \right)$ where for this study: $P = \text{ft}$ $W = \text{lbs}$ $A = \text{sq in}$ $V_o = \text{fps}$ $K = \text{constant}.$</p>	<p>1. Equations (1) and (2) best fit the experimental data in the two specified velocity ranges. Equation (3) (which is the equation reported by Petry, 1910, see THEORETICAL INVESTIGATIONS) proved considerably less accurate.</p> <p>2. Total penetration must be at least 3 penetrometer body diameters plus the nose length before entrance effects can be neglected and the validity of these equations assured.</p>

QUALITATIVE STATE OF THE ART

A considerable amount of qualitative information on the impact penetration problem has resulted from the numerous experimental studies presented in the Literature Review. The effect of various independent variables on penetrometer output and soil-penetrometer interaction is summarized below.

Effect of Penetrometer Characteristics

1. *Weight*

An increase in weight yields an increase in total penetration, an increase in rise time and total duration time, and a decrease in measured decelerations.

2. *Diameter*

An increase in diameter yields a decrease in total penetration, a decrease in rise time and total duration time, and an increase in measured decelerations.

3. *Nose Sharpness*

- (a) An increase in nose sharpness yields an increase in total penetration and an apparent increase in soil-penetrometer contact area and pressure.
- (b) The occurrence of an acceleration-time peak is less likely with sharper noses.
- (c) A soil nose forms more frequently on blunt tipped penetrometers.

4. *General*

The sensitivity to in situ soil properties is greatest for low weight, large diameter, and moderately sharp nosed penetrometers.

Pre-Impact Flight Parameters

1. *Penetrometer Velocity*

- (a) An increase in impact velocity yields an increase in total penetration, an increase in measured decelerations, and a decrease in rise time and total duration time.

- (b) A given soil layer will produce higher measured decelerations for higher instantaneous velocities.

2. *Impact Angle*

- (a) An increase in the impact angle yields a decrease in total penetration, a decrease in measured decelerations, and an increase in rise time and total duration time.
- (b) The impact angle has a considerable effect on the existence and magnitude of an acceleration-time peak.

Effect of Soil Parameters

1. *Soil Type*

- (a) Clay
 - i. Smooth acceleration-time signature.
 - ii. Low measured decelerations.
- (b) Silt
 - i. Relatively smooth acceleration-time signature.
- (c) Sand
 - i. Rough acceleration-time signature consisting of high frequency variations about the average signature and "jumps" in the signature.
 - ii. Air blast is frequently observed in dry sands.
 - iii. Sand is comminuted during penetration.
- (d) Gravel
 - i. Larger measured decelerations than in sand.
 - ii. Rougher acceleration-time signature than sand.

2. *Density*

An increase in soil density yields an increase in measured decelerations, a decrease in total penetration, and a decrease in rise time and total duration time.

3. *Degree of Saturation*

Impact forces will increase considerably as the percent by weight of solids increases and will increase to a lesser extent as the percent by weight of water increases.

4. *Particle Specific Gravity*

An increase in G_s yields an increase in the inertia component of the soil resistance.

5. *WES Cone Index*

An increase in the WES Cone Index yields a decrease in total penetration.

Effect of Air Pressure

1. *Possible Effects*

- (a) A change in the excess pore air pressures depending on the volume change tendencies of the soil mass.
- (b) A change in the nature of grain contacts.
- (c) A change in soil inertial resistance due to a change in both the nature of grain contacts and the resulting soil mass affected.

(The actual effect will depend on soil particle grain size, shape and mineralogy and the magnitude of the air pressure.)

2. *Effects on Certain Soil Types*

(a) Gravel

- i. If the grain size is sufficiently large and the rate of penetration sufficiently small, the air pressure may have little effect.

(b) Sand

- i. The effect on the nature of grain contacts and soil inertial resistance is relatively small.
- ii. If the excess pore air pressures tend to be negative at 760 Torr, total penetration, rise time, total duration time, and the amount of ejecta will be greater at lower air pressures. Measured decelerations will be less.

- iii. The reverse will be true if the excess pore air pressures tend to be positive at 760 Torr.

(c) Silt

- i. The conclusions pertaining to the excess pore air pressure will be the same as those for sands.
- ii. The effect on the nature of grain contacts and soil inertial resistance may be significant particularly at very low air pressures (high vacuums).

Although considerable qualitative information is available on this problem, there does exist a lack of understanding of the soil deformation pattern developed during penetration. Also, it is apparent that the value of the impact penetration test is dependent on the development of a quantitative understanding for the problem.

THEORETICAL APPROACH

In order to become a useful technique for determining in situ soil properties, analytical expressions relating independent and dependent variables of the impact penetration problem must be developed. These expressions might be developed by following either a theoretical or an empirical approach. The feasibility of solving the impact problem theoretically was examined first because analytical expressions derived in this way would:

1. Provide direct correlation to the desired soil properties,
2. Permit extrapolation to conditions not yet encountered experimentally,
3. Yield a more basic understanding of soil penetrometer interaction, and
4. Eliminate much costly testing.

This feasibility study was initiated by reviewing the existing theoretical solutions.

Existing Theoretical Solutions

Several of the existing theoretical solutions to the impact penetration problem are quite similar and will be grouped together in this discussion.

1. The equations reported by Robins (1742), Euler (1745), Poncelet (1829), Resal (1895), Petry (1910), and Schmid (1969) are all derived from Newton's Second Law of Motion and an assumption concerning the functional relationship between the soil resistance and the instantaneous penetrometer velocity. The accuracy of the resultant equations depends entirely on the accuracy of the functional relationship assumed. In a study designed to develop a relationship between the constants appearing in these equations and in situ soil properties, an inaccurate functional relationship will yield an illogical and complex variation in the constant-soil property relationship as the values of the other independent variables are changed. Partially as a result of this fact, relationships between the equation constants and in situ soil properties are not well understood. The identical form of the expressions for total penetration reported by Poncelet-Petry and developed by Young (1969) from extensive test results might indicate that the Poncelet-Petry assumptions are the most accurate.
2. Scott (1962) reported a similar type of solution except that
 - (a) the soil penetration resistance is assumed to be some function of penetration instead of instantaneous velocity, and
 - (b) through a simple model, the weight of the soil moving with the penetrometer is included.
 The critical comments mentioned above also apply to this solution.
3. Several solutions have been reported (McCarty and Carden, 1962; and Schmid, 1966, 1969) in which soil is assumed to be either a perfectly elastic, plastic, or viscous material. Although there may exist a few special cases of each type, soil generally cannot be represented by such simple models. Impact penetration of lunar soil or a terrestrial lunar soil simulant is probably not one of those special cases.

4. Moore (1967) has developed a solution based on the principle of the Conservation of Energy and several assumptions. The statistical study conducted by Mitchell et al. (1969) in which several theoretical solutions were evaluated concluded that the best equation for total penetration is of a form quite similar to Moore's.
5. The solutions reported by Scott (1962) and Shipley (1967) are based on the static bearing capacity theory of soils modified to include inertial soil resistance. This inertial soil resistance is determined by assuming the velocity field within the soil mass. The accuracy of solutions derived in this way depends primarily on the accuracy of the assumed velocity field. Although existing experimental information on the actual velocity field occurring in soils during impact penetration is quite meager, these studies indicate that the "general shear" velocity field usually assumed is valid in only limited cases. Also, it appears that the actual velocity field is a function of penetration.
6. Schmid (1966) and Tsai (1967) have derived solutions in which soil is assumed to be represented by rheological models consisting of springs and dashpots. To determine penetration as a function of time, a functional relationship for the soil resistance as a function of time must be assumed. In general, the soil resistance versus time plot:
 - (a) Assumes a fixed shape only within limited ranges of the independent variables, and
 - (b) Is a complex curve which would be difficult to represent mathematically.

It is quite possible that this solution may be valid for special cases. Impact penetration of lunar soil or a terrestrial lunar soil simulant is probably not one of those cases.

7. Thompson (1966) has developed a set of partial differential equations which govern the impact penetration problem. This study is one of the most rigorous existing theoretical approaches to this problem. These equations cannot be solved in closed form and it appears that they are too highly nonlinear to be solved numerically.

Another Theoretical Approach Evaluated

In addition to existing theoretical solutions, the feasibility of solving the problem by employing the basic dynamic, kinematic, constitutive, and conservation equations that govern the behavior of materials was examined. These basic equations were written in differential form and combined to yield a set of partial differential equations governing the impact penetration problem. A review of the state of the art of dynamic constitutive equations for soils was conducted in conjunction with this phase of the feasibility study. Then, several numerical techniques for solving problems of this type including the Finite Element Method, the Particle in Cell Code, and the Hemp Code were reviewed. This type of theoretical approach to the impact penetration problem was terminated because it appeared to be impractical at the present time for the following reasons:

1. Applicable soil constitutive relationships are not available, and their determination would involve a major undertaking, and
2. The available numerical solution methods are not sufficiently general to analyze soil behavior in this problem.

Conclusions

We feel that an attempt to develop a theoretical solution to the impact penetration problem is not justified at this time. Certainly one or more of the existing theoretical solutions to the problem may be valid under certain conditions. This is evidenced by the similarities between a few of these solutions (Moore, 1967; Poncelet, 1829; Petry, 1910) and equations developed statistically from experimental data. Unfortunately, the inadequacies in existing test data discussed in the following section inhibit the determination of whether impact penetration of lunar soil is one of these conditions. Neither does the test data provide a basis for the derivation of new theoretical solutions which may better describe the impact penetration of lunar soil. Therefore, before additional theoretical investigations are pursued, a special test program should be conducted.

EMPIRICAL APPROACH

The desired analytical expressions relating the dependent and independent variables of the impact penetration problem can be developed by following an empirical approach. In fact, several analytical expressions developed from terrestrial experimental test data have been reported in the literature. Before designing the experimental program required to develop empirical analytical expressions for the impact penetration of lunar soil, the relative and absolute merits of existing expressions and the factors limiting their extrapolation to the lunar environment were examined.

Existing Empirical Analytical Expressions

The dependent variables that have been considered in previous empirical investigations are the total penetration, the maximum deceleration experienced by the penetrometer, and the rise time (time to reach the maximum deceleration). Relationships derived for the latter two variables are not discussed in this section because their derivations have been based on only limited test results. The existing empirical expressions relating total penetration to the independent variables of this problem are summarized below.

1. McCarty and Carden (1962):

$$P = \frac{K'm^{1/2}V_0^{2/3}}{D} \quad (\text{low velocity})$$

$$P = K''mV_0^{3/2} \quad (\text{high velocity})$$

$K', K'' = \text{constants.}$

2. Woodward, Clyde, Sherard, and Associates (1962 - 1967):

$$P = \frac{1}{\alpha} \ln(1 + \beta V_0) \quad \text{or} \quad P = \frac{1}{d} \ln(1 + bV_0^2)$$

$\alpha, \beta, d, b = \text{constants.}$

3. Mitchell et al. (1969):

$$P = K \rho Q^{1/2} V_0 + P_0 \text{ for } V_0 \leq 200 \text{ fps}$$

$$K = \text{constant}$$

4. Young (1969):

$$P = 0.53 \rho Q^{1/2} \ln(1 + 2. \times 10^{-5} V_0^2) \text{ for } V_0 < 200 \text{ fps}$$

$$P = 0.0031 \rho Q^{1/2} (V_0 - 100) \text{ for } V_0 \geq 200 \text{ fps}$$

An attempt to evaluate both the relative and absolute merits of these expressions utilizing existing experimental test data proved generally inconclusive due to the following inadequacies in the test data.

1. Each experimental program utilized penetrometers of different dimensions and frequently even different shapes making interpretation and interrelation of the available test data difficult. Often it was impossible to determine whether the equation was in error because of the manner in which the penetrometer shape and dimensions or the other independent variables were handled.
2. Tests in which the in situ soil properties were well controlled have usually been limited to very low impact velocities (10 to 60 fps). In no study has the penetration at zero impact velocity been determined. It was found that all of the above expressions could be made to fit most of these test results reasonably well. In most cases, at least two additional points — one at a high impact velocity and one at zero impact velocity — would have been required to evaluate these expressions.
3. In very few test programs were the soil properties varied over a sufficiently wide range to accurately identify their effect on total penetration.

An additional well-planned experimental program will be required before conclusive statements concerning the relative and absolute merits of the above expressions can be made. In general, the accuracy of the above expressions when determined from the same test data used to develop the expressions is on the order of $\pm 20\%$. Therefore, the impact penetration test has the potential to yield approximately the same accuracy as the other common techniques for determining the in situ soil properties mentioned in the Introduction.

Extrapolation to the Lunar Environment

The factors that may restrict extrapolation of terrestrial experimental test data and resultant empirical expressions to the lunar environment are:

1. The influence of the air pressure at the soil surface has been studied only under limited conditions (e.g., very small, light penetrometers impacting at low velocities).
2. The effect of the gravitational field has not been experimentally evaluated.

Existing test results indicate that the air pressure at the soil surface may have a very important effect on the output of the penetrometer. The probable effect of the reduced gravitational field can only be estimated qualitatively at present. Its probable effect will be to increase the total penetration and the characteristic times of the acceleration-time signature while decreasing the measured accelerations. The effect of the air pressure at the soil surface can and should be evaluated experimentally, but the effect of the gravitational field might best be estimated theoretically.

Conclusions

The accuracy achieved by previous empirical investigations supports the further development of the impact penetration test as a means of determining in situ soil properties. Additional experimental testing will be required to fill gaps in existing terrestrial test results and to provide a basis for the extrapolation of these test results to the lunar environment.

EXPERIMENTAL PROGRAM

Before pursuing further theoretical or empirical investigations, an experimental program should be conducted which will:

1. Yield an improved understanding of the deformation pattern **within the soil** mass during penetration.
2. Provide test data to evaluate existing theoretical and empirical analytical expressions relating the dependent and independent variables of the impact penetration problem.
3. Form a basis from which new theoretical and empirical analytical expressions can be developed if existing expressions prove inadequate.
4. Provide test data on which extrapolation of terrestrial test results to the lunar environment can be based.

The following factors were considered in designing an experimental program to meet these goals.

Dependent Variables

In a laboratory investigation, a wide variety of dependent variables could be measured. Because the acceleration-time signature of the penetrometer is expected to be the eventual penetrometer output, it will be used in this program. This signature will be obtained by mounting a crystal accelerometer on the penetrometer. In addition, the deflection of the soil surface, the amount and distribution of ejecta, and the deformation pattern within the soil target will be considered. A combination of photographic and direct measurement techniques will be employed to evaluate these dependent variables.

Penetrometer

The selection of the penetrometer to be used in this investigation was based on a consideration of the following:

1. The ease with which the penetrometer can be adapted to anticipated environments,
2. The sensitivity of the penetrometer to desired soil properties at the desired depths,
3. The ability to analyze penetrometer output analytically based on present day knowledge in the field of soil mechanics,

4. Similarity to other soil mechanics problems such as pile driving and impact loaded footings,
5. Repeatability of penetrometer output including desired insensitivity to extraneous conditions, and
6. The number of basic dimensions required to characterize the penetrometer.

The penetrometer selected for this experiment program is a cone-tipped right-circular cylinder having the following dimensions.

Overall Length = 1.5 feet

L/D of Nose ≈ 2

Diameter = $1\frac{1}{2}$ in.

Weight ≈ 8 lbs

Material = Steel

Soils

The criteria established for selecting the soil to be tested in this program were:

1. The soil should simulate lunar soil as much as possible.
2. The soil composition should not undergo major changes over the range in environmental conditions to be evaluated.
3. The soil should not require excessive amounts of time to prepare for testing.

We believe that a dry granular soil, such as a fine sand, would best satisfy these criteria, and the lunar soil simulant developed by Mitchell et al. (1970a) will certainly be considered.

Independent Variables

The independent variables controlling impact penetration include penetrometer pre-impact flight variables, environmental variables, and soil property variables.

1. Penetrometer pre-impact flight variables

The purpose of this study and the state of the art of interpreting impact penetrometer data does not justify the evaluation of the effects of impact angle, rotational velocity, etc., at this time. Instead, the penetrometer will be constrained to motion in which its axis of revolution and velocity vector are coincident and normal to the soil surface. Also, the penetrometer will have zero rotational velocity about its axis of revolution. The remaining pre-impact flight variable is V_0 , impact velocity. The range in impact velocity to be investigated is 0 - 200 fps.

2. *Environmental variables*

It is impractical at this time to attempt to evaluate experimentally the effects of the gravitational field and temperature on impact penetration. Also, the only soil pore fluid to be studied will be "air". The remaining environmental variable is p , air pressure at the soil surface. The range in air pressure at the soil surface to be investigated is 1×10^{-1} to 760 Torr.

3. *Soil property variables*

For one particular dry granular soil, the only soil property that can be varied is e , void ratio. The range in void ratio to be investigated is $e_{\text{maximum}} - e_{\text{minimum}}$. For any given void ratio, two soils may differ in the following properties.

- G_s - Specific gravity of the solids
- D_{10} - Particle diameter below which 10% by weight of the particles are finer
- D_{60} - Particle diameter below which 60% by weight of the particles are finer
- q - Shape of gradation curve
- R_0 - Roundness of particles
- S_0 - Sphericity of particles
- M - Mineralogy.

The range in the later variables to be studied will be as wide as possible within reasonable time and cost constraints. The number of tests to be conducted will depend on the variability of the dependent variables over the anticipated range of independent variables to be investigated. At present, we anticipate that approximately fifty tests will be needed.

Velocity Generating and Measuring Devices

Several possible velocity generating devices were considered for this program. For reasons of safety and reproducibility, a compressed air gun was finally selected. A simplified schematic diagram of the air gun to be fabricated for this program is shown in Figure 2-6 and the operation of the gun is outlined below.

1. The penetrometer is placed in the position shown in the diagram.
2. The solenoid valve is activated to close the line connecting the pressure vessel to the top of the penetrometer.
3. The air pressure is built up in the pressure vessel to the desired test pressure.

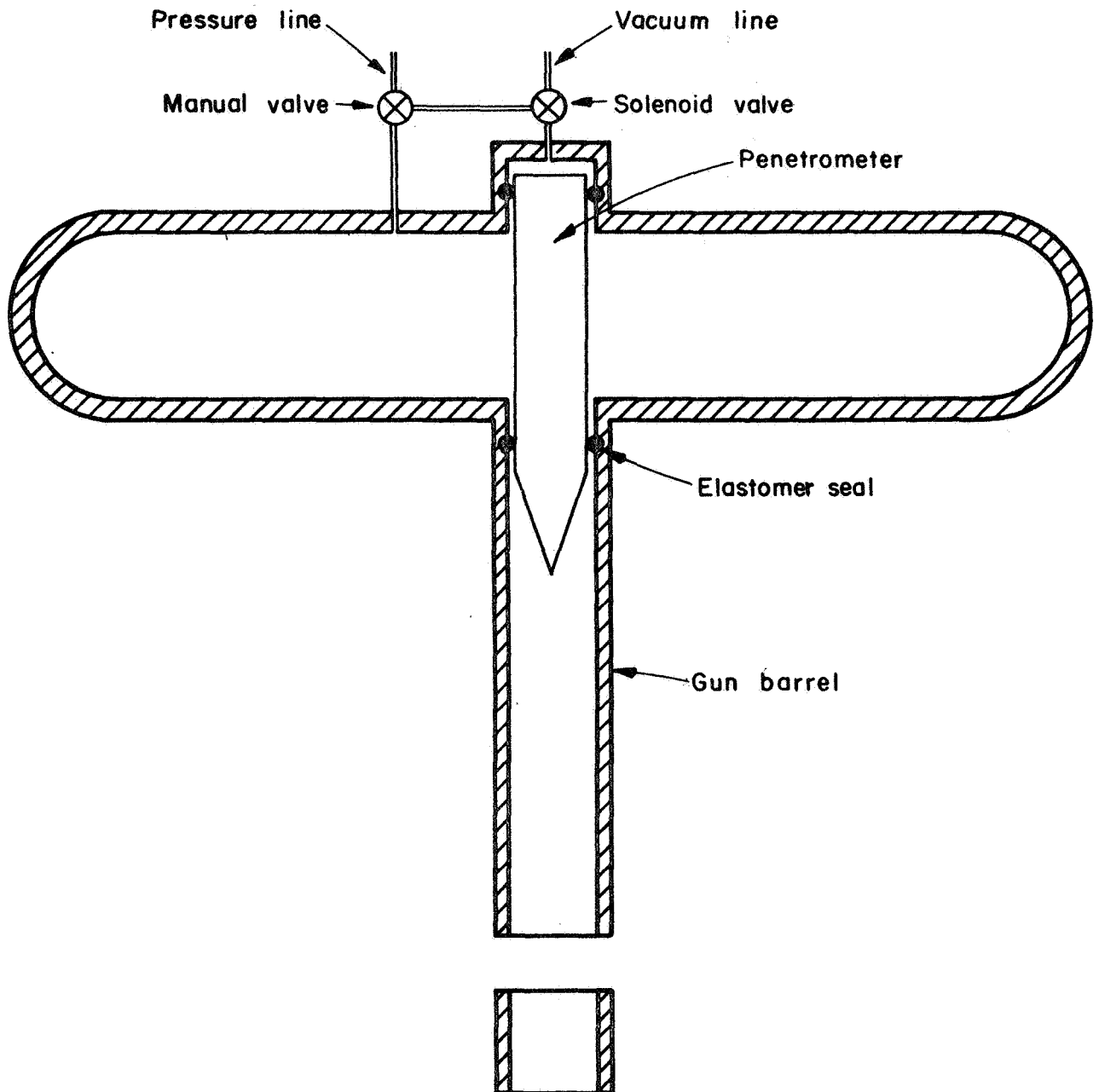


Fig. 2-6. Schematic diagram for compressed air gun.

4. The solenoid valve is activated to open the line connecting the pressure vessel to the top of the penetrometer, thus firing the penetrometer.

The velocity of the penetrometer will be determined in a velocity trap consisting of a pair of photocells connected to an oscilloscope equipped with a camera.

Vacuum Chamber

The design and construction of a vacuum chamber in which to conduct tests of this sort would involve a major undertaking. However, such a vacuum chamber has already been built and is in use at the Ames' Research Center. Mr. D. V. Gault of Ames has kindly offered the use of this chamber if our testing can be performed without disrupting studies presently being conducted in the chamber. We appreciate this offer and intend to make every effort to attempt to design a program acceptable to Mr. Gault.

Conclusion

A conceptual design of an experimental program necessary to advance the state of the art of impact penetration has been completed. The fabrication of the equipment required to conduct this experimental program is now in progress.

CONCLUSIONS

The use of the impact penetration test as a technique for determining in situ soil properties is promising. Indications are that the accuracy to which soil properties can be determined by this type of test is approximately the same as that exhibited by other common tests mentioned in the Introduction. At the same time, the impact penetration test possesses several advantages when compared to these other tests particularly if the soil deposit to be evaluated is located in a remote area such as on an extraterrestrial body.

The existing quantitative expressions relating the dependent and independent variables of the impact penetration problem need further study. This is particularly evident when the effect of differences

between terrestrial and extraterrestrial environments are considered. Unfortunately, inadequacies in existing experimental test data prohibit additional justifiable theoretical or empirical quantitative investigations.

Therefore, an experimental program has been designed to provide a basis for additional theoretical and/or empirical quantitative investigations. A conceptual design of this experimental program has been completed.

SYMBOLS

A	frontal area of the penetrometer
a	acceleration
c	soil cohesion
CRH	caliber radius head of ogive noses
D	diameter of penetrometer
D ₁₀	particle diameter below which 10% by weight of the particles are finer
D ₆₀	particle diameter below which 60% by weight of the particles are finer
e	soil void ratio
F	vertical soil resistance
g	acceleration of gravity
G _s	specific gravity of soil solids
K ₀	coefficient of earth pressure at rest
L	characteristic length of penetrometer
M	mineralogy of soil particles
m	penetrometer mass
N	Standard Penetration Test "blow count"
N _c , N _γ , N _q	soil bearing capacity factors
n	penetrometer nose shape and dimensions constant
P	total impact penetration
P ₀	total penetration at zero impact velocity
p	air pressure at the soil surface
Q	penetrometer frontal loading (= W/A)
q	type of soil gradation curve
r	penetrometer radius
R ₀	soil particle roundness
S	soil constant
S ₀	soil particle sphericity
t	time
t _m	total duration time of the penetration process
t _r	rise time (time to reach maximum deceleration)
V	instantaneous penetrometer velocity
V ₀	impact velocity
W	penetrometer weight

z	instantaneous depth of penetration
ϕ	soil angle of internal friction
ρ_p	penetrometer mass density
ρ_t	soil target mass density
σ_1, σ_3	major and minor principle stresses in the soil target

REFERENCES

- Awoshika, A., and Cox, W. R. (1968), "An Application of Similitude to Model Design of Soil-Projectile System," University of Texas, Austin, Texas, NASA CR-1210, November 1968.
- *Benson, F. J. et al. (1968), "The Conceptual Design of a Terradynamics Laboratory," Sandia Corporation, SC-CR-68-3754, June 1968.
- Carden, H. D. (1967), "Experimental Study of the Application of the Penetrometer Technique to the Lunar Surveying Staff Concept," Langley Research Center, Langley Station, Hampton, Virginia, NASA TN D-3937, May 1967.
- Caudle, W. N. et al. (1967), "The Feasibility of Rapid Soil Investigations Using High-Speed, Earth Penetrating Projectiles," International Symposium on Wave Propagation and Dynamic Properties of Earth Materials, Albuquerque, New Mexico, August 1967.
- *Cetiner, A., and Reeves, G. N. (1968), "Numerical Solution for Projectile Penetration into Particulate Media," Sandia Corporation, SC-CR-68-3752, September 1968.
- Clark, L. V., and McCarty, J. L. (1963), "The Effect of Vacuum on the Penetration Characteristics of Projectiles into Fine Particles," Langley Research Center, Langley Station, Hampton, Virginia, NASA TN D-1519, January 1963.
- *Colp, J. L. (1965), "An Experimental Investigation of the Continuous Penetration of a Blunt Body into a Simulated Cohesionless Soil," Sandia Corporation, SC-RR-65-260, December 1965.
- Colp, J. L. (1968), "Terradynamics: A Study of Projectile Penetration of Natural Earth Materials," Sandia Corporation, SC-DR-68-215.
- *Colp, J. L. et al. (1968), "A Trailing-Camera Technique for Studying Projectile Penetration into Earth Materials," Sandia Corporation, SC-DR-67-3029, March 1968.
- *Colp, J. L. (1969), "The Use of Instrumented Penetrometers to Determine Subsoil Conditions at Inaccessible Sites," Sandia Corporation, SC-DR-69-573, October 1969.

* References with asterisks are not mentioned in the text, but are included as background material.

Euler, L. (1745), "Neue Grundsätze der Artillerie," Berlin, reprinted as Vol. 14, Series II of "Euler's Opera Omnia," Teubner, Berlin, 1922.

Hanks, B. R. and McCarty, J. L. (1966), "Investigation of the Use of Penetrometers to Determine the Capability of Dust Materials to Support Bearing Loads," Langley Research Center, Langley Station, Hampton, Virginia, NASA TN D-3200, January 1966.

McCarty, J. L. and Carden, H. D. (1962), "Impact Characteristics of Various Materials Obtained by an Acceleration-Time-History Technique Applicable to Evaluating Remote Targets," Langley Research Center, Langley Station, Hampton, Virginia, NASA TN D-1269, June 1962.

*McCarty, J. L., Beswick, A. G., and Brooks, G. W. (1964), "Application of Penetrometers to the Study of Physical Properties of Lunar and Planetary Surfaces," Langley Research Center, Langley Station, Hampton, Virginia, NASA TN D-2413, August 1964.

McCarty, J. L. and Carden, H. D. (1968), "Response Characteristics of Impacting Penetrometers Appropriate to Lunar and Planetary Missions," Langley Research Center, Langley Station, Hampton, Virginia, NASA TN D-4454, April 1968.

Mitchell et al. (1969), "Materials Study Related to Lunar Surface Exploration, Final Report," submitted to George C. Marshall Space Flight Center, NASA Contract NSR 05-003-189, Space Sciences Laboratory Series 10 Issue 28, March 1969.

Mitchell et al. (1970a), "Lunar Surface Engineering Properties Experiment Definition, Final Report," submitted to George C. Marshall Space Flight Center, NASA Contract NAS 8-21432, Space Sciences Laboratory Series 11 Issue 9, January 1970.

Mitchell et al. (1970b), "Lunar Surface Engineering Properties Experiment Definition, Final Report," submitted to George C. Marshall Space Flight Center, NASA Contract NAS 8-21432, Space Sciences Laboratory Series 11 Issue 49, July 1970.

Moore, H. J. (1967), "The Use of Ejected Blocks and Secondary Impact Craters as Penetrometers on the Lunar Surface," Appendix A of "Preliminary Geologic Evaluation and Apollo Landing Analysis of Areas Photographed by Lunar Orbiter III," NASA, June 1967.

- *NASA (1966), "Lunar Soil Mechanics in Relation to LEM Landing Problems," Manned Spacecraft Center Internal Note No. 66-EF-1, April 6, 1966.
- Petry, L. (1910), "Monographies de Systems d'Artillerie," Brussels.
- Philco (1966a), "Research, Development, and Preliminary Design for the Lunar Penetrometer System Applicable to the Apollo Program - Final Report," Publication No. U-3556, April 1966.
- Philco (1966b), "Research, Development, and Preliminary Design for the Lunar Penetrometer System Applicable to the Apollo Program - Final Report," Publication No. U-3608, June 1966.
- Poncelet, J. V. (1829), "Cours de Mechanique Industrielle," First Edition.
- *Poor, A. R., Cox, W. R., and Reese, L. C. (1965), "Behavior of a Sandy Clay Under Vertical Impact of Geometric Shapes," University of Texas, Austin, Texas, available from the Clearinghouse for Federal Scientific and Technical Information as N65-33501.
- Reichmuth, D. R. (1967), "Soil Projectile Interaction During Impact," Dissertation, University of Texas, Austin, Texas, January 1967.
- Resal, H. (1895), "Sur la penetration d'un Projectile dans les Semifluides et les Solides," cr. 120, pp. 397 to 401.
- Robins, B. (1742), "New Principles of Gunnery," London.
- Roddy, D. J., Rittenhouse, J. B., and Scott, R. F. (1962), "Dynamic Penetration Studies in Crushed Rock Under Atmospheric and Vacuum Conditions," Jet Propulsion Laboratory, Calif. Institute of Technology, Pasadena, Calif., Technical Report No. 32-242, April 1962.
- Rowe, R. D. and Selig, E. T. (1962), "Penetration Studies of Simulated Lunar Dust," prepared for presentation at Seventh Symposium on Ballistic Missile and Aerospace Technology, August 1962.
- Schmid, W. E. (1966), "The Determination of Soil Properties In Situ by an Impact Penetrometer," Princeton Soil Engineering Research Series No. 3, Princeton University, Princeton, New Jersey, prepared for Air Force Cambridge Research Laboratories, Contract No. AF19(628)-2427, Project No. 7628, Task No. 76280, Scientific Report No. 1, January 1966. (Available from Defense Documentation Center as AD 634 043.)

- Schmid, W. E. (1969), "Penetration of Objects into the Ocean Bottom (The State of the Art)," Final Report, to U.S. Naval Civil Engineering Laboratory, Port Hueneme, California, Contract No. N62399-68-C-0044, Project No. Y-F015-21-02-005A, March 1969.
- Scott, R. F. (1962), "Problem of the Penetration of a Projectile into Soil, a Soil-Like Medium, or Compressible Rock (Pumice)," four unpublished reports, October and November 1962.
- Scott, R. F. (1970), "In-Place Ocean Soil Strength by Accelerometer," Journal of the Soil Mechanics and Foundations Division, Proc. American Society of Civil Engineers, Vol. 96, No. SMI, January 1970.
- Shipley, E. N. (1967), "Surveyor and LM Penetration in a Model Lunar Soil," Bellcomm Inc. Technical Memorandum TM-67-1014-1, February 23, 1967.
- Thompson, L. J. (1966), "Dynamic Penetration of Selected Projectiles into Particulate Media," Sandia Corporation, SC-RR-66-376, July 1966.
- Thompson, L. J. et al. (1969), "The Effect of Soil Parameters on Earth Penetration of Projectiles," Sandia Corporation, SC-CR-69-3231, July 1969.
- *Thorman, H. C. (1963), "Review of Techniques for Measuring Rock and Soil Strength Properties at the Surface of the Moon," Society of Automotive Engineers, Automotive Engineering Congress, Detroit, Michigan, January 1963.
- Tsai, Kuei-wu (1967), "Strength Response Parameters of Natural Soil Surfaces and Their Application to the Landing Problem of Aircraft," Dissertation, Princeton University, Princeton, New Jersey, June 1967.
- USAE - WES (1957), "Studies of Aerial Cone Penetrometer, Laboratory Study of Mechanical Principles," U.S. Army Engineer Waterways Experiment Station, Corps of Engineers, Vicksburg, Mississippi, Technical Report No. 3-462, No. 1, July 1957.
- USAE - WES (1958), "Studies of Aerial Cone Penetrometer, Field Tests," U.S. Army Engineer Waterways Experiment Station, Corps of Engineers, Vicksburg, Mississippi, Technical Report No. 3-462, No. 2, April 1958.

Vey, E. and Nelson, J. D. (1965), "Studies of Lunar Soil Mechanics," I.I.T. Research Institute Project No. M272, Phase II Final Report, Contract No. NASr -65(02), February 1965.

Vey, E. and Nelson, J. D. (1966), "Studies of Lunar Soil Mechanics," I.I.T. Research Institute Project No. M272, Phase III Final Report, Contract NASr -65(02), May 1966.

Womack, D. P. and Cox, W. R. (1967), "Measurement of Dynamic Characteristics of Soils with Penetrometers," The University of Texas, Austin, Texas, NASA CR-849, August 1967.

Woodward, Clyde, Sherard, and Associates (1962-1967), Special Projects Division, Fifty-two reports to the Sandia Corporation on soil studies associated with Sandia impact penetrations tests.

*Young, C. W. and Ozanne, G. M. (1966), "Compilation of Low Velocity Penetration Data," Sandia Corporation, SC-RR-66-306A, June 1966.

Young, C. W. (1969), "Depth Prediction for Earth-Penetrating Projectiles," Journal of the Soil Mechanics and Foundations Division, Proceedings of the American Society of Civil Engineers, Vol. 95, No. SM3, May 1969.

Chapter 3. LUNAR SOIL STABILIZATION USING URETHANE FOAMED PLASTICS

T. S. Vinson, T. Durgunoglu, and J. K. Mitchell

INTRODUCTION

The surface of the moon consists of a fragmental surface layer (called a "soil" by us, referred to as the "regolith" by some) overlying blocky or coherent material. Lunar surface operations of various types related to basing that may be contemplated for the post-Apollo period will be influenced directly by the characteristics of this layer.

Therefore, where it is determined that existing lunar materials may not be satisfactory in terms of strength, compressibility, or permeability, some form of stabilization such as the alteration of properties to improve performance may be necessary.

Relative to lunar payload limitations, the most desirable stabilizer would be one that stabilizes the greatest volume of soil per unit weight of stabilizer transported to the moon. Existing stabilizers used in terrestrial applications have a relatively low ratio of stabilized volume to initial weight of stabilizer. The use of a foamed plastic as a stabilizing agent has been investigated for lunar application, because it offers the prospect of low-density systems.

Of the nine commercially available foamed plastic types (see Vinson and Mitchell, 1970) polyurethanes (urethanes) were selected. Their choice was based on consideration of their potential to stabilize lunar materials and to meet the lunar physical and environmental constraints.

The **purpose** of this research program has been to evaluate urethane foamed plastics as lunar soil stabilizing agents. The emphasis thus far has been primarily on soil grouting; i.e., the stabilization of a soil mass by injection of a liquid chemical system. However, limited feasibility studies have also been made on lunar soil stabilization by

1. pouring or spraying urethane foamed systems on soil deposits, and,
2. by mixing urethane foamed systems with soil deposits, i.e., admixture stabilization.

Previous studies (Vinson and Mitchell, 1970) have concentrated on:

1. Study of the organic chemistry of urethane foamed plastic.
2. Development of urethane foamed plastic grant systems for use under terrestrial conditions.
3. Evaluation of the strength, permeability, and other pertinent mechanical properties of soils stabilized in the terrestrial environment urethane foams.

The research program during the past year has involved:

1. Development and use of apparatus to investigate the influence of the lack of atmosphere on the urethane foaming process.
2. Stabilization of soil masses by injection grouting in vacuo.
3. Feasibility study of admixture stabilization using urethane foamed plastic.

Each phase is discussed in the following sections. First, however, a brief summary of our studies for the past contract year is given.

PREVIOUS STUDIES

Chemistry of Polyurethane Foamed Plastics

Urethanes are produced by the reaction of polyhydroxy compounds (polyols) with polyisocyanates. Both single-chain or cross-linked polymeric structures may be formed. Flexible foams usually contain only a small amount of cross-linking, whereas rigid foams are most often highly cross-linked. The equivalent weights of flexible-foam polyols may average 1000 units; whereas, rigid-foam polyols usually average 70 to 150 units.

Catalysts, generally tertiary amines and tin salts, may be added to a urethane system to control or accelerate the rate of reaction. In a foam system, this allows gelation to be synchronized with maximum rise of the foam.

Surfactants may be added to a system to control cell surface tension and thus render the foam large-celled or fine-celled. The foam structure

is produced by blowing agents. Two classes of chemical blowing agents that expand to form a gas in the polymer structure are available. In the first, the gas is produced by a chemical reaction within the polymer. In the second, a chemical blowing agent decomposes or gasifies (evaporates) in the presence of the exothermic heat of reaction.

Experimental Laboratory Results

Table 3-1 lists a number of urethane systems developed for use in a laboratory soil grouting program. These systems were found to satisfy several criteria established for a potential lunar grout; namely,


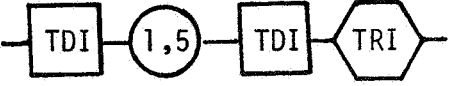
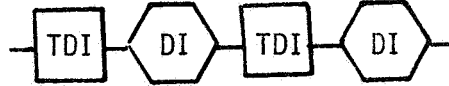
1. low viscosity prior to set, so that relatively fine-grained materials could be treated
2. control over setting times
3. simple application
4. ease in handling
5. durability, and
6. relative absence of toxicity and other hazards.

Table 3-2 summarizes strength, elasticity, and permeability results for "soil cylinders" and cores taken from spherical stabilized masses. The injection procedure associated with each type of test sample is described by Vinson and Mitchell (1970) and Vinson (1970).

The results in Table 3-2 indicate that

1. Urethane plastic could be made to foam in the voids of the soil mass
2. Significant strengthening and the impermeabilization of a granular soil, No. 20 Monterey sand, could be effected in the laboratory by the injection of urethane foamed plastic systems, and
3. Stabilizer densities are considerably less than 1.0 g/cm^3 .

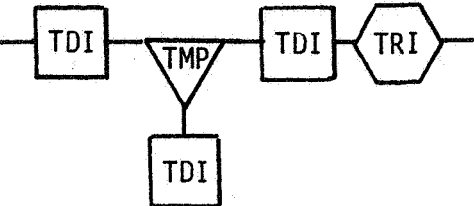
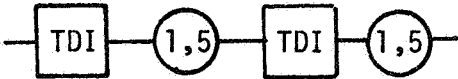
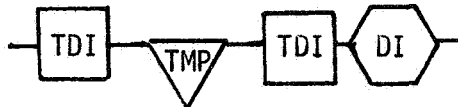
Table 3-1. Urethane foam systems developed
for laboratory injection program.

Trials	Chemical system constituents	Wt (g)	Major conceptual framework*
44G,H,K	TDI**	59.2	
	triethylene glycol (TRI)	46.3	
	polyethylene glycol	1.5	
	castor oil	5.0	
	diacetone		
	alcohol	3.0	
	adipic acid	3.0	
	L-531	1.0	
48A,B,C	TDI	61.4	
	1,5 pentanediol	17.3	
	triethylene glycol (TRI)	24.9	
	castor oil	10.0	
	diacetone		
	alcohol	3.0	
	adipic acid	0.8	
	L-531	1.0	
51,A,B	TDI	67.2	
	diethylene glycol (DI)	37.8	
	castor oil	10.0	
	diacetone		
	alcohol	1.5	
	adipic acid	2.0	
	L-531	1.0	

* The "major conceptual framework" is an idealization of the actual urethane molecule formed in a given system; it is the most representative molecule that can be visualized for a system.

** TDI = toluene diisocyanate

Table 3-1. (Cont'd)

Trials	Chemical system constituents	Wt (g)	Major conceptual framework*
39T,U,V,GS	TDI	62.5	
	triethylene glycol (TRI)	20.9	
	TMP†	18.6	
	castor oil	5.0	
	diacetone		
	alcohol	2.0	
	adipic acid	0.6	
	L-531	1.0	
54U,W	TDI	68.1	
	1,5 pentanediol	37.4	
	castor oil	15.0	
	adipic acid	1.3	
	L-531	1.0	
55G,H,J	TDI	64.2	
	diethylene glycol (DI)	24.4	
	TMP	15.5	
	castor oil	10.0	
	diacetone		
	alcohol	5.0	
	adipic acid	1.2	
	L-531	1.0	

† TMP = 2-ethyl-2-(hydroxymethyl)-1,3-propanediol

Table 3-2a. Summary of strength and stress-strain properties of stabilized masses of No. 20 Monterey sand.

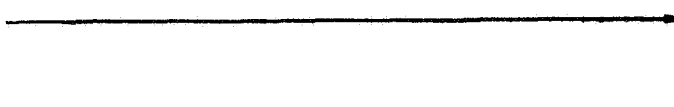

Chemical system & specimen	Foam density (g/cc)	Sample type	Compressive strength (psi)	E, tangent modulus of elas. (psi)
44G1	0.59	soil cylinder 	5249	7.4×10^5
44H1	0.59		5270	7.5×10^5
44K1	0.59		4675	8.2×10^5
48A1	0.61		5155	7.6×10^5
48B1	0.70		4780	8.8×10^5
48C1	0.59		5310	8.8×10^5
51A1	0.63		2973	5.8×10^5
51B1	0.63		3305	8.5×10^5
39T1	0.63		2070	7.9×10^5
39V1	0.63		3568	10.8×10^5
39U1	0.64		3993	8.7×10^5
54W1	0.69		4620	4.5×10^5
54U1	0.74		3037	6.6×10^5
55G1	0.67		3230	7.5×10^5
55M1	0.67		3600	7.5×10^5
55J1	0.63	core 	2950	7.5×10^5
39GS1	0.38		6250	1.11×10^6
39GS3	0.38		6240	1.25×10^6
39GS5	0.38		5200	1.25×10^6

Table 3-2b. Summary of permeability of stabilized masses of No. 20 Monterey sand.

Chemical system & specimen	Foam density (g/cc)	Sample type	Permeability (cm/sec, average)
44I2	0.59	soil cylinder	1.11×10^{-4}
44J2	0.59		2.77×10^{-5}
48D2	0.65		impermeable
48F2	0.63		
51G2	0.66		
51C2	0.66		
39W2	0.65		
39X2	0.65		
54F2	--		
54V2	0.73		
55K2	0.66	core	
55I2	0.66		
39GS8	0.38		
39GS9	0.38	core	

DESIGN AND PERFORMANCE OF VACUUM APPARATUS

Introduction

An understanding of the formation of foamed plastics in vacuo is essential before urethane chemical systems can be designed for use in actual lunar engineering problems. A crude vacuum apparatus (Vinson and Mitchell, 1970) was developed to establish whether a foamed plastic could be formed in vacuo. It consisted of a vacuum desiccator, an air-magnetic stirrer, and a McLeod vacuum gage connected to a vacuum pump. With this apparatus it was possible to develop a chemical system that foamed and hardened in vacuo, but gave little insight into the foam formation mechanism. Further, it was extremely difficult to conduct tests in rapid succession as the space in the vacuum desiccator was extremely limited.

Design and Performance of Vacuum Apparatus

A new apparatus that overcomes the difficulties described above was constructed, as shown in Figures 3-1, 3-2, and 3-3. This vacuum apparatus was designed to allow the following studies:

1. Injection into soil masses in vacuo.
2. Admixture stabilization using urethane chemical systems in vacuo (with slight apparatus modifications).
3. Development of urethane spray systems in vacuo.

The vacuum chamber is steel, 18 inches in diameter and 12 inches high. The inside surface of the chamber is nickel-plated for easy cleaning. The top plate is detachable so that mixing jars and other equipment can be easily removed. An O-ring seal is used to prevent air-leakage. A vacuum of 50 millitorr is reached after a pumpdown time of 10 minutes.

A glass trap is located between the pump and the vacuum chamber to prevent contamination of the pump oil by condensable vapors. The trap conductance is high and causes no more than 10% reduction in pump speed. Dry ice and acetone are used as a refrigerant in the trap.

Toluene diisocyanate (TDI) and polyol, the two major components in

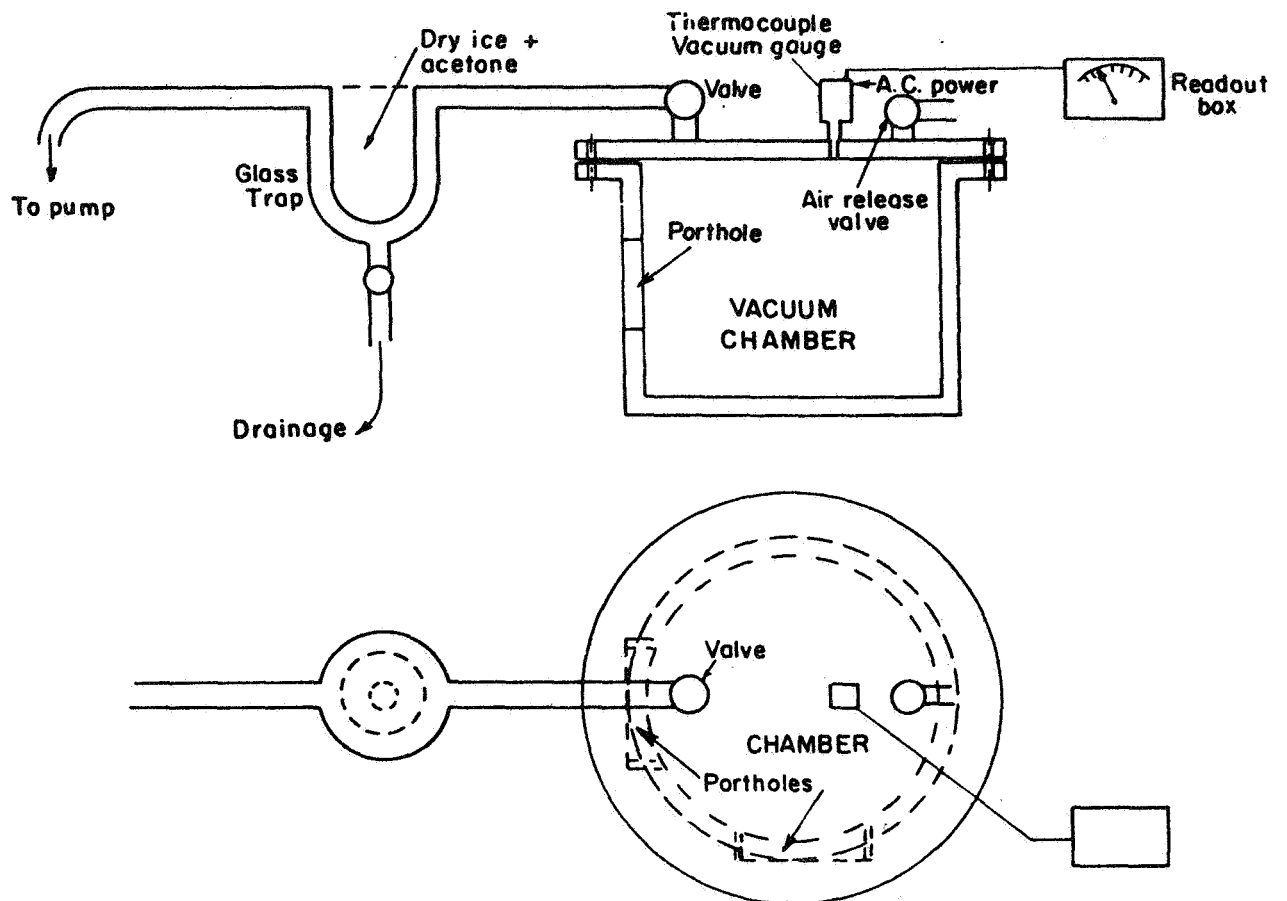
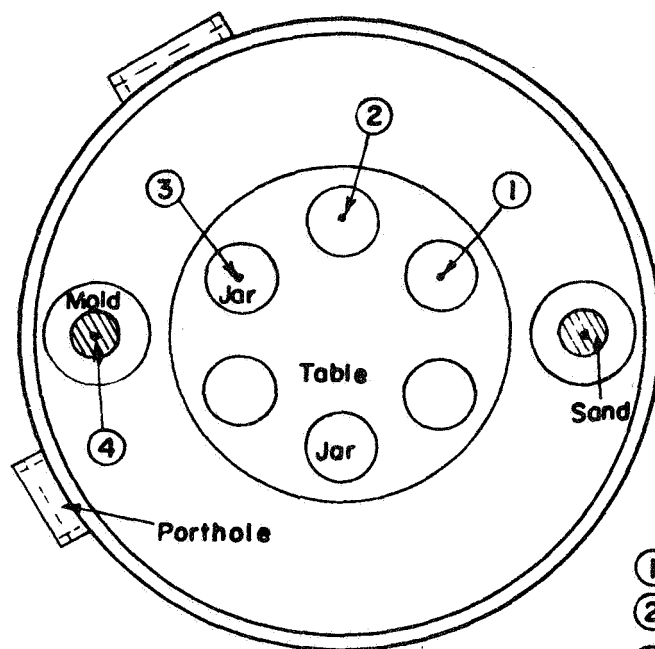
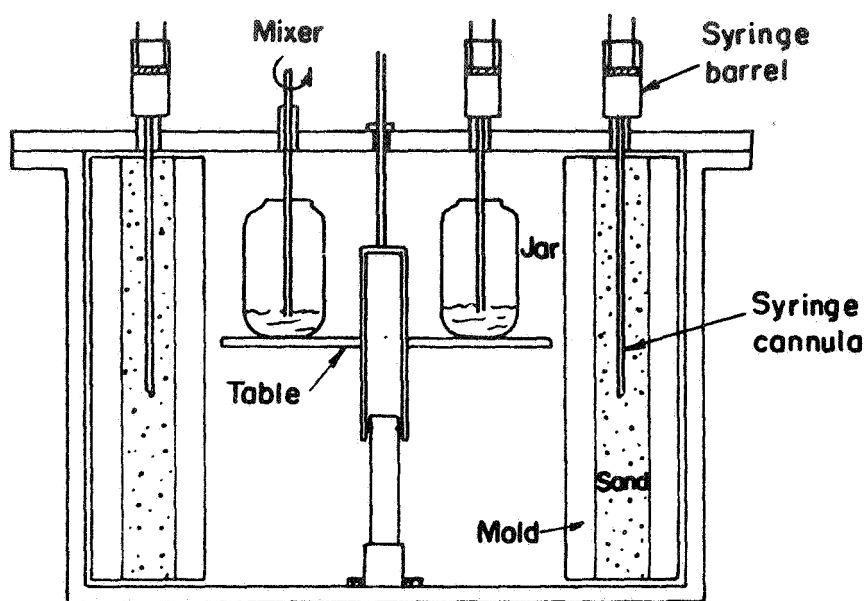


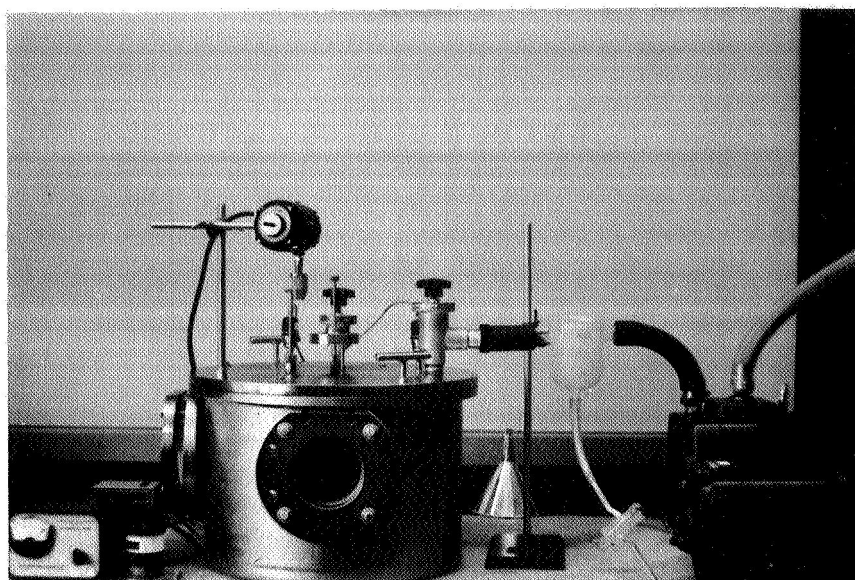
Fig. 3-1. Schematic diagram of vacuum apparatus.



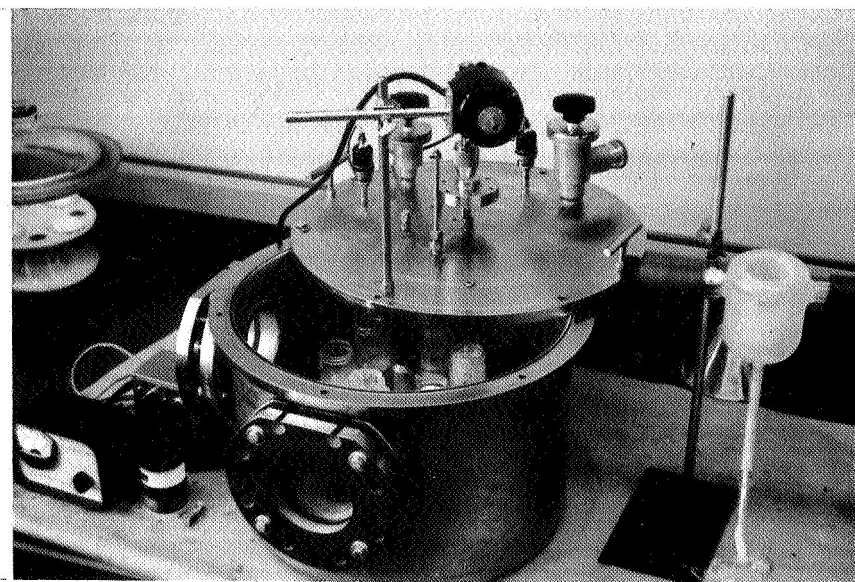
Legend

- ① Injection of polyol
- ② Injection of TDI
- ③ Mixing
- ④ Injection of associated system into soil

Fig. 3-2. Schematic diagram of mixing table and soil injection molds in vacuum apparatus.



(a) Front View



(b) Top View

Fig. 3-3. Vacuum apparatus for foam formation studies.

urethane chemical systems, can be introduced into a mixing jar in the vacuum chamber through separate lines, or by injection into the chamber in an "associated state."*

If the components are introduced into the system by separate lines, the procedure is to puncture a rubber seal with a syringe and inject the TDI or polyol into a mixing jar in the vacuum chamber. The puncture is resealed with vacuum grease after each operation to prevent air-leakage. During the injection operation, the vacuum in the chamber increases to approximately 200 millitorr. With the pump in continuous operation, the chamber returns to 50 millitorr after approximately 2 minutes. The components are mixed with a rotary stirring shaft. The shaft is sealed with O-ring rotary shaft seals. There is no change in the vacuum reading during the mixing operation.

Urethane systems can be injected into soil masses contained in hollow polypropylene molds. The injection procedure is to insert a syringe cannula, 5.0 inches long, through a rubber seal fitted to the top of the chamber, into the polypropylene mold. (As before, the rubber seal is resealed with vacuum grease after the operation.) Two rubber stoppers, one with a hole through which the cannula can be inserted, are placed at either end of the mold to prevent movement of the soil mass. During this operation the vacuum increases to approximately 100 millitorr.

All operations are observed from either one of the two porthole windows. The vacuum inside the chamber is measured using a thermocouple vacuum gage.

* An "associated state" may be thought of as a chemical state in which the polyol and TDI molecules in a given system have come into alignment. That is to say, OH groups on the polyol molecules are in close proximity to the NCO groups on the TDI molecules. They have not at this time reacted in the sense of forming a polymeric structure, but there is a distinct formation of a homogeneous solution.

FOAM FORMATION IN VACUO

Theory

The theoretical considerations allowing the development of a foamed plastic system for use in vacuo have been described in detail in a previous report (Vinson and Mitchell, 1970). In summary, those considerations may be stated as follows:

1. To withstand the internal gas pressure in vacuo, the tensile strength of the foam bubble skin must be considerably stronger than at atmospheric pressure. In developing urethane foamed plastic systems in vacuo, the polymer structure of the urethane plastic must be formed rapidly enough to develop the required tensile strength or no foam will be produced.
2. The ability to form a polymer rapidly is a function primarily of the relative rate of reactivity of TDI with various constituents in the chemical system. Thus, chemical constituents with a rapid rate of reactivity must be chosen if a foam is to be developed in vacuo.
3. It is known that the vaporization temperature of certain chemicals decreases as the pressure in their surroundings decreases. This is true for the tolylene diisocyanate common to all urethane chemical systems. Therefore, if a desirable foam structure is to be produced, the system should be formulated to minimize vaporization; i.e., a high vaporization temperature is desirable.

Experimental Results

Foam formation in vacuo.

Pursuant to the theoretical requirements stated above, several urethane foam systems were developed and tested in glass jars in the vacuum apparatus. Table 3-3 lists these systems.

In some trials, vaporization of the polyisocyanate component of the systems was minimized by employing the technique of "prepolymerization"; i.e., a measured amount of the polyol component was mixed with the TDI prior to injection into the vacuum apparatus. Effectively, the average

Table 3-3. Urethane foam systems tested in vacuo.

Trial	Chemical system constituents	Wt (%)	Wt (gm)	Mixing conditions	Comments
VIA	TDI triethanolamine triethylene glycol I531 (surfactant) adipic acid	60.9 26.0 13.1 1.0 0.5	12.18 5.20 2.62 0.20 0.10	mixed in vacuum apparatus (MIA)	TDI vaporizing; foam produced but very non-uniform
VIB	same as VIA, but no adipic acid			MIA	TDI vaporizing; foam again non-uniform but better than in VIA
VIC	same as VIA, but with adipic acid	0.3	0.06	MIA	Same as VIA
VID	same as VIB, plus H ₂ O	0.5	0.10	MIA	same as VIA, but more blowing
VIE	same as VIB, plus H ₂ O	0.3	0.06	MIA	same as VIA, but more blowing
VIM	same as VIC			MIA	pre-poly 1.0-g triethylene glycol with TDI. Reasonably good foam; still non-uniform
VIN	same as VIC			MIA	pre-poly 2.0 triethanolamine with TDI; apparently too much triethanolamine. Resultant plastic no good.

Table 3-3. (Cont'd)

Trial	Chemical system constituents	Wt (%)	Wt (gm)	Mixing conditions	Comments
V2A	TDI triethanolamine adipic acid L531	63.6 36.4 0.3 1.0	12.72 7.28 0.06 0.20	MIA	very poor foam
V2B	same as V2A			MIA	pre-poly 2.0-g triethanolamine with TDI; very poor foam
V3A	TDI triethanolamine triethylene glycol L531	57.6 28.3 14.1 1.0	11.52 5.66 2.82 0.20	MIA	no foam formed
V3B	same as V3A, plus adipic acid	0.3	0.06	MIA	foam no good
V3D	same as V3B			inject in associated state	pre-poly 0.5-g triethanolamine with TDI; cool components, reasonably good foam

molecular weight of the TDI component was increased, and its vaporization tendency in vacuo decreased. It was not found necessary to employ any special techniques to preclude vaporization of the polyols.

It may be seen that, in general, most of the systems tested yielded unsatisfactory foams. There may be at least three reasons for these results. First, with the exception of one system, all systems were mixed in the vacuum apparatus. The mixing in this single instance was found to be poor. Typically, a reaction would take place at the interface of the TDI and the polyol components before the system could be thoroughly mixed. This initial reaction led to a polymeric structure that probably deviated considerably from the predicted conceptual framework. The net result was a weak, friable foam.

Second, while the urethane systems tested in the vacuum apparatus were designed to have a rapid polymer formation ability, and in fact did exhibit rapid polymer formation under terrestrial conditions, the rate of reactions was apparently still too low relative to vacuum conditions. Observations of the foam formation in vacuo indicated that during the first few seconds of reaction, the polymer structure did not develop the required tensile strength to preclude the escape of internal gas. It was only after the reaction was reasonably far along (typically after 15 to 20 seconds) that a foam structure began to develop. Even at this time only large foam bubbles appeared, indicating that the internal gas was at a very low pressure before it could be effectively confined.

Finally, the temperature of the system during the reaction was extremely high. The general effects of the high temperature are a disruption in the buildup of the polymer structure and high internal gas pressures which, again, cause a poor foam structure to be formed.

To overcome the difficulty of mixing the components in the vacuum apparatus, several attempts were made to introduce associated systems into the vacuum apparatus. For the majority of the systems, it was found that the reaction time* was too fast (less than 5 seconds) to

* The reaction time is defined as the time between association and the formation of a polymeric structure sufficiently developed as to preclude injection grouting, or the time between association and an obvious reaction of any nature.

allow introduction into the chamber. To overcome this problem, the components were cooled before association. This allowed the reaction time to be increased to approximately 15 seconds in one system (V3D), making injection into the apparatus possible. However, while the foam produced in such an operation was better than that produced with the same system when mixing was done in the apparatus, it was still unsatisfactory.

Further attempts to increase the polymer formation ability or to reduce the heat of reaction for foams generated in the absence of soil were discontinued when it was discovered that behavior in soil was distinctly different than it was in an open glass jar.

Soil grouting in vacuo.

Cylinders of two types of soil were grouted in vacuum following the procedure described above. It was found that masses of No. 20 Monterey sand could be stabilized in vacuo using either system 39 (Table 3-1) or system V3D (Table 3-3). Stress-strain relationships in unconfined compression tests are shown in Figure 3-4 for three soil cylinders. All of the cylinders had unconfined compressive strengths of approximately 4500 psi. The foam densities in the stabilized masses were approximately 0.50g/cc.

It is of interest to note that the unconfined compressive strength for V3H (system 39) is approximately the same as the unconfined compressive strength for soil cylinders grouted using the same system under terrestrial conditions.

· Injections into a lunar soil simulant (Houston, Namig, and Mitchell, 1970) did not prove as successful as injections into No. 20 Monterey sand. Penetration grouting, i.e., filling the interstitial voids within a soil mass with a stabilizing agent, was not possible because of the relatively fine-grained nature of the simulant. Thus, no soil cylinders were formed. When an injection was attempted, the associated urethane system would seek a path of least flow resistance, typically along the wall of the cylindrical injection mold. Some foaming occurred which tended to compact the lunar soil simulant somewhat.

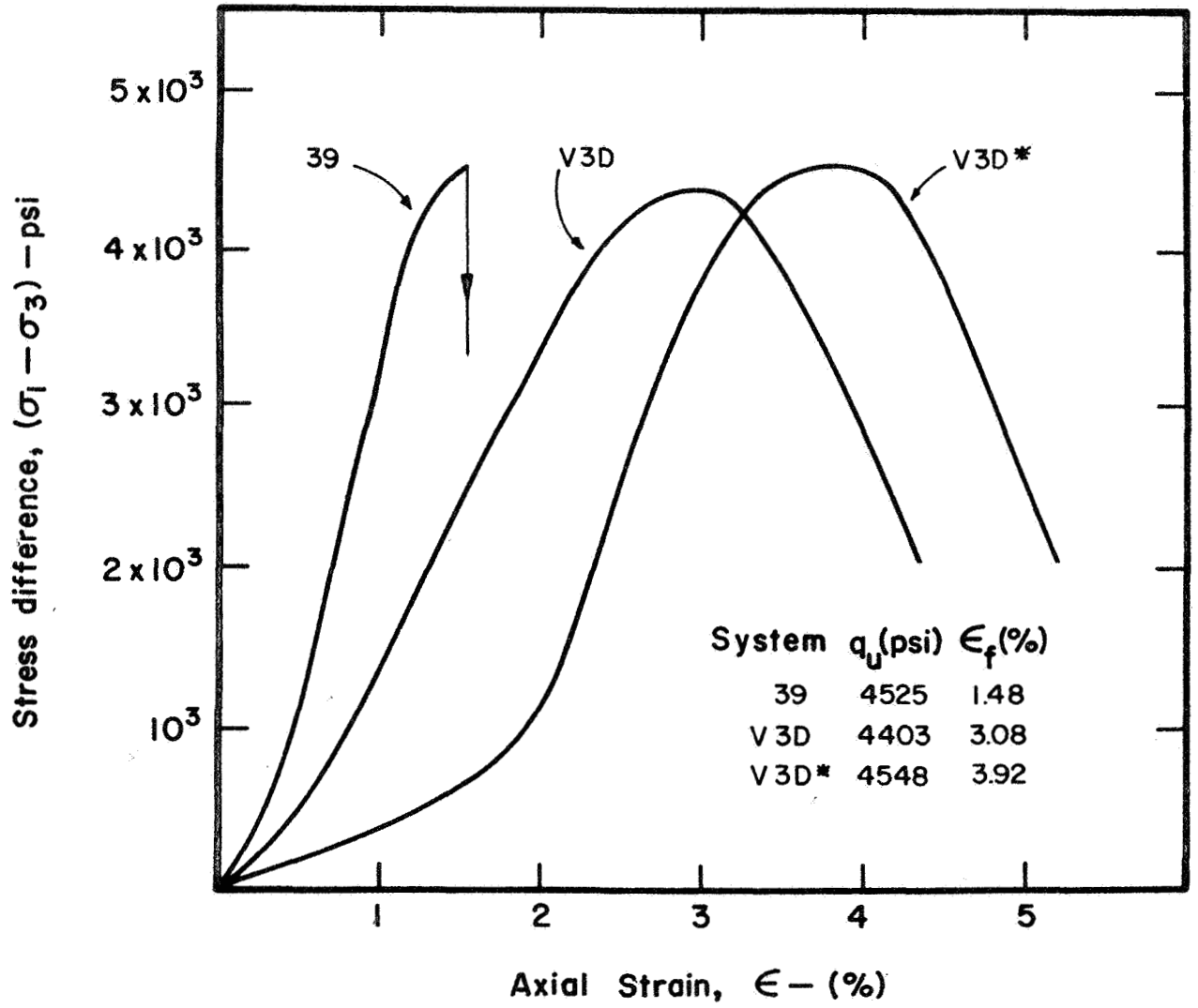


Fig. 3-4. Relationship between stress and strain for No. 20 Monterey sand stabilized in vacuo.

Perhaps the most significant experimental fact resulting from grouting soil masses in vacuo is that it is not necessary to use a urethane system with a rapid polymer formation ability to form a foam structure. (This does not imply that a rapid polymer formation ability will not be necessary in a "pour-on" or "spray" lunar urethane stabilization application.) There are at least two factors that allowed the foam to form in a soil mass. First, the soil acts as a heat sink for the urethane systems. Thus, the polymeric structure develops to a greater degree before blowing occurs. Further, there is less disruption of the associated system and less blowing in the system due to the heat of the reaction vaporizing some of the components. Also, the gas that is produced is at a lower pressure because of the lower temperature of the system.

Second, the soil particles confine the expanding foam. In an open container, such as the glass jars used in the experiments, there is no confinement of the foam structure. The foam bubbles expand to a size where the internal gas pressure is in equilibrium with the tensile stress in the bubble skin. If equilibrium cannot be established, the bubble bursts. In the soil mass, however, the foam bubbles can only fill up the voids in the soil mass. While some elongation of the foam bubble can occur, it is probably negligible in the overall foaming process.

ADMIXTURE STABILIZATION

The feasibility of using urethane foamed plastic as an admixture lunar stabilizing agent was investigated by mixing system 39 (Table 3-1) with the lunar soil simulant. The resultant material was then compacted in a cylindrical mold and allowed to cure for one day before unconfined compressive tests were conducted. Figure 3-5 shows the results of these tests. As illustrated, the cylinders had unconfined compressive strengths of 700, 4350, and 2880 psi relative to foam contents of 5, 10, and 15 per cent (by total dry weight of soil). These are extremely encouraging results and indicate that urethane foamed plastics have potential as lunar admixture stabilizing agents.

The data further illustrate that there is an optimum foam content relative to achieving the highest unconfined compressive strength. This

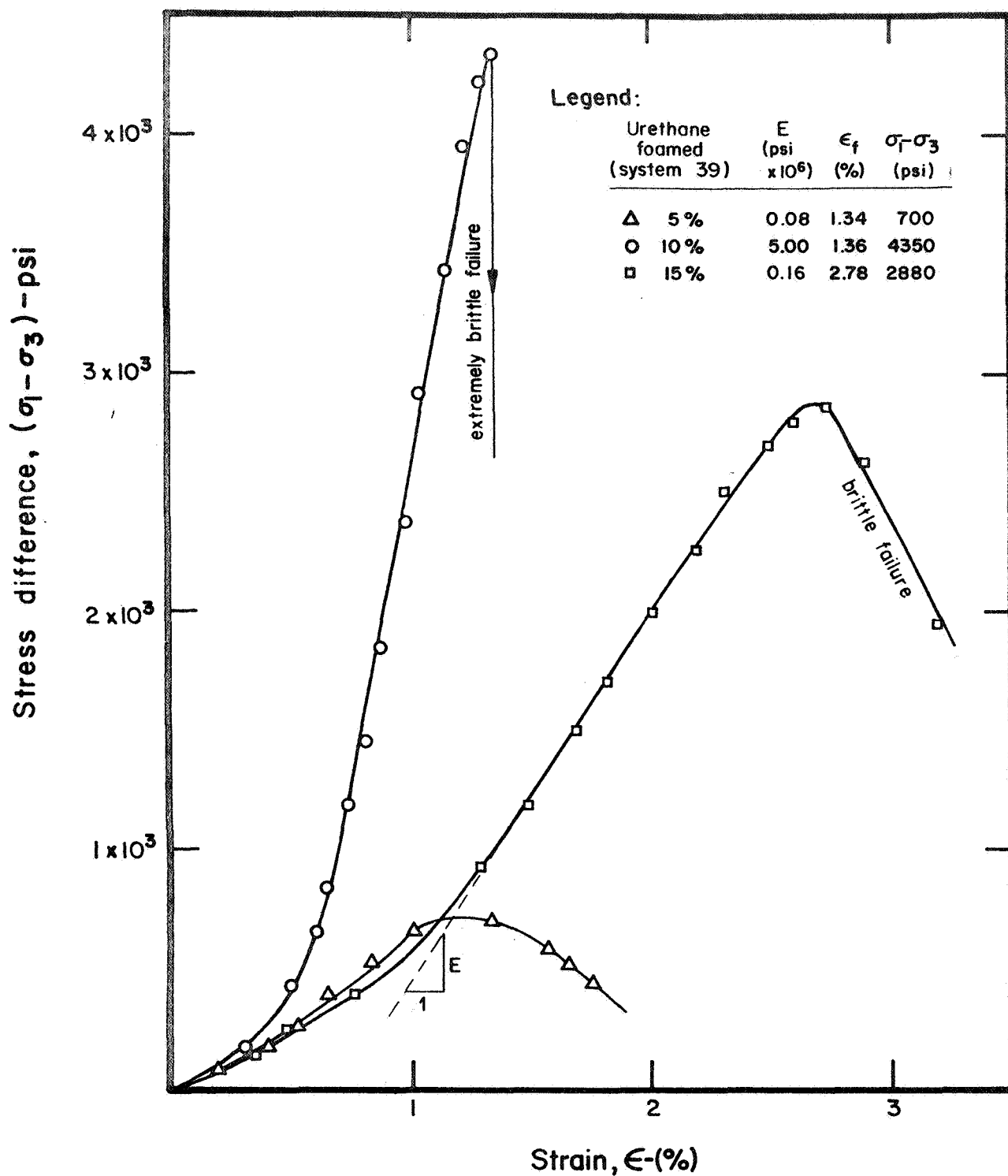


Fig. 3-5. Typical stress-strain behavior of stabilized simulated lunar soil.

is also true of most terrestrial admixture stabilizing agents. For System 39 and the lunar soil simulant, it is apparently 10 per cent.

CONCLUSIONS AND RECOMMENDATIONS

Lunar Soil Stabilization by Soil Grouting

The results of this research program indicate that grouting of fragmented rock masses or coarse-grained soil masses using urethane foamed plastic should be possible in the lunar environment. Urethane systems have been developed that can cause such masses to have high unconfined compressive strengths. The degree of impermeabilization attained in these systems remains to be determined. While the effects of temperature on the foaming process have not been investigated, it is felt that systems could be formulated, or that the existing systems could be modified, to allow foam formation within a reasonable range of temperatures.

Admixture Lunar Soil Stabilization Using Urethane Foamed Plastics

The use of urethane or other foamed plastics as admixture lunar soil stabilizing agents appears to be highly feasible and may represent a realistic approach for stabilizing fine-grained lunar soil deposits. The effect of the lunar environment on the admixture stabilization process must be investigated. Further, the mechanical difficulties associated with this type of stabilization technique must be assessed.

Pour and Spray-on Urethane Foam System Applications

It was not possible to develop a suitable urethane foam system for lunar pour or spray-on applications. This failure was primarily due to a mechanical system failure. It is felt that the vacuum apparatus used could not accommodate urethane systems with the extremely rapid polymer formation ability necessary for such applications. However, it is recommended that research work in this area be continued since pour or spray-on applications may still represent a useful approach to lunar soil stabilization for construction purposes.

REFERENCES

Houston, W., Namig, L., and Mitchell, J. K. (1970), "Lunar Soil Simulation," Lunar Surface Engineering Properties Experiment Definition, Final Report presented to NASA George C. Marshall Space Flight Center, Vol. I of IV, Jan. 1970.

Vinson, T. S. (1970), "The Application of Polyurethane Foamed Plastic in Soil Grouting," Dissertation presented to the University of California, Berkeley, in partial fulfillment of the requirements for the degree of Doctor of Philosophy.

Vinson, T. S., and Mitchell, J. K. (1970), "Foamed Plastic Chemical Systems for Lunar Soil Stabilization Applications," Lunar Surface Engineering Properties Experiment Definition, Final Report presented to NASA George C. Marshall Space Flight Center, Vol. I of IV, Jan. 1970.

Chapter 4. FEASIBILITY STUDY OF ADMIXTURE
SOIL STABILIZATION WITH PHENOLIC RESINS
(T. Durgunoglu and J. K. Mitchell)

INTRODUCTION

The feasibility of using phenolic resins as admixture stabilizing agents was investigated. The purpose was to determine whether a less expensive chemical resin system than the urethanes could be used for soil stabilization. The following characteristics are desired for any system that might be used for stabilization of unconsolidated soils:

1. Easy mixing with soil,
2. A controllable curing time,
3. Good compaction properties,
4. Ease of handling, and
5. Relative absence of toxicity.

Further treated soil should have substantially higher strength and lower permeability values than untreated soil.

This section presents results of tests conducted to find chemical systems satisfying these criteria. Engineering property data for soil masses stabilized with some different phenolic resin systems developed are also presented.

LABORATORY PROCEDURES

Chemistry of Phenolic Resins

Phenolic resin is a thermosetting* type of resin which is obtained as a condensation product of formaldehyde with phenols.

Phenol-formaldehyde resins, commonly termed "phenolics," are produced by the stepwise polymerization of formaldehydes with phenols. The type of product formed in the reaction is determined by the functionality of the monomers (phenols); i.e., by the average number of reactive

* Thermosetting resins are insoluble in common solvents due to formation of covalently cross-linked structure.

functional groups per monomer (Fig. 4-1) molecule. Polyfunctional monomers, such as phenols with more than two functional groups per molecule, give branched or cross-linked polymers. Catalysts are added to control or to accelerate the reaction.

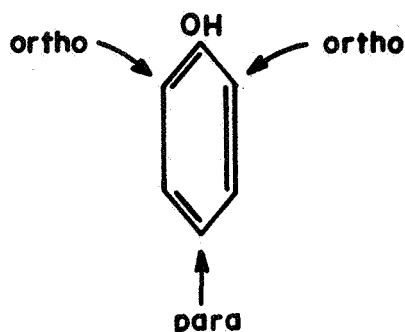


Fig. 4-1. Active hydrogen atoms in phenol.

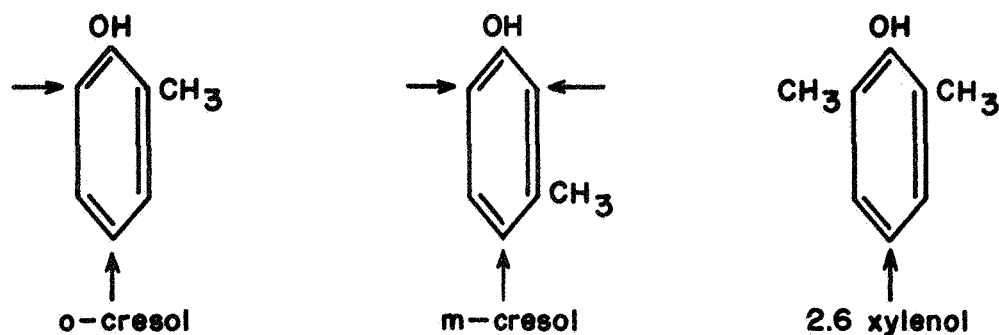
Formaldehydes.

Formalin is the general-purpose formaldehyde in aqueous solution form regularly available at 37% by weight. Paraformaldehyde is a mixture of polyoxymethylene glycols, $\text{HO}-(\text{CH}_2\text{O})_n\text{H}$, with n in the range of 8 to 100.

It is available in powder form at 95% by weight. It was used for this research program because a large amount of water would be objectionable in the system.

Phenols.

The basic structure of pure phenol can be represented as in Fig. 4-1. However, commercial phenol obtained from coal tar is likely to contain varying amounts of impurities. It is necessary to control the nature of these homologs,* since they have different numbers of active hydrogen atoms (Fig. 4-2).



Arrows indicate active hydrogen atoms

Fig. 4-2. Some homologs of phenol.

Discussion of the effects of these homologs on reactions is outside the scope of this research program. Phenols were carefully examined before they were used, and colorless phenol was taken as an indication of purity.

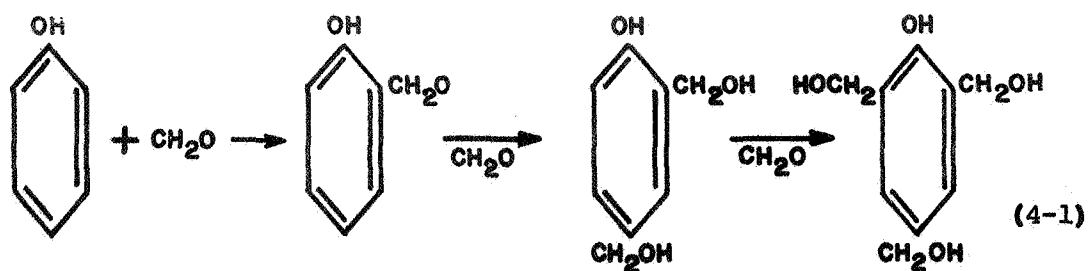
Reaction of phenol and formaldehyde.

Phenols react with aldehydes to give condensation products. The reactions are always catalyzed, either by acids or by bases. The nature of the product is greatly dependent on the type of catalyst and the mole

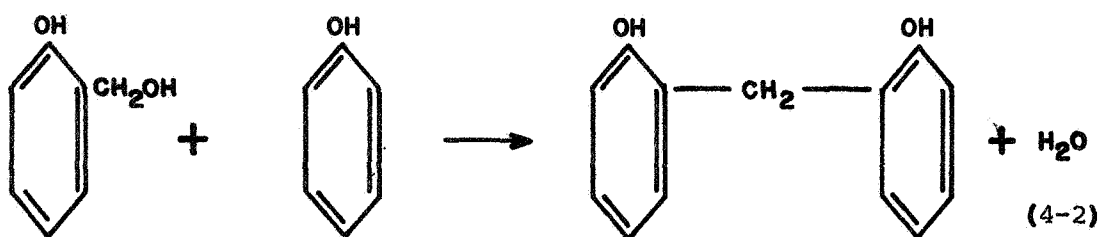
* A homolog is a simple derivative of the original molecule.

ratio of the reactants. Major reactions can be summarized as follows:

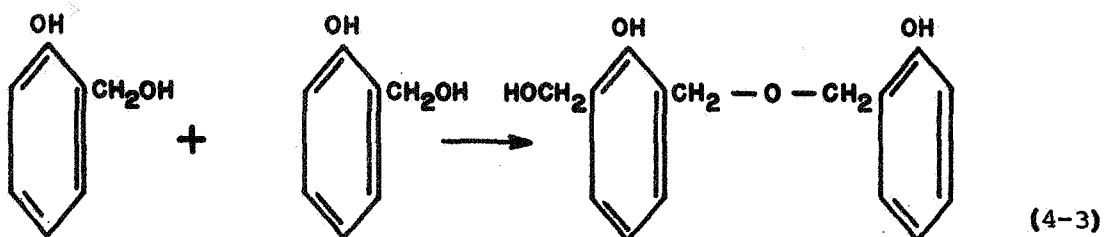
1. Addition to give methylol phenols.



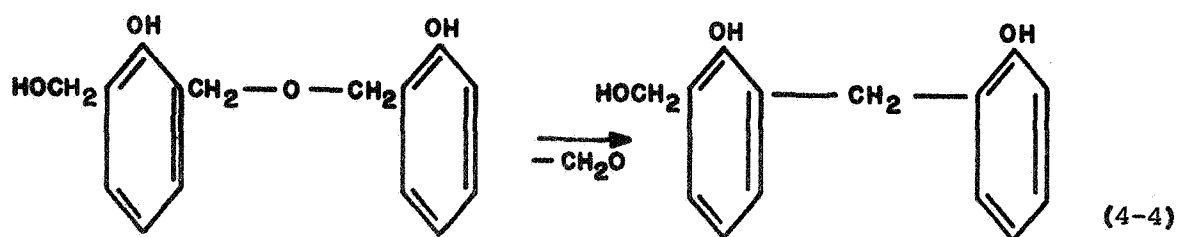
2. Condensation of methylol phenol and a phenol to give a methylene bridge.



3. Condensation of two methylol groups to give an ether bridge.



4. Decomposition of ether bridges to methylene bridges and formaldehyde.



Factors influencing the reactions.

The following factors influence the reactions:

1. Nature of phenols. As mentioned before, the reactivity of phenol is greatly influenced by its structure. Comparative reactivity of some homologs of phenol can be ordered with reactivity varying from more to less, as follows: m-cresol, phenol, o-cresol, 2,6 xylenol.
2. The mole ratio of reactants. Thompson (1941) has studied the effect of the formaldehyde-to-phenol ratio on tensile, compressive, and impact strengths of the cured resin. The properties improve as the ratio increases from 1.0 to 3.5. The effect of this ratio on compressive strength of resin is given in Figure 4-3.
3. Catalysts. The speed, as well as the course of the reaction, is greatly affected by the presence of different acid or alkali catalysts. Although the formaldehyde-to-phenol ratio is the main factor, the type of product formed also depends greatly on the choice of the catalyst. Alkaline catalysts favor the formation of phenolic alcohols, acid catalysts favor the formation of methylene bridges.
4. Temperature. The reaction rate approximately doubles for every 10 °C rise in temperature.

Analytical Laboratory Procedure

It was necessary to determine what proportions of chemicals should be used to achieve optimum engineering properties of treated soil. This was accomplished by taking a 1.5 to 1.0 mole ratio of formaldehyde-to-phenol as recommended by different investigators. (Thompson, 1941). Later, a 1.7 to 1.0 ratio was used in order not to have unreacted phenol in the system; 0.3 mole of sodium hydroxide was used for each mole of phenol for preparing the resin.

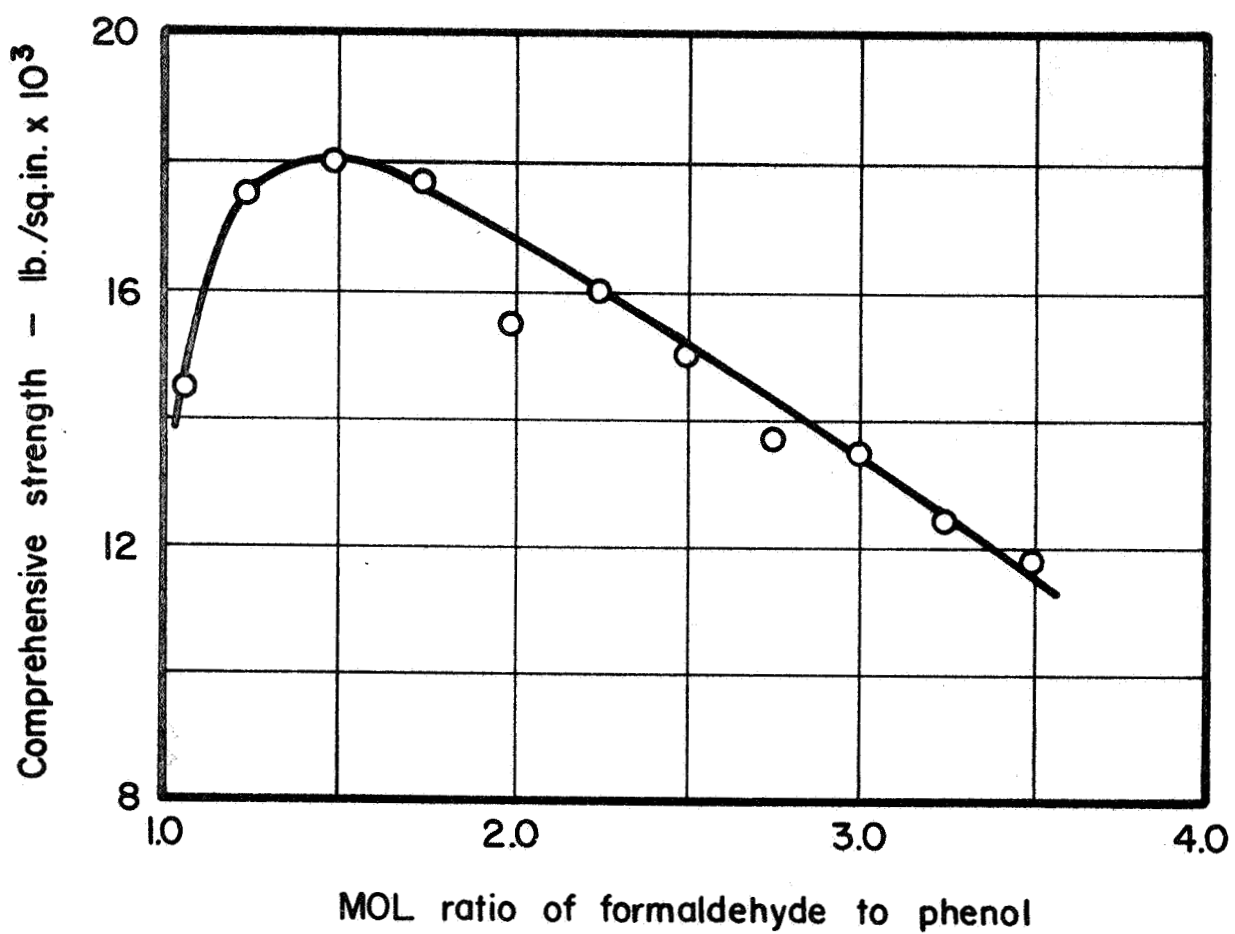


Fig. 4-3. Effect of proportion of reactants on the compressive strength of phenol-formaldehyde cast resins. (After Thompson, 1941.)

Experimental Laboratory Procedure

Soil.

A moderately expansive, light brown, inorganic sandy clay (CL) from Pittsburg, California, was used. Classification data for this soil are summarized below:

1. Percent sand, 33%; percent silt, 43%; percent clay, 24%;
LL(%), 35; PL(%), 19.
 2. Maximum dry density, 118.9 psf
 3. Optimum water content, 13.5%
- } Modified AASHO.
4. Mineralogical analysis of the clay fraction showed that the clay minerals present are predominantly montmorillonite with a trace of kaolinite.

Preparation of resin.

A special flask was used for preparing the resin to be used in treating the soil. First, the desired amount of paraformaldehyde was poured into the flask. Then phenol was added. After adding a certain amount of water and sodium hydroxide, the batch was mixed using a constant speed mixer. The temperature was kept nearly constant at about 77 °C. This was necessary, since temperature will increase exponentially and cause the reaction to be violent. Typical time-temperature curve is given in Figure 4-4. The resin was cooked* about 2 to 2½ hours until the appearance of the first turbidity. The resin was neutralized by adding the proper amount of some organic acid such as lactic acid.

Specimen preparation.

Soil at the desired water content was mixed with activated resin.[†] Mixing was continued until a homogeneous mix was obtained. Specimens

* The reaction described in the previous section takes place during the cooking process.

† Laboratory-cooked resin was activated by adding different amounts of acids and bases before mixing with soil.

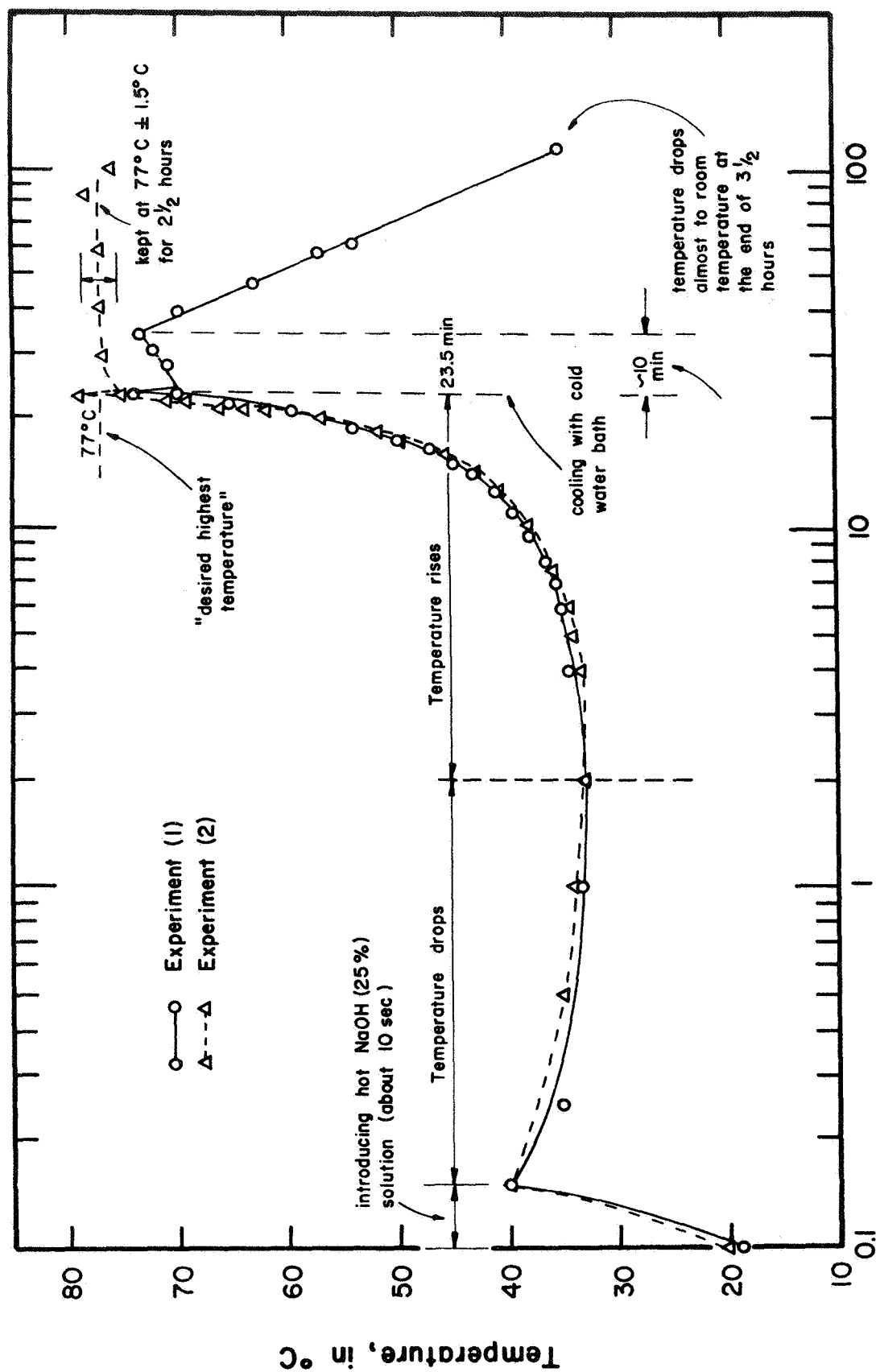


Fig. 4-4. Typical reaction time vs temperature for mole ratio of F/P = 1.5, and 0.3 mol NaOH for 1 mol phenol as catalyst.

were compacted in 1.4-inch-diameter Harvard miniature compaction molds using the general procedure described by Wilson (1964). Seven layers of soil with fifteen tamps per layer were used for the preparation of all specimens. Compactive effort was held constant by applying 12.5 pounds of force to the compaction foot.

RESIN SYSTEMS DEVELOPED

A summary of resin systems developed in the laboratory and the amount of ingredients used in these systems are given in Table 4-1.

ENGINEERING PROPERTIES OF STABILIZED SOIL MASSES

The unconfined compression test was chosen as a standard for evaluating the strength of the stabilized soil masses. A summary of test results is given in Tables 4-2 and 4-3. All of the specimens were cured at constant temperature in a 100% humidity room. The low strength values indicated that the resin systems were not properly hardened inside the soil masses. It is believed that this was due to the presence of a large amount of water in the system. Therefore, in future studies, the water content should be held as low as possible. Hardening mechanisms of the resin were studied by adding different amounts of acidic and basic catalysts to the resin. An amount of sulfuric acid sufficient to produce a pH value less than 2.0 resulted in satisfactorily cured resins in the absence of soil. However, the use of basic catalysts did not yield satisfactorily hardened resin; no perceptible curing was observed.

SUMMARY AND CONCLUSIONS

The feasibility of using phenolic resins as admixture soil stabilizers was studied. The chemistry of resin systems, controlling factors of reactions, and the effects of different factors on curing were also investigated.

Several systems were developed which, on theoretical grounds, appear to offer some potential for stabilization. It was found, however, that soils treated with these materials were not satisfactorily stabilized. The probable cause of this poor performance was the inclusion of large amounts of water in the resin system. To avoid the inclusion of excess water in treated soil systems, powder resin forms should be investigated.

Table 4-1. Amount of ingredients in resin systems.

Systems	Chemical ingredients	HCHO-to- C_6H_5OH ratio	Amt. of catalyst	Amt. of H_2O (gr)	Resini- fication temp (°C)	Resini- fication time (hrs)	Amt. of $HO-(CH_2O)_nH$ (95%, gr)	Amt. of C_6H_5OH (gr)	Amt. of NaOH (gr)	Amt. of $C_3H_6O_3$ (85%, gr)
1	$HO-(CH_2O)_nH$ (M.W.=90.09)									
	C_6H_5OH (M.W.=94.11)									
	NaOH (M.W.=40.00)	1.5/1.0	0.3 mole of NaOH for each mole of C_6H_5OH	344.5	74	3½	219.5	436.0	55.80	148.50
	H_2O (M.W.=18.00)									
2	$C_3H_6O_3$ (M.W.=90.08)									
	as system 1	1.5/1.0	"	344.5	75	2½	219.5	436.0	55.80	148.50
3	as system 1	1.7/1.0	1.5 gr of NaOH for each mole of C_6H_5OH	172.2	77	2½	250.0	436.0	6.96	18.42
4	$HO-(CH_2O)_nH$ (M.W.=90.09)	1.7/1.0	none	none	not cooked	—	250.0	436.0	none	none
	C_6H_5OH (M.W.=94.11)									

Table 4-2. Summary of test results for system 3.

Trial	Catalyst	pH	Resin (%)	Water content (%)	Dry density (pcf)	Unconfined compressive strength (psi)
1	Base (NaOH)	9.0	15	2.2	120.2	26.7
2	Base (NaOH)	10.0	15	2.2	117.3	20.0
3	Base (NaOH)	10.4	15	2.2	110.0	14.0
4	Base (NaOH)	10.0	15	2.2	107.2	13.0
5	Base (NaOH)	10.0	15	7.2	106.1	10.0
6	Acid (H_3PO_4)	2.4	15	2.2	113.5	36.7
7	Acid (H_3PO_4)	1.8	15	2.2	117.0	44.7
8	Acid (H_3PO_4)	1.9	10	7.2	122.2	60.0
9	Acid (H_3PO_4)	1.9	5	7.2	115.3	70.0

* Specimens were cured 7 days.

Table 4-3. Summary of test results for system 4.

Trial	Catalyst	Curing time (days)	Resin (%)	Water content (%)	Dry density (pcf)	Unconfined compressive strength (psi)
1	Acid (H_2SO_4)	5	15	2.2	100.0	26
2	Base (NaOH)	5	10	2.2	109.8	20
3	Acid (H_2SO_4)	5	5	2.2	107.8	16
4	Acid (H_2SO_4)	5	10	7.2	107.9	26
5	Acid (H_2SO_4)	5	5	7.2	104.0	24
6	Acid (H_2SO_4)	4	5	12.2	111.7	11
7	Acid (H_2SO_4)	4	10	2.2	111.1	10
8	Base (NaOH)	2	15	2.2	100.2	~0
9	Base (NaOH)	2	10	7.2	101.5	~0
10	Acid + resor- cinol	2	15	2.2	96.5	5
11	Base + resor- cinol	2	10	2.2	101.7	~0

REFERENCES

Thompson, W. R. (1941), *Chem. Inds.* 48, pp.450-456.

Wilson, S. D. (1964), "Suggested Method of Test for Moisture-Density Relations of Soils Using Harvard Compaction Apparatus," *Procedures for Testing Soils*, 4th ed., ASTM, 1964.